A Thesis submitted for the Degree of

Doctor of Philosopy

OVERHUNG BORING BARS---The performance of undamped and damped bars under static and dynamic conditions when machining metals

Y.H.J.Au

DEPARTMENT OF

PRODUCTION TECHNOLOGY

JUNE 1980

BRUNEL UNIVERSITY

To my mother and Eileen

ABSTRACT

The work of the author was to investigate the static, dynamic and machining behaviour of some new designs of slug damped boring bars with a 10 to 1 overhang ratio. The bars were mounted on a centre lathe.

The static behaviour of a boring bar in relation to the geometric form errors that might be produced during boring was studied both analytically and experimentally. Specifically, two types of errors were considered, namely,

a) errors that arise on entry of the boring tool into the workpiece, known as the "bell-mouth" errors; and

b) reproducibility of eccentricity errors, known as the "copying" errors.

The theory for "bell-mouth" errors did not seem to fit the results well; however, the theory did prove that such errors could exist. The theory for "copying" errors agreed remarkably well with the results provided that the initial eccentricity was small compared with the depth of cut.

The dynamical behaviour of the slug damped boring bar was modelled by a mathematical analogue. Despite its inability to properly account for the compressibility effect of the gaseous damping fluid, the model revealed the possibility of design improvements. In consequence, the optimally-tuned slug-damped tungsten-bunged bar was conceived, manufactured and tested along with a solid bar for comparison purposes, a slug-damped recessed bar and a slug-damped steel-bunged bar.

The machining behaviour of a boring bar was studied in terms of the maximum depth of cut that it could cope before the occurrence of chatter. At first, a stability model was developed based on the mathematical analogue formulated in the study of the dynamical behaviour. But since this analogue did not fit

the results accurately, a second and more precise model was set up using the frequency response obtained from dynamic experiments instead. The concept of negative damping coefficient was used; and a one-to-one correspondence between the asymptotic value of the negative damping coefficient and the limiting depth of cut was found to exist. By virtue of this, it is in principle possible to predict the limiting depth of cut of any machine tool system whose frequency response characteristics are known.

Compared with other bars tested, the optimally-tuned tungsten-bunged bar was found to have the best dynamic and machining characteristics as reflected in the limiting depth of cut of 0.105" (2.67 mm) to 0.110" (2.79 mm) at the feed of 0.0065"/rev (0.165 mm/rev) and the speed of 500 rpm on a 3½" dia. bore (140 m/min) of EN8 steel. By constrast, the solid bar was hardly able to cut stably even at the light cut of 0.005".

ACKNOWLEDGEMENT

The author wishes to acknowledge Professor R W New for his many valuable suggestions and supervision in the course of this research, in particular, for his conception and design of the tungsten-bunged boring bar.

The author is also indebted to all the technical staff in the Department of Production Technology, in particular, Messrs E H Cittern, S Mutters, and G Neller for their help in the manufacture of the equipment and the setting up of the instruments.

Special gratitude is owed to the Science Research Council for their generous financial support, and to Mrs A Brindley for typing this thesis.

LIST OF FIGURES

CONTENTS

1. INTRODUCTION

The designer of overhung boring bars is often faced with two conflicting requirements:

(1) the bar must be rigid enough to resist chatter and to minimize errors of geometric form; and

(2) it must be long enough to profile bore deep into the workpiece.

Naturally the main consideration is to eliminate the occurrence of chatter by means other than increasing stiffness brought about by the reduction in overhang.

Given a fixed overhang ratio, it is possible to increase the stiffness of the boring bar by utilizing stiffer materials of high modulus of elasticity. Tungsten-carbide which has a modulus of elasticity 2.5 to 3 times that of steel is often used. Nevertheless, in addition to being expensive to manufacture, the tungsten bars are very brittle and are readily fractured if they are dropped.

Another way of increasing resistance to chatter is to employ damping devices in the boring bar. The wide variation in chatter frequencies, that occurs when the bar is used over a wide range of cutting condition and workpiece materials, virtually rules out the use of highly tuned spring-type vibration absorber. The use of impact damper does not provide a satisfactory answer either, due to the fact that the device operates only when a certain level of vibration is exceeded and even then it serves only to limit the build up of the amplitude but not to suppress the vibration altogether. The use of Lanchester damper, as reported by Hahn[1], for the suppression of chatter is a feasible proposal. Such a device possesses a

damping characteristic which is operative over a wide range of frequencies and hence is a suitable candidate for consideration. In the same paper, Hahn performed a simple analysis of the dynamical behaviour of the Lanchester-damped boring bar based on a simple yet revealing lumped-parameter model in which the respective masses of the bar and of the slug-damper were coupled together by a linear dashpot. From his analysis, Hahn concluded that the dynamic performance of the bar improves as the ratio of the absorber mass to the equivalent mass of the bar, termed for short the mass ratio, increases. Despite the simplicity of the model, this conclusion is still valid for the real physical system and offers possible scope for improved boring bar design.

A greater mass ratio can be achieved by way of increasing the absorber mass or reducing the equivalent mass of the bar or both. Physically, there are limitations on the manner that the two masses can be altered. The absorber mass, for example, cannot be increased without causing any possible reduction in the effective stiffness of the bar. Similarly, reducing the equivalent mass of the bar will bring about the same effect. The search for an optimum is obvious; but it must be conducted in a logical and analytical manner. Otherwise time and financial resources will not be utilised efficiently.

Various stability theories have been developed whereby the stability borderline can be evaluated. Unfortunately, the stability borderline thus evaluated is not directly related to the cutting parameters such as depths of cut, feeds or speeds, and hence the usefulness of these theories is severely limited. Improvements to these theories are needed.

In view of the problems presented, this project was conducted in the hope to find a satisfactory solution and to make recommendations. The work was executed in the following stages.

(1) Tentative analysis of geometrical form error under stable machining conditions.

(2) The generation and removal of form errors.

(3) Analytical and experimental investigation of the dynamic behaviour of boring bars.

(4) Optimal design of boring bar in terms of its frequency response characteristic and its resistance to chatter during boring.

(5) Stability analysis of boring bar during boring using the concept of negative damping as the source of instability.

(6) Stability boring tests to determine the stability borderline in terms of the limiting depth of cut. Also problems arising from the boring tests, namely, chip curl and fracture, and removal of chips from deep bores.

(7) Correlating negative damping to the limiting depth of cut.

The exposition of this thesis essentially follows this order.

References for Chapter 1

(1) HAHN R S "Metal cutting chatter and its elimination" Trans ASME 75, 1953, p 1073

2. LITERATURE SURVEY

Profile boring is a machining process relied upon to generate truly round holes of straight or curved profiles. The principal tool involved is the boring bar which in the main consists of a boring tool held in the free end of the bar. Metal removal is achieved by means of the relative rotational and axial motions between the workpiece and the boring bar. To a manufacturer employing profile boring operations, two issues are of immediate concern:- 1) the accuracy of profile generated and 2) the ability of the boring bar to resist chatter. While it is true that the phenomenon of chatter always results in a poorer machining accuracy, for the sake of discussion we consider here that the first issue is related to the stable machining alone and the second to unstable machining.

Stable machining simply means chatter-free machining. It follows that the dynamics of the machine-tool and of the cutting process can be ignored in any theoretical considerations of geometrical errors that may appear on the finished workpiece as a result of the boring operation. The subject will be taken up in section 2.1.

Unstable machining, on the other hand, refers to machining in which chatter is present. On account of the generally high frequency associated with the chatter phenomenon, the dynamics of the machine-tool and the cutting process cannot be assumed negligible. Their significance is shown up in theories put forward by investigators in this subject. A survey of their work is presented in sections 2.2, 2.3, 2.4 and 2.5.

Finally,with a knowledge of the theoretical development, we are then in a position to appreciate how the theories are put into practice by

looking at some different designs of boring bars that are available on the market or have been made known in publications. This is presented in section 2.6.

2.1 GEOMETRIC FORM ERRORS AND ECCENTRICITY ERRORS IN BORING

Hahn[1] was one of the first investigators who looked into the problem of geometric form error. By considering the case of precision boring in which the hole, as shown in fig.2.1, has an initial eccentricity e_r and a final eccentricity e_f as a result of the machining, Hahn arrived at the expression

$$e_f = \frac{K_w}{K_w + K_q} e_r \qquad (2.1)$$

in which K_w is a material constant defined as the rate of increase of thrust force with respect to the depth of cut, and K_q the stiffness value at tool point.

According to Tlusty and Koeingsberger[2] the practical value of K_q for stable machining is much higher than that of K_w, being of the order of hundreds or even up to a thousand, the final eccentricity e_f in eqt(2.1) is, therefore, much less than the initial eccentricity e_r. Since the term $K_w/(K_w + K_q)$ is a measure of the error retained, it is called the "copying error".

Hahn developed eqt(2.1) further to include the case in which the hole is bored out n times in succession, the final eccentricity e_f is then

$$e_f = \left(\frac{K_w}{K_w + K_q} \right)^n e_r$$

Obviously the precision is drastically improved as the number of passes n increases.

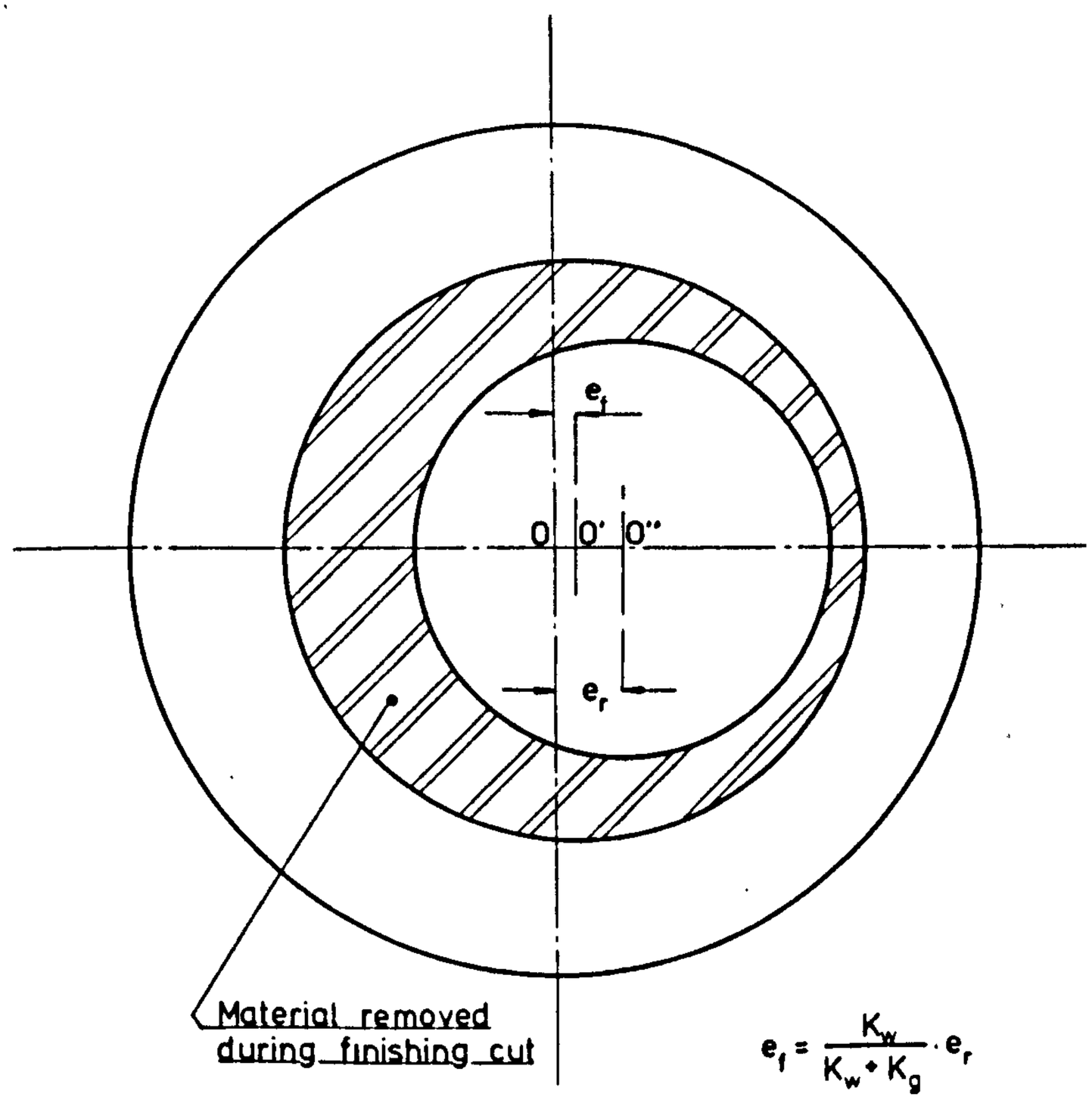

O . Centre of rotation of workpiece

O'. Centre of finished bore

O''. Centre of pre-finished bore

Fig 2.1 Effect of initial eccentricity on final eccentricity of finished bore

The effect of stiffness of machine tool structure, of which the boring bar is one, on the geometric accuracy was also studied by Birchall et al[3] at PERA. Taking a general machining situation in which the tool was to take a nominal depth of cut d', they derived that the total depth of metal removed, u_n, after n cuts was

$$u_n = nd' - \mu d' \cdot \left[1 - \left(\frac{\mu}{1+\mu}\right)^n\right] \quad (2.2)$$

where $\mu = \frac{C}{K}$ in which C designates the rate of change of thrust force with respect to the depth of cut and K is the static stiffness at the tool point in the direction of the thrust force.

We can identify μ in eqt(2.2) with the ratio K_w/K_q in eqt(2.1) and by the previous comment of K_w/K_q, is seen to be small in magnitude. As the number of cuts n is increased, eqt(2.2) becomes

$$u_n = nd' - \mu d'$$

On the right side of the equation, the first term denotes the total nominal depth of metal that would have been removed were there no tool deflections and the second term represents the amount of geometric error consequent upon the operation. This error is seen to settle down to a final value as the number of cuts n becomes large and can be reduced if the value of μ is made small. The observation is in accord with that of Hahn.

Tlusty and Koenigsberger[2,4] identified two causes of geometric errors:- 1) the variation in the depth of cut due to an initial form error Δ is copied in the cut to produce a final form error δ after the cut; and 2) the variation in the resulting compliance between the tool and the workpiece during the tool travel. With regard to (1) which is virtually the case discussed by Hahn, Tlusty and Koenigsverger obtained the relation,

$$\delta = \frac{\mu}{1+\mu}\Delta \quad (2.3)$$

where μ is defined in the same manner as that of Bitchall et al and is the ratio K_w/K_q in the work of Hahn. It is, therefore, to be expected that eqts(2.1) and (2.3) are in complete agreement. In respect of (2), Tlusty and Koenigsberger noted that the error after one cut is

$$\delta = a(\mu_{max} - \mu_{min})$$

where a is the depth of cut. The equation indicates that this type of error depends on the depth of cut as well as on the variation of the compliance.

By likening a round boring bar to a simple cantilever and hence the stiffness at the tool point is

$$K = \frac{3EI}{L^3} = \frac{3E\left(\frac{\pi D^4}{64}\right)}{L^3} = \frac{\frac{3\pi}{64}ED}{(L/D)^3} \qquad (2.4)$$

where E is the modulus of elasticity, $I = \frac{\pi D^4}{64}$, the second moment of area, L and D the respective length and diameter of the cantilever, Au and New[5] looked into the effect of diameter on the acceptable L/D ratio, known as the overhang ratio, and on the overhung length of steel boring bars. Three cases are considered:- 1) precision boring practice, 2) normal workshop practice, and 3) stability borderline conditions. The results are presented graphically in fig. 2.2.

2.2 VIBRATIONS IN CUTTING

Vibrations in cutting are commonly referred to as chatter. When chatter occurs, the tool and work move relative to each other in the plane normal to the cut surface. Whether chatter will be maintained or suppressed, according to Tlusty[4], depends on 1) the dynamics of the cutting process, 2) the dynamics of the machine tool at the tool point, and 3) the mutual directional orientation of 1) and 2). Tlusty showed the relation in the form

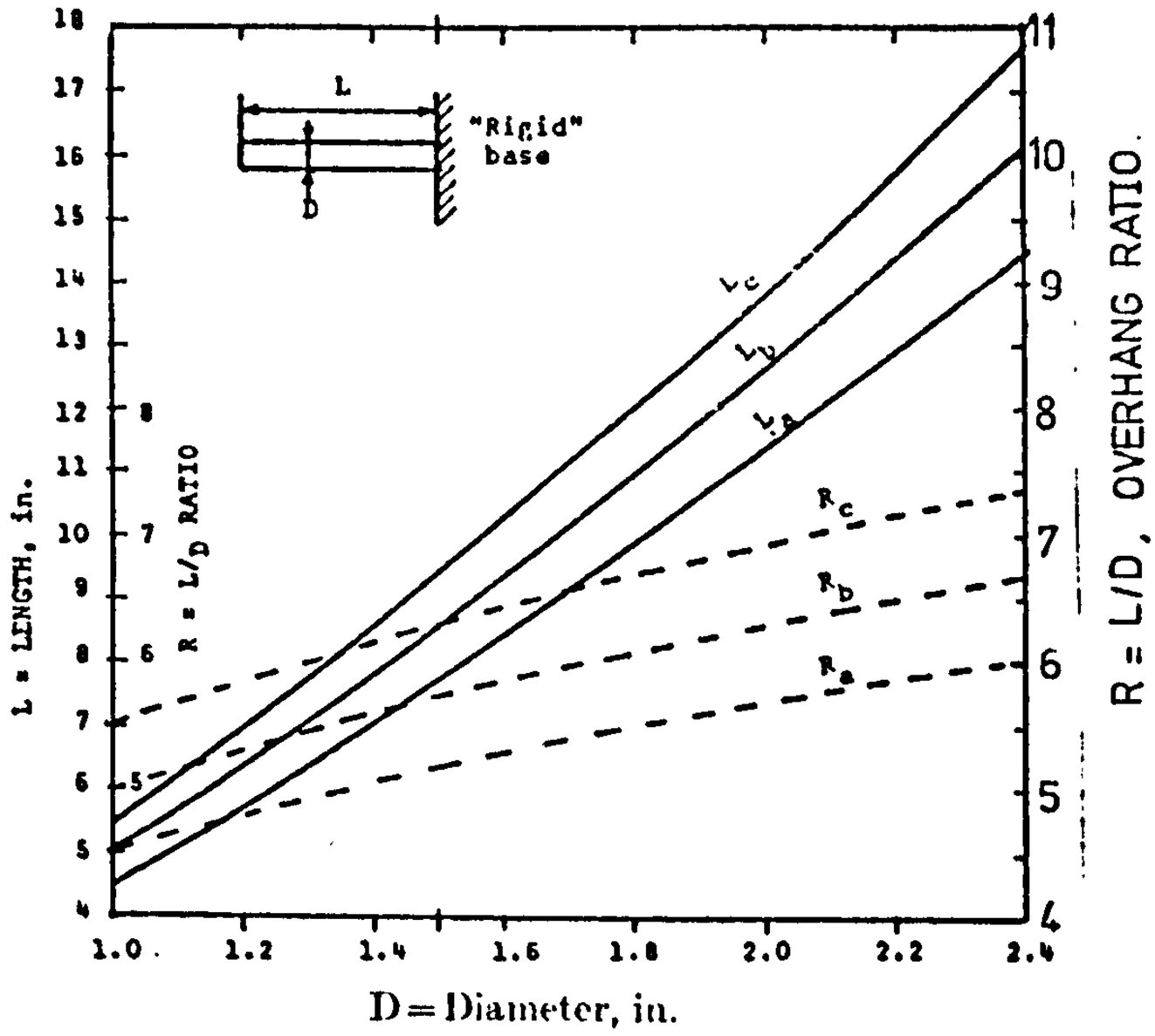

Fig 2.2 Effect of diameter on acceptable L/D ratio and overhung length of steel boring bars. (a) Precision boring practice; (b) Normal workshop practice; (c) Stability borderline conditions. (5)

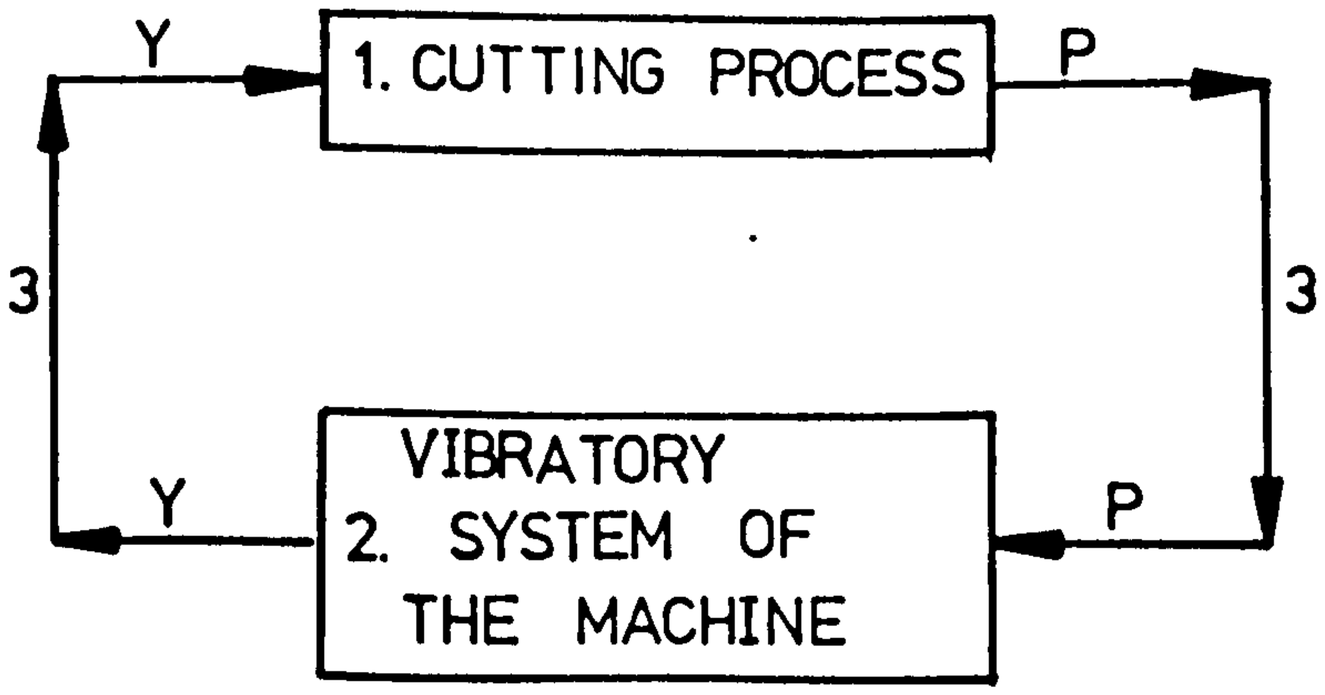

Fig 2.3 Basic diagram of chatter (4)

of a block diagram as in fig. 2.3, from which it is obvious that fluctuations of the cutting process produce a cutting force variation P that acts on the machine tool and creates a vibration Y. The loop is closed by way of Y causing further fluctuations of the cutting process.

There are three main types of vibration that may occur in cutting. First, there is the free vibration that is seen to arise immediately after an impact or shock. The vibration normally dies down fast enough if the machine tool possesses sufficient damping. Second, there is the forced vibration generated from a source either inside or outside the cutting process itself. Intermittent cutting, for example, belongs to the source generated and maintained by the nature of the cutting process alone. In contrast, unbalance in machine tool drive brings about vibrations from a source outside the cutting process. Despite this distinction, all forced vibrations possess the unique feature that the frequencies are constant and are readily determined and their suppressions are, therefore, relatively straight forward. Third, there is the self-induced vibration, so called because the cutting process itself provides sufficient energy to initiate and to maintain vibration. By virtue of this definition, self-induced vibration will include primary chatter, regenerative chatter and chatter due to mode-coupling effects. This type of vibration is much more difficult to investigate and hence to suppress due to the fact that its frequency of vibration varies with variations in the cutting process dynamics, in the dynamics of the machine tool and in their mutual orientation.

In the study of vibrations in machining, the term 'stability borderline' is very often used. From the control engineering point of view, stability of a linear dynamical system is determined by the nature of its characteristic roots. According to Porter[6], there are the following distinctions of stability:-

1) A system is 'marginally stable' if its impulse response remains bounded as the time $t \rightarrow \infty$. This corresponds to the characteristic equation having exactly one pair of imaginary conjugate roots, other roots may be negative real or complex conjugate with negative real parts.

2) A system is 'asymptotically stable' if its impulse response dies down as the time $t \longrightarrow \infty$. This corresponds to characteristic roots that are negative real or complex conjugate with negative real parts.

3) A system is 'unstable' if its impulse response becomes unbounded as time $t \rightarrow \infty$. This corresponds to characteristic roots that are positive real or complex conjugate with positive real parts.

These distinctions can also be depicted graphically by the s-plane representation. In fig. 2.4 is shown an s-plane which is divided into four quadrants by the $\sigma-$ and $\omega-$ axes which can be regarded as the real and imaginary axes respectively. A characteristic root has the form of a complex number which can be represented as a point in the s-plane. We are then able to make the following identifications:-

1) Marginal stability is said to occur when all characteristic roots fall in the region defined by $\sigma \leqslant 0$

2) Asymptotic stability is said to occur when all characteristic roots lie in the region defined by $\sigma < 0$

3) Instability is said to occur when there is at least one characteristic root lying in the region defined by $\sigma > 0$

Based on these identifications, the 'stability borderline' can be taken to correspond to the ω-axis in the s-plane of fig. 2.4 because the system becomes unstable if any of its roots cross the ω-axis into right-half plane.

2.3 DYNAMICS OF CUTTING PROCESS

The study of the cutting process dynamics is mainly concerned with the amplitude and phase relations between the tool displacement and the resulting cutting force variations. Reviewing the work of previous investigators, Armarego and Brown[7] remarked that the cutting process itself has inherent periodicity in the sense that the cutting force varies periodically despite a constant metal removal rate. The periodicity may be caused, for instance, by the successive built-up-edge formation and fracture[8,9], the chip segmentation[10-14], and the discontinuous chip formation[15-17]; but the force variations thus produced are small in comparison with those which give rise to self-induced vibrations.

The first attempt to model mathematically the process of self-induced vibration in cutting was made by Arnold[8]. His model was formulated on the basis of a particular characteristic of the cutting process which is the negative slope of the cutting force versus cutting speed curve and with the assumption that the machine tool system could be approximated to a simple spring-mass-dashpot system. He demonstrated that the negative slope was analogous to some measure of the negative damping due to the cutting process and that if this damping exceeded the positive damping that the machine tool system created, instability would result.

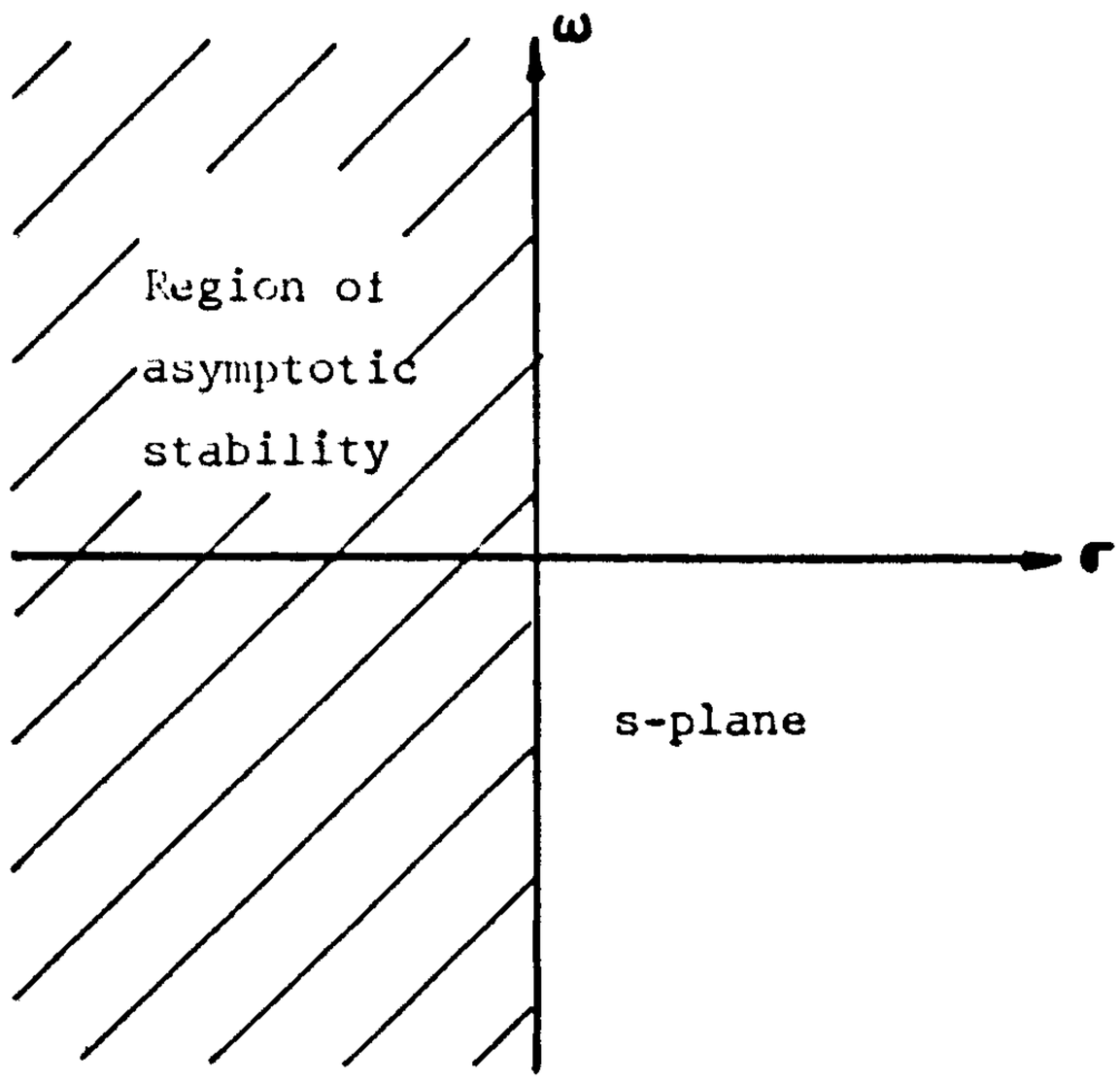

Fig 2.4 Region of asymptotic stability in the s-plane [6].

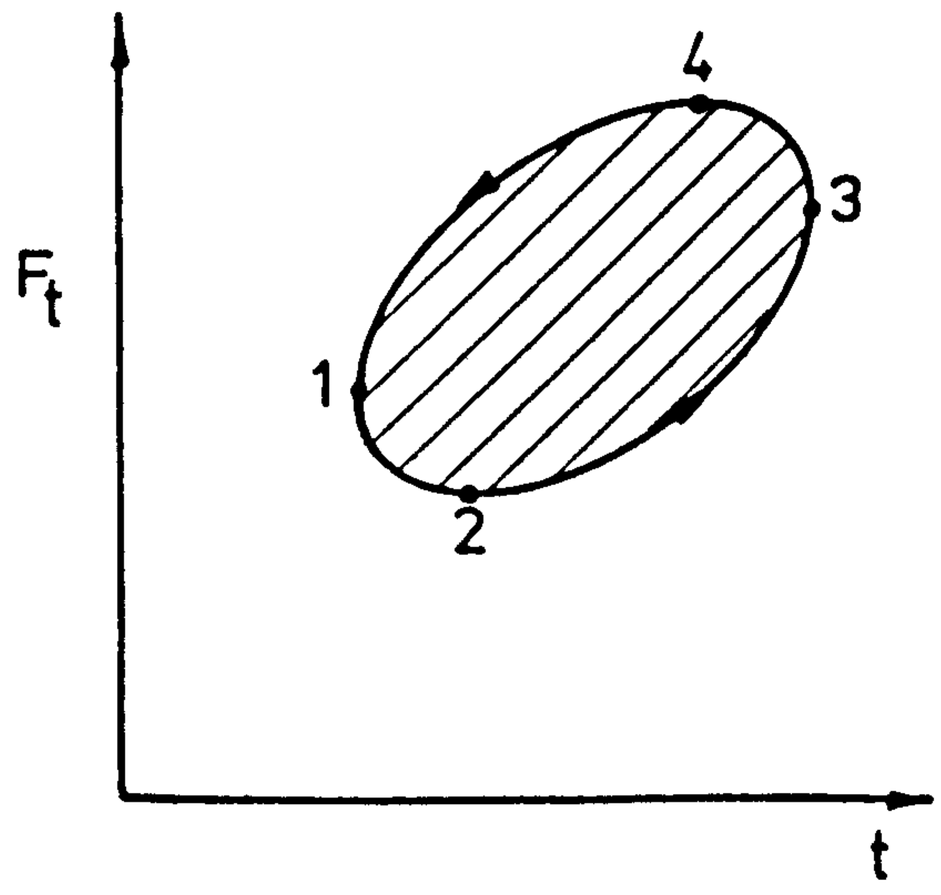

Fig 2.5 Energy loop (shown shaded) in cutting. F_t denotes the thrust force component and t the depth of cut [11].

Commenting on Arnold's work, Doi and Kato[9], and Hahn[10] pointed out that the negative slope of the cutting force curve was not steep enough to explain the self-induced vibration. Hahn even quoted cases of zero slope at high cutting speeds and yet chatter occured. Shaw and Holken[11], however, remarked that these criticisms were improper since they were based on force values measured under steady-state conditions. To add support to their view, they quoted the data of Holken obtained under dynamic cutting conditions and showed that 1) dynamic forces were in general lower than steady-state forces and 2) the negative slope of the dynamic force-speed curve was much steeper.

In an effort to explain the occurrence of self-induced vibration, Doi and Kato[9] suggested that it was primarily due to the phase lag of cutting force behind the vibrational movement and that the lag was inherent in the cutting process. By virtue of this lag, some energy was available to maintain vibration. Shaw and Holken[11] derived expressions of the cutting and thrust forces for the cases of decreasing and increasing depths of cut. They concluded that the instantaneous forces at any particular depth of cut were higher for decreasing depth than for increasing depth as is shown by the elliptical curve in fig. 2.5. The shaded area in the ellipse is the energy available in each cycle to maintain vibrations.

Smith and Tobias[12] disagreed with the contention that force lag was an inherent feature of the cutting process. They suspected that such a force lag was a product of the low frequency chatter of the test machine used in the experiment of Doi and Kato. From the results of the wave-producing experiments they conducted, they concluded that the

thrust force lagged the tool oscillation at frequencies of oscillation below 40 Hz; but above this frequency the force led the tool oscillation. Wave-producing experiments refer to experiments in which cutting is performed on a plain surface with the tool oscillating sinusoidally normal to the surface. Their results are reproduced in fig. 2.6. Nothing conclusive was, however, said of the main cutting force.

Shumsheruddin[13] repeated the experiment conducted by Smith and Tobias using the same set-up. He found out that the force lag at low frequencies as reported by Smith and Tobias was partly caused by the speed-dependent torsional oscillation of the test machine as a result of the torque fluctuations brought about by the cutting force fluctuations. It, therefore, cannot be concluded that the force lag is caused by the cutting process alone. For the test machine used, the torsional characteristic was found to differ at low and high speeds because of the different gear arrangements required to obtain these speeds. Shumsheruddin remarked that, had this been taken into account, the force lag observed at low frequencies would be more pronounced. Apart from this, he also made the following observations:- 1) the thrust force variation always leads the tool oscillation, the amount of lead increasing with cutting, and 2) the main cutting force lags the tool oscillation at low and medium speeds, but at higher speeds, it leads the oscillation, the amount of lead increasing with cutting speed.

Albrecht[14] conducted a similar wave-producing experiment and observed that both the thrust and main cutting forces led the tool oscillation, the lead increasing with frequency. Although results obtained by various investigators are apparently different, Das et al[18] noticed

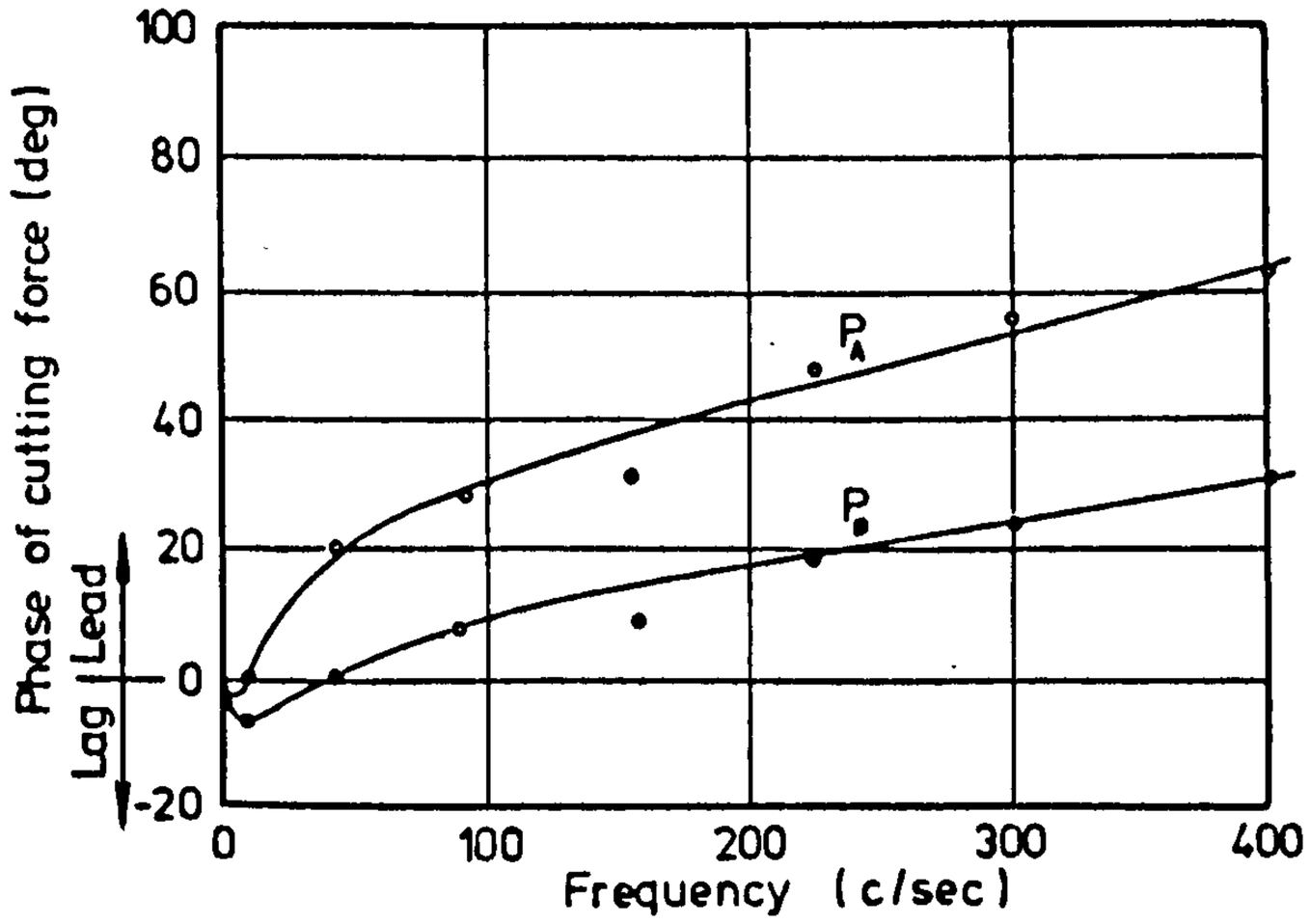

Fig 2.6 Typical experimental results concerning phase relation between normal thrust P_A and tangential thrust P_B and the chip thickness variation, as a function of the frequency of oscillation[12]

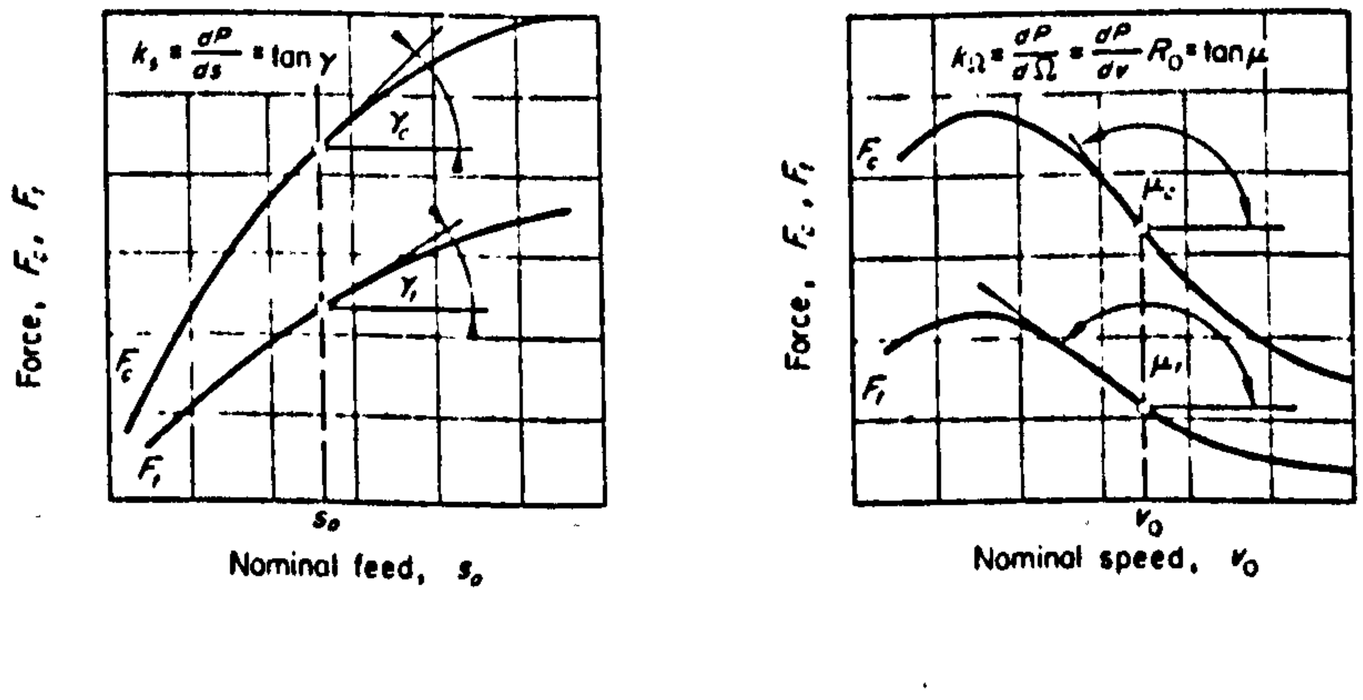

Fig 2.7 Determinations of cutting coefficients[15]

a) cutting force coefficient k_s

b) cutting speed coefficient k_Ω

some points of agreement among them:-

1) the main cutting force and the thrust force components are neither in phase with each other nor with the tool motion;
2) the thrust force component always leads the tool motion while the main cutting force component either lags or leads the tool motion; and
3) the phase and amplitude of the force component depend on the wave-length of the wave generated on the workpiece.

On account of this, it is reasonable to model the dynamic cutting force components, namely, the main cutting and the thrust forces, such that they consist of an in-phase component and a quadrature component to account for the force lag or lead effects. Thus, using complex variable representation in which the real part is designated as the in-phase component and the imaginary part as the quadrature component, a force increment dP may be written

$$dP = P(\cos\theta + j\sin\theta) \qquad (2.5)$$

P is the absolute magnitude of the force increment dP, and θ the amount of phase lead or lag that dP has relative to the tool motion. It must be noted that dP disappears at steady-state cutting. The in-phase component $P\cos\theta$ is produced by the uncut chip thickness variation and is in general much larger in magnitude compared with the quadrature component. The quadrature component $P\sin\theta$ is produced by the variations of 1) the cutting speed, 2) the instantaneous cutting direction, 3) the tool clearance and rake angles, 4) the feed rate and 5) the free surface slope.

Two models of the dynamic cutting process will be presented in the two sections that follow. Both are often employed in the machining stability analysis.

2.3.1 CUTTING FORCE MODEL OF TOBIAS AND FISHWICK[15]

By considering changes from one steady-state to another, Tobias and Fishwick showed that small, but otherwise arbitrary, changes of uncut chip thickness s by ds, feed rate r by dr, and rotational speed Ω by $d\Omega$ caused a variation of cutting force dP that may be written

$$dP = wk_1 ds + wk_2 dr + wk_3 d\Omega \qquad (2.6)$$

where w is the chip width; k_1, k_2, and k_3 are termed the dynamic cutting force coefficients. For the case of turning, they related these coefficients to the steady-state coefficients k_s and k_Ω by

$$k_2 = 2\pi \frac{(k_s - k_1)}{\Omega} \qquad (2.6.1)$$

and

$$k_3 = k_\Omega \frac{(k_s - k_1)}{\Omega}$$

where k_s and k_Ω are the slopes of the respective steady-state force-feed and force-speed curves as shown in Fig 2.7.

According to Tobias and Fishwick, since the dependence of the cutting speed is negligibly small in general, then dr and ds will depend only on the normal oscillation of the tool. The variation of the uncut chip thickness ds can be expressed as the difference between the two successive passes x(t-T) and x(t) where T is the time lag between them, and for sinusoidal oscillation dr=jx(t). Eqt (2.5) then becomes

$$dP = wk_1 [\, x(t) - \mu x(t-T) \,] + jwk_2 x(t) \qquad (2.7)$$

where μ is defined as the overlapping factor which is a measure of the influence of the previous pass on the present pass in terms of force. Eqt (2.7) is seen to have the same form as eqt (2.5).

2.3.2 CUTTING FORCE MODEL OF TLUSTY[4]

In this cutting force model, the cutting force P is related to the chip width b, and to the uncut chip thickness variation $(Y-Y_o)$ where Y and Y_o are the vibrations of two successive cuts of the tool relative to the workpiece in the direction normal to the nominal cut surface. The relation is $P = -br(Y-Y_o)$ (2.8)

Tlusty called r a coefficient and reasoned that its value was constant and real if all other cutting conditions, apart from b, were held fixed. It follows that the cutting force P changes instantaneously with the change in the uncut chip thickness $(Y-Y_o)$; and eqt (2.8) may be regarded as a special case of eqt (2.5) in which the quadrature force component $P\sin\theta$ disappears. By virtue of the fact that the in-phase component $P\cos\theta$ is often much larger than the quadrature component $P\sin\theta$, Tlusty's assumption that r is real, though inexact, yields a simple yet functional expression as eqt (2.8). In some of his later work, Tlusty recognised and accounted for the complex nature of r and the resulting cutting force expression is then in complete accord with eqt (2.5).

With reference to eqt (2.6) of Tobias and Fishwick, the dynamic force coefficient k_2 can be expressed in terms of k_1 and k_Ω by eqt (2.6.1) and so eqt (2.7) can be seen to be in terms of k_s, k_Ω, and k_1. As mentioned previously, k_s and k_Ω are static coefficients that are readily determined from steady-state experiments, but k_1 is a dynamic coefficient which, according to Tobias and Fishwick, can only be determined from dynamic experiments. Collecting dynamic cutting data will involve a great deal more work because an additional parameter, namely, the frequency of oscillation, has to be incorporated into the design and the performance

of the experiments. For this reason, results that are obtained from one particular dynamic condition may become completely useless in another. Naturally one would prefer theories that permit one to predict the dynamic cutting force on the basis of the well-documented knowledge of the steady-state cutting force data. Any attempt to develop such theories will have to start from the hypothesis that a causal relationship exists between the steady-state and dynamic cutting.

Das and Tobias[16], Wallace and Andrew[17,19], Albrecht[14], and Grieve and Rubenstein[20] believed that this causal relationship exists. That is to say, the dynamic force can be determined from fundamental principles by taking account of the effects of cutting parameters such as the uncut chip thickness, the cutting speed, the instantaneous cutting direction, the tool clearance and rake angles, the feed rate and the free surface slope. The theories of Albrecht[14] and Wallace and Andrew[17,19] only allow a qualitative description of the dynamic cutting force which indicates that the chip formation mechanism in vibratory cutting may produce either a leading or lagging force relationship. On the other hand, the theories of Das and Tobias[16] and Grieve and Rubenstein[20] attempt to quantify the dynamic cutting force but the agreement between predicted and experimental results is poor.

Some investigators, notably Doi and Kato[9], and at one time, Tobias and Fishwick[15] believe there is something more which only occurs in dynamic cutting and so the dynamic cutting force can only be determined by way of dynamic cutting tests. According to Doi and Kato, the force phase lag is a fundamental effect believed to be induced by the action of the friction force on the tool face because the friction force cannot

change instantaneously with changes in uncut chip thickness.

2.4 DYNAMIC CHARACTERISTICS OF MACHINE TOOL STRUCTURE

The dynamic characteristic of a mechanical system is usually presented graphically by means of 1) its amplitude response and 2) its phase response to a sinusoidal input that varies over a range of frequencies of interest. Typical amplitude and phase responses are shown in the respective diagrams (a) and (b) of Fig 2.8. There is also a neater graphical representation known as the harmonic response locus which combines the magnitude and the phase in the form of a polar plot as shown in Fig 2.8c.

In mathematical terms, the dynamic characteristic of a system is described by the dynamic receptance defined as the displacement per unit force and is a function of frequency. Since displacement and force are vector quantities, a further clarification is needed on the term dynamic receptance: if the displacement of interest and the applied force which is the input are in line, the receptance is called the direct receptance; if the displacement and the force are in different directions, the receptance is called the cross receptance. For obvious reasons, receptance is best represented by a complex function which may take the general form of $g + jh$ where both g and h are some functions of the frequency ω and they are related to the amplitude and phase by the expressions

$$\text{amplitude} = \sqrt{g^2 + h^2}$$

and

$$\text{phase} = \tan^{-1}\frac{h}{g}$$

In the context of control engineering, the dynamic receptance of a mechanical system is equivalent to its transfer function defined as the

(a)

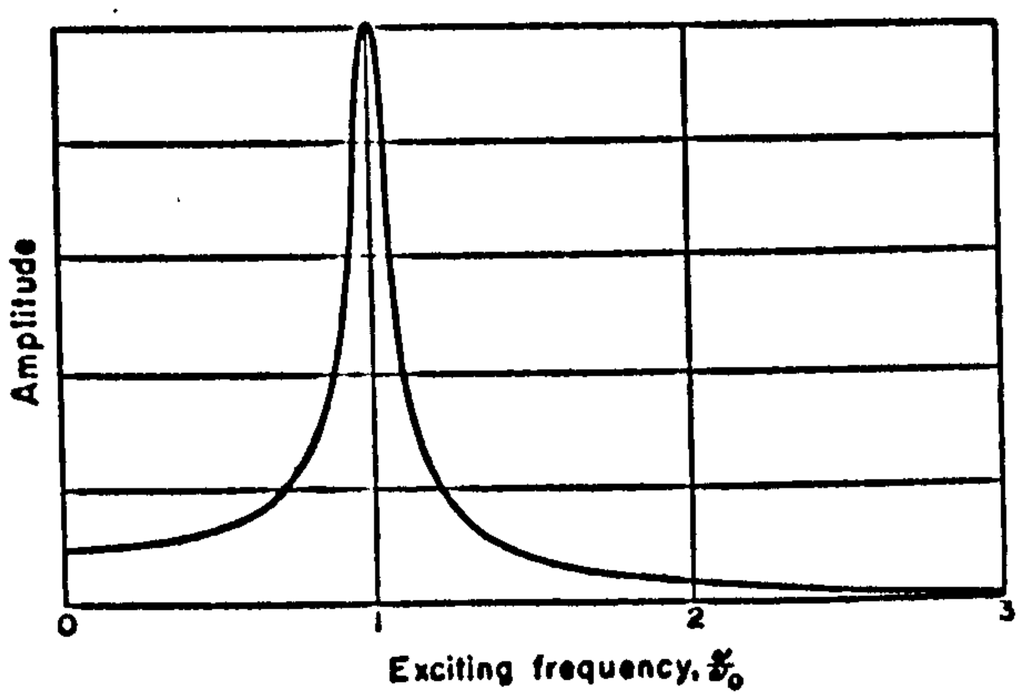

(b)

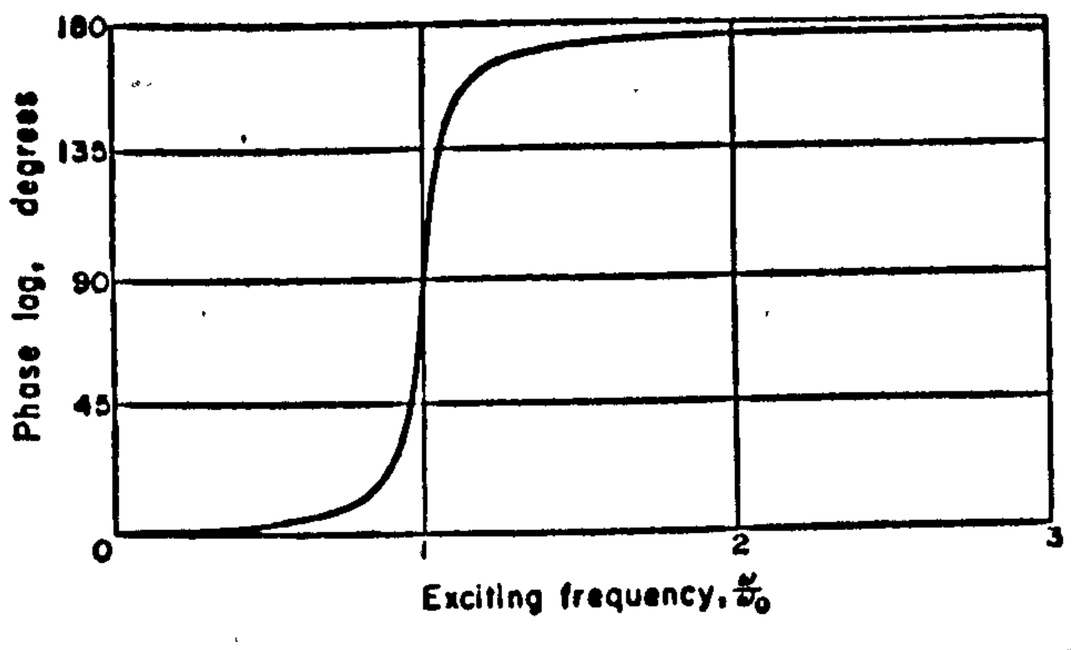

(c)

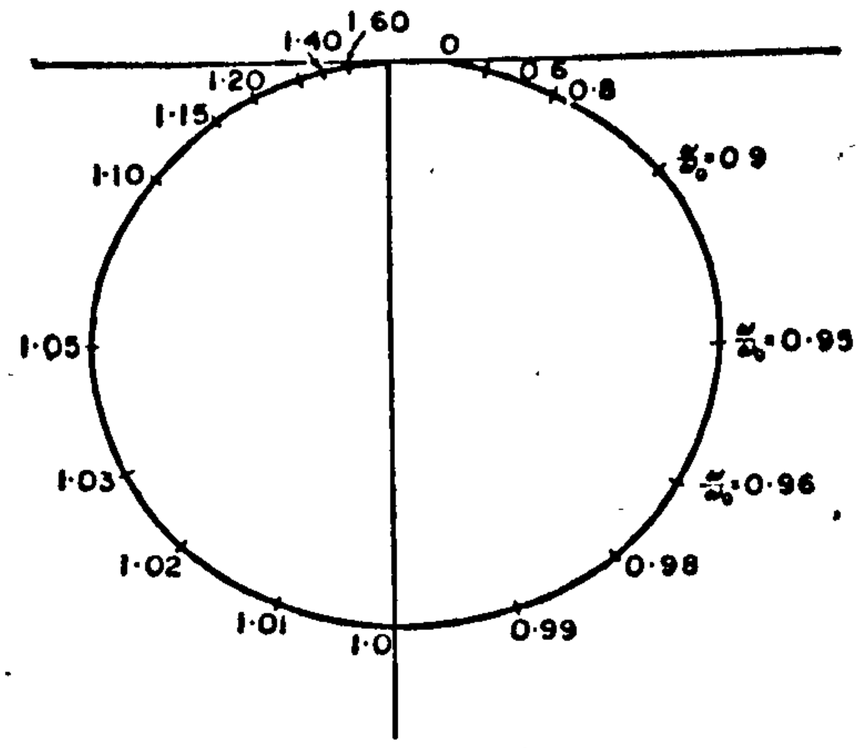

Harmonic response locus

Fig 2.8 Typical diagrams of:

a) the amplitude response

b) the phase response

c) the harmonic response locus[24]

ratio of the Fourier transform of the output signal to that of the input signal. By virtue of this definition, the input force is not necessarily restricted to a sinusoid; other waveforms are equally acceptable. Until recently, the main difficulty in applying input forces of the form other than sinusoid lies in the tedious computation of the Fourier transforms of the input and output. However, with the advent of high-speed digitization, storage and processing facilities and the availability of digital spectrum analyser, the task is performed much faster and more reliably.

Input force signals fall into two classes: 1) deterministic and 2) stochastic. Some typical signals are shown in Fig 2.9a. Class 1 includes the familiar sinusoids which may be fixed or sweeping with time. They are deterministic because they are time-definable. In the dynamic experiments with sinusoidal input, the instruments required are normally an exciter, an oscillator with its power amplifier, a vibration meter and a phasemeter. For the case of fixed sinusoidal input, the input signal is held constant at one particular frequency while the output response is measured. Since the frequency is changed in a discrete manner, the resulting response curves are, strictly speaking, a connected set of points because values between two successive points are not measured. Often such measurements are carried out manually. In contrast, a sweeping sine input is necessarily equipped with the appropriate automatic recording instruments. Since the frequency is varied in a continuous fashion, the resulting response plot is continuous. However, great care must be exercised to ensure that the mechanical system being measured remains in a quasi steady-state by keeping the sweeping rate reasonably low.

Examples of stochastic signals are the random noise, pseudo-random noise

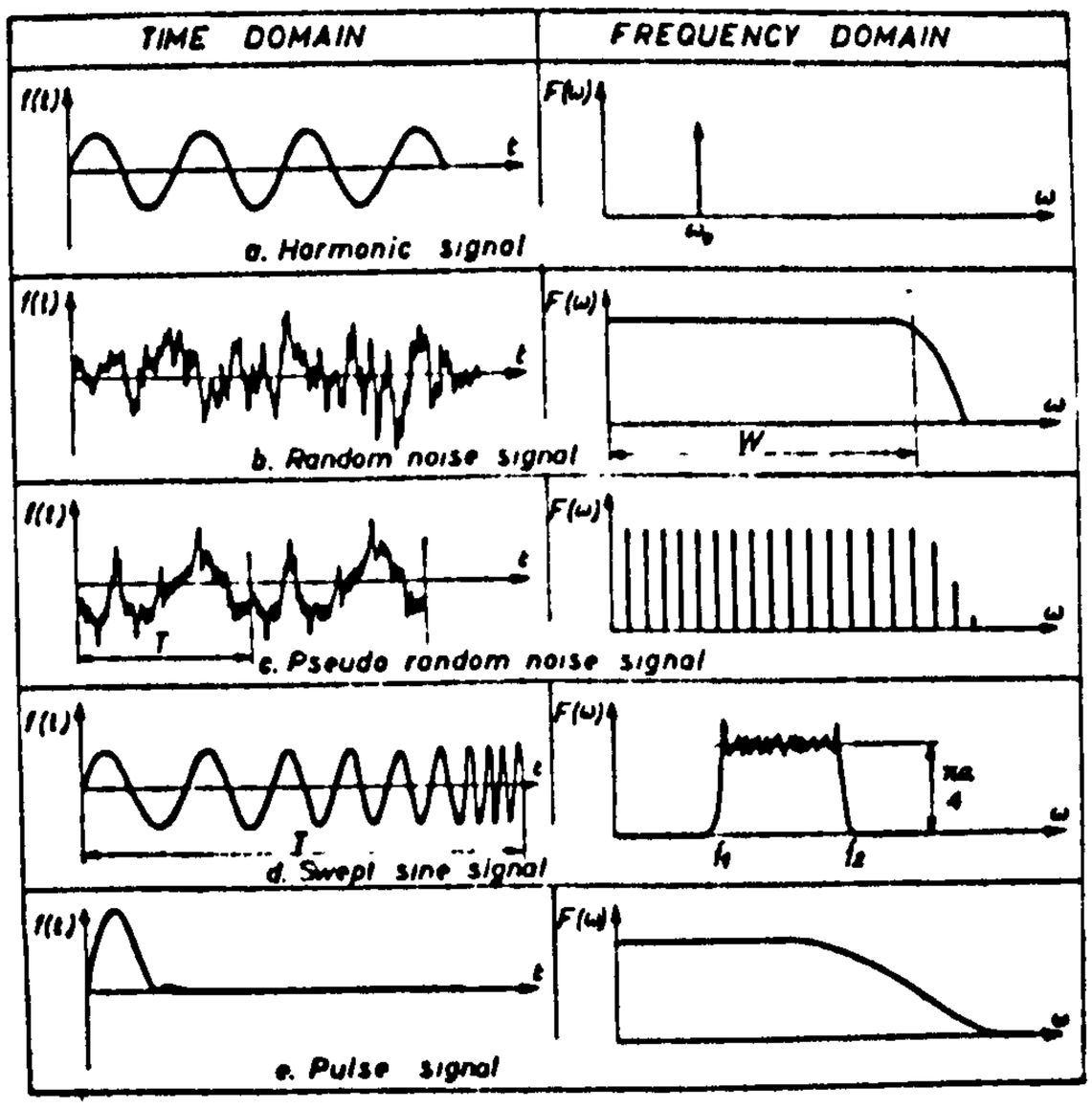

Fig 2.9a Different excitation signals and their frequency contents[22]

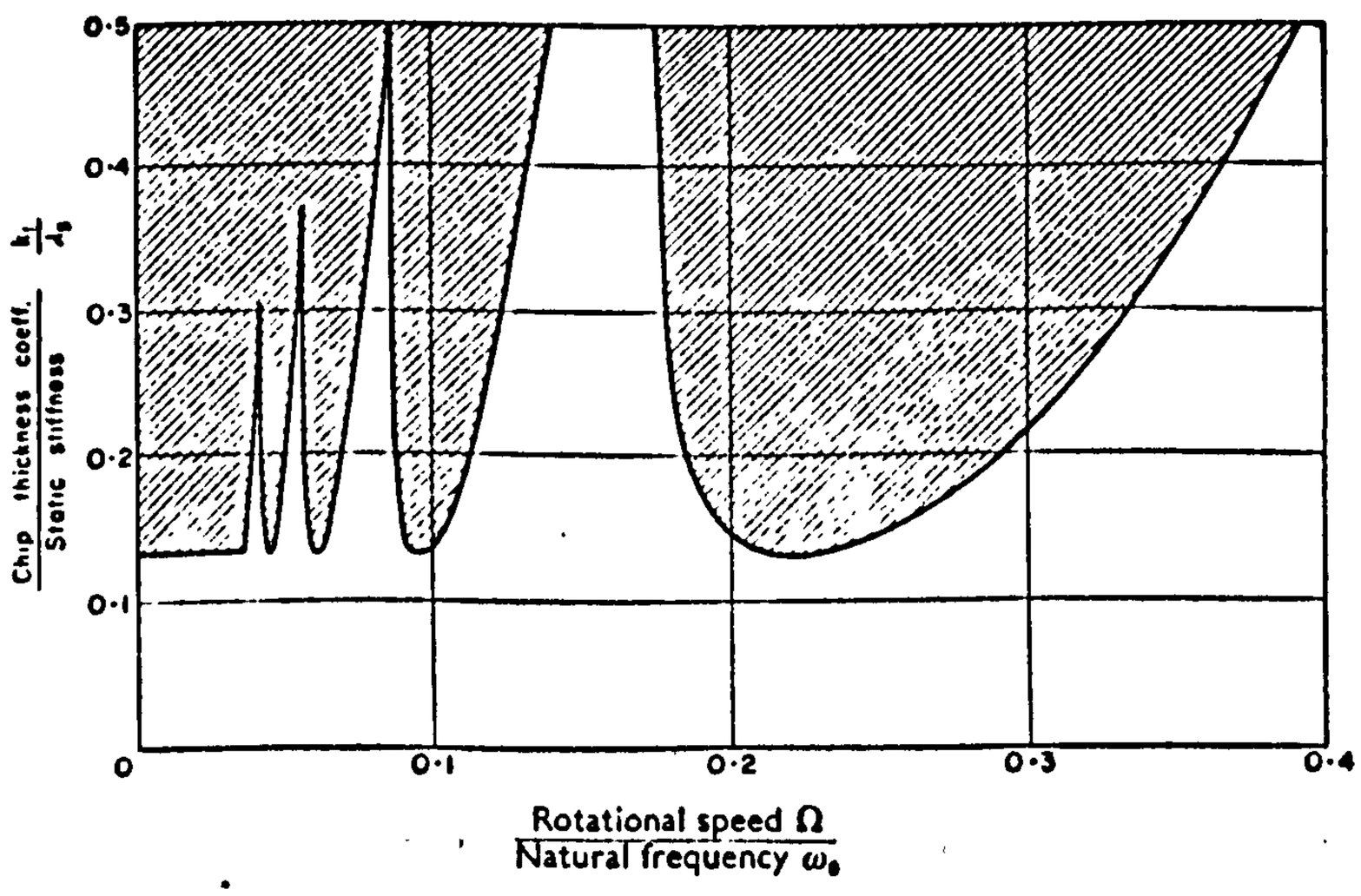

Fig 2.9b A typical stability chart [24]

and pulse signals. In a random noise signal, all frequencies within a bandwidth are present simultaneously and hence a continuous frequency spectrum. A pseudo-random signal is random within a period T, but otherwise is periodic with the periodicity T. This signal has a discrete frequency spectrum. A pulse signal is generally taken to refer to an approximation to a Dirac impulse which possesses a flat power frequency spectrum. Upon excitation with stochastic signals, the system responds to all these frequencies simultaneously, and the data required for the determining of the transfer function within a frequency range is obtained in a matter of seconds.

Apart from the speed advantage, a stochastic signal is more representative of what is usually encountered in true machining conditions. In fact, the noise signals often associated with a machining process can be successfully applied as a form of input signal. Thus, the influence of various machining parameters such as speed, and feed rate, on the dynamic characteristic can be individually studied. By this method, it is possible to relate the definite influence of feed rate, for example, to the dynamic characteristic of the machine tool. By using the pulse signal as an input, it is not even necessary to use an exciter as a means of delivering the input. Three advantages are immediately obvious:

1) there is no need to find room for the exciter, which may sometimes pose a serious problem if the mounting space is just not available,
2) there is no special consideration of the moving mass of the exciter whose presence may significantly affect the dynamics of the machine being tested, and
3) a pulse signal is easily produced by means of a hammer and if waveforms of a variety of frequency contents are desired, striking heads with different degrees of hardness can be used.

The pulse signal is usually registered by a load cell mounted in between the striking head and its body[22], or by a crystal type impact transducer placed on the area to be struck[23].

According to Opitz and Weck[21], experiments with stochastic signals give rise to two types of errors that are inherent in the process, namely the statistical and systematic errors. They reckoned that, on account of the inevitable features of filter bandwidth in the instrumentation, a small statistical error is not compatible with a small systematic error. For this reason, a compromise is needed so that both types of errors are kept within allowable limits. Correction procedures[21,22] were devised to minimise both types of errors.

2.5 STABILITY ANALYSIS

It has been shown in section 2.3 that the incremental cutting force dP under vibratory cutting conditions can be represented by the eqt (2.5) which is repeated here as $dP = P(\cos\theta + j\sin\theta)$ (2.5) where it should be noted that both $P\cos\theta$ and $P\sin\theta$ are functions of the cutting process parameters. This incremental force dP excites a machine tool structure whose cross receptance is expressed as a complex variable $g + jh$, and produces a displacement $x(t)$ which is some function of the time t. By the definition of cross receptance,

$$(g + jh) = \frac{x(t)}{dP}$$

or $$dP(g + jh) = x(t) \qquad (2.9)$$

For the case of regenerative chatter, successive cuts overlap and the wave on the work surface of the previous cut continuously modifies the incremental cutting force dP. By the definition of stability borderline

in section 2.2, which is that the amplitudes remain constant in successive cuts, then $x(t) = x(t - T)$ (2.10)

The stability borderline is determined by solving eqts (2.5), (2.9), and (2.10) simultaneously. Since dP in eqt (2.5) can be regarded as some function of the cutting process parameters, it is possible to present this stability borderline graphically in terms of one of the cutting process parameters and the cutting speed as shown in Fig 2.9b. This type of diagram is also known as the stability chart. Various methods of stability analysis have been proposed, but while they differ in details, their basic approach is in accord with what has been just described. We shall look into three methods which have features that merit some attention.

2.5.1 METHOD OF TOBIAS AND FISHWICK[15]

The method, in its original form, is concerned with a single-degree-of-freedom system. For this reason, it is suitable only when the machine tool under study has modes of vibrations that are well separated from each other. The prerequisite is a knowledge of the system parameters such as the mass, spring stiffness and damping, which is not easy to acquire because of the tedious curve-fitting procedure involved following the collection of dynamic data. The cutting force equation used has a similar form to eqt (2.5) and includes the effects of not only the uncut chip thickness variation, but also the variations of the rate of tool penetration and of the rotational speed. The stability is then evaluated from the equation of motion in which the cutting force function is taken as the applied force.

Gurney and Tobias[24] presented a graphical representation of the method of Tobias and Fishwick. The procedure is first to construct vectors for both the machine tool and cutting process dynamics and then to relate them graphically in the manner described by the equation of motion. The vectorial representation of the machine tool dynamics is, in fact, the harmonic response locus which is readily determined by way of experiments even for mechanical systems of considerable complexity. It follows that, unlike the original method, values of the system parameters need not be computed and the analysis is not necessarily confined to the single-degree-of-freedom system.

Thus far, the stability borderline is specified in terms of the dynamic chip thickness coefficient k_1 (see eqt 2.6) whose relation with uncut chip thickness, the really desired quantity to be of value to machinists, is not easy to establish, and so the potential advantage of this method is not fully realised.

Das and Tobias[16] recognised the existence of the causal relation between the static and dynamic cutting as mentioned in section 2.3, if proper account is taken of the effects due to instantaneous shear plane length, instantaneous cutting direction, and instantaneous effective shear angle. They concluded that it is possible to draw useful stability charts in terms of the limiting uncut chip thickness beyond which instability occurs.

2.5.2 METHOD OF TLUSTY AND POLACEK[4]

The method is concerned with a general machine tool structure which may

have any number of modes of vibrations. In this method it is not necessary to know the values of the system parameters directly such as mass, damping and stiffness. The dynamics of the machine tool is determined experimentally and is presented graphically by a pair of curves known as the real receptance curve $G(\omega)$ and the imaginary receptance curve $H(\omega)$. $G(\omega)$ and $H(\omega)$ are respectively the real and imaginary parts of the cross-recetance g + jh measured between the direction of the cutting force and the normal to the cut surface. The incremental cutting force equation is a repeat of eqt (2.8), ie

$$P = -br(Y - Y_o) \qquad (2.8)$$

in which, as has been mentioned in section 2.3.2, r is assumed as a real constant if all other conditions, apart from the chip width b, are kept fixed.

According to Tlusty and Polacek, at the stability borderline, the limiting chip width is

$$b_{lim} = \frac{1}{2rG_{min}} \qquad (2.11)$$

where G_{min} denotes the minimum value of the real receptance curve $G(\omega)$. Since r is assumed real, the cutting force equation of(2.8)only accounts for the effect of changes in the uncut chip thickness, but ignores the effects of the rate of tool penetration and the rotational speed. Ignoring the rate of tool penetration will result in a higher value of the limiting chip width than that given in eqt (2.11). In addition, the effect of rotational speed on stability is in general observed to be insignificant within the practical machining range. For these reasons, eqt (2.11) provides a safe estimate of the limiting chip width b_{lim}.

The real constant r in eqt (2.11) has yet to be determined. According to Peters and Vanherck[25], r has a value identical to that of the incremental cutting stiffness k_1, which they define as the incremental cutting force per unit chip area of increment. The increments of chip area are effected by changes in the feed rate or uncut chip thickness or both from one steady-state condition to another. Thus, the value of r is a steady-state quantity whose values are determined from steady-state cutting tests. The limiting chip width can then be evaluated from eqt (2.11).

2.5.3 METHOD OF MERRITT[26]

The method is based on the theory of linear control. Merritt likened the phenomenon of machine tool chatter to the dynamical performance of a closed loop control system as is depicted in Fig 2.10. There are two feedback paths:

(1) the primary path which models the effect of changes in the position of the cutting tool thus causing corresponding changes in the cutting force, and

(2) the regenerative path with a time delay element μe^{Ts} that models the overlapping effects of successive cuts.

The cutting force function F(t) is assumed to be in direct proportion to the instantaneous uncut chip thickness u(t), hence

$$F(t) = k_c u(t)$$

where k_c, being a constant, is called the directional cutting stiffness. Such a cutting force model is bound to be approximate for it ignores the dynamics of the cutting process. The exact stability borderline which is rather complicated is then determined by means of a special

chart. According to Merritt, a simpler stability criterion is also possible, which is that chatter-free performance is assured if the directional cutting stiffness is less than one half of the minimum directional dynamic stiffness of the machine tool structure.

Since Merritt, the control loop approach has been preferred by investigators like Opitz and Bernard[27] who studied the behaviour of lathes and milling machines. The popularity is partly due to the wealth of control theories available and partly due to the high computational speeds afforded by computers which cut down the time of stability analysis to a practical and economical level.

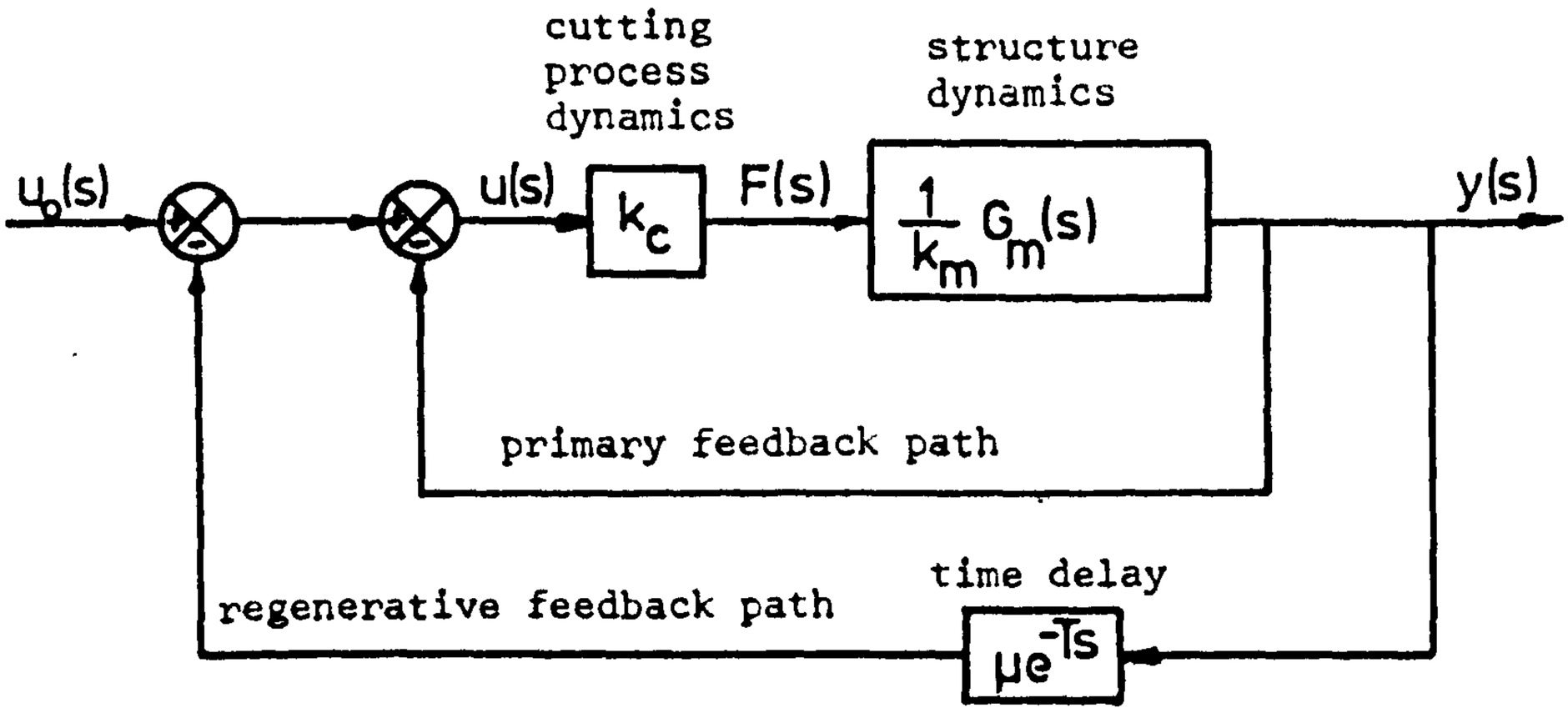

Fig 2.10 Block diagram of chatter loop (26)

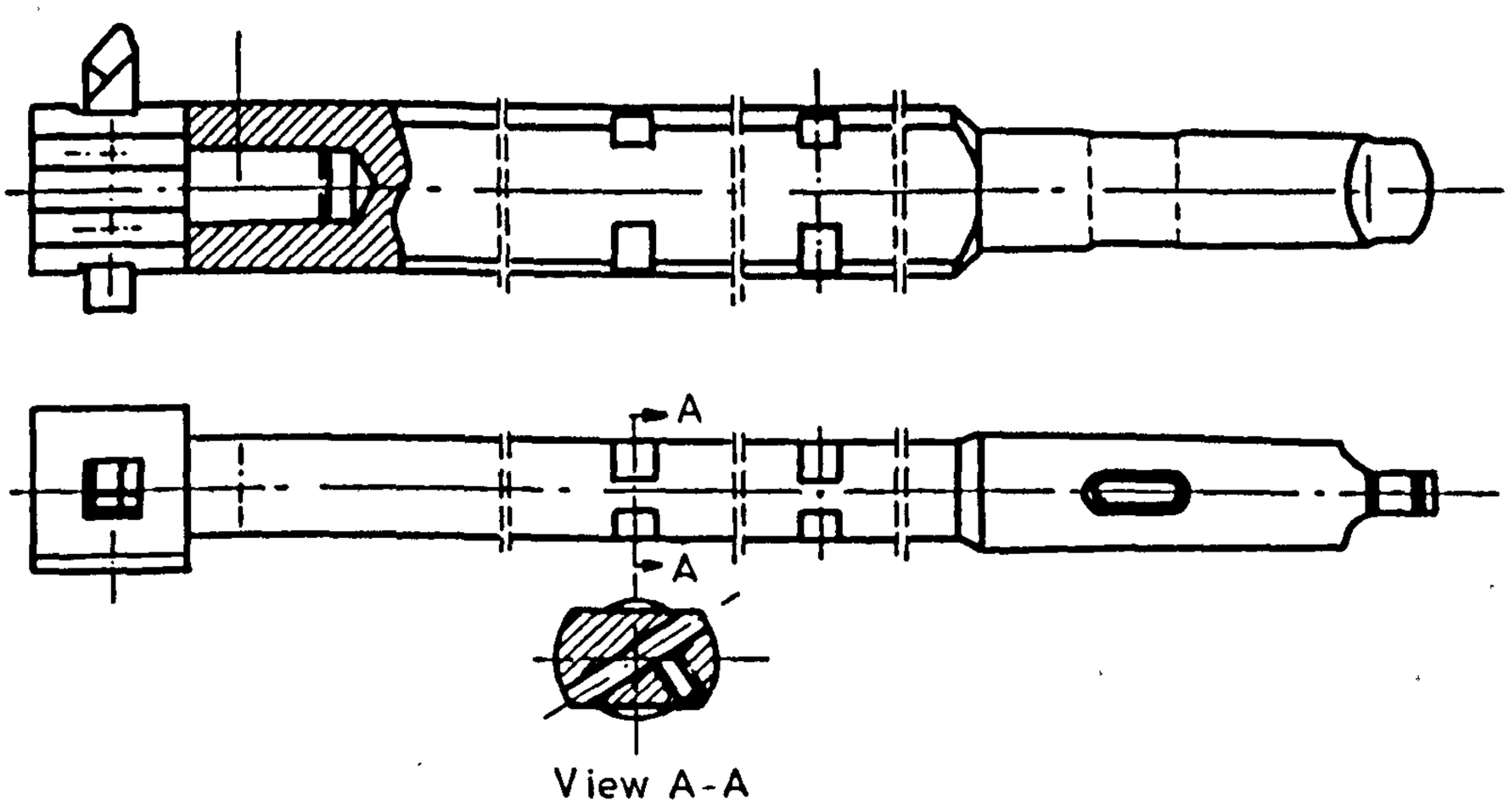

Fig 2.11 A design of boring bar using the principle of mode-coupling (30)

2.6 SURVEY OF BORING BARS

Some designs of boring bars will be surveyed and classified according as the principles involved. A few of these may make use of more than one principle for their effective operations and whenever this is the case, mention will be made of the other principles involved wherever the bars are described in the text.

2.6.1 IMPROVED STIFFNESS

The main advantage of having a high stiffness in a boring bar is in the maintenance of good geometric form accuracy. Eqt (2.4) in section 2.1 indicates three ways whereby high values of stiffness can be obtained:

(1) increasing the Young's Modulus of Elasticity E,

(2) increasing the second moment of area I, and

(3) reducing the overhung length of the boring bar L.

The last two ways are dictated by the configuration of the workpiece and the consideration of swarf removal and ccolant passage. In practice, if conditions allow, boring bars are often supported with steadies, which effectively reduces the overhang. Increasing the Young's Modulus E is achieved quite commonly by use of stiffer bar material such as tungsten carbide or other tungsten-based alloys. Tungsten carbide, for example, has an E about 2.5 times that of steel. Sandvik Ccromant[28] marketed a type of tungsten carbide boring bar designated as TNS with a removable preset head for use on NC machines. Features include coolant channels cut out in the body for swarf removal. The main deterrents for using tungsten carbide are in the high costs involved and the inherent brittleness which requires special care in handling.

Effective stiffness can also be enhanced by way of arranging a pair of boring tools on the boring bar such that the cutting forces generated cancel out each other. Smolenskii[29] described one such design in which the pair of boring tools are adjustable at the root end of the boring bar so as to cut variable steps or recesses in a workpiece. The main drawback is, however, its inability to cope with profile boring.

2.6.2 INTELLIGENT USE OF MODE-COUPLING

According to Kuchma[30], the effective stiffness of a boring bar may be increased by means of a mechanism known as mode-coupling which, briefly, is the phenomenon of mutual interchanges of vibrational energies between two modes of vibration of the bar. By machining diametrically opposite flats as in Fig 2.11, Kuchma observed that the bar then possesses two coupled modes and that the dynamic stability depended on the tool setting angle relative to the principal modal directions. He claimed that there was a particular angle at which the stability of the bar was at the maximum value even higher than that of an equivalent round solid bar. Parker[31] and Kato et al[32] also provided results to support this view.

Thomas et al[33], however, disagreed with the findings of Kuchma and his supporters. Assording to Thomas et al, the machined flats on the bar do not bring about any overall improvement in stability but rather the optimum performance is lower than that of an equivalent round solid bar.

Inada et al[34] reported on a boring bar whose design is shown sketched in Fig 2.12 with its analogous model shown in Fig 2.13. The bar is composed of a body shank and an internal plate fitted into a slit of the

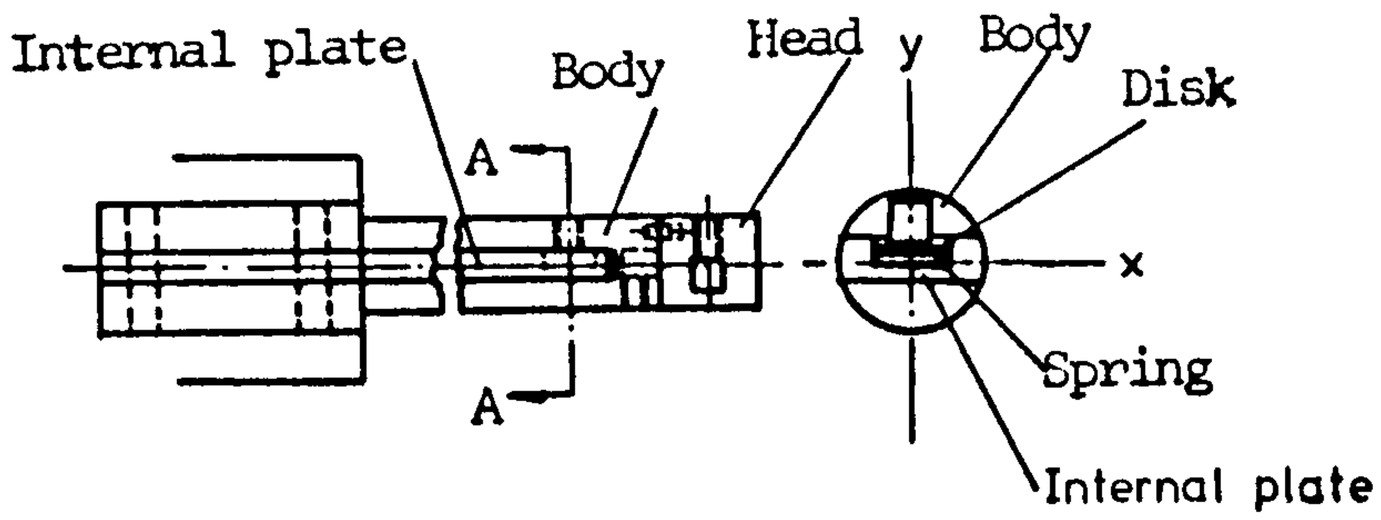

Fig 2.12 The N-bar of S Inada and H Nakazawa [34]

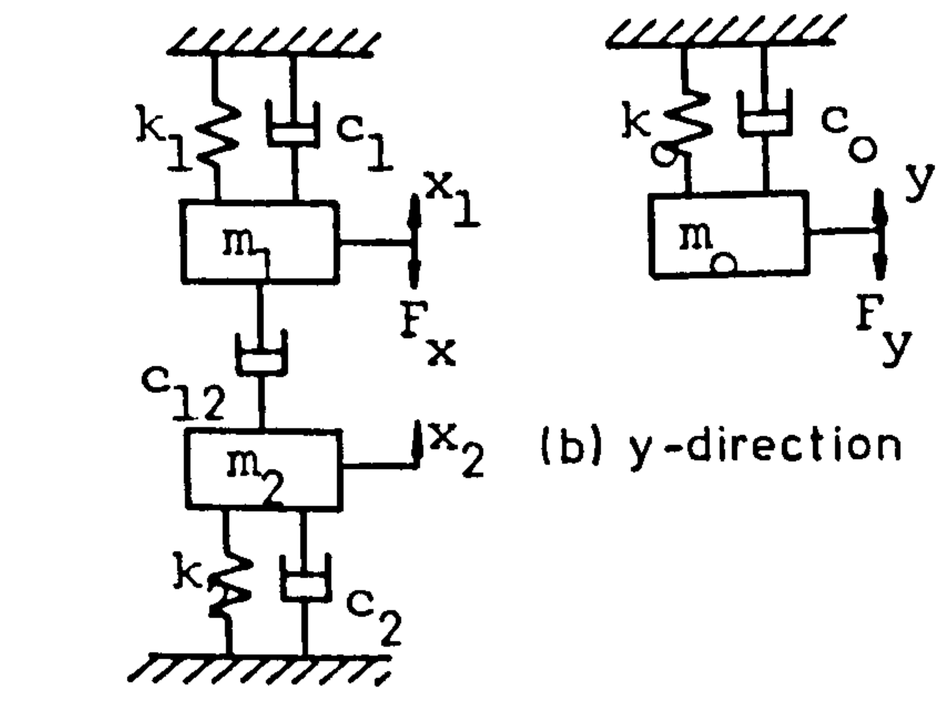

Fig 2.13 The lumped-parameter models of the N-bar in the x- and y-directions [34]

body. Both parts can be deflected independently of each other in the direction X whereas they are allowed to deflect only as a single unit in the direction Y as in Fig 2.12. The free end of the internal plate is machined with a recess such that the spring and disk can be accommodated. The damping force arising between the body and the internal plate is provided by the disk-spring combination and can be varied by a set-screw pressed on the disk. According to Inada et al, the bar performs best at the tool-setting angle of 0° and 120°. For the bar with a 6 to 1 overhang ratio and a tool-setting angle of 120°, the bar was claimed to be able to remove steel up to 6mm deep at a cutting speed of 60 m/min as opposed to 2mm deep using an equivalent round solid bar under the same condition.

2.6.3 IMPROVED DAMPING

All materials possess some degree of inherent damping properties, some more than others. Materials such as manganese copper alloy also known by the trade name Sonosto[35] have an inherently high damping property which can be used to advantage as building materials wherever high damping is demanded. However, these materials are in general less stiff than steel and so the overall improvements in dynamic stiffness are not very impressive.

For mathematical convenience, damping is normally assumed to take one of three forms: 1) viscous damping, 2) hysteretic damping, and 3) coulomb or dry-friction damping. In viscous damping, the damping force[36] is proportional and opposite to the velocity. The energy dissipated per cycle is proportional to the forcing frequency and becomes infinitely small as the frequency is made to approach zero. In hysteretic damping[37]

the damping force is proportional to the displacement and opposite to the velocity. Unlike viscous damping, the energy loss per cycle is independent of the forcing frequency. Coulomb or dry-friction damping[38,39] is said to occur when the damping force is opposite in direction to the velocity, and remains constant in magnitude whose value is a function of the materials that make up the pair of surfaces in contact, the surface textures and the magnitude of the normal force. Energy is dissipated through the relative displacement between the mating surfaces.

Very often, boring bars are designed to operate with vibration dampers. According to Welbourn and Smith[39], dampers may be classified in respect of the principles of damping involved:

(1) Tuned auxiliary masses vibrating to give a force opposing the motion -

A typical example is the tuned and undamped absorber which can be modelled by the analogue shown in Fig 2.14. In this analogue, a spring-mass absorber is coupled to the main mass m, and is tuned to the frequency of the excitation force ω_e such that $\omega_e^2 = k_2/m_2$. The absorber introduces two resonant frequencies to the main mass as is shown by the response curve in Fig 2.15. This type of absorber can only be used when there is a known and constant forcing frequency and is, therefore, practically useless in suppressing the unstable chatter type of vibration.

(2) Energy absorption and dissipation from the system -

a) Impact dampers --------- These refer to the class of dampers in which the energy is absorbed through the impacts of one body with another. Stabor bar[40] is one example. The bar, whose sketch

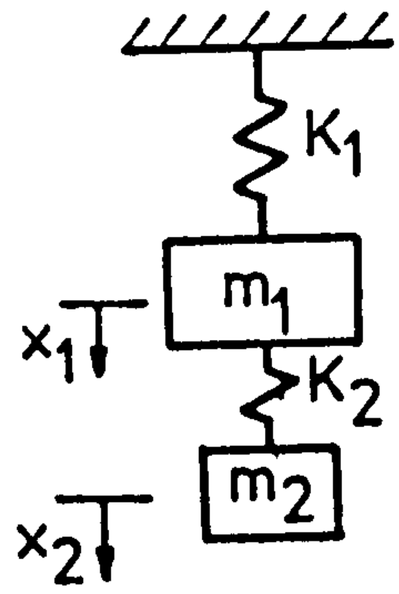

Fig 2.14 A spring-mass system with an undamped absorber

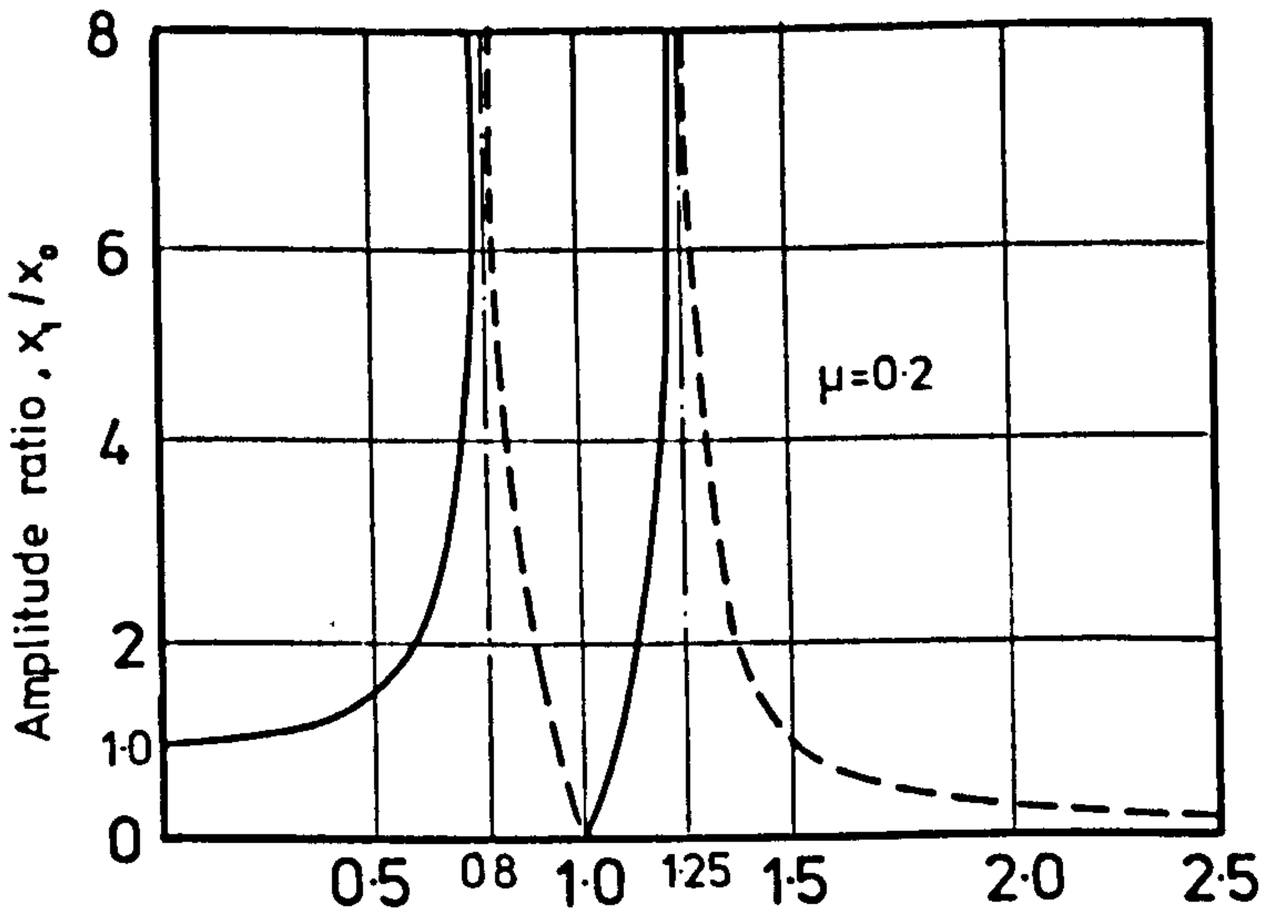

Fig 2.15 Response curve of the system in Fig 2.14. The absorber introduces two resonant frequencies of the main mass.

is shown in Fig 2.16, consists of a steel tube containing an adjustable impact damper. A cantilever spring supports an impact mass within a conical chamber in the tool-holder. The distance between the mass and the anvil can be set for optimum performance by adjusting a graduated nut which moves the supporting spring axially. Any vibration of the bar will be suppressed or reduced through the mass striking the conical seating of the chamber. Thomas et al[33] modelled the Stabor bar by a two-degree-of-freedom system shown in Fig 2.17, from which its dynamic response subjected to harmonic force input was analysed. From their findings, a gain of 100% in metal removal rates was claimed over an equivalent round solid bar at an overhang ratio of 5 to 1 when cutting at 400 rev/min. They also remarked that while it was virtually impossible to use a solid bar with 7 to 1 overhang or above, the stabor bar with the same overhang ratio achieved what the 5 to 1 solid bar did in terms of the stable depth of cut. The behaviour of impact dampers was also studied by Masri and Caughey[41] and Sadek[42]. Another common type of impact damper is similar in appearance to the Lanchester damper which will be described soon. However, due to the larger clearance between the slug and the hole, the mechanism of operation is regarded as impact damping.

b) Viscous dampers ------- As the name indicates, these dampers can all be modelled by the viscous damping analogue. The most commonly known damper is the Lanchester damper, two sketches of which are shown in Fig 2.18 a) and b) for the respective cases of boring blind holes and through holes. Energy is dissipated by way of the flow of fluid in the clearance between the slug and the hole.

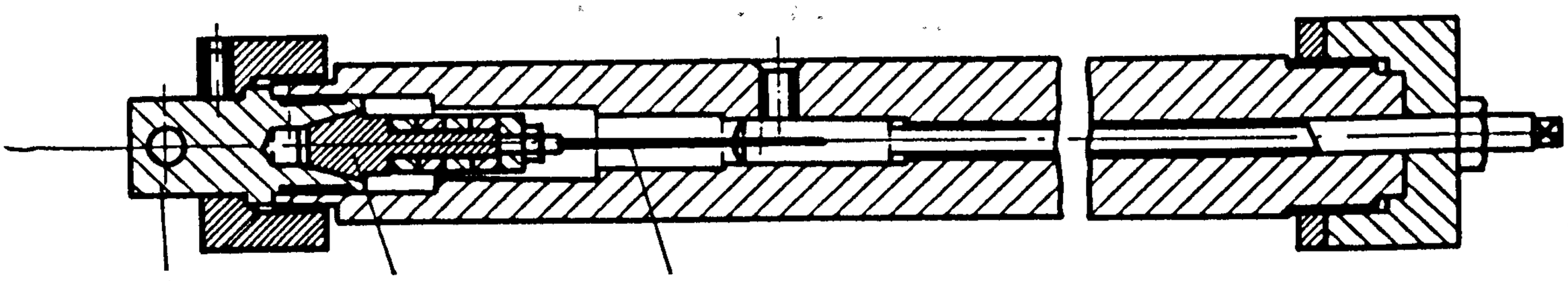

Fig 2.16 The schematic drawing of the Stabor Bar [33] showing

1) toolholder and conical chamber
2) impact mass
3) cantilever spring

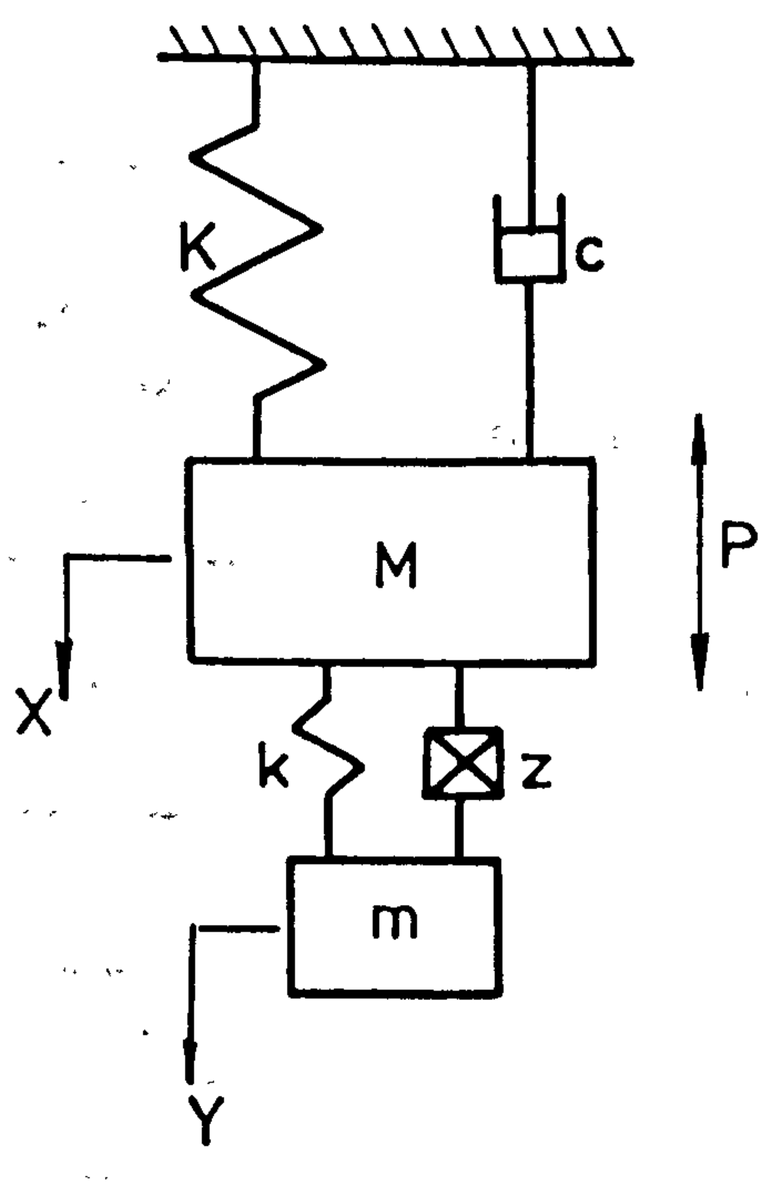

Fig 2.17 The analogous model of Stabor Bar[33]

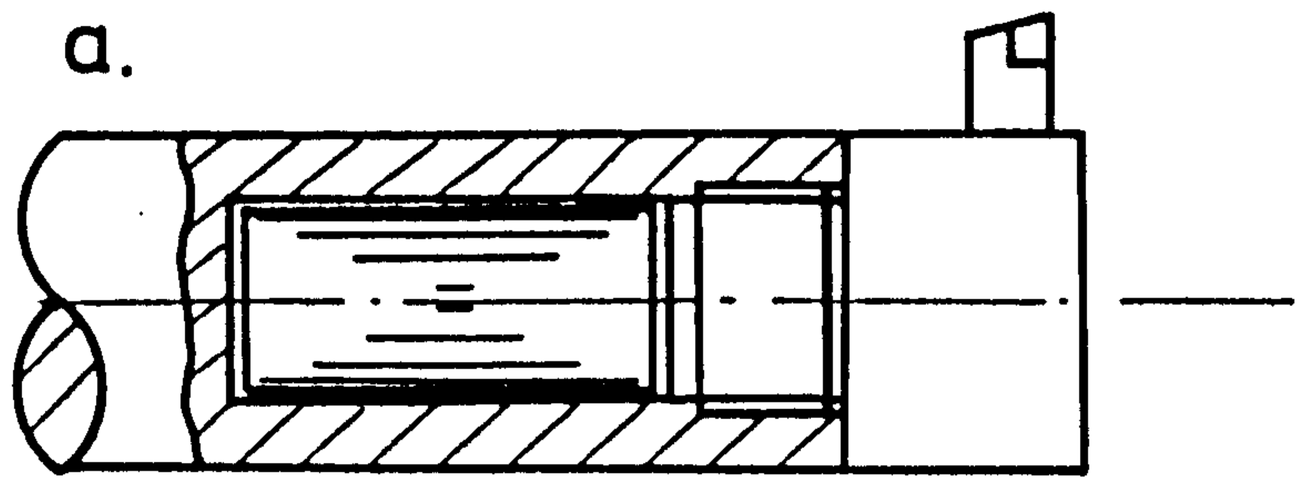

Fig 2.18 Two designs of Lanchester Damper for use in boring bars: (a) for blind hole boring; (b) for through hole boring.

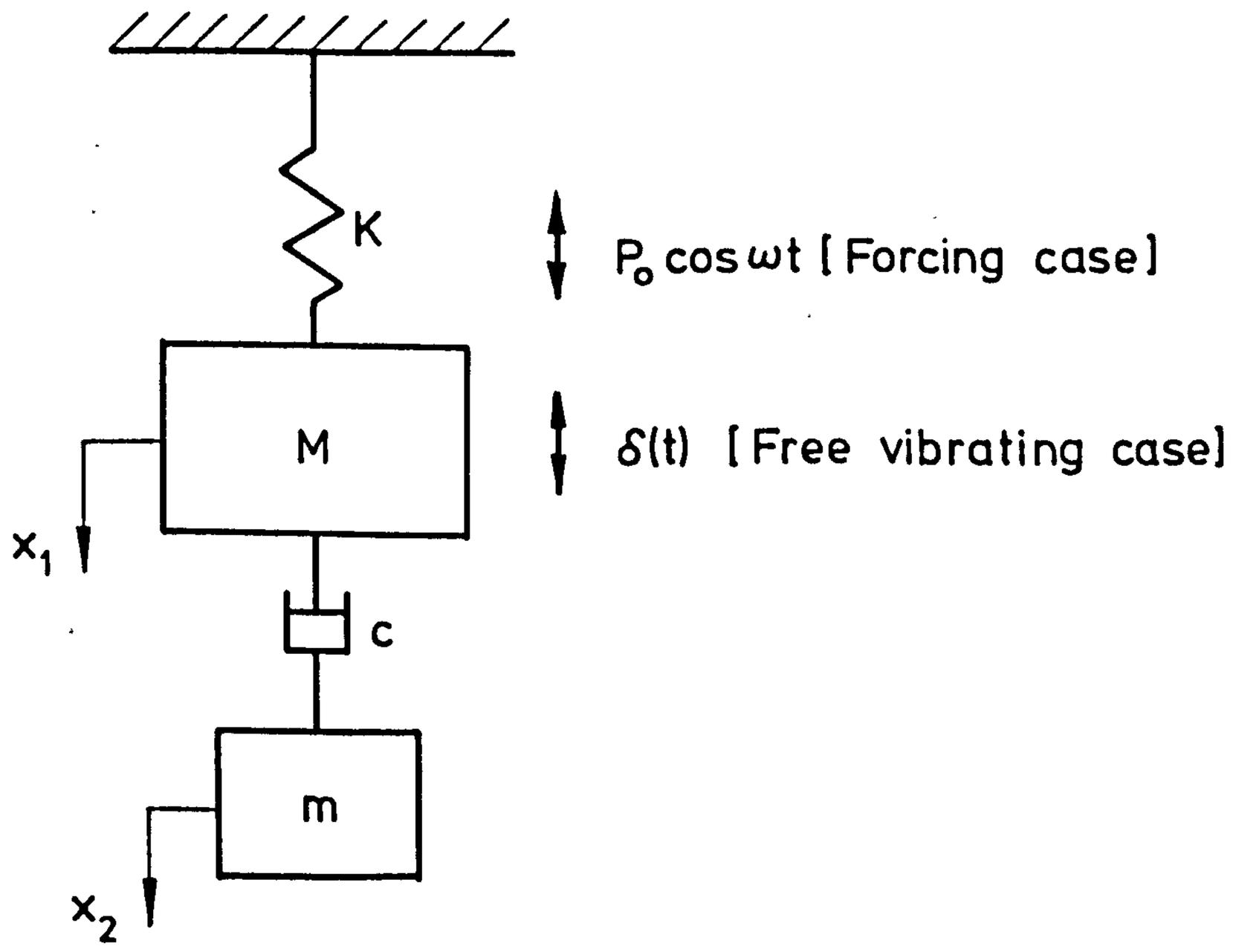

Fig 2.19 Analogy of basic Lanchester Damper

Den Hartog[36] modelled the Lanchester damper by the analogue as shown in Fig 2.19 and studied its sinusoidal response. Using the same analogue, Hahn[43] studied its transient response and Kato et al[32] studied its machining stability. Whether the damping is assumed viscous or impact in nature will depend on the amount of clearance between the slug and the hole: the smaller the clearance, the more viscous is the damping.

In 1966, there appeared on the market under the trade name of Ceco[44] two designs of boring bar, one rotatory and the other non-rotatory. Both incorporate a Lanchester damper located close behind the boring tool. It was claimed that satisfactory performance was possible up to 9 to 1 overhang ratio. Lamdon and Revva[45] also reported on a similar design of Lanchester-damped boring bar, but the bar shank was made of carbide instead of steel.

c) Coulomb or dry-friction dampers ------ These are dampers that dissipate energy as friction losses through the relative movement between each pair of surfaces in contact. They have been applied with success in industry to deaden gear noise in large gear design and to reduce torsional vibrations. This idea of friction damping is also reflected in some designs of the boring bars that appear on the market.

Kennametal De-vibrator[46],first reported in 1963, is one example. It consists of a set of inertial discs made from a type of heavy tungsten alloy, Kennertium. The discs are held under pressure in series at the cutting end of the boring bar as shown in Fig 2.20.

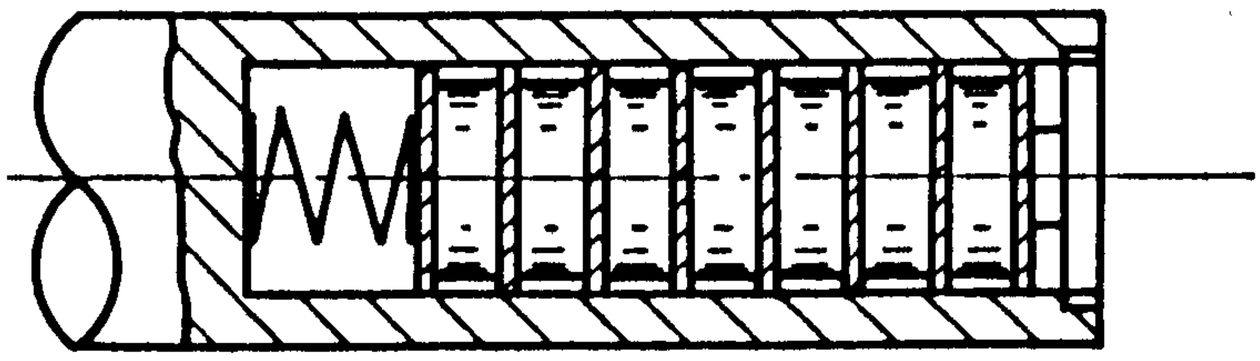

Fig 2.20 A schematic drawing of the De-Vibrator showing a set of inertial discs held by a light spring.

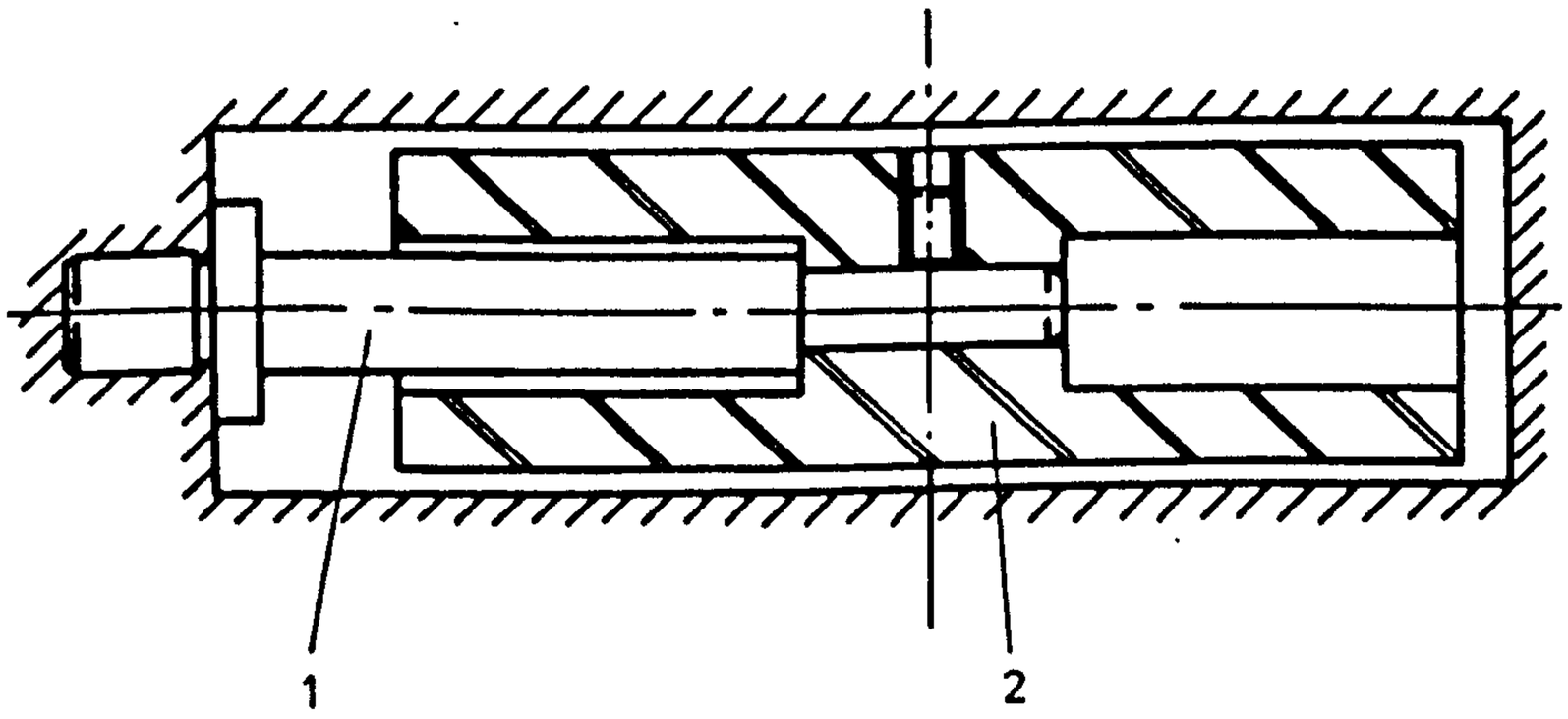

Fig 2.21 The Vibration Absorber of PERA[49] showing

1) cantilever spring; and
2) absorber mass

The pressure is provided by means of a compressed spring also connected in series with the discs. The body of the bar is made of tungsten carbide and the boring head is held in position by a drawbar. The De-vibrator works by dissipating friction energy between the discs consequent upon their relative movements and by impact damping arising from the random impacts of the discs with their enclosure. Its manufacturer claimed in 1971 that it had produced the then largest boring bar[47] incorporating a Kennametal De-vibrator. The total weight is 1100 lbf (2420 kgf) and it measures 5 in (51 mm) in diameter by 72 in (2337 mm) in length. Holes up to 71 in (1803 mm) deep were reported to have been machined successfully.

In 1968, Guskov[48] reported that an adjustable boring bar vibration damper was manufactured and successfully tested at Kirov, a machine tool plant in Russia. Its features are similar to the Kennametal De-vibrator except: (1) that the discs are held under pressure by means of an adjustable bolt passing through the centres of all discs and (2) that the damper is located ahead of the tool. Obviously, this design does not permit blind-hole boring.

(3) Combinations of types (1) and (2) to give a compromise between the characteristics of the two types -

A typical example is the tuned and damped absorber described in PERA reports 91[49] and 133[50]. Its sketch is reproduced in Fig 2.21. The slug is a cylindrical mass made of heavy alloy and is mounted on the end of a cantilever spring, the base end of which is fixed to the

body of the boring bar. Using an analogue as reproduced in Fig 2.22, the PERA team[50] analysed the harmonic response as well as the stability of the damper. Based on these results, they gave recommendations of damper dimensions, and the choice of fluid on the basis of its viscosity for optimum damping. Commenting on the theoretical harmonic response of various dampers, Den Hartog[36] pointed out that the design such as PERA's was usually three times as efficient as a Lanchester damper. Nevertheless, he also noted that the design of a correct spring was often difficult because the small amplitude of the main mass was obtained at the expense of large deflections and hence stresses in the damper spring.

Some variations of the PERA damper exist and are illustrated in Fig 2.23. In diagram a), the springs are in the form of two plastic plates which are also damping elements. In diagram b), according to Revva[51], the cylindrical slug is suspended on rubber rings and the clearance is filled with a fluid. Despite the variations, their dynamic performance is affected by the same parameters, namely:

i) the mass of slug

ii) the clearance

iii) the width and thickness of the rubber or plastic material

iv) the type of plastic material, and

v) the damping fluid.

Both Revva[51] and Hahn[36] remarked that a bigger mass was always desirable.

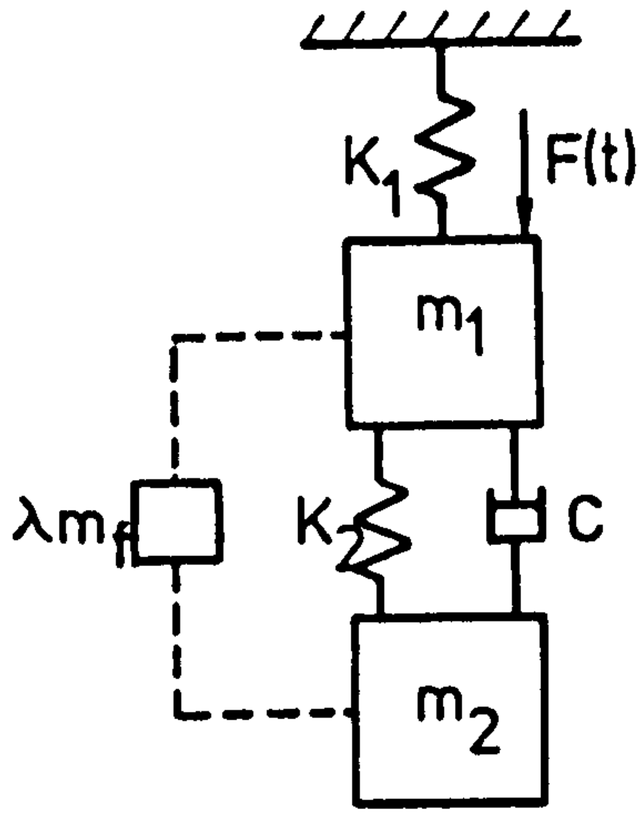

Fig 2.22 Analogy of PERA boring bar

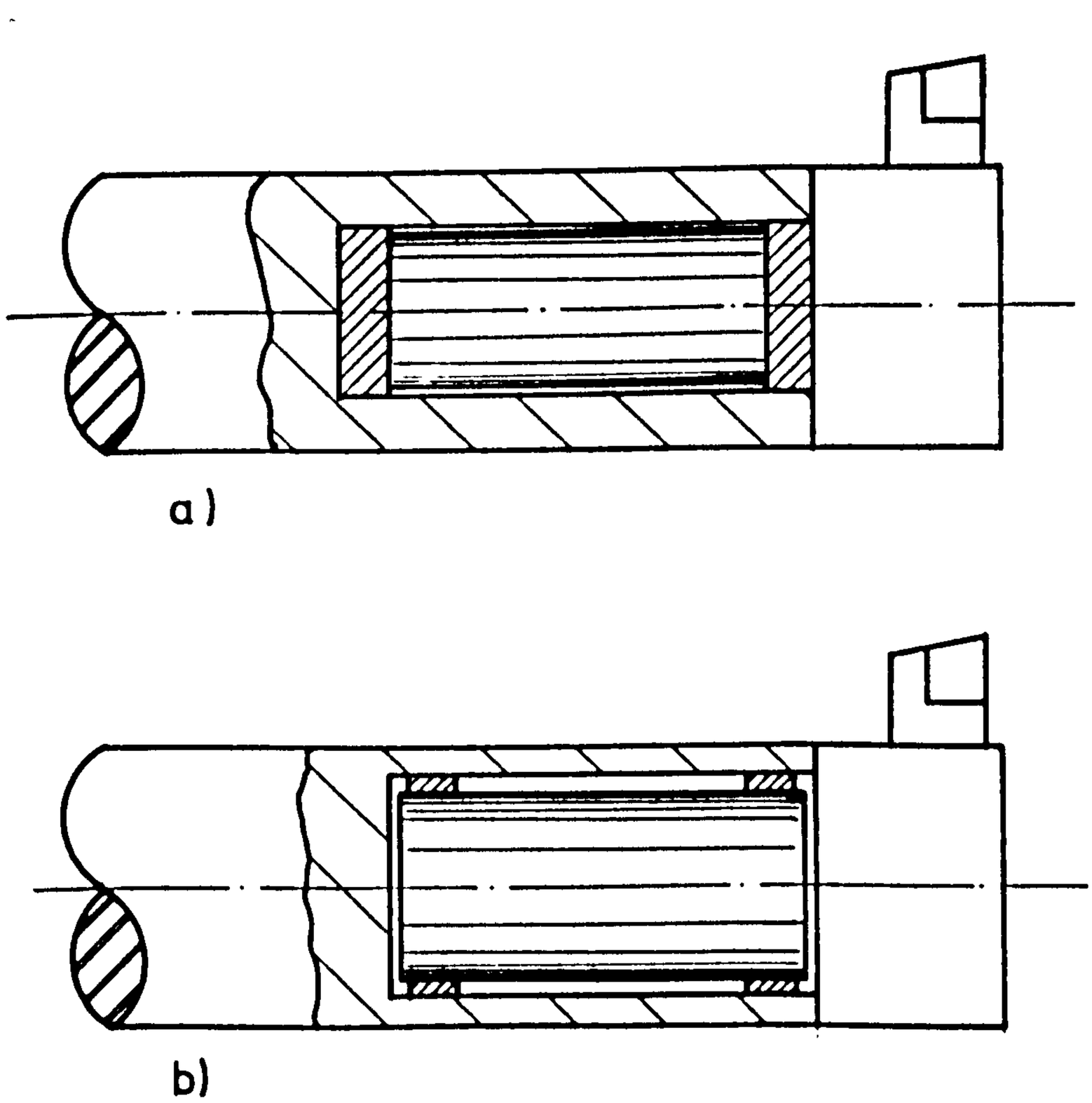

Fig 2.23 Some variations of the PERA absorber:
a) slug suspended on two rubber end plates; and
b) slug suspended on two rubber rings[28].

REFERENCES FOR CHAPTER 2

(1) HAHN, R.S. "Solving production boring problems", The Tool Engineer, April 1953 pp. 85-88

(2) TLUSTY, J. and KOENIGSBERGER, F. "New concepts of machine tool accuracy" Annals of the CIRP 1971 Vol. XVIV pp. 261-273

(3) BIRCHALL, T.M., LEWIS, F.A. and NEW, R.W. "Application of research results in machine tool design and development", Int. J. Mach. Tool Des. Res. 1961, Vol. 1, pp. 110-147.

(4) TLUSTY, J. "Machine Tool Structures", Pergamon Press, Oxford 1970 Vol. 1.

(5) AU, Y.H.J. and NEW, R.W. "Profile boring operations - current research into overhung boring bars" Paper presented at the 2nd Int. Conf. on Production Research (Copenhagen) August 1973. Int. J. Prod. Res. 1974 Vol. 12 No. 2. pp. 247-261.

(6) PORTER, B. "Stability criteria for linear dynamical systems" Oliver and Boyd Ltd. 1967 pp. 21-29

(7) ARMAREGO, E.J.A. and BROWN, R.H. "The Machining of Metal", Prentice Hall Inc., New Jersey 1969 pp. 292-332

(8) ARNOLD, R.N. "The mechanism of tool vibration in the cutting of steel" Proc. Inst. Mech. Engrs., 154, 1946 p.261

(9) DOI, S. and KATO, S. "Chatter vibrations of lathe tools" Trans. ASME 78 1956, p. 1127.

(10) HAHN, R.S. "Metal cutting chatter and its elimination" Trans. ASME 75, 1953, p. 1073.

(11) SHAW, M.C. and HOLKEN, W. "On self-excited vibrations of metal cutting" Industrie-Anzliger 6, No. 63, Aug. 1957, 35 Essen: Verlag W. Girardet

(12) SMITH J.D. and TOBIAS, S.A. "The dynamic cutting of metals" Int. J. Machine Tool Des. and Res. 1, 1961, p. 283

(13) SHUMSHERUDDIN, A.A. Ph.D. Thesis, University of Birmingham 1965.

(14) ALBRECHT, P. "The dynamics of the metal cutting process" Trans. ASME, Series B, J. of Engng. for Ind. 87, 1965, p. 429.

(15) TOBIAS, S.A. and FISHWICK, W. "A theory of regenerative chatter" The Engineer (London) 1958 Vol. 205 p. 199.

(16) DAS, M. K. and TOBIAS, S.A. "The relation between the static and dynamic cutting of metals", Int. J. Mach. Tool Des. Res. 1967, Vol. 7, pp. 63-89.

(17) WALLACE, P.W. and ANDREW, C. "Machining Forces: some effects of tool vibration" J. Mech. Eng. Sci. Vol. 7, 1965, p. 152.

(18) DAS, M.K., KNIGHT, W.A. and SADEK, M.M. "A critical assessment of cutting force models in the analysis of machine tool instability" Int. J. Mach. Tool Des. Res. 1970, pp. 87-104

(19) WALLACE, P.W. and ANDREW, C. "Machining Forces: some effects of removing a wavy surface", J. Mech. Eng. Sci. Vol. 8, 1966, p. 129.

(20) GRIEVE, R.J. and RUBENSTEIN, C. "An experimental investigation of the dynamic cutting of steel" Int. J. Mach. Tool Des. Res. 1973, Vol. 13, pp. 1-16.

(21) OPITZ, H. and WECK, M. "Determination of the transfer function by means of special density measurements and its application to the dynamic investigation of machine tools under machining conditions" Int. J. Machine Des. and Res. 1969, pp. 349-378

(22) PETERS, J. "Comparative Assessment of Harmonic, Random, Swept Sine and Shock excitation, Methods for the Identification of machine tool structures with rotating spindles", Annals of CIRP, Vol. 24/1/ 1975, pp. 291-296.

(23) TLUSTY, J. LAU, K.C. and PARTHIBAN, K. "Use of Shock Compared with Harmonic Excitation in Machine Tool Structure Analysis" Trans. ASME J. of Engng. for Industry, Feb. 1974, pp. 187-195.

(24) GURNEY, J.P. and TOBIAS, S.A. "A graphical method for the determination of the dynamic stability of machine tools", Int. J. Mach. Tool Des. Res. 1961, Vol. 1, pp. 148-156.

(25) PETERS, J. and VANHERCK, P. "Machine tool stability tests and the incremental stiffness", Annals of the CIRP 1969, Vol. XVII pp. 225-232.

(26) MERRITT, H.E., "Theory of self-excited machine tool chatter. Contribution to machine tool chatter research - 1", Trans. ASME J. of Engng. for Industry, Nov. 1965. pp. 447-454.

(27) OPITZ, H. and BERNALDI, F. "Investigation and calculation of the chatter behaviour of lathes and milling machines". Annals of the CIRP 1970, Vol. XVIII, pp. 335-343.

(28) SANDVIK COROMANT "Tungsten Carbide Boring Bar" Machinery and Production Engng. Dec. 1973, Vol. 123, p.793

(29) SMOLENSKI, B.L. "A Cantilever Boring Bar" M/C and Tooling XXXIII 1962, No. 9, pp. 50-51.

(30) KUCHMA, L.K. "Boring bars with improved resistance to vibration" The Engineer's Digest, Feb. 1957, Vol. 18 No. 2, pp. 68-70.

(31) PARKER, E.W. "Dynamic Stability of a Cantilever Boring Bar with machined flats under regenerative cutting conditions", J. of Mech. Engng. Science, 1970, Vol. 12, No. 2, pp. 104-114.

(32) KATO, S. MARUI, E, and KURITA, H. "Some Considerations on Prevention of Chatter Vibration in Boring Operations", J. of Engng. for Industry, Trans. ASME, August 1969, Series B, Vol. 91, pp. 717-730.

(33) THOMAS, M.D., KNIGHT, W.A. and SADEK, M.M. "The Impact Damper as a Method of Improving Cantilever Boring Bars", J. of Engng. for Industry, Trans. ASME, August, 1975, pp. 859-866.

(34) INADA, S. Nakazawa, H. KUMEGAWA, H. and NAKAYAMA, G. "On a Method to prevent chatter in Boring Operations (Manufacture and Test of new Anti-Chatter Boring Bar") Bulletin of The JSME 1974, Vol. 17, No. 108, pp. 835-840.

(35) LANGHAM, J.M. "A new high-damping Manganese Copper Alloy" 17th Annual Pacific Conf. of American Foundrymen's Society, SMM Technical paper No. 6, April 1968.

(36) DEN HARTOG "Mechanical Vibration", Fourth Edition, McGraw Hill, 1956.

(37) BISHOP, R.E.D. and JOHNSON, D.C. "The Mechanics of Vibrations" Cambridge Univ. Press, 1960.

(38) JACOBSON, L.S. and AYRE, R.S. "Engineering Vibrations" McGraw Hill, 1958.

(39) WELBOURN, D.B. and SMITH, J.D. "Machine Tool Dynamics". Cambridge Univ. Press, 1970.

(40) TRC "Overcoming Vibration in Machine Tools" Techlink. No. 1209 Subject Code 3, 10, 24 Dept. of Trade and Industry, U.K.

(41) MASRI, S.F. and CAUGHEY, T.K. "On the stability of the Impact Damper", J. of Applied Mechanics, Trans. ASME, Sept. 1966, pp. 586-592.

(42) SADEK, M.M. "The Behaviour of the Impact Damper", Proceedings of the Institution of Mechanical Engineers, Vol. 180, Part I, 1965-1966.

(43) HAHN, R.S. "Design of Lanchester Damper for Elimination of Metal-cutting Chatter", Trans. ASME, Vol. 73, 1953.

(44) "Ceco damped bars and quills" Machinery and Production Engineering, March 9, 1966, Vol. 108, pp. 542-544.

(45) LAMDON, E.A. and REVVA, V.F. "Cemented carbide Boring Bars with Dynamic Vibration Dampers", Machine and Tooling, Nov. 1968, Vol. 39, pp. 39-41.

(46) "Kennametal De-vibrators for boring and turning operations", Machinery, Nov. 13, 1963, p. 1123.

(47) "Largest Kennametal Devibrator Boring Bar", Machinery and Production Engineering, 27 October 1971, Vol. 119 p. 607.

(48) GUSKOV, B.S. "Adjustable Boring Bar Vibration Damper", Machine and Tooling 1968, Vol. 39, Issue No. 12, p. 31.

(49) PERA No. 91, "Investigation into Overhung Boring Bars - Part III, the Dynamic Behaviour of a Tuned and Damped Viscous Absorber" Production Engineering Research Association.

(50) PERA No. 133, "Investigation into Overhung Boring Bars - Part VI Performance of a Tuned and Damped Boring Bar", Production Engineering Research Association.

(51) REVVA, V.F. "Slug Damping and Boring Bars for Fine Boring" Machine and Tooling 1962, Vol. 33, No. 7, p.23.

3. THEORIES OF BORING BAR - STATIC CUTTING FORCES AND TENTATIVE ANALYSES OF FACTORS AFFECTING GEOMETRIC FORM AND ECCENTRICITY OF FINISHED BORES

3.1 NOMENCLATURE

e_f = eccentricity of finished bore,

e_r = eccentricity of pre-finished bore,

F_t = tangential cutting force,

F_r = radial cutting force,

F_f = feed cutting force,

t = instantaneous depth of cut

s = feed per revolution

v = cutting speed

R_t = tangential cutting force coefficient defined as the force per unit depth of cut and per unit feed

R_r = radial cutting force coefficient defined as the force per unit depth of cut and per unit feed

x_1 = deflection in the direction of radial force during the first revolution

y_1 = deflection in the direction of tangential force during the first revolution

t_o = set depth of cut

s_o = set feed

x_n = radial deflection during the nth revolution

X_1 = radial deflection at the end of the first revolution

Y_1 = tangential deflection at the end of the first revolution

X_n = radial deflection at the end of the nth revolution

Z = feed reduction due to deflections x_n and y_n.

α = X_1/t_o

V_o cutting speed blank with eccentric bore

μ = overlapping factor,

K_t = stiffness of boring bar in tangential direction,

K_r = stiffness of boring bar in radial direction,

λ = overhung length of boring bar,

L = circumference of bore

$u = \frac{e_f}{e_r}$, copying error

ℓ = travelled distance of tool tip from entry

$\beta_t = R_t / K_t$

$\beta_r = R_r / K_r$

3.2 INTRODUCTION

Elastic deflections of the boring bar and the geometric form errors thereby produced will be discussed in this chapter. Factors believed to affect the geometric form include the bar stiffness, the depth of cut and the feed per revolution. The cutting speed, however, is not considered since in the practical speed range, the cutting force components are found to be constant. Two types of error will be looked into:- (a) errors that arise on entry of the boring tool into the workpiece, and (b) reproducibility of eccentricity errors.

3.3. EMPIRICAL CUTTING FORCE EQUATION

It is very difficult to obtain a reliable cutting force equation from the consideration of cutting mechanics. More often a realistic description of the forces can be achieved by means of an empirical equation of the form,

$$F = At^a s^b v^c \qquad (3.1)$$

where F is the machining force of interest, t is the depth of cut, s is the feed per revolution and v is the cutting speed.

In eqt (3.1) , A, a, b, and c are constants whose values are determined from cutting tests and they are unique for every machining material as well as the tool geometry (and condition of the cutting edge).

Equation 3.1 is suited to represent the tangential, radial and feed cutting force components.

In tests where the data collected are numerous, the business of finding the values of A, a, b and c is formidable. It will be shown that the cutting speed has negligible effects on the force over a wide range of practical speeds. For this reason it is convenient to consider instead a simplified empirical equation of the form

$$F = At^a s^b \qquad (3.2)$$

so that only constants A, a, and b have to be determined.

To find these constants, a curve-fitting procedure is adopted and is described briefly as follows. From the cutting force data available as a result of the cutting tests, it is possible to construct a family of graphs with forces against depths of cut for each feed. Both the forces and depths of cut are drawn to a logarithmic scale. If equation 3.2 is suitable, the family of graphs will be linear and parallel with each other. Their common gradient is given by a as is obvious from the following equation,

$$\log F = \log (As^b) + a \log t,$$

which is obtained by taking logarithm on both sides of eqt. 3.2.

The next step requires the use of another logarithmic form of the equation (3.2.). It is

$$\log F = \log (At^a) + b \log s$$

It is now possible to draw a family of graphs with forces against feed for each depth of cut. Both the force and the feed are drawn to a logarithmic scale. The common gradient of the graphs is equal to b.

Now that a and b are determined, it is a simple matter to draw a graph of the force F against the quantity $t^a s^b$. As can be seen from equation

(3.2), the graph is linear, passes through the origin and has a gradient of A.

3.4. GEOMETRIC FORM ERRORS CAUSED BY MACHINING FORCES IN BORING

3.4.1 Workpiece with a concentric bore

The pre-finished bore is concentric with the axis of rotation. Deflections in the feed direction are assumed to be negligible for the reason that longitudinal stiffness of the bar is much higher than its transverse stiffness.

Let the cutting force coefficient, R, be defined as the force per unit area of cut, then

$$R = \frac{F}{t_o s_o}$$

at the depth of cut t_o and feed s_o. In particular, the tangential and radial coefficients are respectively,

$$R_t = \frac{F_t}{t_o s_o} \qquad (3.3)$$

$$\text{and } R_r = \frac{F_r}{t_o s_o} \qquad (3.4)$$

Small variations in t_o and s_o bring about variations in F_t and F_r. Nevertheless these changes are small and so R_t and R_r can be assumed constant in the neighbourhood of t_o and s_o.

At the start of the cut, the tool engages the workpiece at the full depth of cut to which it is set, but with zero area of cut then increasing until at the end of the first revolution it has sunk into the workpiece at its full feed. If the circumference of the bore is L, and at a distance ℓ from entry, the actual feed will be given by

$(\frac{\ell}{L} s_o - z_1)$ where z_1 is the axial deflection of the bar.
As the area of cut increases, the bar deflects away from the set depth of cut t_o by an amount x_1 so that the actual depth of cut is $(t_o - x_1)$.

Arnold [1] showed that for a cantilever type single-point tool, the axial deflections resulting from the two transverse deflections in the respective radial and tangential directions are:

$$z_{1x} = \frac{x^2}{2\lambda} \quad \text{and} \quad z_{1y} = \frac{y^2}{2\lambda}$$

where x_1 and y_1 are the respective radial and tangential deflections and λ is the overhang of the cantilever which in this case is the boring bar. Since λ is large and x_1, y_1 are small deflections, z_{1x} and z_{1y} are insignificant.

At the distance ℓ from entry, the static force balance between the radial force and the spring restoring force of the bar is

$$R_r (t_o - x_1) \frac{\ell}{L} s_o = K_r x_1$$

and in the tangential direction,

$$R_t (t_o - x_1) \frac{\ell}{L} s_o = K_t y_1$$

Defining β_r and β_t as, $\beta_r = \frac{Rr}{Kr}$ and $\beta_t = \frac{R_t}{K_t}$, then from the previous two force-balance equations

$$\beta_r (t_o - x_1) \frac{\ell}{L} s_o = x_1$$

and $$\beta_t (t_o - x_1) \frac{\ell}{L} s_o = y_1$$

from which
$$x_1 = \frac{\beta_r t_o s_o \frac{\ell}{L}}{(1 + \beta_r s_o \frac{\ell}{L})} \qquad (3.5)$$

and
$$y_1 = \frac{\beta_t t_o s_o \frac{\ell}{L}}{(1 + \beta_r s_o \frac{\ell}{L})} \qquad (3.6)$$

At the end of the first cut, $\ell = L$, $x_1 = X_1$ and $y_1 = Y_1$.

Thus from equations (3.5) and (3.6)

$$X_1 = \frac{\beta_r t_o s_o}{(1+\beta_r s_o)} \qquad (3.7)$$

$$\text{and} \quad Y_1 = \frac{\beta_t t_o s_o}{(1+\beta_r s_o)} \qquad (3.8)$$

To develop realistic equations specifying deflections during the second and subsequent revolutions of the workpiece, the concept of an overlapping factor, μ, is introduced. The factor μ accounts for the influence of the preceding cut on the current cut and will vary between zero and unity corresponding to the cases of no overlap and full overlap respectively. In this sense, μ is similar to the overlapping factor defined by Tobias [2] in his machining stability analysis for regenerative chatter. In the present situation, it is not an exact representation since during the early stages of boring the effects of material previously left by the tool are not due to the deflection only, but also follow from the combination of the shape of the tool tip and the feed. This effect is illustrated in Fig. 3.1 showing (a) a sharp nose radius; (b) a nose radius equal to the magnitude of the feed, and (c) a nose radius much greater than the magnitude of the feed. In case (a), the area of cut, and so deflection, remains constant after completion of the first revolution if any secondary effect of elastic recovery is ignored. In case (b), interference occurs on the second and subsequent revolutions so that deflection increases to maintain the force balance, but this effect rapidly diminishes with successive revolution of the workpiece and rapidly tends to a constant level. In case (c), the geometry effect of the tool is much more significant during the initial revolutions, but again it rapidly diminishes, the resulting deflection tending

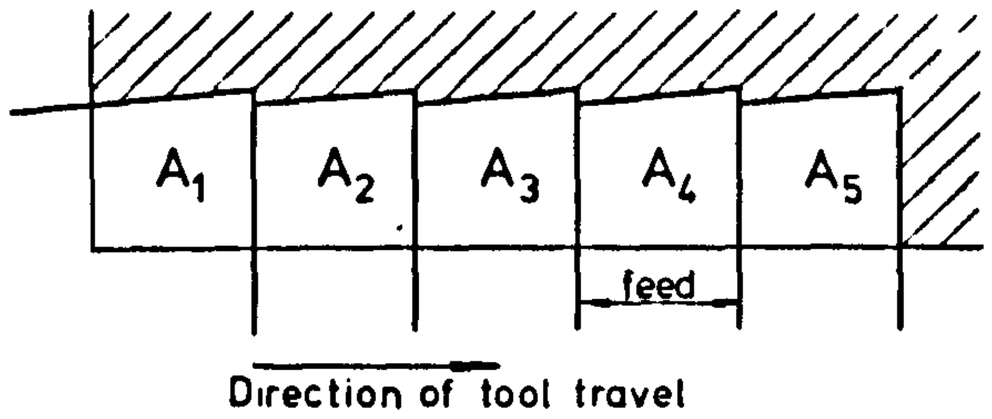

a) nose radius = 0

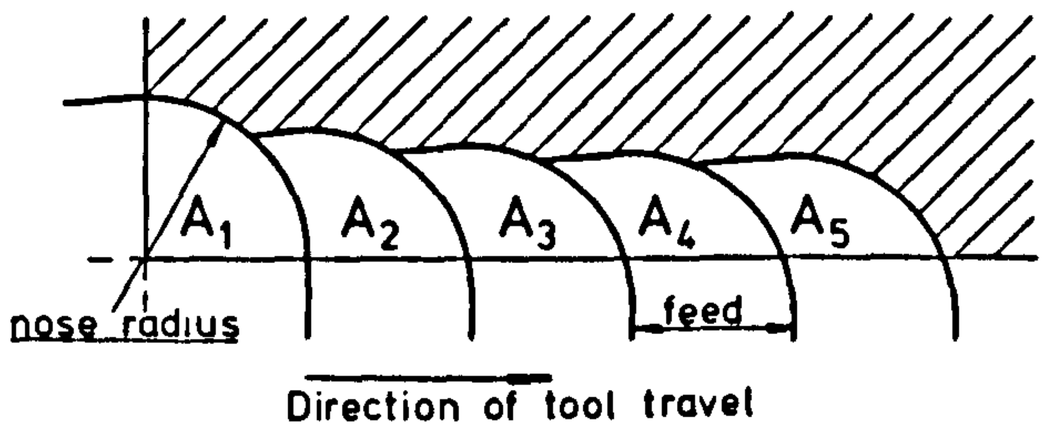

b) nose radius = feed

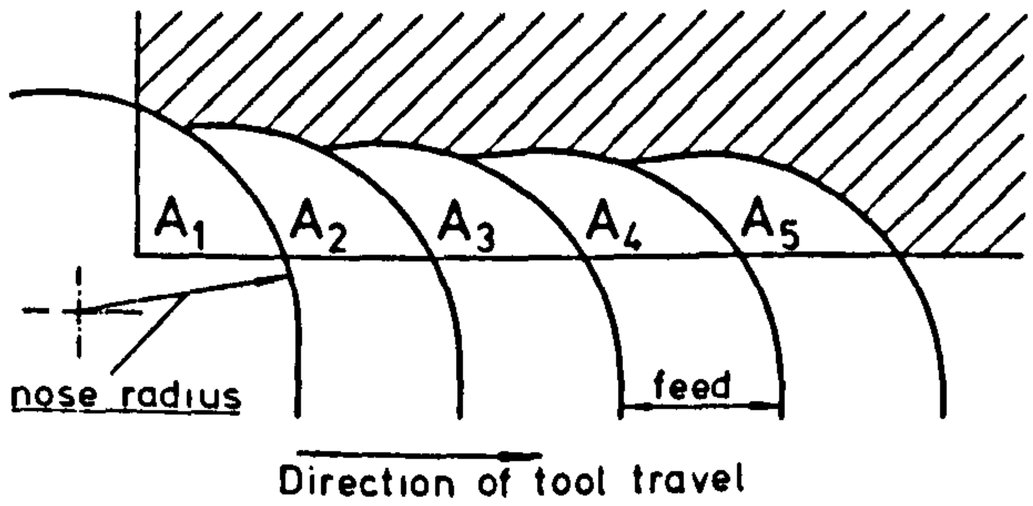

c) nose radius > feed

Fig 3.1 Effect of nose radius and deflection of tool on chip cross-section A_i (i = 1, 2, 3, ... n)

quickly to a constant level.

In spite of these practical complications, the following analysis presents a workable method the results of which agree qualitatively with those observed on a finished bore, recognising of course that the value of μ will depend on the particular nose radius and feed used.

Introducing μ for the second revolution, we obtain

$$\beta_r [t_o - (x_2 - \mu x_1)] s_o = x_2$$

and $$\beta_t [t_o - (x_2 - \mu x_1)] s_o = y_2$$

which in terms of x_2 and y_2 respectively give

$$x_2 = X_1 \left(1 + \frac{\mu}{t_o} x_1\right) \qquad (3.9)$$

and $$y_2 = x_2 \frac{\beta_t}{\beta_r} \qquad (3.10)$$

It is possible to generalize the derivation to the nth cut during which the tool is deflected x_n and y_n away from the position at which the tool is set to cut. The force balance equations are:

$$\beta_r [t_o - (x_n - \mu x_{n-1})] s_o = x_n$$

$$\beta_t [t_o - x_n - \mu x_{n-1})] s_o = y_n$$

which can be re-written as:

$$x_n = X_1 \left(1 + \frac{\mu}{t_o} x_{n-1}\right) \qquad (3.11)$$

and $$y_n = x_n \frac{\beta_t}{\beta_r} \qquad (3.12)$$

Equation (3.11) which relates to deflection x_n in the radial direction is of immediate interest. Expanding it gives:

$$x_n = X_1 + X_1^2(\frac{\mu}{t_o}) + X_1^3(\frac{\mu}{t_o})^2 + X_1^4(\frac{\mu}{t_o})^3 + \ldots + X_1^{n-1}(\frac{\mu}{t_o})^{n-2} + X_1^{n-1}(\frac{\mu}{t_o})^{n-1}x_1$$

in which the 2nd term to the 2nd last term inclusive form a geometrical progression and can be summed. Thus,

$$x_n = X_1 + X_1^{n-1}(\frac{\mu}{t_o})^{n-1}x_1 + \frac{X_1(\frac{\mu}{t_o})\left(1-[X_1(\frac{\mu}{t_o})]^{n-2}\right)}{\left(1-X_1(\frac{\mu}{t_o})\right)} \qquad (3.13)$$

In particular, at the completion of the nth cut,

$$X_n = X_1 + \frac{X_1^2(\frac{\mu}{t_o})\left(1-[X_1(\frac{\mu}{t_o})]^{n-1}\right)}{\left(1-X_1(\frac{\mu}{t_o})\right)} \qquad (3.14)$$

Since $X_1 < t_o$, or $X_1 = \alpha t_o$ where α is less than unity, the higher powers of $\frac{x_1}{t_o} = \alpha$ must be increasingly smaller and X_n as given in equation (3.14) will converge to a maximum value as n increases. Thus,

$$X_{n\to\infty} = X_1 + \frac{X_1^2(\frac{\mu}{t_o})}{\left(1-X_1(\frac{\mu}{t_o})\right)} \qquad (3.15)$$

But since $X_{n\to\infty} < t_o$, then from equation (3.15)

$$t_o > X_1 + \frac{X_1^2(\frac{\mu}{t_o})}{\left(1-X_1(\frac{\mu}{t_o})\right)}$$

which can be simplified to

$$\alpha < \frac{1}{(1+\mu)} \quad \text{or} \quad \mu < \frac{1-\alpha}{\alpha} \qquad (3.16)$$

if $\propto \mu < 1$ which is valid because $0 \leqslant \mu \leqslant 1$ and $0 < \propto < 1$

With reference to either equations (3.14) or (3.15), it can be seen that with a smaller depth of cut, feed and a small overlapping factor, the deflection X_n at the tool tip decreases. A smaller overlapping factor can result from a sharper nose radius and a larger trailing clearance. Above all, the most effective way to reduce X_n is to increase the stiffness of the boring bar. Since X_n increases at a reduced rate as n increases in equation (3.14), and eventually tends to a constant value of $X_{n\to\infty}$ as given in equation (3.15), the geometric form of the bore will take up the shape of a bell-mouth. For this reason, it will be referred to simply as the "bell-mouth" error in future.

3.4.2. Workpiece with eccentric bore

The pre-finished bore has an eccentricity e_r relative to the axis of rotation. During cutting, the instantaneous depth of cut varies from a minimum t_{min} to a maximum t_{max} if the boring bar is infinitely rigid and they are related to eccentricity e_r by

$$2e_r = t_{max} - t_{min} \qquad (3.17)$$

Since the bar is not infinitely rigid but has a stiffness K_r in the radial direction, at the position of maximum depth of cut, it is deflected such that

$$x_{max} = \frac{F_r}{K_r}$$

where F_r is the radial cutting force at the actual depth of cut $(t_{max} - x_{max})$ and is given by equation (3.2), i.e.

$$F_r = A_r t^a s^b$$

in which $t = (t_{max} - x_{max})$

Hence, $$x_{max} = \frac{A_r (t_{max} - x_{max})^a s^b}{K_r}$$

or $$x_{max} = \frac{A_r \, t_{max}^{\,a} \, (1 - \frac{x_{max}}{t_{max}})^a \, s^b}{K_r}$$

Since $\frac{x_{max}}{t_{max}} \ll 1$ and the index a is in general less than unity, little error arises if we approximate $(1 - \frac{x_{max}}{t_{max}})^a$ by $(1 - a\frac{x_{max}}{t_{max}})$

so that $$x_{max} \doteq \frac{A_r t_{max}^{\,a} s^b}{K_r} (1 - a \frac{x_{max}}{t_{max}})$$

from which

$$x_{max} \doteq \frac{A_r t_{max}^{\,a} s^b}{K_r} \Big/ (1 + \frac{A_r t_{max}^{\,a} s^b}{K_r} \cdot \frac{a}{t_{max}}) \qquad (3.18)$$

Similarly for x_{min} at the position of minimum depth of cut

$$x_{min} \doteq \frac{A_r t_{min}^{\,a} s^b}{K_r} \Big/ (1 + \frac{A_r t_{min}^{\,a} s^b}{K_r} \cdot \frac{a}{t_{min}}) \qquad (3.19)$$

Equations (3.18) and (3.19) can be expressed in terms of the mean depth of cut t which is defined as

$$t = t_{max} - e_r = t_{min} + e_r,$$

and they respectively become

$$x_{max} \doteq \frac{A_r t^a s^b}{K_r} \cdot \frac{(1 + \frac{e_r}{t})^a}{1 + a \frac{A_r s^b t^{(a-1)}}{K_r} (1 + \frac{e_r}{t})^{(a-1)}} \qquad (3.20)$$

and $$x_{min} \doteq \frac{A_r t^a s^b}{K_r} \cdot \frac{(1 - \frac{e_r}{t})^a}{1 + \frac{a A_r s^b t^{(a-1)}}{K_r} (1 - \frac{e_r}{t})^{(a-1)}} \qquad (3.21)$$

When $\frac{e_r}{t} \ll 1$ and since a is in general less than unity,

$$(1 + \frac{e_r}{t})^a \doteq (1 + a\frac{e_r}{t}) \quad \text{and} \quad (1 - \frac{e_r}{t})^a \doteq (1 - a\frac{e_r}{t})$$

Similarly, $(1 + \frac{e_r}{t})^{(a-1)} \doteq (1 + (a-1)\cdot\frac{e_r}{t})$ and $(1 - \frac{e_r}{t})^{(a-1)} \doteq (1 - \frac{(a-1)\cdot e_r}{t})$

Thus, equations (3.20) and (3.21) become,

$$x_{max} \doteq \frac{A_r t^a s^b}{K_r} \cdot \frac{1 + a\frac{e_r}{t}}{1 + a\frac{A_r s^b t^{(a-1)}}{K_r}\left(1 + \frac{ae_r}{t} - \frac{e_r}{t}\right)} \tag{3.22}$$

and $$x_{min} \doteq \frac{A_r t^a s^b}{K_r} \cdot \frac{1 - a\frac{e_r}{t}}{1 + \frac{aA_r s^b t^{(a-1)}}{K_r}\left(1 - \frac{ae_r}{t} + \frac{e_r}{t}\right)} \tag{3.23}$$

The eccentricity error, e_f, on the finished bore is related to x_{max} and x_{min} by the equation,

$$2e_f = x_{max} - x_{min} \tag{3.24}$$

And if we define the "copying" error as $u = \frac{e_f}{e_r}$, (3.24a), which indicates the extent to which the eccentricity error is copied, and for $\frac{e_r}{t} \ll 1$, then

$$u \doteq \frac{A_r t^a s^b}{K_r}\left[\frac{1 + \frac{ae_r}{t}}{e_r + \frac{aA_r s^b t^{(a-1)}}{K_r}\left(e_r + \frac{ae_r^2}{t} - \frac{e_r^2}{t}\right)} - \frac{1 - \frac{ae_r}{t}}{e_r + \frac{aA_r s^b t^{(a-1)}}{K_r}\left(e_r - \frac{ae_r^2}{t} + \frac{e_r^2}{t}\right)}\right]$$

Ignoring terms containing $\frac{e_r^2}{t}$ since it is smaller than $\frac{e_r}{t}$, the above equation simplifies to

$$u \doteq \frac{1}{1 + \frac{K_r t^{(1-a)}}{aA_r s^b}}$$

$$\text{or} \qquad u \doteq \frac{1}{1+K} \tag{3.25}$$

$$\text{where } K = \frac{K_r t^{(1-a)}}{aA_r s^b} \tag{3.26}$$

Fig. 6.26 shows the "copying" error in relation to the parameter K as defined in equation (3.26). As K increases from zero, the "copying" error decreases from unity. K can be made large by:-

(1) increasing the bar stiffness, K_r,

(2) increasing the depth of cut t since (1-a) is positive in equation (3.26), and

(3) decreasing the feed s.

A_r is the material constant whose value in general increases with the increase in the ultimate tensile strength of the material.

REFERENCES FOR CHAPTER 3

1. ARNOLD, R.N. "The Mechanism of Tool Vibration in the Cutting of Steel" Proc. Inst. Mech. Engrs. 154, 1946 p. 261.

2. TOBIAS, S.A. "Chatter in Simple Machine Tool System" Machine Tool Vibration, Blackie, London, 1965 p. 157.

4. THEORIES OF BORING BAR - FREQUENCY RESPONSE

4.1 NOMENCLATURE

T = kinetic energy,

V = potential energy,

$2F$ = dissipative energy rate,

Q = forcing function,

m = equivalent mass of boring bar considered at free end,

m_s = mass of slug,

m_f = mass of damping fluid,

$\beta_{c,f}$ = a correction factor, the square root of which converts the relative-velocity between bar and slug to the average velocity of damping fluid, and are defined as;

$$\beta_c = \left(\frac{R_2}{a}\right)^2, \text{ for slug rolling or sliding in cavity}$$

and

$$\beta_f = \frac{1}{2}\left(\frac{R_2}{a}\right)^2 \quad \text{for slug "floating" in cavity}$$

λ = radius of gyration of slug about longitudinal axis,

R_2 = radius of slug,

a = radial clearance between slug absorber and cavity,

x_1 = instantaneous vibration of bar at position of centre of slug,

x_2 = instantaneous vibration of slug at its central transverse plane,

x_o = instantaneous vibration of bar at free end,

G = ratio of amplitudes, i.e. x_1/x_o,

K = equivalent stiffness of bar considered at free end,

c = coefficient of viscous damping,

P_o = applied force vector at free end of bar,

ω = angular frequency of the applied force,

X_o = vector vibration amplitude of bar at free end,

X_1 = vector vibration amplitude of bar at position of centre of slug,

X_2 = vector vibration amplitude of slug at its central transverse plane,

$\omega_n = \left(\frac{K}{m+G^2 m_s}\right)^{\frac{1}{2}}$ = angular undamped natural frequency of bar with a tight-fit slug,

ℓ = $1 + \left(\frac{\lambda}{R_2}\right)\left(\frac{m_f}{m_s}\right) \beta_{cf}$, a mass correction factor for slug and fluid,

c_c = $2m_s\omega_n$, "critical" damping coefficient,

h = $\frac{\omega}{\omega_n}$, frequency ratio

m_{eq} = equivalent mass of the single-slug-damped bar in the analogous single-degree-of-freedom system,

c_{eq} = equivalent damping coefficient of the single-slug-damped bar in the analogous single-degree-of-freedom system

k_{eq} = equivalent spring stiffness of the single-slug-damped bar in the analogous single-degree-of-freedom system

ΔF = damping energy dissipated per cycle,

c_{opt} = optimum damping coefficient for the case of constant amplitude excitation

ΔF_{opt} = damping energy dissipated per cycle corresponding to c_{opt},

μ = $G^2 \frac{m_s}{m}$, mass ratio,

X_{st} = $\frac{Po}{K}$, static deflection of bar under the point of application of loading Po at free end,

θ = phase lag of amplitude behind impressed force,

S = $\left|\frac{X_o}{X_{st}}\right|^2$, amplitude ratio squared,

R = h^2, frequency ratio squared,

Q = $\left(\frac{2c}{\ell c_c}\right)^2$ damping factor squared,

Z = $\frac{\mu}{(1+\mu)\ \ell}$, mass ratio factor,

T = $\frac{1}{1-Z}$, resonant frequency ratio squared for the case of zero damping,

E_i = Young's Modulus at the ith section of bar,

I_i = second moment of area, at the ith section of bar,

y_o = deflection of the bar at the free end, used in Section 4.5.1.

$y(x)$ = deflection of bar at a distance x measured from the fixed end, in Section 4.5.1,

ℓ_1 = overhung length of boring bar, in Section 4.5.1.

$\bar{\rho}_i$ = mass per unit length of boring bar, in Section 4.5.1.

h_b = bung length

4.2 HARMONIC RESPONSE OF SINGLE-SLUG-DAMPED BORING BAR

A real physical system such as a boring bar is a distributed system in that its mass, damping and stiffness properties are distributed in the elements that make up the system. The resulting mathematical model requires the use of partial differential equations which are difficult to handle. However, since only the fundamental mode is of concern in most vibration situations, the boring bar in its simplest but realistic form may be regarded as a lumped parameter system consisting of discrete elements of mass, dashpot and spring. The resulting mathematical model involves only ordinary linear differential equations the solutions of which are readily determined.

Assuming a lumped parameter system, we set out in this chapter to formulate a mathematical model using the technique of Lagrange equation whereby the differential equations of motion are obtained. But since this has been discussed in detail by Ng and New [1] as summarized in Appendix B, rather than repeat their work the ensuing discussion concentrates on the physical significance of the analogue with discrete elements of mass, dashpot, and spring. A phasor representation of the forces arising from these elements seems to be more revealing and is, therefore, used to facilitate explanation.

From the mathematical model, the following points are taken up and examined:-

(1) amplitudes and phase responses of the boring bar,

(2) the equivalent mass and equivalent damping concept,

(3) the resonant frequency,

(4) the occurrence of the minimum amplitude at resonance for a particular damping known as the optimum damping, and

(5) the design considerations of bung length in respect of minimum amplitude at resonance. Each of these will be studied successively.

4.3. THE MATHEMATICAL MODEL

To set up the equations of motion, use is made of the Lagrange equation which, in the fundamental form for generalized co-ordinates q_i, is

$$\frac{d}{dt}\left(\frac{\partial T}{\partial \dot{q}}\right) - \frac{\partial T}{\partial q} + \frac{\partial F}{\partial \dot{q}} + \frac{\partial V}{\partial q} = Q$$

where T is the kinetic energy of the system; V, the potential energy; F. the dissipative energy/; rate and Q. the generalized external force acting on the system.

Ng and New [1] derived the expressions for T, V and F as a function of the coordinates x_1 and x_2, which are summarized as below.

(1) Kinetic energy, T

From equation (B2), which is repeated here, in Appendix B,

$$T = \frac{1}{2}\frac{m}{G^2}\dot{x}_1^2 + \frac{1}{2}m_s\dot{x}_2^2 + \frac{1}{2}m_s\left(\frac{\lambda}{R_2}\right)^2(\dot{x}_1 - \dot{x}_2)^2 + \frac{1}{2}m_f\beta_c(\dot{x}_1 - \dot{x}_2)^2 \qquad (B.2)$$

(2) Potential energy, V

Two potential energies * will be involved, namely, the gravitational potential energy brought about by the vertical component of displacement of the slug and the elastical potential energy due to the straining of the boring bar. Only the latter

* Strictly speaking, one can name three potential energies. The third arises from the compressibility of the fluid flowing in the gap. But this is ignored in the present analysis.

is, however, considered whilst the former is assumed to be negligible in comparison. Thus, the potential energy is

$$V = \frac{1}{2} k x_o^2 = \frac{1}{2} \frac{K}{G^2} x_1^2 \qquad (4.1)$$

(3) Dissipative energy

The damping force is assumed to be proportional to the relative velocity $(\dot{x}_1 - \dot{x}_2)$ between the bar and the slug at the central position of the slug. The constant of proportionality, known as the damping coefficient, is designated by c and the dissipative energy, is, therefore,

$$F = \frac{1}{2} c (\dot{x}_1 - \dot{x}_2)^2 \qquad (4.2)$$

(4) Forcing function, Q

Since the harmonic response is to be studied, the forcing function is

$$Q = P_o \cos \omega t = \mathrm{Re}\{ P_o e^{j\omega t} \}$$

where Re means "the real part of".

The force P_o is applied at the free end. But since we are concerned with the motion on the transverse plane of the slug centre, where the motions x_1 and x_2 are measured, the force P_o has to be converted as follows. The work done by the force P_o to cause a displacement x_o at its point of application is $P_o x_o$. Similarly, the work done by a force Q_o to cause a displacement x_1 at its point of application is $Q_o x_1$. For both energies to be equal, it is necessary that

$$Q_o = P_o \frac{x_o}{x_1}$$

But from equation (B.1), $x_1 = Gx_o$, then

$$Q_o = \frac{P_o}{G}$$

The equivalent forcing function in the plane of x_1 and x_2 is, therefore,

$$Q = \text{Re} \left\{ \frac{P_o}{G} e^{j\omega t} \right\} \qquad (4.3)$$

Substituting equations (B.2), (4.1), (4.2) and (4.3) into the Lagrange equation will yield the differential equations of motion which are

$$\frac{m}{G^2}\ddot{x}_1 + (m_s\frac{\lambda^2}{R_2^2}+m_f\beta_c)(\ddot{x}_1 - \ddot{x}_2) + c(\dot{x}_1-\dot{x}_2) + \frac{K}{G^2}x_1 = \frac{P_o}{G}e^{j\omega t} \qquad (4.4)$$

and
$$m_s\ddot{x}_2 - (m_s\frac{\lambda^2}{R_2^2}+m_f\beta_c)(\ddot{x}_1 - \ddot{x}_2) - c(\dot{x}_1-\dot{x}_2) = 0 \qquad (4.5)$$

From the consideration of equations (4.4) and (4.5), an analogous model can be found for this single-slug-damped boring bar. The model, as shown in Fig. 4.1, consists of two masses, $\frac{m}{G^2}$ and m_s, coupled by a dashpot c and an inertia coupling factor $(m_s \frac{\lambda^2}{R_2^2} + m_f\beta_c)$. The main mass $\frac{m}{G^2}$ is connected to the free end of a spring of stiffness $\frac{K}{G^2}$ and the impressed force is designated by $\frac{P}{G} e^{j\omega t}$.

Assuming steady-state solutions of the form

$$x_1 = X_1 e^{j\omega t}$$

and

$$x_2 = X_2 e^{j\omega t}$$

where X_1 and X_2 are amplitude phasors that are complex quantities, equations (4.4) and (4.5) are respectively transformed into algebraic equations. Thus,

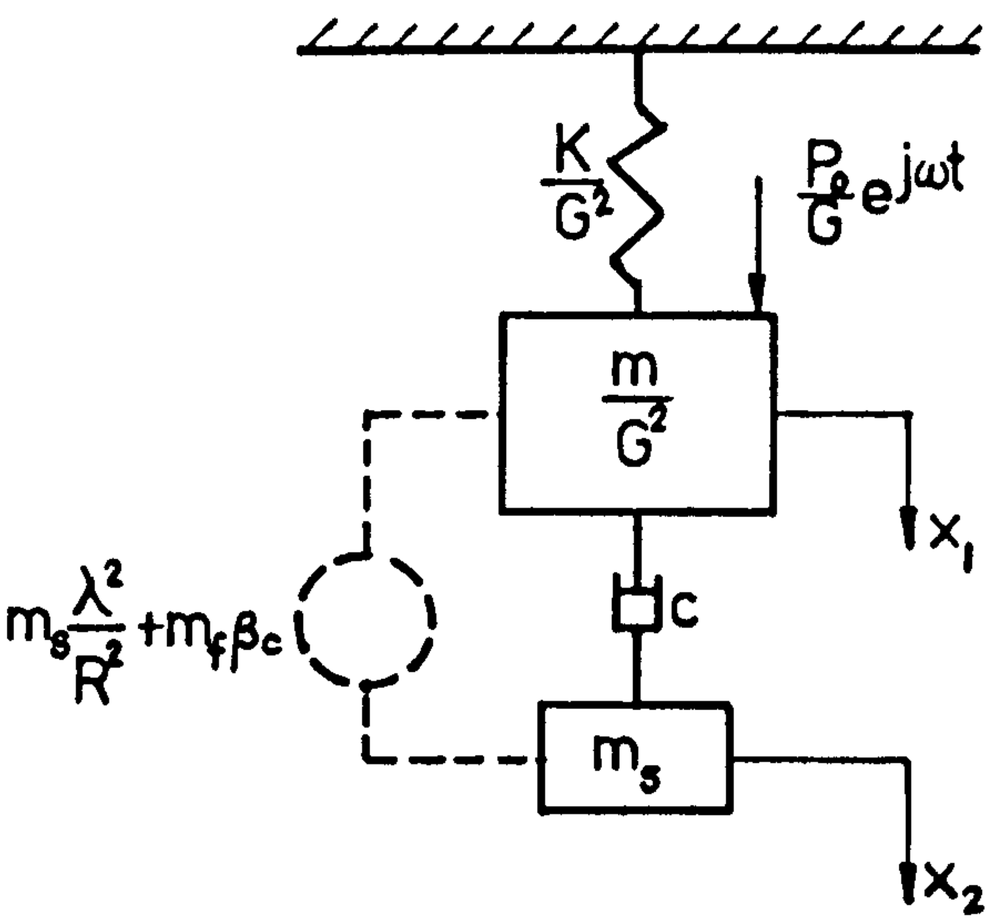

Fig 4.1 An analogous model of the single-slug-damped boring bar

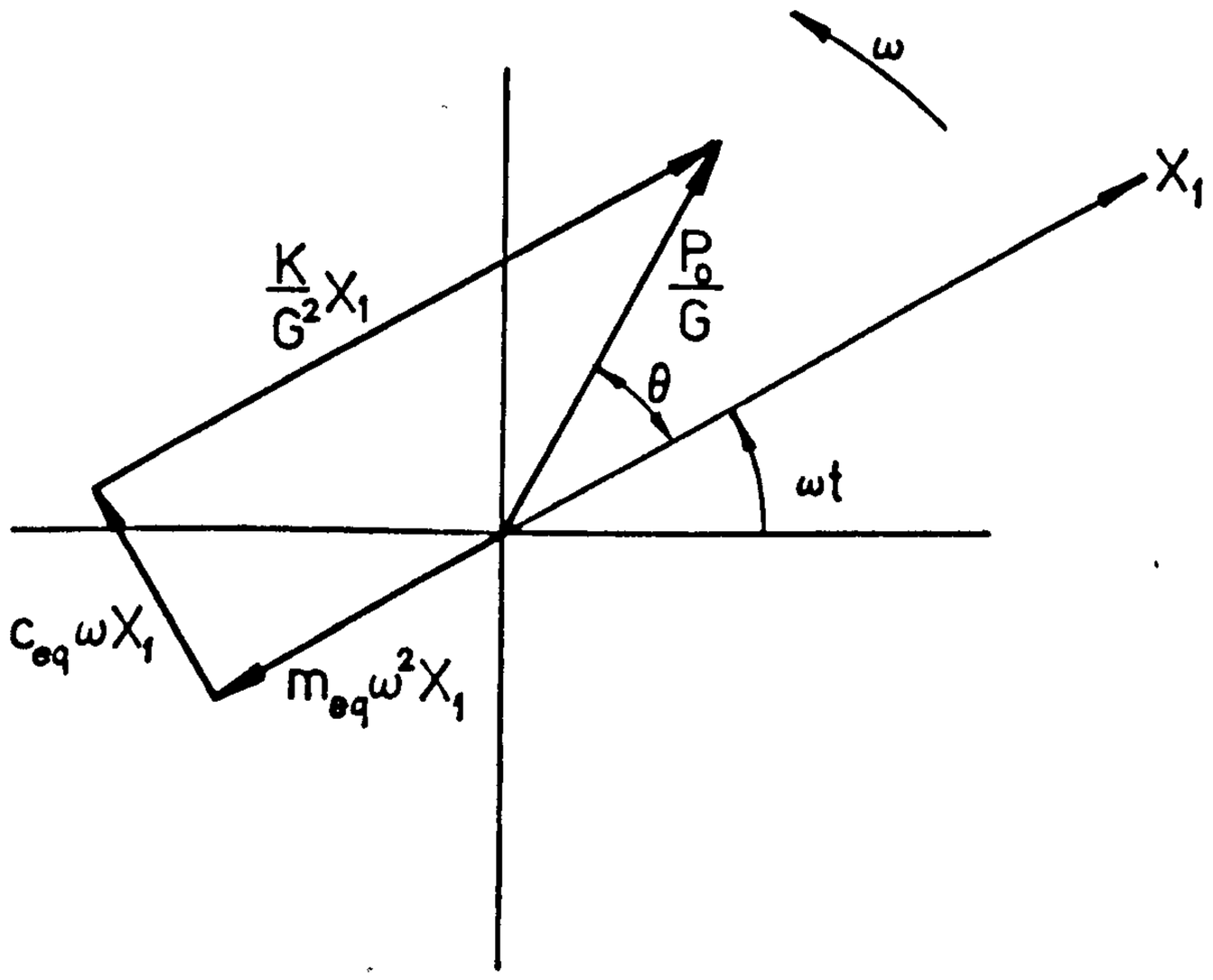

Fig 4.2 A phasor representation of the forces involved in the analogue of Fig 4.1 - before resonance

$$\left[-\omega^2\left(\frac{m}{G^2}+m_s\frac{\lambda^2}{R_2^2}+m_f\beta_c\right)+j\omega c+\frac{K}{G^2}\right]X_1-\left[-\omega^2\left(m_s\frac{\lambda^2}{R_2^2}+m_f\beta_c\right)+j\omega c\right]X_2=\frac{P_o}{G}$$

(4.6)

and,

$$-\left[-\omega^2\left(m_s\frac{\lambda^2}{R_2^2}+m_f\beta_c\right)+j\omega c\right]X_1+\left[-\omega^2\left(m_s+m_s\frac{\lambda^2}{R_2^2}+m_f\beta_c\right)+j\omega c\right]X_2=0$$

(4.7)

Rewrite equation (4.7) to give a complex amplitude ratio, i.e.

$$\frac{X_2}{X_1}=\frac{-\omega^2\left(m_s\frac{\lambda^2}{R_2^2}+m_f\beta_c\right)+j\omega c}{-\omega^2\left(m_s+m_s\frac{\lambda^2}{R_2^2}+m_f\beta_c\right)+j\omega c}$$

the modulus of which is found to be

$$\left|\frac{X_2}{X_1}\right|=\sqrt{\frac{\left[\left(m_s\frac{\lambda^2}{R_2^2}+m_f\beta_c\right)\omega^2\right]^2+(\omega c)^2}{\left[\left(m_s+m_s\frac{\lambda^2}{R_2^2}+m_f\beta_c\right)\omega^2\right]^2+(\omega c)^2}}$$

If we define the critical damping $c_c = 2m_s\omega_n$, in which $\omega_n=\sqrt{\frac{K}{m+m_sG^2}}$ is the angular undamped natural frequency of the boring bar with a tight-fit slug; and let $h=\frac{\omega}{\omega_n}$ and $\ell=\left(1+\frac{\lambda^2}{R_2^2}+\frac{m_f}{m_s}\beta_c\right)$ which is a measure of the fluid mass and the slug rolling effects, then the last expression for amplitude ratio can be simplified to a non-dimensional form as,

$$\left|\frac{X_2}{X_1}\right|=\sqrt{\frac{(\ell-1)^2+\left(2\frac{c}{c_ch}\right)^2}{\ell^2+\left(2\frac{c}{c_ch}\right)^2}}$$

(4.8)

The quantity ℓ is called the mass correction factor; and h, the frequency ratio.

Two extreme cases are obvious:- (1) when $\frac{c}{c_c} = 0$, $\left|\frac{X_2}{X_1}\right| = 1 - \frac{1}{\ell}$; and (2) when $\frac{c}{c_c}$ tends to infinity, $\left|\frac{X_2}{X_1}\right| = 1$. In the general situation where $\frac{c}{c_c}$ takes up some intermediate value, $\left|\frac{X_2}{X_1}\right| < 1$.

Referring to equations (4.6) and (4.7) that consist of two unknowns X_1 and X_2, we can combine them to eliminate X_2 giving a single equation.

$$-\left[\frac{m}{G^2}+m_s\left(1-\frac{\ell}{\ell^2+\left(\frac{c}{m_s\omega}\right)^2}\right)\right]\omega^2 X_1 + j\left[\frac{m_s\omega\left(\frac{c}{m_s\omega}\right)}{\ell^2+\left(\frac{c}{m_s\omega}\right)^2}\right]\omega X_1 + \frac{K}{G^2}X_1 = \frac{P_o}{G} \qquad (4.9)$$

By virtue of this equation, the original system can be seen to be analogous to a single-degree-of-freedom model that is represented by an equation of motion of the form:

$$m_{eq}\ddot{x} + c_{eq}\dot{x} + k_{eq}x = P\cos\omega t$$

which is equivalent to

$$-m_{eq}\omega^2 X + j\omega c_{eq} X + k_{eq} X = P \qquad (4.9a)$$

Such an analogy offers some definite advantage in the subsequent analysis of experimental data for reasons that will become clear later.

If we make the identifications between the corresponding terms in equations (4.9) and (4.9a), then,

$$m_{eq} = \frac{m}{G^2} + m_s \left(1 - \frac{\ell}{\ell^2 + \left(\frac{c}{m_s \omega} \right)^2} \right) \qquad (4.10)$$

$$c_{eq} = \frac{m_s \omega \left(\frac{c}{m_s \omega} \right)}{\ell^2 + \left(\frac{c}{m_s \omega} \right)^2} \qquad (4.11)$$

and $$k_{eq} = \frac{K}{G^2}$$

Equation (4.9) may also be interpreted as depicting the summation of forces. The terms on the left-hand side correspond to the inertia force, the damping force and the spring force respectively, whereas the term on the right-hand side resembles the applied force. The equal sign indicates that the inertia, damping and spring forces balance the applied force, which is illustrated in the form of a phasor diagram in Fig. 4.2. It must be noted that the inertia,damping,and,spring forces are equivalent forces only, in the sense that they do not physically exist in the analogue of Fig. 4.1. That is to say, apart from the spring force and the applied force, the individual forces that one can identify exerting on the main mass of this analogue are very different from the equivalent forces of equation (4.9). Nevertheless, these individual forces when correctly added must result in the equivalent forces on account of the fact that equation (4.9) is derived from equations (4.6) and (4.7), both of which represent the analogue of Fig. 4.1.

By equations (4.10) and (4.11), it can be seen that the parameters m_{eq} and c_{eq} are variable quantities, the values of which, among other factors, are dependent on the frequency of excitation ω. In particular the

equivalent mass m_{eq} is made up of two parts:-

(i) the main mass $\frac{m}{G^2}$ which is a constant and

(ii) the effective mass of the slug and the fluid in the gap as denoted by the quantity, $m_s\left[1 - \frac{\ell}{\ell^2 + (\frac{c}{m_s\omega})^2}\right]$. The equivalent damping coefficient c_{eq} as given in equation (4.11) indicates the variable nature of the damping present in the analogous single-degree-of-freedom system because of the presence of the frequency term ω. The damping energy dissipated per cycle, i.e. during period T, assuming sinusoidal motion, is,

$$\Delta F = \int_0^T (c_{eq}\dot{x}_1)\dot{x}_1\,dt = \int_0^T c_{eq}\omega^2 X_1^2 \cos\omega t\,dt = \pi c_{eq}\omega X_1^2$$

Substituting equation (4.11) in the last energy expression gives

$$\Delta F = \frac{\pi}{2}(m_s\omega^2)X_1^2 \cdot \frac{2(\frac{c}{m_s\omega})}{\ell^2 + (\frac{c}{m_s\omega})^2} \qquad (4.12)$$

This equation is plotted in Fig. 4.3 with $\Delta F \Big/ \frac{\pi}{2}(m_s\omega^2 X_1^2)$ versus $\frac{c}{m_s\omega}$. Two graphs are shown corresponding to $\ell = 1$ and $\ell = 1.5$.

It can be observed that each graph reaches a maximum value of $\Delta F \Big/ \frac{\pi}{2}(m_s\omega^2 X_1^2)$ indicating a maximum damping energy dissipation ΔF. To find the corresponding $\frac{c}{m_s\omega}$ the quantity $\frac{2(\frac{c}{m_s\omega})}{\ell^2 + (\frac{c}{m_s\omega})^2}$ in equation (4.12) is to be maximized.

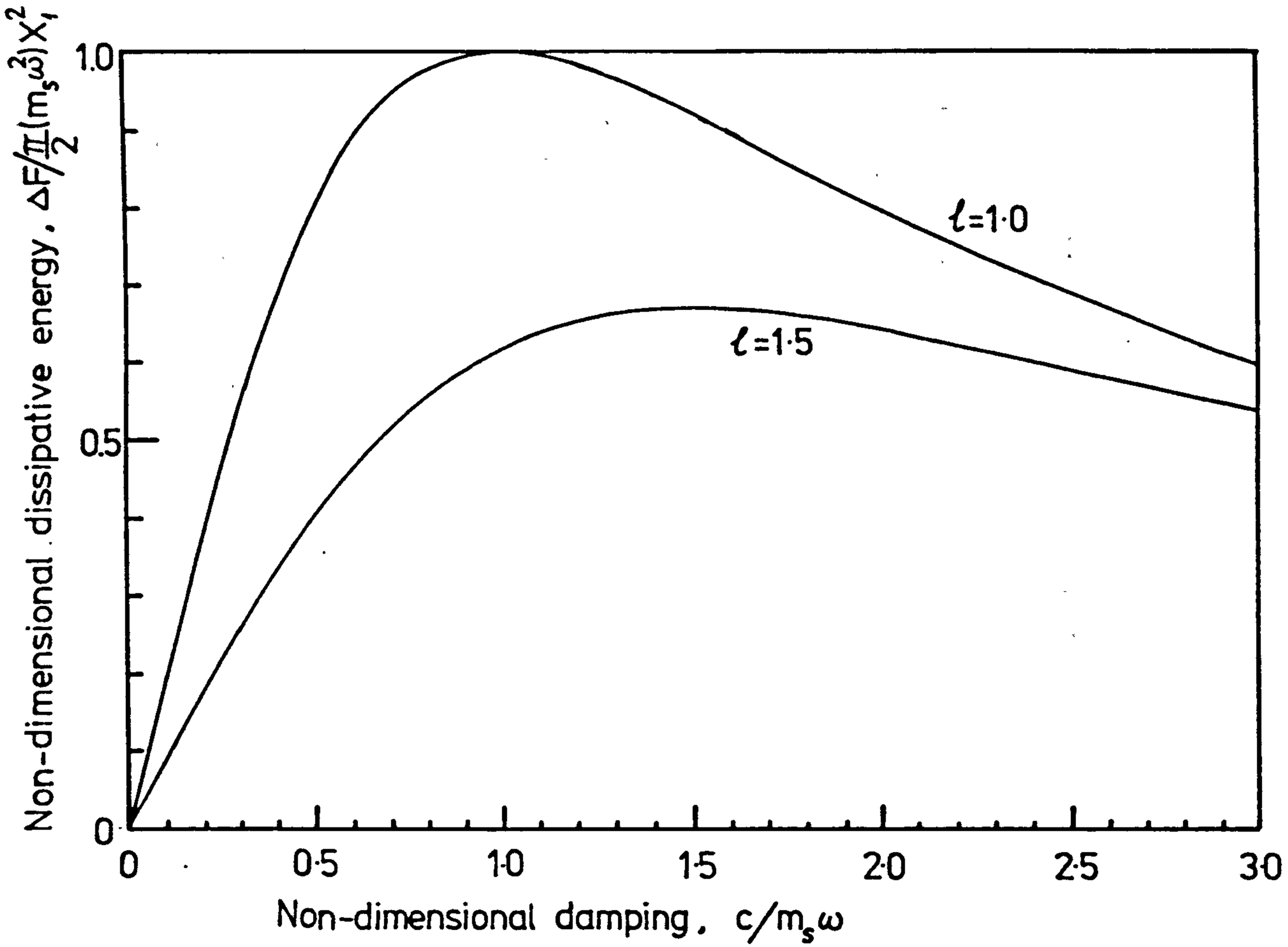

Fig 4.3 Relation between the non-dimensional dissipative energy and the non-dimensional damping

It can be shown that for $\frac{c}{m_s\omega} = \ell$, this quantity reaches a maximum value. Thus, the optimum damping coefficient

$$c_{opt} = m_s\omega\ell \tag{4.13}$$

and the maximum energy dissipated

$$\Delta F_{opt} = \frac{\pi}{2\ell}(m_s\omega^2)X_1^2 \tag{4.14}$$

It must be pointed out that equations (4.13) and (4.14) are valid only for the case of constant amplitude excitation, i.e. constant X_1, since in maximizing ΔF, X_1 is assumed constant. The case of constant force excitation will be dealt with in Section 4.4.

Solving equation (4.9) for the amplitude X_1 gives

$$X_1 = \frac{P_o}{G} \cdot \frac{1}{\left\{\left[\frac{K}{G^2} - \left[\frac{m}{G^2} + m_s\left(1 - \frac{\ell}{\ell^2 + (\frac{c}{m_s\omega})^2}\right)\right]\omega^2\right\} + j\left[\omega\ \frac{m_s\omega(\frac{c}{m_s\omega})}{\ell^2 + (\frac{c}{m_s\omega})^2}\right]}$$

Nevertheless, what is to be measured in the experiment is the amplitude X_o measured at the free end and since from equation (B.1) $GX_o = X_1$, then

$$X_o = \frac{P_o}{G^2} \cdot \frac{1}{\left\{\left[\frac{K}{G^2} - \left[\frac{m}{G^2} + m_s\left(1 - \frac{\ell}{\ell^2 + (\frac{c}{m_s\omega})^2}\right)\right]\omega^2\right\} + j\left[\omega\ \frac{m_s\omega(\frac{c}{m_s\omega})}{\ell^2 + (\frac{c}{m_s\omega})^2}\right]} \tag{4.15}$$

This equation becomes more useful if it is made non-dimensional.

To this aim, we first let

$\mu = G^2 \frac{m_s}{m}$, $X_{st} = \frac{P_o}{K}$. and note that, as defined previously

$h = \frac{\omega}{\omega_n}$, $c = 2m_s\omega_n$, and $\omega_n^2 = \frac{K}{m + m_s G^2}$.

Second, we divide equation (4.15) by X_{st} on the left side and by $\frac{Po}{K}$

on the right side giving

$$\frac{X_o}{X_{st}} = \frac{1}{\left[1 - h^2 + \frac{\frac{\mu \ell}{(1+\mu)} h^2}{\ell^2 + (2\frac{c}{c_c}\frac{1}{h})^2}\right] + j\left[\frac{\frac{\mu}{(1+\mu)} h^2 (2\frac{c}{c_c}\frac{1}{h})}{\ell^2 + (2\frac{c}{c_c}\frac{1}{h})^2}\right]}$$

This is a complex function that has the form $\frac{1}{A + jB}$. From the rules of complex algebra, its modulus is $\frac{1}{\sqrt{A^2+B^2}}$ and its argument is $\mathrm{Tan}^{-1}(\frac{-B}{A})$.

Physically, the amplitude ratio is the modulus and the phase lag of X_o behind X_{st}, i.e. X_o behind P_o because P_o is in phase with X_{st}, is given by the argument. Thus,the amplitude ratio

$$\left|\frac{X_o}{X_{st}}\right| = \sqrt{\frac{1}{\left[1 - h^2 + \frac{\frac{\mu \ell}{(1+\mu)} h^2}{\ell^2 + (2\frac{c}{c_c}\frac{1}{h})^2}\right]^2 + j\left[\frac{\frac{\mu}{(1+\mu)} h^2 (2\frac{c}{c_c}\frac{1}{h})}{\ell^2 + (2\frac{c}{c_c}\frac{1}{h})^2}\right]^2}}$$

which can be simplified to

$$\left|\frac{X_o}{X_{st}}\right| = \sqrt{\frac{h^4 + (\frac{2}{\ell}\frac{c}{c_c})^2 h^2}{\left[h^4 \frac{\mu}{\ell(1+\mu)} + h^2(1-h^2)\right]^2 + \left[(\frac{2}{\ell}\frac{c}{c_c})^2 h^2\right](1-h^2)^2}} \qquad (4.16)$$

And the phase lag θ of amplitude X_o behind the impressed force P_o,

$$\tan\theta = - \frac{\frac{\mu}{\ell(1+\mu)} h^2 (\frac{2}{\ell}\frac{c}{c_c}\frac{1}{h})}{(1-h^2)\left[1 + (\frac{2}{\ell}\frac{c}{c_c}\frac{1}{h})^2\right] + \frac{\mu}{\ell(1+\mu)} h^2} \qquad (4.17)$$

The negative sign in the last equation indicates the phase lag.

Equation (4.16) tallies with the amplitude ratio expression as given in equation (A.7) of Ng and New [1].

When the phase lag θ is $\frac{\Pi}{2}$, the phasor diagram that represents equation (4.9) becomes as shown in Fig. 4.4, from which is concluded that:

the impressed force = the damping force,

and the inertia force = the spring force.

All forces are understood to be equivalent forces.

Symbolically,

$$\frac{P_o}{G} = \left[\frac{m_s\omega\left(\frac{c}{m_s\omega}\right)}{\ell^2+\left(\frac{c}{m_s\omega}\right)^2}\right]\omega X_1$$

and

$$\left\{\frac{m}{G^2}+m_s\left[1-\frac{\ell}{\ell^2+\left(\frac{c}{m_s\omega}\right)^2}\right]\right\}\omega^2 X_1 = \frac{K}{G^2}X_1$$

where ω is understood to be the angular frequency at the phase lag $\theta=\frac{\Pi}{2}$.

Non-dimensional forms of these equations are respectively,

$$\frac{X_o}{X_{st}} = \frac{\ell^2+\left(2\frac{c}{c_c}\frac{1}{h}\right)^2}{\frac{\mu h^2}{(1+\mu)}\left(2\frac{c}{c_c}\frac{1}{h}\right)} \qquad (4.18)$$

and

$$h^2\left[1-\frac{\mu}{(1+u)}\frac{\ell}{\ell^2+\left(2\frac{c}{c_c}\frac{1}{h}\right)^2}\right] = 1 \qquad (4.19)$$

where h is understood to be the frequency ratio $\frac{\omega}{\omega_n}$ at the phase lag $\theta=\frac{\Pi}{2}$.

In any dynamic experiments designed to measure the amplitude and phase responses of the system, the quantities X_o, X_{st}, μ and h at $\theta=\frac{\Pi}{2}$ are either measured directly or readily determined from simple calculations.

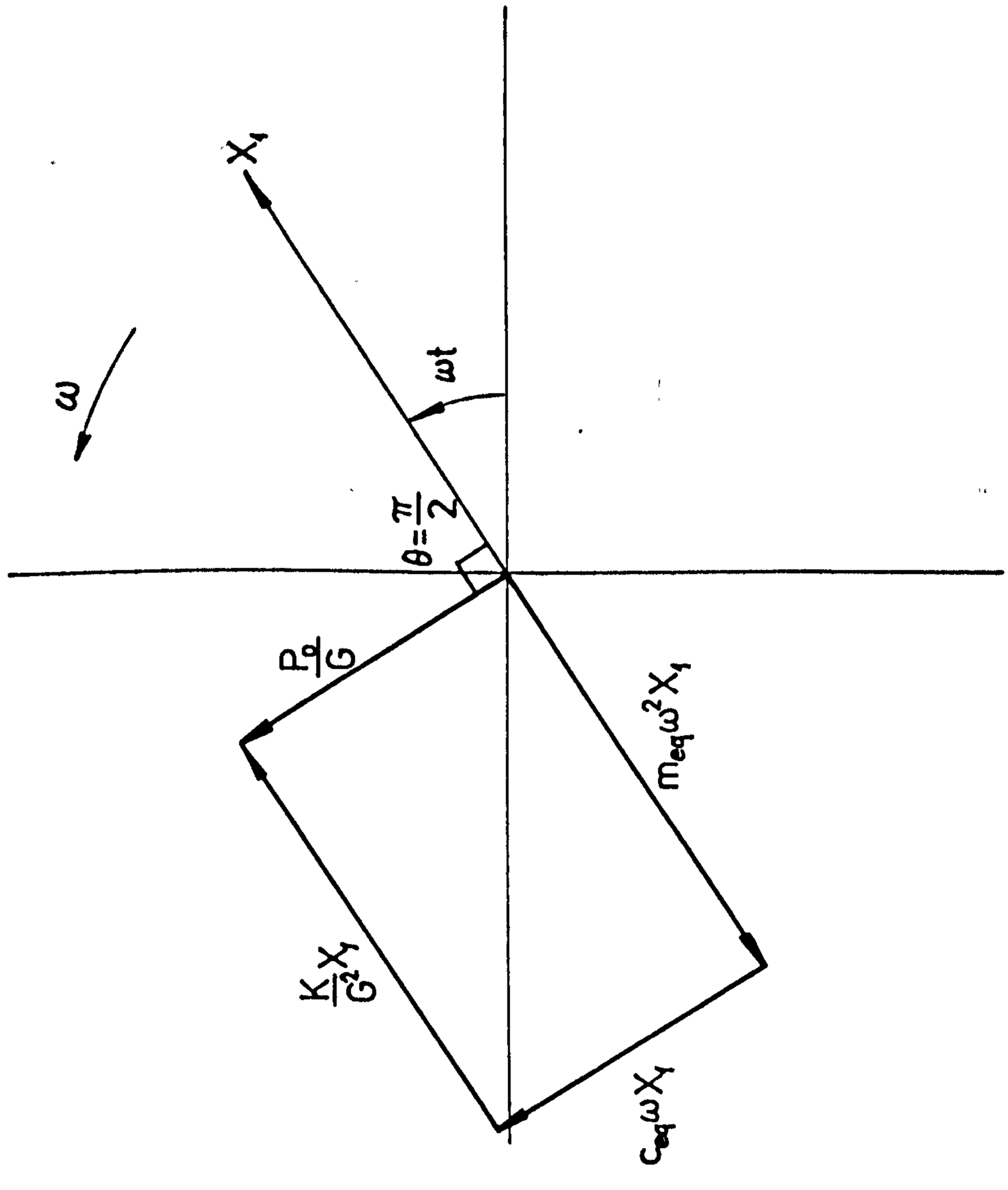

Fig 4.4 The phasor diagram of the forces involved in the analogue of Fig 4.1 when the amplitude lags behind the impressed force by one right angle.

Two unknowns of considerable computational complexities are the mass correction factor ℓ and the damping ratio $\frac{c}{c_c}$. To facilitate algebraic manipulation, instead of $\frac{c}{c_c}$ the quantity $(2\frac{c}{c_c}\frac{1}{h})$ is handled as an unknown unit.

Solving equation (4.19) for $(2\frac{c}{c_c}\frac{1}{h})^2$, we obtain

$$(2\frac{c}{c_c}\frac{1}{h})^2 = \frac{\ell\mu h^2}{(1+\mu)(h^2-1)} - \ell^2 \qquad (4.20)$$

Substituting into equation (4.18) and rearranging gives

$$\ell = \frac{(\frac{X_o}{X_{st}})^2 (h^2-1)\mu h^2}{(1+\mu)\left[1+(h^2-1)^2(\frac{X_o}{X_{st}})^2\right]} \qquad (4.21)$$

which is the expression of the mass correction factor, the amplitude ratio $(\frac{X_o}{X_{st}})$ being that measured at $\theta = \frac{\Pi}{2}$. The damping ratio $\frac{c}{c_c}$ can be obtained from a modified equation (4.20), which is

$$\frac{c}{c_c} = \frac{h}{2}\left[\frac{\ell\mu h^2}{(1+\mu)(h^2-1)} - \ell^2\right]^{1/2} \qquad (4.22)$$

It is noted that h in equations (4.20), (4.21) and (4.22) is the frequency ratio corresponding to $\theta = \frac{\Pi}{2}$.

4.4 OPTIMIZING DAMPING FOR CONSTANT-FORCE EXCITATION

In equation (4.16) which is repeated here

$$\left|\frac{X_o}{X_{st}}\right| = \sqrt{\frac{h^4 + (\frac{2}{\ell}\frac{c}{c_c})^2 h^2}{\left[h^4\frac{\mu}{\ell(1+\mu)} + h^2(1-h^2)\right]^2 + \left[(\frac{2}{\ell}\frac{c}{c_c})^2 h^2\right](1-h^2)^2}} \qquad (4.16)$$

the amplitude ratio $\frac{X_o}{X_{st}}$ is noted to be a function, among other parameters, of the frequency ratio h.

The amplitude ratio will be seen to vary with the frequency ratio h and the former will rise to a peak which is known as the amplitude ratio at resonance. The corresponding frequency ratio is called the resonant frequency ratio. The height of this amplitude ratio at resonance is dependent upon the damping ratio $\frac{c}{c_c}$ and a minimum amplitude ratio at resonance is, at least in theory, attainable if the damping ratio is suitably adjusted - a process known as "tuning". The following paragraphs are devoted to a discussion of the mathematical basis of this process.

4.4.1 Amplitude ratio and frequency ratio at resonance

To simplify algebraic manipulations, the following notations are introduced

$$S = \left| \frac{X_o}{X_{st}} \right|^2$$

$$R = h^2$$

$$Q = \left[\frac{2}{\ell} \frac{c}{c_c} \right]^2$$

and $$Z = \frac{\mu}{\ell(1+\mu)}$$

Equation (4.16) is then transformed to

$$S = \frac{R + Q}{R\,[\,RZ + (1-R)]^2 + Q\,(1-R)^2} \qquad (4.23)$$

The amplitude ratio squared at resonance is obtained by differentiating equation (4.23) with respect to R and equating the result to zero. Thus, after some simplification, equation (4.23) gives

$$R^3 + R^2\left[\frac{2(Z-1)+Q}{2(Z-1)^2} + \frac{3}{2}Q \right] + R\left[\frac{Q[2(Z-1)+Q]}{(Z-1)^2} \right] - \frac{Q^2}{(Z-1)^2} = 0 \qquad (4.24)$$

Consider the two cases when damping assumes zero and infinity respectively.

Case 1: With no damping present the difference between the behaviour of the system in the present case with that of the simple absorber is immediately evident.

Putting c = 0 and hence Q = 0, equation (4.24) degenerates to

$$R^2 \left[R + \frac{1}{Z-1}\right] = 0$$

from which the three roots are $R_{a,b} = 0$

and $R_c = \frac{1}{(1 - Z)}$

The only root of physical significance is R_c giving the frequency ratio squared at resonance and henceforth denoted by T for this particular case. It is related to only two of the system parameters μ and ℓ so that $T = \frac{1}{1 - Z}$

or
$$T = \frac{1}{1 - \frac{\mu}{(1 + \mu)\ell}}^{*} \qquad (4.25)$$

---

* Footnote:

The relationship of equation (4.25), with the corresponding case for the simple Lanchester damper in which rolling of the slug and the kinetic energy of the damping fluid is ignored, can be seen by putting

$\left(\frac{\lambda}{R_2}\right)^2 = \left(\frac{m_f}{m_s}\right)\beta_c = 0$ so that the mass correction factor ℓ becomes unity. This simplified version of equation (4.25) becomes

$\left(\frac{\omega_c}{\omega_n}\right)^2 = 1 + \mu$ and on substituting for ω_n and μ

$$\omega_c^2 = \frac{k}{m + m_s G^2} \cdot \left[1 + G^2 \frac{m_s}{m}\right] \quad \text{or} \quad \omega_c^2 = \frac{k}{m}$$

which is the standard solution for the simple Lanchester damper when the viscous damping coefficient is zero so that no connection exists between the main mass and the damper mass.

For no damping in the system the frequency ratio at resonance is given by

$$\left(\frac{f}{f_n}\right)_{res;\ \frac{c}{c_c}=0} = \left[\frac{1}{1-\frac{\mu}{(1+\mu)\ell}}\right]^{\frac{1}{2}} \qquad (4.26)$$

Case 2: When there is an infinite amount of damping in the system corresponding to the case of the "tight-fit" slug, i.e. $c \to \infty$ and hence $Q \to \infty$, equation (4.24) becomes

$$\frac{R}{(Z-1)^2} - \frac{1}{(Z-1)^2} = 0$$

or simply $R = 1$

That is, for infinite damping the frequency ratio at resonance is given by

$$\left(\frac{f}{f_n}\right)_{res;\ \frac{c}{c_c}\to\infty} = 1^{\dagger} \qquad (4.27)$$

---

† Footnote: This particular case is identical with the case of the simple Lanchester damper, because to obtain infinite damping the clearance around the slug is zero so that the slug cannot roll and there is no fluid mass to consider. The resonant frequency is given by

$$f_n = \frac{1}{2\pi}\left[\frac{k}{m(1+\mu)}\right]^{\frac{1}{2}}$$

which is the natural frequency for the slug being the integral part of the bar.

To obtain the resonant frequencies at intermediate levels of damping, we need to solve equation (4.24) for R. First, substitute T for the quantity $\frac{1}{1-Z}$, and equation (4.24) becomes

$$R^3 + R^2\left[\frac{T^2Q}{2} - T + \frac{3}{2}Q\right] + R\left[T^2Q^2 - 2TQ\right] - T^2Q^2 = 0 \qquad (4.28)$$

Second, since this is a cubic equation in R, we resort to the Cardan's method [2] whereby a new variable y defined as

$$y = R + \frac{1}{3}\left[\frac{T^2Q}{2} - T + \frac{3}{2}Q\right]$$

is introduced and equation (4.28) is transformed to

$$y^3 + 3py + 2g = 0$$

where p and q are defined as

$$p = \frac{1}{3}\left[(T^2Q^2 - 2TQ) - \frac{1}{3}\left(\frac{T^2Q}{2} - T + \frac{3}{2}Q\right)^2\right]$$

$$\text{and } q = \frac{1}{2}\left[\frac{2}{27}\left(\frac{T^2Q}{2} - T + \frac{3}{2}Q\right)^3 - \frac{1}{3}\left(\frac{T^2Q}{2} - T + \frac{3Q}{2}\right)(T^2Q^2 - 2TQ) - T^2Q^2\right]$$

Third, according to Cardan's method, [2] the solution for y is given by,

$$y = \sqrt[3]{-q + \sqrt{q^2 + p^3}} + \sqrt[3]{-q - \sqrt{q^2 + p^3}}$$

and it follows from the definition of the variable y that the frequency ratio at resonance is

$$R^{\frac{1}{2}}_{res} = \left(\frac{f}{f_n}\right)_{res} = \sqrt{y - \frac{1}{3}\left(\frac{T^2Q}{2} - T + \frac{3}{2}Q\right)} \qquad (4.29)$$

Since the resonant frequency is readily measurable from experiment and the damping coefficient c and hence Q are generally not known, it is more appropriate to express Q in terms of other parameters.

Rearranging equation (4.24) in descending order of Q gives a quadratic equation in Q, the solution to which is

$$Q_1 = \frac{-R\left[\frac{T^2R}{2} + \frac{3}{2}R - 2T\right] + \left[R^2\left(\frac{T^2R}{2} + \frac{3}{2}R - 2T\right)^2 + 4T^2R^2(R-1)(T-R)\right]^{1/2}}{2T^2(R-1)} \qquad (4.30)$$

where only the positive sign before the discriminant is chosen because in finding the real solution Q_1 must be positive, and from the previous discussion $1 \leqslant R \leqslant T$. The damping ratio for this particular value of Q_1 is readily available from

$$\frac{c}{c_c} = \frac{\ell}{2} Q_1^{\frac{1}{2}} \qquad (4.31)$$

4.4.2 Optimum damping and optimum frequency ratio

The more realistic method of determining the optimum frequency ratio already referred to is to note in equation (4.23) that there are two independent variables, namely R and Q, which will affect S. Graphically the variables S, R and Q represent a curved surface and the minimum S coinc with the saddle point at which the values of R and Q are regarded as optimum. It is necessary to differentiate S with respect to R and Q, in turn, so arriving at a pair of simultaneous equations from which the optimum point can be determined as follows:

$$\text{Set } \frac{\delta S}{\delta R} = 0 \text{ and } \frac{\delta S}{\delta Q} = 0$$

Simplifying the two equations respectively gives

$$\left\{R[(Z-1)R + 1]^2 + Q(1-R)^2\right\} - (R+Q)\left\{2R(Z-1)[(Z-1)R + 1] + [(Z-1)R + 1]^2 - 2Q(1-R)\right\} = 0 \qquad (4.32)$$

and

$$\left\{R[(Z-1)R + 1]^2 + Q(1-R)^2\right\} - (R+Q)(1-R)^2 = 0 \qquad (4.33)$$

Subtracting equations (4.33) from (4.32) and noting that $(R + Q) \neq 0$ gives

$$Q_{opt} = \frac{2R[(Z-1)R+1](Z-1)+[(Z-1)R+1]^2-(1-R)^2}{2(1-R)} \qquad (4.34)$$

Equation (4.33) is readily simplified, giving two roots in R, namely,

$$R_{opt} = 0$$

which is trivial, and

$$R_{opt} = \frac{2}{2-Z} \qquad (4.35)$$

which is the required root.

Substituting equations (4.35) into (4.34) and simplifying eventually gives,

$$Q_{opt} = \frac{2(1-Z)}{2-Z} \qquad (4.36)$$

Substituting R_{opt} and Q_{opt} for R and Q in equation (4.23) gives the minimum amplitude ratio squared at resonance. Thus

$$S_{opt} = \frac{(2-Z)^2}{Z^2} \qquad (4.37)$$

From equations (4.35) to (4.37), the conditions for most effective use of this particular version of a Lanchester damper applied to a single mass, single degree vibrating system for a given μ ratio can be summarized as follows:-

Optimum frequency ratio, $\left(\frac{f}{fn}\right)_{opt} = \left[\frac{2(1+\mu)\,\ell}{2(1+\mu)\,\ell-\mu}\right]^{\frac{1}{2}}$ (4.38)

Optimum damping ratio, $\left(\frac{c}{c_c}\right)_{opt} = \frac{\ell}{\sqrt{2}}\left[\frac{(1+\mu)\ell-\mu}{2(1+\mu)\ell-\mu}\right]^{\frac{1}{2}}$ (4.39)

Minimum possible amplitude ratio for these optimum conditions

$$\left|\frac{X_o}{X_{st}}\right|_{opt} = \frac{2(1+\mu)\ell}{\mu} - 1 \qquad (4.40)$$

Note:- Equations (4.38) to (4.40) reduce to those for the basic Lanchester damper when rolling and fluid effects are ignored, which can be readily seen by putting the mass correction factor ℓ equal to unity and carrying out minor transforations. Thus, for $\ell = 1$

$$\left(\frac{f}{f_n}\right)_{opt} = \sqrt{2}\left[\frac{1 + \mu}{2 + \mu}\right]^{\frac{1}{2}} \qquad (4.38a)$$

$$\left(\frac{c}{c_c}\right)_{opt} = \frac{1}{\sqrt{2}}\left[\frac{1}{2 + \mu}\right]^{\frac{1}{2}} \qquad (4.39a)$$

$$\text{and } \left|\frac{X_o}{X_{st}}\right|_{opt} = 1 + \frac{2}{\mu} \qquad (4.40a)$$

Equation (4.40a) is identical with that quoted by Den Hartog [3], but to demonstrate that equations (4.38a) and (4.39a) are also identical it must be remembered that in the present analysis

$$\omega_n^2 = \frac{k}{m}\left[\frac{1}{1 + \mu}\right]$$

$$\text{and } c_c^2 = (2m_s)^2 \frac{k}{m}\left|\frac{1}{1 + \mu}\right|$$

In reference (3)

$$L\Omega_n^2 = \frac{k}{m}, \text{ and } Lc_c^2 = (2m)^2 \, L\Omega_n^2$$

so that

$$\omega_n^2 = L\Omega_n^2\left[\frac{1}{1 + \mu}\right]$$

and

$$c_c^2 = Lc_c^2\left[\frac{1}{1 + \mu}\right]$$

Substituting for f_n and c_c in equations (4.38a) and (4.39a) gives

$$L\left(\frac{f}{f_n}\right)_{opt} = \left|\frac{2}{2 + \mu}\right|^{\frac{1}{2}}$$

$$\text{and } L\left(\frac{c}{c_c}\right)_{opt} = \frac{1}{\sqrt{2}}\left[\frac{1}{(1 + \mu)(2 + \mu)}\right]^{\frac{1}{2}}$$

which again are identical with the equations given by Den Hartog.

4.5 OPTIMIZING BUNG LENGTH FOR MINIMUM AMPLITUDE AT RESONANCE FOR CONSTANT-FORCE EXCITATION

Rewrite equation (4.40) such that X_{st} is replaced by $\frac{P_o}{K}$, then

$$|X_o| = \frac{P_o}{K}\left[\frac{2(1+\mu)\ell}{\mu} - 1\right] \qquad (4.41)$$

This is the expression for the minimum amplitude at resonance. Apart from the impressed force P_o which is generally maintained constant in the experiment, the parameters K, ℓ and μ can be manipulated in the design stages so that X_o will be minimized still further.

One of the feasible designs which permit this relative freedom to vary parameters K, ℓ and μ is illustrated in Fig. 4.5. This design incorporates a Lanchester type damper behind the toolpost and a constant diameter forced-fit bung situated at the fixed end. The philosophy behind this particular configuration is to permit variations in the parameters K, ℓ and μ by appropriate selections in (a) the bung length h_b; (b) the bung material; (c) the slug absorber material, and (d) the clearance between the slug and its surrounding cavity. Details of the boring bar design will be taken up in Section 7.2.

The bung length variation causes variations in the stiffness K and the mass ratio μ and so the derivatives of $\frac{dK}{dh_b}$ and $\frac{d\mu}{dh_b}$ exist. Differentiating X_o with respect to h_b in equation (4.41) gives

$$\frac{d|X_o|}{dh_b} = \left(\frac{2\ell}{\mu} + 2\ell - 1\right)\left(-\frac{P_o}{K^2}\right)\frac{dK}{dh_b} + \frac{P_o}{K}\left(\frac{-2\ell}{\mu^2}\frac{d\mu}{dh_b}\right)$$

Since the aim is to minimize $|X_o|$, $\frac{d|X_o|}{dh_b} = 0$ That is,

$$\left(\frac{2\ell}{\mu} + 2\ell - 1\right)\left(-\frac{P_o}{K^2}\right)\frac{dK}{dh_b} + \frac{P_o}{K}\left(\frac{-2\ell}{\mu^2}\right)\frac{d\mu}{dh_b} = 0$$

which can be simplified to

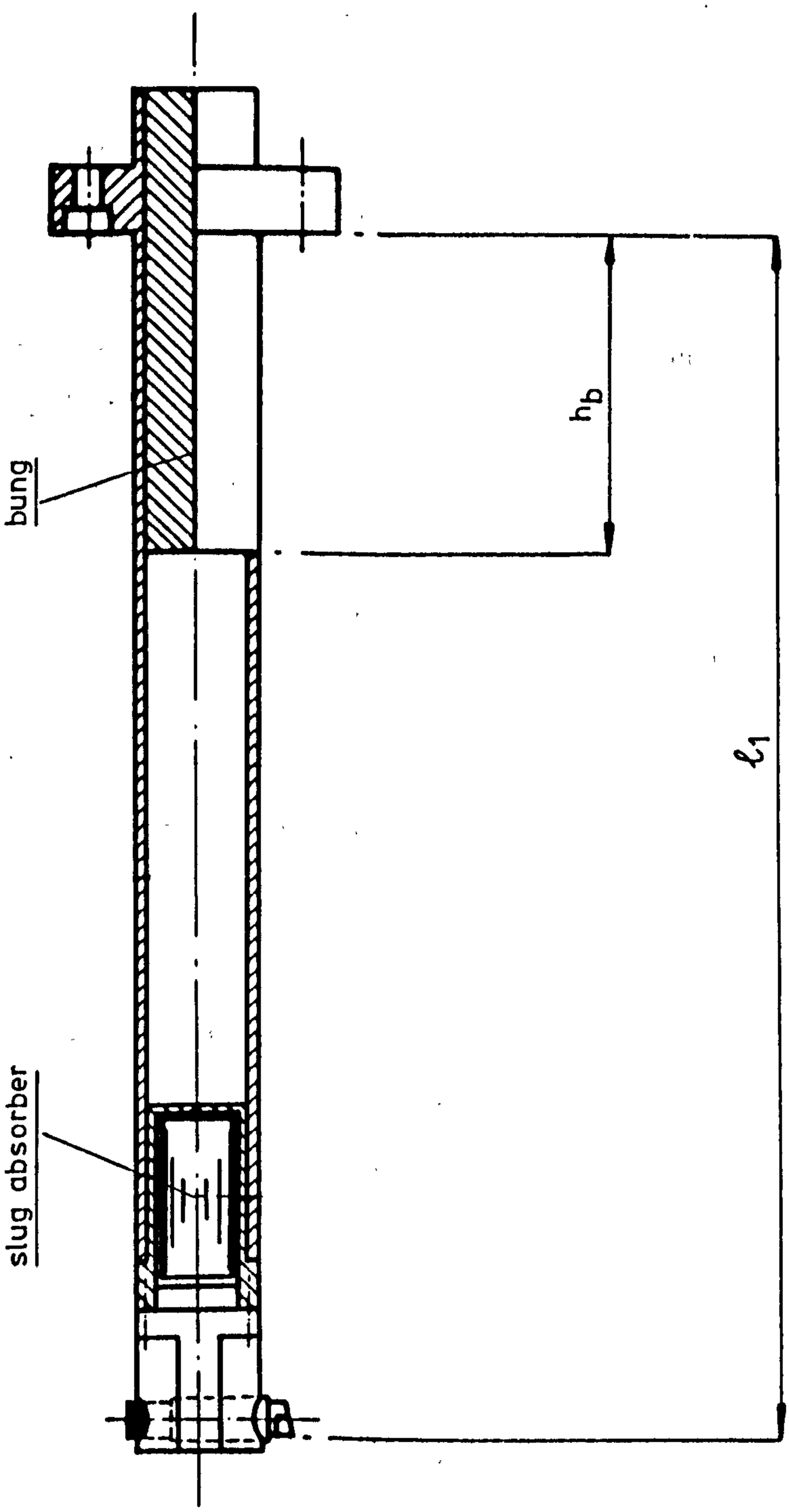

A design of single-slug-damped boring bar forced-fit with a bung. the length of which can be varied to achieve optimum dynamical performance

Fig 4.5

$$\left(\frac{2\ell}{\mu} + 2\ell - 1\right)\frac{dK}{dh_b} + \frac{2\ell K}{\mu^2}\frac{d\mu}{dh_b} = 0 \qquad (4.42)$$

To obtain a solution for the bung length h_b from equation (4.42) requires a knowledge of both the stiffness K and the mass ratio μ as functions of h_b. We shall first be concerned with the determining of K in Section 4.5.1. while the study of μ will be taken up in Section 4.5.2.

4.5.1 Strain energy and equivalent stiffness

From the textbook on strength of materials, the strain energy V stored in a deflected composite beam is given by

$$V = \sum_{i=1}^{n} \frac{E_i I_i}{2} \int \left(\frac{d^2y}{dx^2}\right)^2 dx \qquad (4.43)$$

where the summation is carried out over the total overhung length and n is the total number of sections having different flexural rigidities, $E_i I_i$.

In a linear spring with stiffness K, the strain energy stored within itself caused by a displacement y_o is $\frac{1}{2} K y_o^2$, which is equal to V as in equation (4.43) when K becomes the equivalent stiffness of the bar and y_o the transverse deflection under the point of application of the load at the free end, thus $K = \frac{2V}{y_o^2}$

or $$K = \frac{1}{y_o^2} \sum_{i=1}^{n} E_i I_i \int \left(\frac{d^2y}{dx^2}\right)^2 dx \qquad (4.44)$$

In this expression, the equivalent stiffness K can be determined only if the deflection shape function of the bar is known. For a composite bar possessing different flexural rigidities along its length, it is

virtually impossible to be sure of the exact deflection shape function under forced vibration. Nevertheless, according to Rayleigh,[4] even if the function is approximate, as long as the end conditions are satisfied, the errors that may occur in the calculated natural frequency and hence the stiffness K tend to be quite small. For this reason, a quarter cosine wave

$$y(x) = y_o \left(1 - \cos \frac{\Pi x}{2\ell_1}\right) \qquad (4.45)$$

is chosen as one possible model. In this equation, y(x) and y_o denote the transverse deflection of the bar at the distance x from the fixed end and at the free end respectively; ℓ_1 is the overhung length. With y(x) as given in equation (4.45), its second derivative is given by

$$\frac{d^2y}{dx^2} = y_o \left(\frac{\Pi}{2\ell_1}\right)^2 \cos \frac{\Pi x}{2\ell_1}$$

and the equivalent stiffness K, as given in equation (4.44), becomes

$$K = \left(\frac{\Pi}{2\ell_1}\right)^4 \sum_{i=1}^{n} E_i I_i \int \cos^2 \frac{\Pi x}{2\ell_1}\, dx \qquad (4.46)$$

From the last equation, since K is dependent on the flexural rigidities $E_i I_i$ in different sections of the bar, it follows that K is a function of the bung length h_b as h_b affects the distribution of the flexural rigidities.

4.5.2. Kinetic energy and equivalent mass

The kinetic energy stored in a composite bar due to an inertia loading is

$$T = \sum_{i=1}^{n} \frac{\overline{\rho_i}}{2} \int \dot{y}^2 dx$$

Where $\overline{\rho_i}$ is the mass per unit length in the ith section of the bar and $\dot{y}$ is the time derivative, i.e. velocity of the deflection shape function. For a quarter cosine wave given in equation (4.45) its time derivative is

$$\dot{y}(x) = \dot{y}_o \left(1 - \cos \frac{\Pi x}{2\ell}\right)$$

and the kinetic energy involved is

$$T = \sum_{i=1}^{n} \frac{\overline{\rho_i}}{2} \dot{y}_o^2 \int \left(1 - \cos \frac{\pi x}{2\ell_1}\right)^2 dx \qquad (4.47)$$

A point mass m moving with a velocity y_o possesses kinetic energy $\frac{1}{2} m\dot{y}_o^2$. This is equal to T in equation (4.47) when m becomes the equivalent mass of the bar considered at the point of motion $\dot{y}_o$ and $\dot{y}_o$ becomes the velocity of the bar at the free end. Thus,

$$\frac{1}{2} m\dot{y}_o^2 = T$$

from which $m = \frac{2T}{\dot{y}_o^2}$

But the kinetic energy T is also given in equation (4.47), then the last equation becomes

$$m = \sum_{i=1}^{n} \overline{\rho_i} \int \left(1 - \cos \frac{\Pi x}{2\ell_1}\right)^2 dx \qquad (4.48)$$

From the definition of the mass ratio, $\mu = G^2 \frac{m_s}{m}$ and equation (4.48) the mass ratio μ is observed to be some function of the equivalent mass of the bar, m, which, in turn, is dependent on the mass per unit length $\overline{\rho}_i$. It follows that μ is a function of the bung length h_b as the latter affects the value of $\overline{\rho}_i$.

4.5.3 Iteration method

With reference to equation (4.42) which is the equation from which the optimum bung length h_b is determined, since it contains K, μ and their derivatives $\frac{dK}{dh_b}$, $\frac{d\mu}{dh_b}$, all of which involve some trigonometric functions such as sine and cosine, an exact algebraic solution cannot be obtained.

An alternative is to make use of a numerical computational procedure known as the Newton's iteration method explained as follows.

First, let $f(h_b) = \left(\frac{2\ell}{\mu} + 2\ell - 1\right)\frac{dK}{dh_b} + \frac{2\ell K}{\mu^2}\frac{d\mu}{dh_b}$ (4.49)

from which is obtained its first derivative with respect to h_b, i.e.

$$f'(h_b) = \frac{d^2K}{dh_b^2}\left[\frac{2\ell}{\mu} + (2\ell-1)\right] + \frac{2\ell K}{\mu^2}\left[\frac{d^2\mu}{dh_b^2} - \frac{2}{\mu}\left(\frac{d\mu}{dh_b}\right)^2\right] \quad (4.50)$$

Second, apply the Newton's iterative formula,

$$h_{b(r+1)} = h_{b(r)} - \frac{f_r(h_b)}{f_r'(h_b)} \quad (4.51)$$

where the suffix r indicates the number of iterations; so r starts from unity and increases successively. To start the iteration, an initial value for $h_{b(1)}$ is arbitrarily chosen and the values for $f_1(h_b)$ and $f_1'(h_b)$ are computed from the respective equations (4.49) and (4.50). Using equation (4.51) a new value for the bung length, i.e. $h_{b(2)}$ is calculated, which is the next value to be used for starting the second iterative loop. The successively calculated values for h_b will converge to a steady value and the process is terminated when the required accuracy is reached.

The method as described in Section 4.5 will be used to calculate the bung length h_b in the design of the tungsten-bunged bar, which will be described in Appendix C.

REFERENCES FOR CHAPTER 4

1. NG K.W. and NEW R.W., "Overhung Boring Bars - Part I, Dynamic Behaviour of New Designs of Damped Boring Bars under Forced Vibratory Conditions", Brunel University, Department of Production Technology, SRC Research Report BB1, October 1977

2. BRONSHTEIN I.N. and SEMENDYAYEN K.A., "A Guide Book to Mathematics", Verlag Harri Deutsch 1973, pp 161-162

3. DEN HARTOG J.P., "Mechanical Vibrations", 4th edition 1956, McGraw-Hill, pp 102-104

4. DEN HARTOG J.P., "Mechanical Vibrations", 4th edition 1956, McGraw-Hill, pp 141-147

5. THEORIES OF BORING BAR - STABILITY

5.1 NOMENCLATURE

m_1 = equivalent mass for tangential accelerations of boring bar at free end.

m_2 = equivalent mass for radial accelerations of boring bar at free end

c_1 = equivalent damping for tangential * velocities of boring bar at free end

c_2 = equivalent damping for radial * velocities of boring bar at free end

k_1 = equivalent stiffness for tangential displacements of boring bar at free end

k_2 = equivalent stiffness for radial displacements of boring bar at free end

c_{12} = equivalent tangential damping for a radial velocity

c_{21} = equivalent radial damping for a tangential velocity

k_{12} = equivalent tangential stiffness for a radial displacement

k_{21} = equivalent radial stiffness for a tangential displacement

K_t = spring constant for boring bar in tangential direction

K = spring constant for boring bar in radial direction

$\varepsilon_1 = c_1/m_1$

$\varepsilon_2 = c_2/m_2$

$\eta_1 = c_{12}/m_1$

$\eta_2 = c_{21}/m_2$

$\omega_1^2 = k_1/m_1$

$\omega_2^2 = k_2/m_2$

$\kappa_1 = k_{12}/k_1$

$\kappa_2 = k_{21}/k_2$

a = slope of the radial cutting force - depth of cut curve at the equilibrium position

b = slope of the tangential cutting force - depth of cut curve at the equilibrium position

y_1 = displacement in tangential direction

y_2 = displacement in radial direction

m = equivalent mass of boring bar considered at free end

m_s = mass of slug

m_f = mass of damping fluid

$\beta_{c,f}$ = a correction factor, the square root of which converts the relative velocity between the bar and slug to the "average" velocity of the damping fluid

λ = radius of gyration of slug about longitudinal axis, i.e. $R_2/\sqrt{2}$

R_2 = radius of slug

x_0 = vibration of bar at tool tip

x_1 = vibration of bar at position of centre of slug

x_2 = vibration of slug at centre position

G = ratio of amplitudes, i.e. $|x_1/x_0|$

c = coefficient of viscous damping for translational motion

f_1 = negative viscous damping coefficient

P_0 = applied force at free end of bar

s = variable in the s-domain after the Laplace transformation

μ = $G^2 m_s/m$, mass ratio

ω_n = $[K/(m+G^2 m_s)]^{\frac{1}{2}}$ angular natural frequency for bar when slug is an integral part of bar

f_n = $\omega_n/(2\pi)$, natural frequency for bar when slug is an integral part of the bar.

H = $(f_1/G^2)/(m_s \omega_n)$, negative viscous damping ratio which is a measure of the severity of cutting process for the case of primary chatter

c_c = $2m_s\omega_n$, coefficient of "critical" viscous damping

ℓ = $1+(\lambda/R_2)^2 + (m_f\beta_c/m_s)$, a mass correction factor for absorber slug

ω = angular chatter frequency

h = $\omega/\omega_n = f/f_n$, chatter frequency ratio

f = $\omega/2\pi$, chatter frequency

h_{op} = chatter frequency ratio at maximum stability corresponding to the optimum damping condition of the slug absorber for primary chatter

$\left(\frac{c}{c_c}\right)_{op}$ = optimum damping ratio for primary chatter

H_{op} = maximum negative damping ratio for primary chatter

f_{lo} = maximum negative viscous damping coefficient for primary chatter

h_b = length of bung in boring bar

R_2' = $r_2(1-\cos \phi)$, a cutting force slope

r_2 = a constant depending on the rate at which the radial cutting force increases with the increasing depth of cut

f_2 = negative hystetetic damping coefficient

a' = $a+ R_2'$, a cutting force slope

J = $(f_2/G^2)/(m_s\omega_n)$, negative hysteretic damping ratio which is a measure of severity of cutting process for the case of regenerative chatter

h_{or} = chatter frequency ratio at maximum stability corresponding to the optimum damping condition of the slug absorber for regenerative chatter.

$\left(\frac{c}{c_c}\right)_{or}$ = optimum damping ratio for regenerative chatter

J_{or} = maximum negative damping ratio for regenerative chatter

f_{2o} = maximum negative hysteretic damping coefficient for regenerative chatter

---

* Note: tangential and radial directions refer to the direction of the tangential and radial components of the resultant cutting force respectively.

5.2 PRIMARY CHATTER THEORY OF SINGLE-SLUG-DAMPED BAR

The term "primary chatter" is taken to mean the mode-coupling chatter in which the regenerative effects are considered absent. For the type of chatter pertinent to boring bar, PERA [1] remark that regenerative chatter is not the main cause. Nevertheless, for the comparison with the primary chatter theory, that due to regenerative chatter is also considered and is presented in Section 5.3.

During boring, the tool moves mainly in the plane normal to the axis of the boring bar. Using the lumped-parameter approach, it follows that a plain solid bar can be modelled by a two-degree-of-freedom system which has coordinates y_1 and y_2 representing the movements in the respective tangential and radial directions as indicated in Fig. 5.1. For a single-slug-damped bar, due to the fact that an absorber must be free to move relative to the bar for effective operation, two more coordinates are required to define its motion and the corresponding model must be four-degree-of-freedom. Obviously, the task of studying its stability is much more involved.

There is, however, a simpler approach whereby the number of degrees of freedom of the system can be reduced. The approach is based on the theoretical deductions due to PERA [1,2]. A brief review of the theory leading to the deductions is presented as follows.

As mentioned previously, the plain solid bar is modelled by a two-degree-of-freedom system with coordinates y_1 and y_2 as in Fig. 5.1.
Ignoring the inertia coupling effects, the equations of motion are,

$$(m_1\ddot{y}_1 + c_1\dot{y}_1 + k_1y_1) + (c_{12}\dot{y}_2 + k_{12}y_2) = 0 \qquad (5.1)$$

and $$(c_{21}\dot{y}_1 + k_{21}y_1) + (m_2\ddot{y}_2 + c_2\dot{y}_2 + k_2y_2) = 0 \qquad (5.2)$$

where the symbols are as defined in the Nomenclature 5.1.

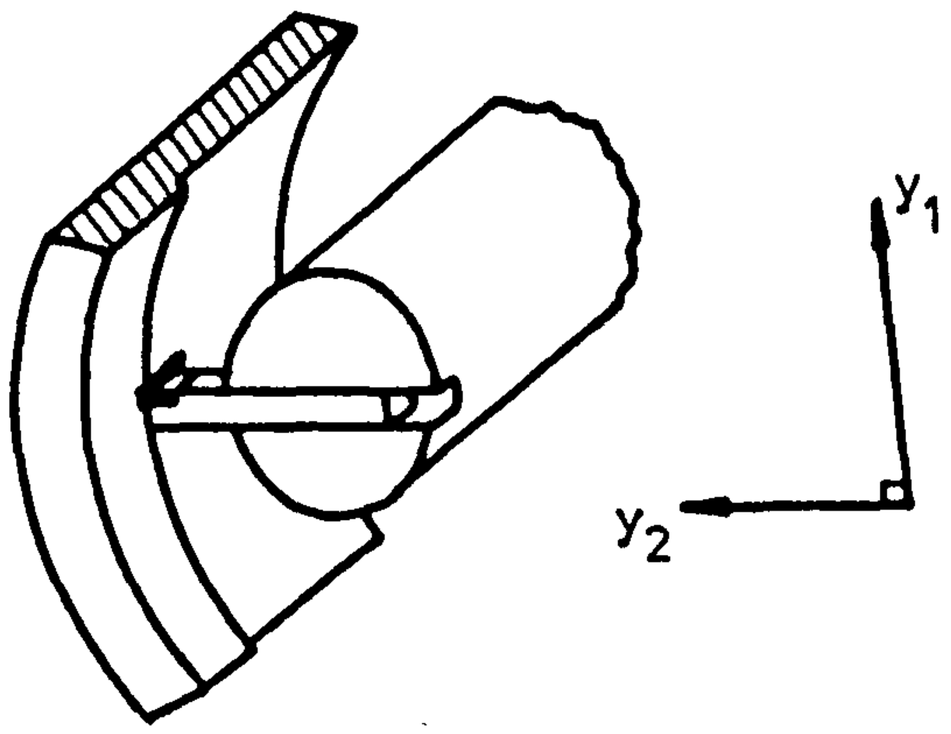

Fig 5.1 Boring bar under cut showing orientation of co-ordinate axes(1)

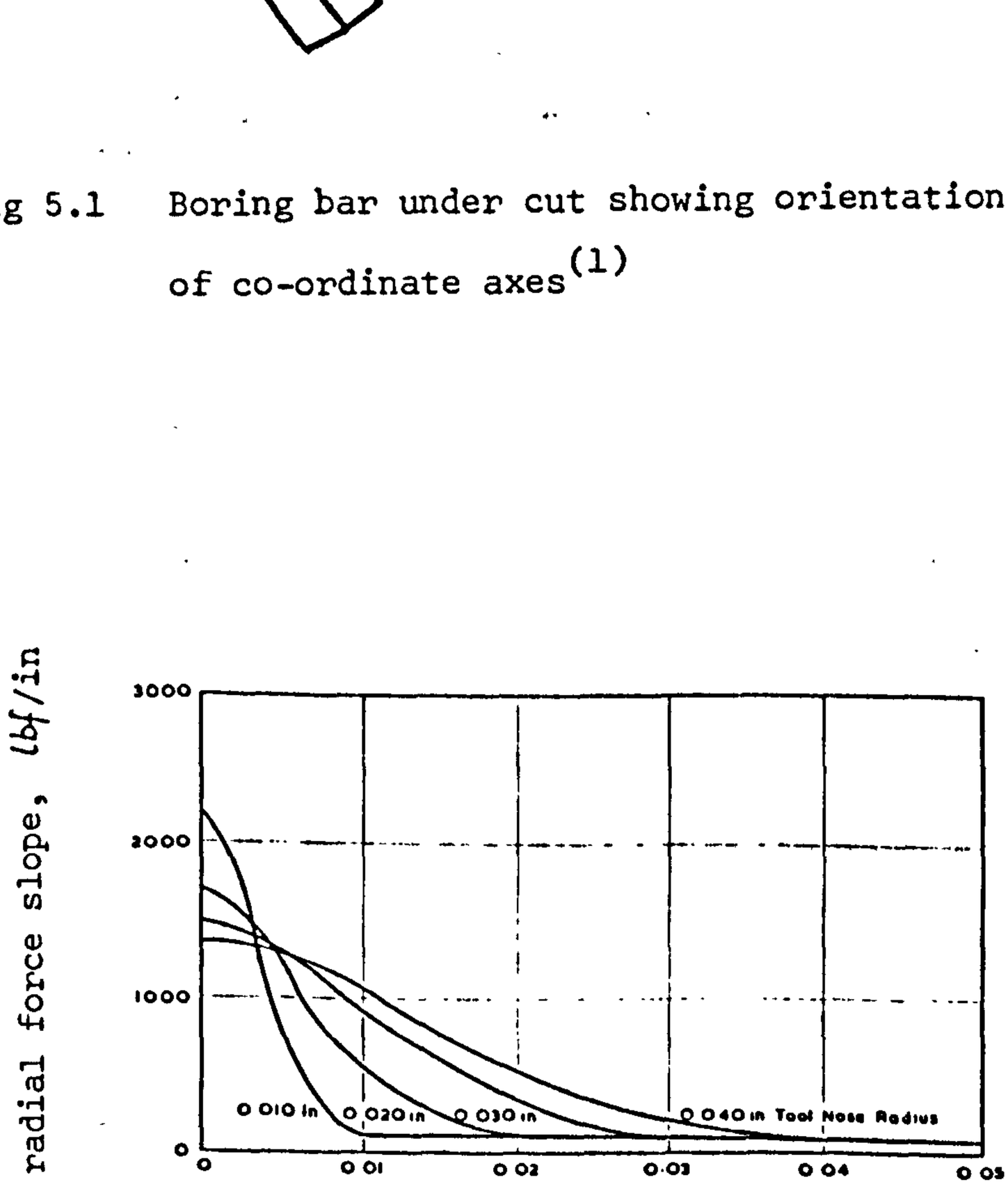

Fig 5.2 Variation of the slope of the radial cutting force curves with depth of cut(1)

The coefficient k_1 in the tangential direction y_1 is equal to the spring constant K_t of the bar along y_1; and the coefficient k_2 in the radial direction y_2 is equal to the sum of the spring constant K along y_2 and of the equivalent spring constant a due to the rate of increase of the radial cutting force with increasing depth of cut at the operating position.

As the radial cutting force is independent of the tangential displacement, $k_{21}=0$. Since an increase in the depth of cut from the equilibrium operating position will cause an increase in the radial cutting force, then according to the definition of k_{12}, it is equal to the rate of increase b of the tangential cutting force with increasing depth of cut.

Hence $k_{12} = b$. Equations (5.1) and (5.2) become

$$(m_1\ddot{y}_1 + c_1\dot{y}_1 + K_t y_1) + (c_{12}\dot{y}_2 + by_2) = 0 \qquad (5.1a)$$

and $$c_{21}\dot{y}_1 + \left[m_2\ddot{y}_2 + c_2\dot{y}_2 + (K + a)\, y_2 \right] = 0 \qquad (5.2a)$$

To study the stability of the system, PERA apply the Routh-Hurwitz criterion to equations (5.1a) and (5.2a). After some manipulation and simplification, it is found that for stability to occur, the following conditions must be satisfied:-

$$\varepsilon_1 + \varepsilon_2 > 0 \qquad (5.3)$$

and $$\omega_1^2 < \omega^2 \frac{\varepsilon_1}{\varepsilon_1 + \varepsilon_2} + \omega^2 \left(\frac{\varepsilon_2 - \kappa_1 \eta_2}{\varepsilon_1 + \varepsilon_2} \right) \qquad (5.4)$$

where the symbols are as defined in Nomenclature 5.1. It is also noted that inequality (5.4) can be written in a form similar to (5.3). That is

$$\varepsilon_1 + \varepsilon_2' > 0$$

such that $$\varepsilon_2' = -\left(\frac{\omega_1^2}{\omega_2^2 - \omega_1^2}\right) \kappa_1 \eta_2 \qquad (5.5)$$

The stability can, therefore, be specified by (5.3) and (5.5) from which PERA [1] suggest two physical interpretations:-

(1) If instability is brought into being by means of violating the condition (5.3), on account of the definitions of ε_1 and ε_2, it suggests that negative damping, either as $(-c_1)$ or $(-c_2)$, is present in the system. As a result, the tool tip must experience a negative resistance to either tangential or radial velocities. This is, however, thought to be physically implausible for it is clear that movements of the tool tip are always opposed by the work material.

(2) If instability is established by means of violating the condition (5.5), ε_2' must be sufficiently small to make the sum of $\varepsilon_1 + \varepsilon_2'$ negative. That ε_2' is always negative can be established as follows. The radial spring constant $k_2 = K + a$ and the tangential spring constant $k_1 = K_t$. For a round solid bar, $K=K_t$ and hence $k_2 > k_1$. Furthermore, since m_1 and m_2 are comparable,

$$\frac{k_2}{m_2} > \frac{k_1}{m_1}$$

or

$$\omega_2^2 > \omega_1^2$$

Also, by the definition of κ_1 and η_2, they are both positive. It follows that

$$\varepsilon_2' = -\left(\frac{\omega_1^2}{\omega_2^2 - \omega_1^2}\right)\kappa_1\eta_2 < 0$$

The value of κ_1 can be increased by reducing the stiffness K_t of the bar resulting in a more negative ε_2'. This is, therefore, in accord with the experience that long and slender boring bars are more prone to chatter.

Inequality (5.5) can be regarded as an expression of the damping condition since ε_1 is a damping factor and hence ε'_2, by the principle of dimensional homogeneity, is necessarily a damping factor. It follows that the product term $\kappa_1\eta_2$ appearing in (5.5) is a damping factor as well even though its component κ_1 is not. In the inequality (5.4), it is noted that $-\kappa_1\eta_2$ occurs in conjunction with ε_2, a positive damping factor in the radial direction. For these reasons PERA[1] conclude that boring bar instability can be simulated in many practical cases by injecting a hypothetical negative damping force which acts in the radial direction.

5.2.1 Stability model with negative viscous damping

The theory to be presented shows how the primary chatter can be suppressed by a suitably tuned absorber slug. A hypothetical negative damping force is used as the excitation force input. The differential equations of motion of the single-slug-damped bar model when excited by a complex force $\frac{P_o}{G} e^{j\omega t}$ are given by equations (4.4) and (4.5) which are repeated here

$$\frac{m}{G^2}\ddot{x}_1+(m_s\frac{\lambda^2}{R_2^2}+m_f\beta_c)\ (\ddot{x}_1-\ddot{x}_2)+c(\dot{x}_1-\dot{x}_2)+\frac{K}{G^2}x_1 = \frac{P_o}{G} e^{j\omega t} \qquad (4.4)$$

and $$m_s\ddot{x}_2 - (m_s\frac{\lambda^2}{R_2^2} + m_f\beta_c)(\ddot{x}_1-\ddot{x}_2) - c(\dot{x} - \dot{x}_2) = 0 \qquad (4.5)$$

For the case of primary chatter, the exciting force is replaced by a negative damping force acting on the main mass m and this force is in the form $f_1\dot{x}_o$ acting in line with the motion x_o at the tool tip in the radial direction. Since both equations (4.4) and (4.5) are formulated with respect to the radial direction of motion in the plane of the slug

centre, the force $f_1\dot{x}_o$ has to be converted accordingly before it can replace $\frac{P_o e^{j\omega t}}{G}$ in equation (4.4) as follows. For a given work done by the negative force $f_1\dot{x}_o$ at x_o, the same work must be done by an equivalent force, say Q_{equ}, at x_1. Thus, $Q_{equ}\, x_1 = (f_1\dot{x}_o)x_o$ and since $x_1 = Gx_o$ by equation (B1), then $Q_{equ} = (f_1/G^2)\dot{x}_1$.

The spring constant K in equation (4.4) refers to the equivalent stiffness in the radial direction during cutting and it includes both the radial stiffness K of the bar and the equivalent stiffness a due to the rate of change of the radial force with depth of cut. Replacing K by (K + a) and $(P_o/G)e^{j\omega t}$ by $(f_1/G^2)\dot{x}_1$, equation (4.4) becomes

$$\frac{m}{G^2}\ddot{x}_1 + \left(m_s\frac{\lambda^2}{R_2^2} + m_f\beta_c\right)(\ddot{x}_1 - \ddot{x}_2) + c(\dot{x}_1 - \dot{x}_2) + \frac{(K+a)}{G^2}x_1 - \frac{f_1}{G^2}\dot{x}_1 = 0 \qquad (5.6)$$

In equations (4.4), (4.5) and (5.6) it is understood that

$$\dot{x}_i = \frac{dx_i}{dt} \qquad \text{and} \qquad \ddot{x}_i = \frac{d^2x_i}{dt^2}$$

We shall use the method of Laplace transform to solve the simultaneous equations (5.6) and (4.5). Thus, assuming the system being initially quiescent, we can replace the differential operators $\frac{d}{dt}$ by s and $\frac{d^2}{dt^2}$ by s^2 in both equations which respectively become

$$\left\{\left[\frac{m}{G^2} + \left(m_s\frac{\lambda^2}{R_2^2} + m_f\beta_c\right)\right]s^2 + \left(c - \frac{f_1}{G^2}\right)s + \frac{(K+a)}{G^2}\right\}X_1 - \left[\left(m_s\frac{\lambda^2}{R_2^2} + m_f\beta_c\right)s^2 + cs\right]X_2 = 0 \qquad (5.7)$$

and

$$-\left[\left(m_s\frac{\lambda^2}{R_2^2} + m_f\beta_c\right)s^2 + cs\right]X_1 + \left[\left(m_s + m_s\frac{\lambda^2}{R_2^2} + m_f\beta_c\right)s^2 + cs\right]X_2 = 0 \qquad (5.8)$$

The transformation yields two algebraic equations (5.7) and (5.8) in another variable s rather than the time variable t. That is to say, $x_1(t)$ and $x_2(t)$ are mapped from the time domain to the respective $x_1(s)$ and $x_2(s)$ in the s-domain. Since the right side of equations (5.7) and (5.8) are zero, the system can be regarded as one which will undergo free vibration and it follows that there is only the transient response to consider. For a linear system such as the one being discussed, stability is decided by its transient response the nature of which, as has been mentioned in Section 2.2., depends on the location of the characteristic roots of the system in the s-plane. The characteristic equation, from which the characteristic roots are evaluated is obtained from solving the determinant of the coefficient matrix of equations (5.7) and (5.8). That is

$$\begin{vmatrix} \left[\frac{m}{G^2}+\left(m_s\frac{\lambda^2}{R_2^2}+m_f\beta_c\right)\right]s^2+\left(c-\frac{f_1}{G^2}\right)s+\frac{(K+a)}{G^2} & -\left[\left(m_s\frac{\lambda^2}{R_2^2}+m_f\beta_c\right)s^2+cs\right] \\ -\left[\left(m_s\frac{\lambda^2}{R_2^2}+m_f\beta_c\right)s^2+cs\right] & \left(m_s+m_s\frac{\lambda^2}{R_2^2}+m_f\beta_c\right)s^2+cs \end{vmatrix} = 0 \qquad (5.9)$$

If all the roots can be evaluated, it is a simple matter to decide the stability of the system by examining the location of the characteristic roots in the s-plane. From section 2.2 and Fig. 2.4, asymptotic stability corresponds to all roots lying to the left of the ω-axis, and since they have negative real parts, the transient response will die away with time. Equation (5.9) is an equation of the 4th degree in s and the task computing all the roots is tedious. Furthermore, since we desire to find the effects of changes in the parameter values of c, K, and a on the stability, it will be necessary to repeat the calculation many times.

In view of the difficulty, an alternative method, known as the method of D-partition [3], will be used here. The method is based on the fact that the ω-axis in Fig. 2.4 divides the s-plane into a domain of stability to its left and a domain of instability to its right. If it is assumed that $j\omega$ is a characteristic root of the equation (5.9), then this equation with s replaced by $j\omega$ gives a mathematical representation of the root locus of the ω-axis, which, for obvious reasons, is called the stability borderline. Thus, we put $s = j\omega$ into equation (5.9) and then equate the real and imaginary parts respectively to zero to yield:

$$\left[\frac{m}{G^2}m_s + \left(\frac{m}{G^2}+m_s\right)\left(m_s\frac{\lambda^2}{R_2^2}+m_f\beta_c\right)\right]\omega^4 - \left[\frac{(K+a)}{G^2}\left(m_s+m_s\frac{\lambda^2}{R_2^2}+m_f\beta_c\right) - \frac{c\,f_1}{G^2}\right]\omega^2 = 0 \tag{5.10}$$

$$\text{and} \quad -\left[c\left(\frac{m}{G^2}+m_s\right) - \frac{f_1}{G^2}\left(m_s+m_s\frac{\lambda^2}{R_2^2}+m_f\beta_c\right)\right]\omega^3 + \left[\frac{(K+a)}{G^2}c\right]\omega = 0 \tag{5.11}$$

For the case of boring bar stability, the damping coefficient c due to the absorber, and the cutting process parameters such as the cutting force slope a and the negative viscous damping coefficient f_1 are of particular interest. Compared with the damping offered by the absorber, that of the bar itself due to its material properties is insignificant. The value of c is dependent on the clearance surrounding the slug absorber as well as on the type of fluid used in the clearance. The cutting force slope is a function of the cutting conditions such as the depth of cut, the feed, and the cutting speed; of the tool geometry; amd of the work material. The negative damping coefficient f_1 is regarded as a hypothetical source of instability and in particular if the bar overhang is kept constant and hence the stiffness, f_1 is also expected to be a function of the cutting process and the work material.

We now solve equations (5.10) and (5.11) simultaneously for c and f_1/G^2 as

$$\left(\frac{f_1}{G^2}\right)^2 = \left\{\frac{(K+a)}{G^2}\left(m_s + m_s\frac{\lambda^2}{R_2^2} + m_f\beta_c\right) - \omega^2\left[\frac{m}{G^2}m_s + \left(\frac{m}{G^2}+m_s\right)\left(m_s\frac{\lambda^2}{R^2}+m_f\beta_c\right)\right]\right\}\frac{\left(\frac{m}{G^2}+m_s\right) - \frac{(K+a)}{\omega^2 G^2}}{\left(m_s + m_s\frac{\lambda^2}{R^2}+m_f\beta_c\right)} \quad (5.12)$$

and $$c^2 = \left\{\frac{(K+a)}{G^2}\left(m_s+m_s\frac{\lambda^2}{R_2^2}+m_f\beta_c\right) - \omega^2\left[\frac{m}{G^2}m_s+\left(\frac{m}{G^2}+m_s\right)\left(m_s\frac{\lambda^2}{R_2^2}+m_f\beta_c\right)\right]\right\}\frac{\left(m_s+m_s\lambda^2/R_2^2+m_f\beta_c\right)}{\left(\frac{m}{G^2}+m_s\right) - \frac{(K+a)}{\omega^2 G^2}} \quad (5.13)$$

To convert equations (5.12) and (5.13) into non-dimensional form, the following symbols are introduced:-

$$\mu = G^2\frac{m_s}{m}\ ,\ \omega_n^2 = \frac{K}{m+G^2m_s}\ ,\ H = \frac{f_1/G^2}{m_s\omega_n}\ ,\ c_c = 2m_s\omega_n\ ,\ \ell = 1+\frac{\lambda^2}{R_2^2}+\frac{m_f}{m_s}\beta_c\ ,\ \text{and}\ \ h = \frac{f}{f_n} = \frac{\omega}{\omega_n}\ .$$

Equations (5.12) and (5.13) then become

$$H^2 = \left(1+\frac{a}{K}\right)\frac{(1+\mu)^2}{\mu^2}\left\{1-\frac{h^2}{\left(1+\frac{a}{K}\right)}\left[\frac{\ell(1+\mu)-\mu}{\ell(1+\mu)}\right]\right\}\left[1-\frac{\left(1+\frac{a}{K}\right)}{h^2}\right] \quad (5.14)$$

and

$$\left(\frac{c}{c_c}\right)^2 = \frac{\ell^2}{4}\left(1+\frac{a}{K}\right)\left\{1-\frac{h^2}{\left(1+\frac{a}{K}\right)}\left[\frac{\ell(1+\mu)-\mu}{\ell(1+\mu)}\right]\right\}\left[\frac{1}{1-\frac{\left(1+\frac{a}{K}\right)}{h^2}}\right] \quad (5.15)$$

Once a particular design configuration of the single-slug-damped bar is chosen, the value of μ, ℓ and K are constant. For a given value of the cutting force slope a, equations (5.14) and (5.15) are the parametric equations that define gnaphically in the H-(c/c_c) plane a locus of the stability borderline as the chatter frequency ratio h varies. The range of variation of h is determined from equations (5.14) and (5.15) by noting that the product of the quantities in the radicals must be positive

in order that H and c/c_c have real solutions. Thus, either

(1) both

$$1 - \frac{h^2}{(1+\frac{a}{K})}\left[\frac{\ell(1+\mu)-\mu}{(1+\mu)}\right] > 0$$

and

$$1 - \frac{(1+\frac{a}{K})}{h^2} > 0$$

leading to $$(1+\frac{a}{K}) < h^2 < (1+\frac{a}{K})\frac{\ell(1+\mu)}{\ell(1+\mu)-\mu} \qquad (5.16)$$

or (2) both

$$1 - \frac{h^2}{(1+\frac{a}{K})}\left[\frac{\ell(1+\mu)-\mu}{(1+\mu)}\right] < 0$$

and

$$1 - \frac{(1+\frac{a}{K})}{h^2} < 0$$

leading to $$(1+\frac{a}{K}) > h^2 > (1+\frac{a}{K})\frac{\ell(1+\mu)}{\ell(1+\mu)-\mu} \qquad (5.17)$$

Since ℓ and μ are positive quantities, $\frac{\ell(1+\mu)}{\ell(1+\mu)-\mu}$ is greater than unity. It follows that the inequality (5.17) cannot be satisfied in any practical design. The range of chatter frequency ratio within which H and c/c_c are real is, therefore, given by the expression (5.16).

5.22 Optimum damping condition to resist primary chatter

It has been mentioned in Section 5.2.1. that the parameters a and f_1 give a measure of the degree of severity of the cutting process.

We now discuss qualitatively how a and f_1 are related to the cutting process. The variation of a in relation to the depth of cut is typically indicated in Fig. 5.2 which is a repeat of Fig. 30 in PERA report 129 (1). In general a decreases as the depth of cut increases and eventually settles

to a constant level when the depth of cut exceeds the tool nose radius. The magnitude of this constant level is usually very small compared to the stiffness value of the boring bar and in the example quoted [1], for the case of cutting steel, a = 80 lbf/in (14 $KN.m^{-1}$) which is only 0.014 times the stiffness of a 10:1 boring bar having a typical value of around 1 $MN.m^{-1}$ or 1 $N.\mu m^{-1}$. It follows that a/K can be ignored in equations (5.14) and (5.15) when the stability borderline corresponds to depths of cut larger than the nose radius. The meaning of f_1, unlike a, is more obscure, as it is expected to be some unknown function of κ_1 and η_2 which according to their definitions, are $\kappa_1 = \kappa_{12}/\kappa_1$ and $\eta_2 = c_{21}/m_2$ as in Section 5.2. It is recognised that κ_1 and m_2 are constants for a particular design configuration of the bar; but κ_{12} and c_{21} seem to relate to the cutting process. In spite of its hypothetical nature, f_1 is the only source of instability injected into the system. It is also common knowledge that as the cutting condition becomes severer in terms of the rate of metal removed, the more is the bar likely to chatter. By following this argument, it is reasonable to suggest that as the severity of the cutting increases, so does the value of f_1 and hence H. The problem of optimising the damping ratio in respect of the ability of the bar to cope with the severest cutting condition is now equivalent to finding the solution to

$$\frac{d[H^2]}{d\left[\left(\frac{c}{c_c}\right)^2\right]} = \frac{d[H^2]}{d[h^2]} \Bigg/ \frac{d\left[\left(\frac{c}{c_c}\right)^2\right]}{d[h^2]} = 0 \qquad (5.16)$$

where $\frac{d[H^2]}{d[h^2]}$ and $\frac{d\left[\left(\frac{c}{c_c}\right)^2\right]}{d[h^2]}$ are determined from equations (5.14) and (5.15) respectively. Equation (5.16) contains the chatter frequency ratio squared h_{op}^2, where the suffix 'op' indicates the best tuned condition

for the suppression of primary chatter. By equation (5.16),

$$h_{op}^2 = (1 + \frac{a}{k})\sqrt{\frac{\ell\ (1 + \mu)}{\ell(1 + \mu) - \mu}} \qquad (5.17)$$

which, on substituting back to equations (5.14) and (5.15) respectively gives

$$H_{op} = (1 + \frac{a}{\kappa})^{\frac{1}{2}} \cdot \frac{(1+\mu)}{\mu}\left[1-\sqrt{\frac{\ell(1 + \mu) - \mu}{\ell(1 + \mu)}}\right] \qquad (5.18)$$

and $\left(\frac{c}{c_c}\right)_{op} = \frac{\ell}{2} \cdot (1 + \frac{a}{\kappa})^{\frac{1}{2}}$ (5.19)

where, as before, the suffix 'op' denotes the best tuned condition. In this equation, the optimum damping ratio $(c/c_c)_{op}$ is seen to be independent of the value of the mass ratio μ. (Strictly speaking, due to the fact that ℓ is influenced by μ in this particular design, $(c/c_c)_{op}$ and μ are implicitly related.) The value of c, however, is related to the mass of the absorber and the μ ratio by virtue of the definition of the term c_c as $c_c = 2m_s\omega_n$, where $\omega_n = \sqrt{\frac{K}{m + G^2 m_s}}$.

If c_c is now expressed in terms of the main mass m, and since $\mu = (G^2 m_s/m)$, then $c_c = \frac{2\mu m}{G^2}\omega_n$. It follows that equation (5.19) can be written as

$$c_{op} = \frac{\mu m}{G^2}\omega_n \cdot \ell\ (1+ \frac{a}{\kappa})^{\frac{1}{2}} \qquad (5.19a)$$

in which c_{op} is noted to be explicitly related to μ.

Since the parametric equations (5.18) and (5.19) define the location on the stability borderline of a point at which the boring bar can cope with the highest degree of severity in the cutting condition, the depth of cut in question is very often far in excess of the nose radius of the cutting tool, it follows that a/K becomes very small, and the value of

$(c/c_c)_{op}$ approaches $\ell/2$, which indicates that the optimum damping ratio is independent of the cutting condition. The advantage of this is immediately obvious because it means that once properly tuned such that $(c/c_c)_{op} = \ell/2$, the absorber always operates at its best irrespective of the cutting condition it is subjected to.

Normally the damping ratio is fixed once the clearance of the absorber slug is decided and the parameters H and a/K which are the measures of the cutting condition, are of more relevance to the stability borderline. For the 10:1 boring bar, the maximum possible ratio of a/K as can be deduced from Fig. 5.2 is around 0.5 for cutting steel. Obviously for the case of the tungsten-bunged bar which possesses a higher stiffness, the value of a/K will be much lower than 0.5 for the cutting of steel. To obtain the parametric equations for the stability borderline in the H-a/K plane, rewrite equation (5.15) in the form

$$\frac{a}{K} = \frac{\left(\frac{2}{\ell}\frac{c}{c_c}\right)^2 h^2 + h^4\left[\frac{\ell(1+\mu)-\mu}{\ell(1+\mu)}\right]}{h^2 + \left(\frac{2}{\ell}\frac{c}{c_c}\right)^2} - 1 \qquad (5.20)$$

Next we substitute equation (5.20) into equation (5.14) and after simplifying, we obtain

$$H = \left(\frac{2}{\ell}\frac{c}{c_c}\right)\frac{1}{\ell}\left[\frac{h^2}{h^2 + \left(\frac{2}{\ell}\frac{c}{c_c}\right)^2}\right] \qquad (5.21)$$

Equations (5.20) and (5.21) are the parametric equations which define the stability borderline in terms of H and a/K.

5.2.3. Optimising bung length for maximum stability against primary Chatter

It has been shown in Section 5.22 that at the optimally damped condition, H_{op} is given by equation (5.18) which is repeated here

$$H_{op} = (1 + \frac{a}{\kappa})^{\frac{1}{2}} \frac{(1+\mu)}{\mu} \left[1 - \sqrt{\frac{\ell(1+\mu) - \mu}{\ell(1+\mu)}}\right] \qquad (5.18)$$

f_{lo} is a measure of the cutting condition which is experienced by the bar with the absorber optimally tuned and is the condition at the stability borderline beyond which primary chatter will occur. a/K is assumed to be insignificantly small at the stability borderline that $(1+a/K)^{\frac{1}{2}}$ in equation (5.18) is approximated to unity. Furthermore, since $H_{op} = (f_{lo}/G^2)/(m_s\omega_n)$ and $\omega_n = (K/m+G^2m_s))^{\frac{1}{2}}$, equation (5.18) can be written in the form:

$$f_{lo} \doteq \sqrt{Km(1+\mu)} \cdot \left[1 - \sqrt{\frac{\ell(1+\mu)-\mu}{\ell(1+\mu)}}\right] \qquad (5.22)$$

For the particular design of boring bar such as that shown in Fig. 4.5 in which a constant diameter forced-fit bung has a variable length that affects the values of K, m and μ in equation (5.18), it turns out that there is a particular length h_b of the bung at which f_{lo} becomes maximum resulting in the highest stability borderline. To find this, it is necessary to solve the equation

$$\frac{df_{lo}}{dh_b} = 0 \qquad (5.23)$$

The level of complexity involved in solving this equation clearly depends on the nature of the mathematical functions for $K(h_b)$ and $m(h_b)$ both of which are functions of the bung length h_b and are determined by the consideration of the respective strain and kinetic energies within the system in a manner similar to that described in Sections 4.5.1 and 4.5.2.

Since mathematical functions for K and m are ofter very complicated, an exact solution for equation (5.23) is hardly possible and it follows that the iterative method as presented in Section 4.5.3 will also be of use here for finding the optimum bung length h_b.

5.3. REGENERATIVE CHATTER THEORY OF SINGLE-SLUG-DAMPED BAR

In Appendix IV of PERA Report 133 [2], it is proved that regenerative chatter may be simulated by a hypothetical negative hysteretic damping force. The proof is presented here briefly as follows.

At the stability borderline, the boring tool is assumed to oscillate harmonically with the chatter frequency ω in the radial direction with the motion,

$$y_2 = a_2 \sin \omega t \qquad (5.24)$$

which is sustained by virtue of the undulating surface left from the previous cut which has the wave equation,

$$y_2 = a_2 \sin (\omega t + \phi) \qquad (5.25)$$

where ϕ is the phase lag of the wave in equation (5.24) as compared with that in equation (5.25). The amplitude a_2 for the two consecutive cuts are assumed to be equal, because at the stability borderline, the chatter amplitude neither grows or decays.

The variations in the uncut chip thickness is $a_2 \left[\sin \omega t - \sin (\omega t + \phi)\right]$ and if r_1 and r_2 denote the rates at which the cutting forces in the respective y_1 and y_2 directions increase with incresing depth of cut, then the cutting force increments in y_1 and y_2 directions are respectively given by

$$P_1 = -r_1 a_2 \left[\sin\omega t - \sin(\omega t + \phi)\right]$$

and

$$P_2 = -r_2 a_2 \left[\sin\omega t - \sin(\omega t + \phi)\right]$$

which can be expressed in terms of the displacements y_2 and the

velocity $\dot{y}_2$ as respectively

$$P_1 = R_1' y_2 + \frac{S_1}{\omega} \dot{y}_2 \qquad (5.26)$$

and $$P_2 = R_2' y_2 + \frac{S_2}{\omega} \dot{y}_2 \qquad (5.27)$$

where $R_1' = r_1 (1-\cos \phi)$, $R_2' = r_2 (1-\cos\phi)$, $S_1 = r_1 \sin \phi$ and $S_2 = r_2 \sin \phi$

The terms $\frac{S_1}{\omega}\dot{y}_2$ and $\frac{S_2}{\omega} \dot{y}_2$ in equations (5.26) and (5.27) can be simulated by the negative hysteretic damping terms when $\sin \phi > 0$. It may be expected that these two terms act as a source of instability in the system, which will be made clear as follows. The equations of motion for the plain solid bar modelled as before by a two-degree-of-freedom system and subjected to the force increments P_1 and P_2 are given by

$$(m_1 \ddot{y}_1 + c_1 \dot{y}_1 + K_t y_1) + (c_{12} - \frac{S_1}{\omega}) \dot{y}_2 + (k_{12} + R_1') y_2 = 0 \qquad (5.28)$$

and $$(c_{21} \dot{y}_1 + k_{21} y_1 + m_2 \ddot{y}_2) + (c_2 - \frac{S_2}{\omega}) \dot{y}_2 + (K + a + R_2') y_2 = 0 \qquad (5.29)$$

Using the Routh-Hurwitz criterion, PERA establish that the necessary and sufficient conditions for boring bar stability are,

$$\epsilon_1 + \epsilon_2 - \frac{S_2}{\omega m_2} > 0 \qquad (5.30)$$

and $$\epsilon_1 + \left[- \left(\frac{\omega_1^2}{\omega_2^2 - \omega_1^2 + \frac{R_2'}{m_2}} \right) (K_1 \frac{R_1'}{K}) \eta_2 \right] > 0 \qquad (5.31)$$

These two conditions can be expressed as

$$\epsilon_1 + \epsilon_2'' > 0 \qquad (5.30a)$$

and $$\varepsilon_1 + \varepsilon_2''' > 0 \qquad (5.31a)$$

where $$\varepsilon_2'' = \varepsilon_1 - \frac{S_2}{\omega m_2}$$

and $$\varepsilon_2''' = -\left[\frac{\omega_1^2}{\omega_2^2 - \omega_1^2 + \frac{R_2'}{m_2}}\left(\kappa_1 \frac{R_1'}{K}\right)\eta_2\right]$$

By the principle of dimensional homogeneity, ε_2'' and ε_2''' in equations (5.30a) and (5.31a) can be regarded as damping terms and instability results if ε_2'' or ε_2''' is larger than ε_1. It follows that negative hysteretic damping is a convenient source of instability for simulating regenerative chatter. This might suggest that separate tuning is required for the suppression of primary and regenerative chatter. However, according to PERA [2], it turns out that tuning for primary chatter suppression using negative viscous damping model is quite adequate for the suppression of regenerative chatter as well.

5.3.1. Stability model with negative hysteretic damping

The forcing function on the right-side of the equation of motion (4.4) now has the form $-\left(\frac{f_2}{\omega}\right)\dot{x}_1$ where $-f_2$ is the negative hysteretic damping coefficient and ω is the angular chatter frequency. The equations of motion become

$$\frac{m}{G^2}\ddot{x}_1 + \left(m_s\frac{\lambda^2}{R_2^2} + m_f\beta_c\right)(\ddot{x}_1 - \ddot{x}_2) + c(\dot{x}_1 - \dot{x}_2) + \frac{(K+a')}{G^2}x_1 - \frac{f_2/G^2}{\omega}\dot{x}_1 = 0 \qquad (5.32)$$

and $$m_s\ddot{x}_2 - \left(m_s\frac{\lambda^2}{R_2^2} + m_f\beta_c\right)(\ddot{x}_1 - \ddot{x}_2) - c(\dot{x}_1 - \dot{x}_2) = 0 \qquad (4.5)$$

In equation (5.32) a' is different from a for primary chatter. In this case $a' = a + R_1'$.

Assuming that the system is initially quiescent, and applying Laplace transform to the set of equations (5.32) and (4.5), the characteristic equation of the system is obtained from the determinant of the coefficient

matrix of equations (5.32) and (4.5). That is

$$\begin{vmatrix} \frac{m}{G^2}+(m_s\frac{\lambda^2}{R_2^2}+m_f\beta_c)s^2+(c-\frac{f_2/G^2}{\omega})s+\frac{(K+a')}{G^2} & -\left[(m_s\frac{\lambda^2}{R_2^2}+m_f\beta_c)s^2+cs\right] \\ -\left[(m_s\frac{\lambda^2}{R_2^2}+m_f\beta_c)s^2+cs\right] & (m_s+m_s\frac{\lambda^2}{R_2^2}+m_f\beta_c)s^2+cs \end{vmatrix} = 0 \qquad (5.33)$$

We obtain the parametric equations for the stability borderline in three stages. First, s is replaced by jω. Second, real and imaginary parts of the resulting equation are both equated to zero such that

$$\left[\frac{m}{G^2}m_s+(\frac{m}{G^2}+m_s)(m_s\frac{\lambda^2}{R_2^2}+m_f\beta_c)\right]\omega^4-\left[\frac{(K+a')}{G^2}(m_s+m_s\frac{\lambda^2}{R_2^2}+m_f\beta_c)\right]\omega^2+\frac{cf_2\omega}{G^2}=0 \qquad (5.34)$$

and $$-c(\frac{m}{G^2}+m_s)\omega^3+\frac{f_2}{G^2}(m_s+m_s\frac{\lambda^2}{R_2^2}+m_f\beta_c)\omega^2+\frac{(K+a')}{G^2}c\omega=0 \qquad (5.35)$$

Finally, $\frac{c}{c_c}$ and J are solved, bearing in mind the definition of the dimensionless parameter; $J^2=\left(\frac{f_2/G^2}{m_s\omega_n}\right)^2$. That is,

$$J^2=h^2\omega_n^2\frac{(1+u)^2}{u^2}\left[1-\frac{(1+\frac{a'}{K})}{h^2}\right](1+\frac{a'}{K})\left[1-\frac{\ell(1+\mu)-\mu}{\ell(1+\mu)}\cdot\frac{h^2}{(1+\frac{a'}{K})}\right] \qquad (5.36)$$

and $$(\frac{c}{c_c})^2=\frac{\ell^2}{4}(1+\frac{a'}{K})\left[1-\frac{\ell(1+\mu)-\mu}{\ell(1+\mu)}\cdot\frac{h^2}{(1+\frac{a'}{K})}\right]\left[\frac{1}{1-\frac{(1+\frac{a'}{K})}{h^2}}\right] \qquad (5.37)$$

from which the stability borderline expressed in the J - $\frac{c}{c_c}$ plane can be calculated.

Similar to the derivation for the case of primary chatter, it can be shown that for real values of J and (c/c_c) the chatter frequency ratio h in the equations (5.36 .) and (5.37 .) is allowed to take on values in the interval,

$$\left(1+\frac{a'}{K}\right) < h^2 < \frac{\ell(1+\mu)}{\ell(1+\mu)-\mu}\left(1+\frac{a'}{K}\right) \qquad (5.38)$$

5.3.2. Optimum damping condition to resist regenerative chatter

We shall describe first in a qualitative fashion how a'/K and J are related to the cutting process. The value of J in regenerative chatter, similar to H in primary chatter, is proportional to the severity of the cutting condition. By the relation that $a' = a + R_2'$ where R_2' $= r_2 (1-\cos \phi)$ the maximum value of which is $R_2' = 2r_2$ when $\phi = \pi$ and that r_2 is comparable to a as is obvious from their definitions, the maximum value of a' is $a+2r_2 \doteq 3a$ approximately. Hence, assuming as in Section 5.2.2. that a/K = 1/140, then $a'/K \doteq 3a/K \doteq 3/140$. It follows that for all practical situations when the depth of cut exceeds the nose radius, a'/K can be safely assumed negligible and hence $(1+a'/K) \doteq 1$.

In view of this observation, the problem of optimising the damping condition to achieve the most enhanced stability borderline is equivalent to solving the following equation

$$\frac{d\left[J^2\right]}{d\left[\left(\frac{c}{c_c}\right)^2\right]} = \frac{d\left[J^2\right]}{d\left[h^2\right]} \Bigg/ \frac{d\left[\left(\frac{c}{c_c}\right)^2\right]}{d\left[h^2\right]} = 0 \qquad (5.39)$$

for the frequency ratio squared at the best-tuned condition, denoted by the symbol h_{or}^2. Thus, after some simplification, equation (5.39) becomes

$$h_{or} = \sqrt{\frac{1}{2}\left[1+\frac{\ell(1+\mu)}{\ell(1+\mu)-\mu}\right]\left(1+\frac{a'}{K}\right)} \qquad (5.40)$$

The corresponding J_{or} and $(c/c_c)_{or}$ are respectively

$$J_{or} = \frac{\omega_n}{2\ell}\left(1+\frac{a'}{K}\right)\sqrt{\frac{\ell(1+\mu)}{\ell(1+\mu)-\mu}} \qquad (5.41)$$

and $$\left(\frac{c}{c_c}\right)_{or} = \frac{\ell}{2}\sqrt{\left(1+\frac{a'}{K}\right)\frac{\ell(1+\mu)-\mu/2}{\ell(1+\mu)}} \qquad (5.42)$$

Since $(1+a'/K) \doteq 1$, equations (5.41) and (5.42) are simplified to

$$J_{or} = \frac{\omega_n}{2\ell}\sqrt{\frac{\ell(1+\mu)}{\ell(1+\mu)-\mu}} \qquad (5.43)$$

and $$\left(\frac{c}{c_c}\right)_{or} = \frac{\ell}{2}\sqrt{\frac{\ell(1+\mu)-\mu/2}{\ell(1+\mu)}} \qquad (5.44)$$

Normally, (c/c_c) is fixed once a particular slug absorber size is chosen. Since both parameters J and a'/K are functions of the cutting process, it may be more useful to obtain stability borderline indicative of the critical cutting condition as represented by J and a'/K. For this reason, equation (5.37) is rewritten in the form

$$\frac{a'}{K} = \frac{\left(\frac{2}{\ell}\frac{c}{c_c}\right)^2 h^2 + h^4\left[\frac{\ell(1+\mu)-\mu}{\ell(1+\mu)}\right]}{h^2+\left(\frac{2}{\ell}\frac{c}{c_c}\right)^2} - 1 \qquad (5.37a)$$

It is noted that the right-side of this equation is identical to that of equation (5.20) for a/K for the suppression of primary chatter.

Substituting equation (5.37a) in equation (5.36) gives

$$J = \left(\frac{2}{\ell}\frac{c}{c_c}\right)\frac{1}{\ell}\left[\frac{h^3\omega_n}{h^2+\left(\frac{2}{\ell}\frac{c}{c_c}\right)^2}\right] \qquad (5.36a)$$

The pair of parametric equations (5.37a) and (5.36a) trace out graphically

in the J-a'/K plane the required stability borderline.

5.3.3. Optimising bung length for maximum stability against regenerative chatter

The optimisation applies to the design of boring bar shown in Fig. 4.5. At the optimum damping, the cutting condition corresponding to the stability borderline is given by equation (5.43) which is repeated here for reference,

$$J_{or} = \frac{\omega_n}{2\ell} \sqrt{\frac{\ell(1+\mu)}{\ell(1+\mu)-\mu}} \qquad (5.43)$$

On account of the fact that $J_{or} = \frac{f_{2o}/G^2}{m_s \omega_n}$ and $\omega_n = \sqrt{\frac{K}{m + G^2 m_s}}$ equation (5.43) can be expressed in the form

$$f_{2o} = \frac{K}{2} \frac{\mu}{\sqrt{[\ell(1+\mu)-\mu][\ell(1+\mu)]}} \qquad (5.45)$$

where K and μ are functions of the design configuration, in this case, the bung length h_b as it is allowed to vary. When the bung length h_b is increased, K is expected to increase but μ to decrease. It is, therefore, apparent that a maximum f_{20} exists at a certain bung length obtainable from solving the differential equation

$$\frac{df_{2o}}{dh_b} = 0 \qquad (5.46)$$

Since this equation is very similar to equation (5.21) any comments pertinent to equation (5.23) will also be applicable to equation (5.46).

REFERENCES FOR CHAPTER 5

1. PERA No. 129 "Investigation into overhung boring bars - Part V - Behaviour under chatter conditions". Production Engineering Research Association, August 1964, pp. 20-29

2. PERA No. 133 "Investigation into overhung boring bars - Part VI - Performance for a tuned and damped boring bar". Production Engineering Research Association, December 1964, pp. 28-29.

3. PORTER, B. "Stability criteria for linear dynamical systems", Oliver and Boyd Ltd., 1967, pp. 116-138.

6. EXPERIMENTS ON STABLE MACHINING AND THE GEOMETRIC FORM ERRORS

Geometric form errors are a function of the cutting conditions and the materials to be cut. They are also a function of the stiffness of the boring bar. This chapter will describe four experiments which are such related that if anyone is ignored, the picture of geometric form errors would be incomplete. The first experiment attempts to establish some empirical cutting force equations from which forces can be calculated once the cutting conditions are given. The second experiment sets out to determine the equivalent radial stiffness of the tungsten-bunged bar which will be used in the subsequent form error experiments. The third and fourth experiments deal with the respective "bell-mouth" error and the "copying" error. Their theories have been developed in section 3.4.1 and section 3.4.2.

6.1. DETERMINING EMPIRICAL EQUATIONS

6.1.1. Object:- It is to determine by means of metal cutting tests the forces and how they are related to the depth of cut, t, and the feed rate s. The metal is EN8.

6.1.2. Instrumentation and equipment

(1) Coromant Standard E141 S1P type boring tool with a nose radius of 0.010" (0.254 mm). Fig. 6.1 shows the tool geometry.

(2) PERA Dynamometer serial 001 - This design was used at PERA for boring and turning operations. Fig. 6.2 which is reproduced from Fig. 33 of PERA Report 90[1], illustrates a drawing of the dynamometer and the circuit diagram for strain gauges. The dynamometer measures the three principal cutting forces, i.e. tangential, radial and feed forces, by means of strain gauges such arranged that cross-couplings are minimised and that temperature correction is provided.

Type:-
Coromant Standard E141 S1P

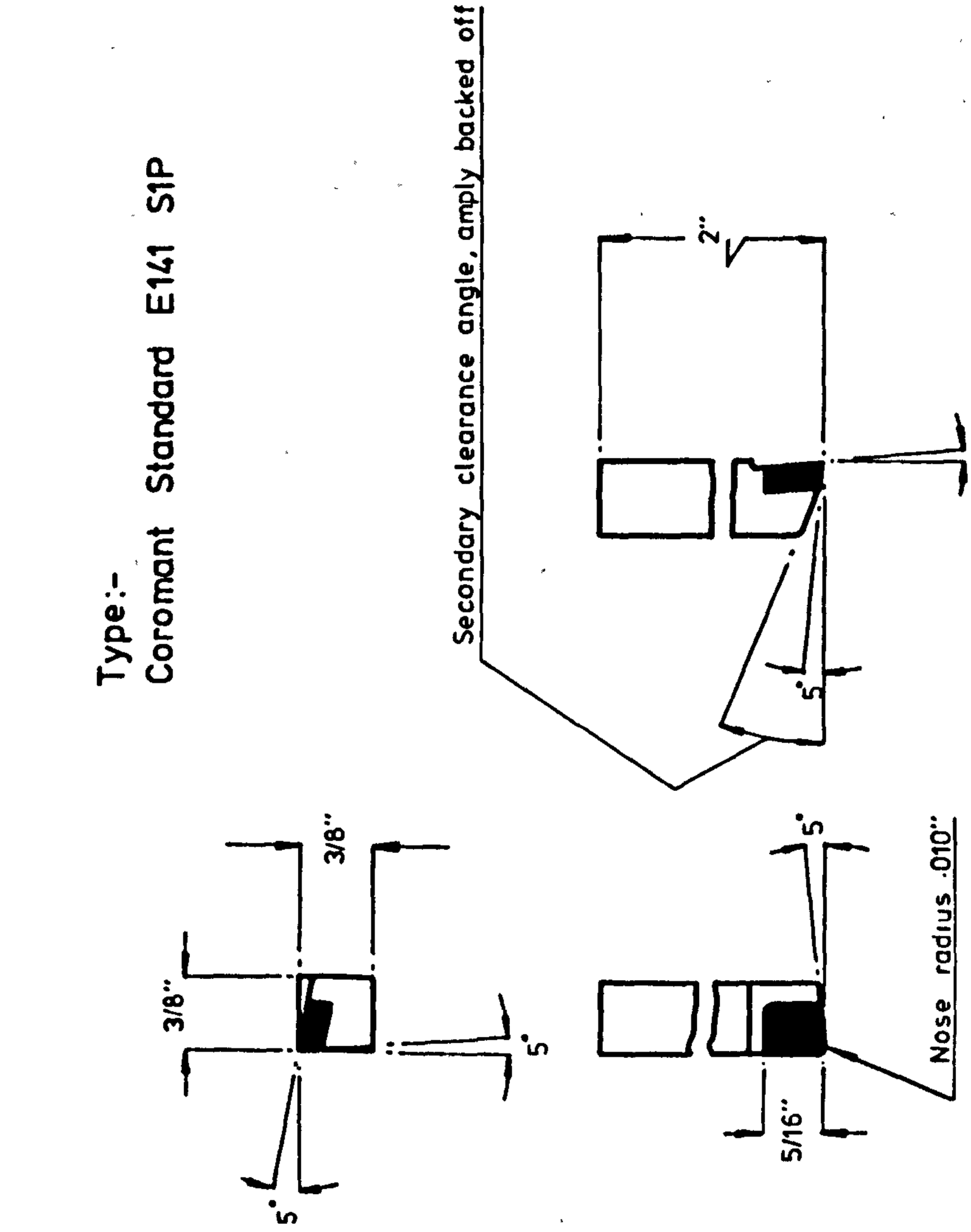

Fig 6.1 Nomenclature and type of boring tool

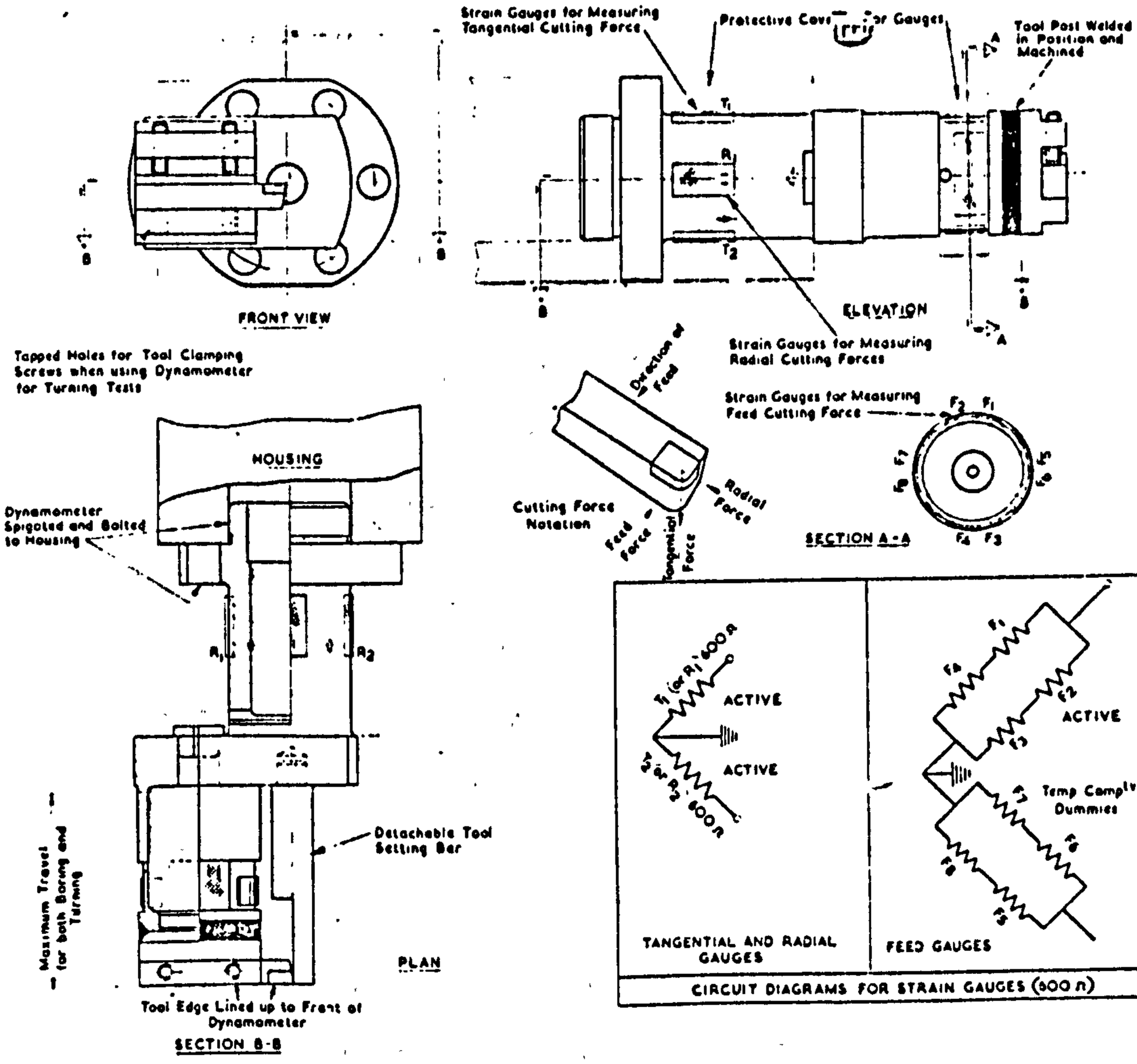

Fig 6.2 Prototype three co-ordinate lathe tool dynamometer from Fig 33 of Ref (1)

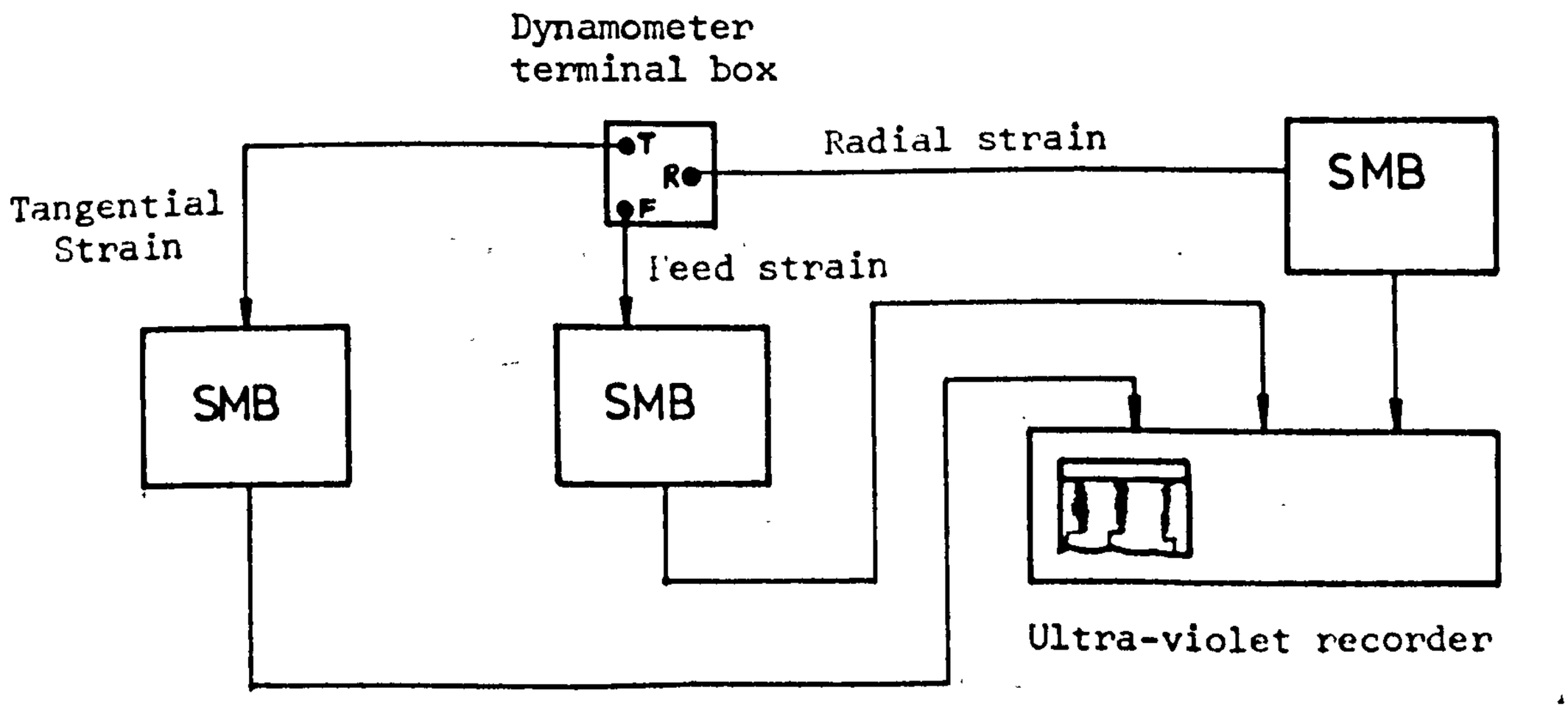

SMB = strain measuring bridge

Fig 6.3 Block diagram of instruments used for strain measurement

(3) Carrier Frequency Bridges, Philips PR 9307 - These are strain measuring bridges with two possible output options:- current and voltage. The voltage output is capable of delivering a maximum of 1 V d.c. corresponding to the full scale deflection on the meter of the bridge.

(4) Ultra-violet recorder, Southern Instruments M1330 - Ten channels of recording traces are available but only three are used for the principal cutting force components.

(5) Work specimen - EN8 steel as rolled. Nominal dimensions are:-

outside diameter = $4\frac{1}{4}$" (108 mm)

inner diameter = $3\frac{1}{8}$" (79.4 mm)

and thickness = 1" (25.4 mm)

The mechanical properties and its composition of EN8 will be discussed in section 6.3.2.

(6) Bakelite tool packings - These are placed around the cutting tool principally to prevent heat generated in the cutting process from reaching the strain gauge elements on the dynamometer and secondly to enable the tool to be set on centre.

(7) Lathe - Holbrook Centre Lathe with 6" swing.

6.1.3. Procedure

The experiment was conducted in two stages:

(1) Dynamometer calibration

In Fig. 6.3 is shown a block diagram of the arrangement of the strain measuring bridge, and the ultra-violet recorder used for both calibration and cutting tests. For calibration, the dynamometer was firmly secured on a test bed and suitably connected as shown in Fig. 6.3. Before loads were applied, the bridges had to be balanced so that all meters indicated zero deflections. Static loads were then applied in the

radial direction in steps of 50 lbf (222.4N) from zero load to a maximum of 300lbf(1334.4N) while deflections on each of the three meters were noted at each load increment. Unloading was done in steps of 50 lbf (222.4N) until all loads were removed, and again meter deflections were read at each load decrement. The unloading part of the cycle is necessary to detect possible hysteresis in the dynamometer.

The cycle of loading and then unloading was repeated in the tangential and feed directions and meter readings were taken.

(2) Cutting tests

The dynamometer was bolted on the saddle of the lathe and the boring tool was set on centre. The dynamometer, the strain measuring bridges and the recorder were connected as shown in Fig. 6.3. The principle of operation is briefly as follows. The cutting forces that acted on the tool tip set up strain signals in the strain gauges and corresponding levels of strain were indicated on the meter as pointer movement. A proportional voltage output from the bridge was fed into the ultra-violet recorder to drive a light pen to produce a movement such that it is proportional to the amount of strain in the strain gauge. The movement was "written" by the light pen onto the ultra-violet light sensitive paper and so a permanent record is provided for cutting forces conversion.

The cutting conditions were designed to change in the following manner:-

(a) depth of cut - from 0.003" to 0.060"
(b) feed rate - from 0.0030"/rev to 0.0135"/rev.
(c) spindle speed - 90, 120, 150, 204, 273, 363 rpm which provide a range of surface cutting speeds from 55 to 600 ft/min, whose magnitudes also depend on the hole diameters.

Each cutting condition was repeated twice so that there were available three values of the cutting forces from which their average was determined.

6.1.4. Results and discussion

(1) Dynamometer calibration

Fig. 6.4. shows a graph of the static tangential load versus the percentage full-scale deflection (% fsd) on the meter of the tangential strain measuring bridge. The bridge was set to a sensitivity level of 1.0 mV . If F_t is the tangential load in lbf, and R_t the reading in % fsd on the tangential bridge, then from Fig. 6.4, the gradient of the graph is given by $\frac{300}{190.5}$ lbf/% fsd and R_t is related to F_t by $R_t = \frac{190.5}{300} F_t$

i.e. $$R_t = 0.635\ F_t \qquad (6.1)$$

It can be seen from Fig. 6.4. that the tangential load F_t also brings about a deflection on the meter of the feed strain measuring bridge and if the amount of deflection is denoted by R_f in % fsd, then

$$R_f = \frac{11}{300} F_t$$

i.e. $$R_f = 0.037\ F_t \qquad (6.2)$$

The load F_t, however, does not seem to produce any significant strain in the radial direction.

When radial loads were applied, deflections on the meters of tangential, radial and feed strain measuring bridges were observed. The relation is as shown in Fig. 6.5 and we can write similar equations as before. Thus,

$$R_r = \frac{-180.6}{300} F_r$$

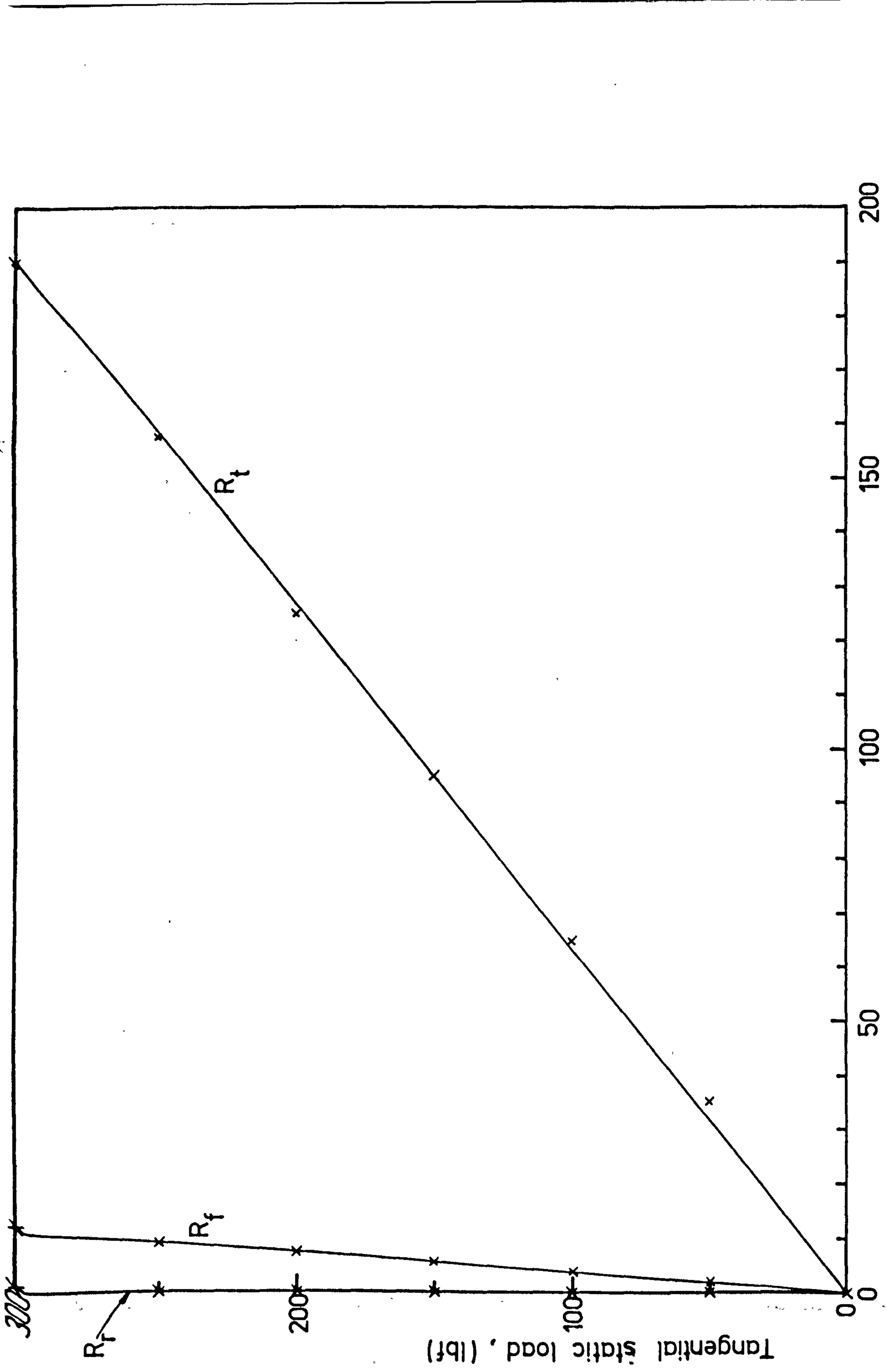

Fig 6.4 Calibration graph for tangential static load in relation to percent full-scale deflection of the strain measuring bridge meter

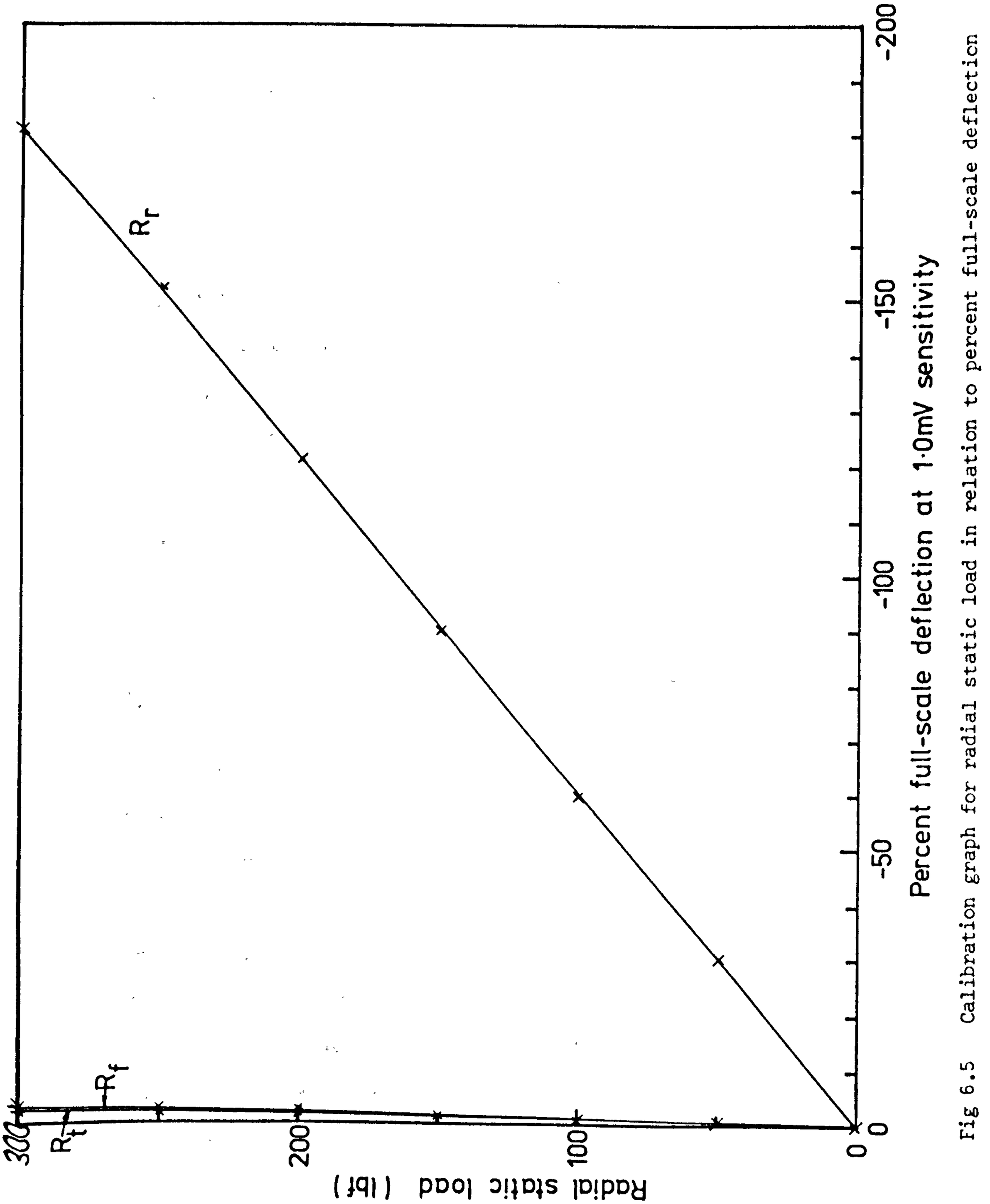

Fig 6.5 Calibration graph for radial static load of the strain measuring bridge meter

i.e. $R_r = -0.602\ F_r$ (6.3)

$R_f = \frac{-3}{300} F_r$

i.e. $R_f = -0.010\ F_r$ (6.4)

and $R_t = \frac{-2.3}{300} F_r$

i.e. $R_t = -0.008\ F_r$ (6.5)

In a similar fashion, when feed loads and their resulting meter deflections were related as in Fig. 6.6, we obtain the following equations,

$R_f = \frac{30.6}{300} F_f$

i.e. $R_f = 0.102\ F_f$ (6.6)

and $R_r = \frac{-9.7}{300} F_f$

i.e. $R_r = -0.032\ F_f$ (6.7)

The tangential deflection on the meter of the measuring bridge in this case is insignificant and therefore no equation is needed for its representation.

In Figs. 6.4, 6.5 and 6.6 it can be observed that the loading and unloading cycle coincides and follows the same straight line. It is this one-one correspondence between the force to be measured and the % fsd on the strain measuring meter that makes this dynamometer suitable for cutting force determination.

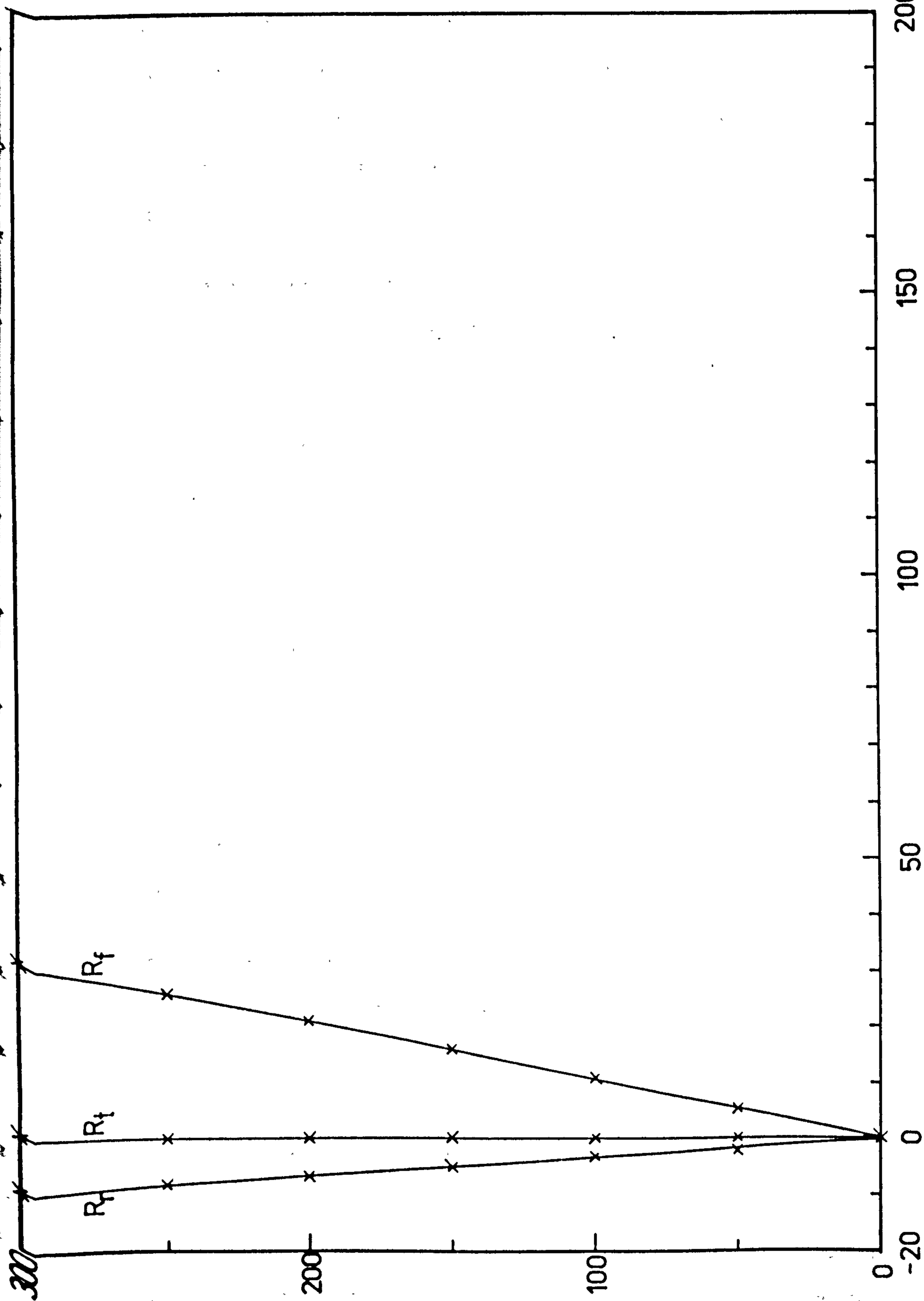

Fig 6.6 Calibration graph for feed static load in relation to percent full-scale deflection of the strain measuring bridge meter

A cutting force with its three principal components F_t, F_r and F_f will bring about meter deflections in the respective tangential, radial and feed strain measuring bridges and these deflections can be determined from combining equations (6.1) to (6.7) in the following manner.

For tangential meter deflections

$$R_t = 0.635\ F_t - 0.008\ F_r \qquad (6.8)$$

For radial meter deflections

$$R_r = -0.602\ F_r - 0.032\ F_f \qquad (6.9)$$

And for feed meter deflections

$$R_f = 0.037\ F_t - 0.010\ F_r + 0.102\ F_f \qquad (6.10)$$

Using Cramer's rule, equations (6.8) to (6.10) can be solved simultaneously for F_t, F_r and F_f. Thus,

$$F_t = 1.575\ R_t - 0.021\ R_r - 0.007\ R_f \qquad (6.11)$$

$$F_r = 0.030\ R_t - 1.653\ R_r - 0.519\ R_f \qquad (6.12)$$

and $$F_f = -0.568\ R_t - 0.155 R_r + 9.756\ R_f \qquad (6.13)$$

It should be noted that R_t, R_r and R_f in equations (6.11) to (6.13) are meter deflections measured in % fsd with the bridge sensitivity set on 1 mV.

In the cutting tests the strain values were not read off from the meter but instead were permanently recorded on the ultra-violet light sensitive paper by means of the recorder so that measurements were to be done at a later time. It is, therefore, necessary to determine the correspondence between the full-scale deflection on the meter and the movement of the light pen. It has been mentioned in Section 6.1.2

that 100% fsd corresponds to an output voltage of 1 V dc which is applied on the recorder to drive the light pen and this correspondence is not affected by the sensitivity setting on the strain measuring bridge. For this reason, the conversion from a displacement of the light pen to the R's values which are used in equations (6.11) to (6.13) to determine the principal force components has to be carried out in two stages:-

(1) The correspondence between the displacement of the light pen and the 100% fsd on the meter has to be found; and

(2) the conversion of the meter deflection in % fsd from a sensitivity setting at which the cutting tests results were recorded to the sensitivity setting of 1 mV for which equations (6.11) to (6.13) are valid.

In stage (1) it is found that 100% fsd on the meters corresponds to the light pen displacements of 123 mm, 129mm, and 113 mm for the respective tangential, radial and feed strains. That is to say, % fsd in the tangential strain meter is $\frac{M_t}{123} \times 100$; % fsd in the radial strain meter is $\frac{M_r}{129} \times 100$; and % fsd in the feed direction is $\frac{M_r}{113} \times 100$.

M is the displacement of the light pen measured in mm and the suffices t, r, and f designate the tangential, radial and feed directions respectively.

To carry out stage (2), it is noted that % fsd at any one sensitivity setting can be converted to 1 mV setting by multiplying this % fsd by the corresponding sensitivity setting. For example, x % fsd at the sensitivity of 0.1 mV is equal to 0.1 x % fsd at 1 mV. Thus,

$$R_t = \frac{M_t}{123} \times 100 \times S \qquad (6.14)$$

$$R_r = \frac{M_r}{129} \times 100 \times S \qquad (6.15)$$

and $R_f = \frac{M_f}{113} \times 100 \times S$ (6.16)

where S is the sensitivity setting on the bridge at which the cutting tests results were recorded.

The two sets of equations (6.14) to (6.16) and (6.11) to (6.13) will be used extensively in the empirical curve fitting procedure to be described presently.

(2) Cutting tests results and empirical curve fitting

(a) Effect of cutting speed on cutting forces

It has been reported in a number of literature surveys that within a certain range of cutting speeds, the cutting forces are substantially constant. Koenigsberger[2] observed that the cutting forces decrease with increasing cutting speed below 300 ft/min while above this speed the forces are approximately constant over a wide range of speeds for the machining of steel with carbide tools. PERA[1] observed the same phenomenon but that the change occurs at a lower speed of 225 ft/min when machining a common grade of cast iron with carbide tools. In practical machining conditions, the cutting speed is normally 300 ft/min and above for steel. If it can be confirmed that within this practical range of speeds the forces are approximately constant then the whole design of the experiment will be much simplified since one less parameter is to be considered. Our aim is, therefore, to find the relationship of the cutting forces and the practical cutting speeds.

Fig. 6.7 shows a typical cutting force trace. Irregular fluctuations were observed and were found to increase in intensity as the tool showed signs of wear. The mean cutting force is obtained by first measuring the height of the step on the trace and then applying two corresponding

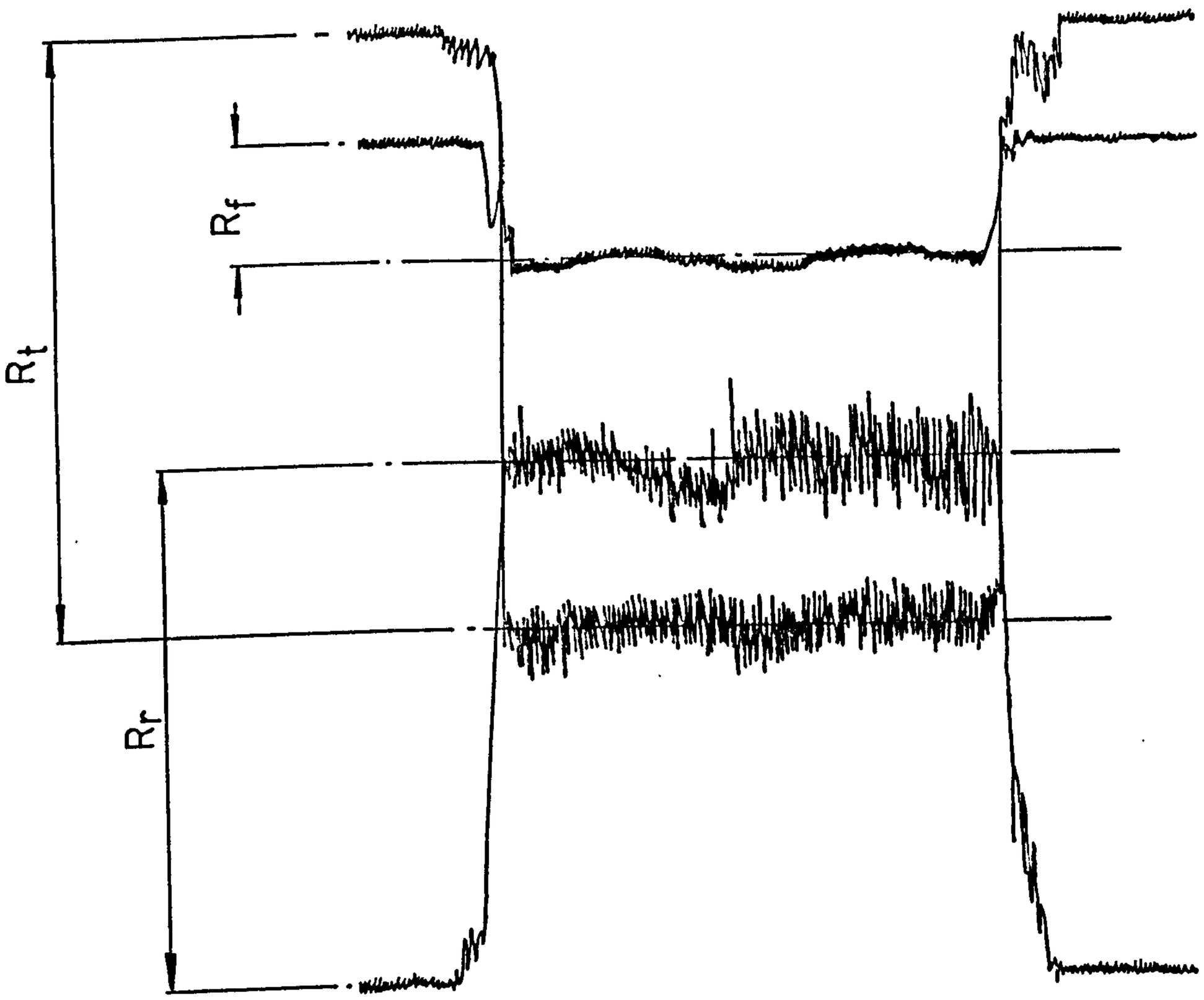

Fig 6.7 Typical cutting force trace

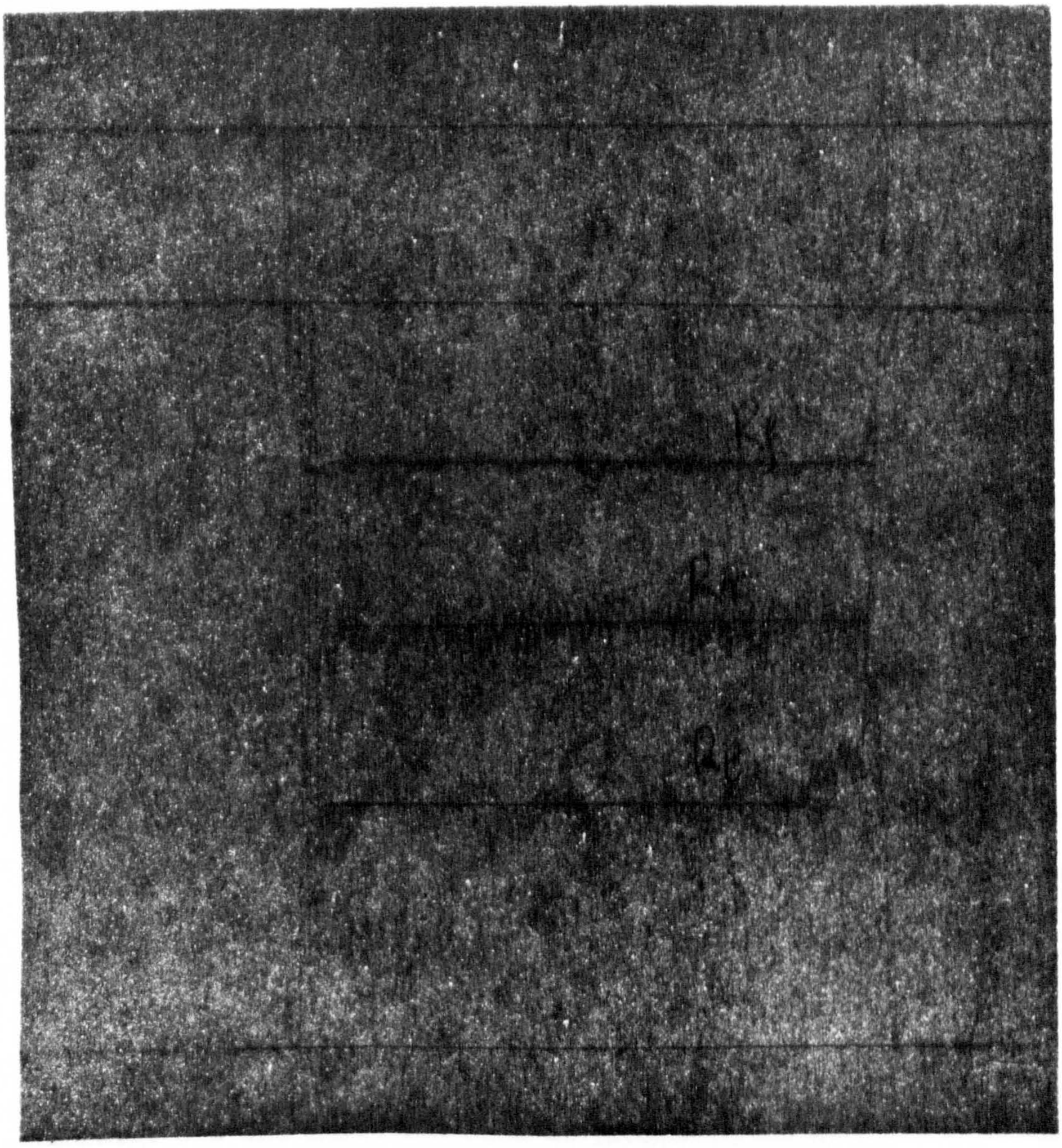

Fig 6.7 Typical cutting force trace

equations chosen from equations (6.11) to (6.16).

Fig. 6.8 shows two sets of graphs in which the tangential force in (a) and the radial force in (b) are plotted as a function of the cutting speed and the feed rate is constant at 0.0053"/rev. Three depths of cut are considered, namely, 0.005", 0.0020" and 0.060". In general it can be said that below 200 ft/min the cutting forces F_t and F_r decrease with increasing speed and above 250 ft/min, F_t and F_r can be regarded as substantially constant up to about 600 ft/min even though a tendency for the forces F_t and F_r to creep up slightly is detected in all graphs.

The feed force is not shown in Fig. 6.8 and it will not be considered in any future discussion because the feed force is comparatively small in relation to other principal forces and since it acts along the most rigid direction of the boring bar, the resulting deflection is too small to be significant.

In Fig. 6.9 are shown two sets of graphs in which the tangential force in (a) and the radial force in (b) are plotted as a function of the cutting speed and the feed rate is 0.0095"/rev. There are three graphs in each set and they correspond to depths of cut of 0.010", 0.020" and 0.060". It can be observed that within a range of speeds from 250 ft/min to 600 ft/min, cutting forces F_t and F_r may be approximated by a constant although F_t and F_r show a slight trend to increase with the speed.

(b) Fitting empirical equations

(i) Tangential cutting force, F_t

The curve fitting procedure adopted was described in Section 3.3. Basically it concerns the finding of A, a and b in the empirical equation (3.2) which is

$$F = At^a s^b \qquad (3.2)$$

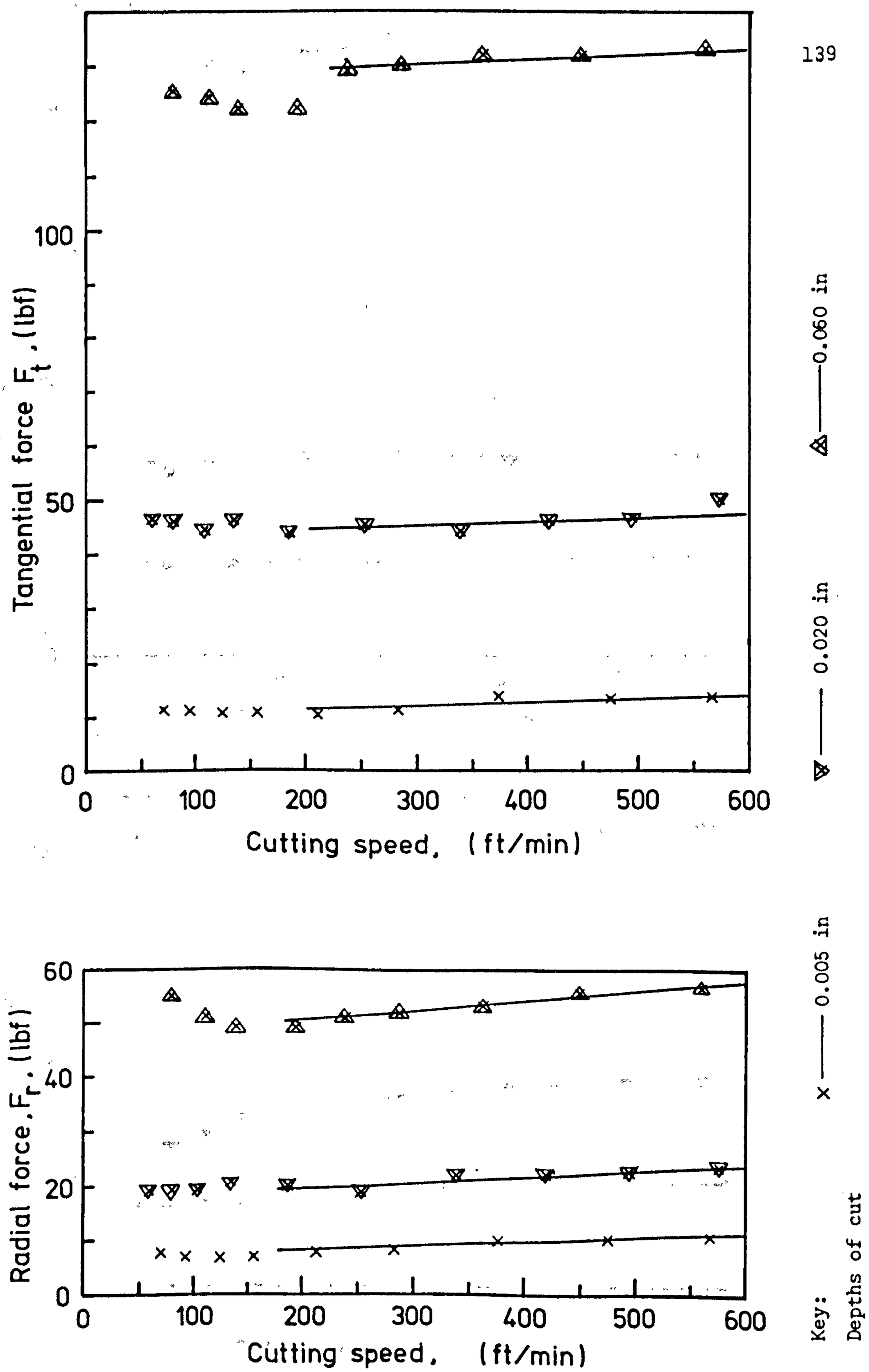

Fig 6.8 Tangential and radial forces versus cutting speed.
Feed = 0.0053"/rev.

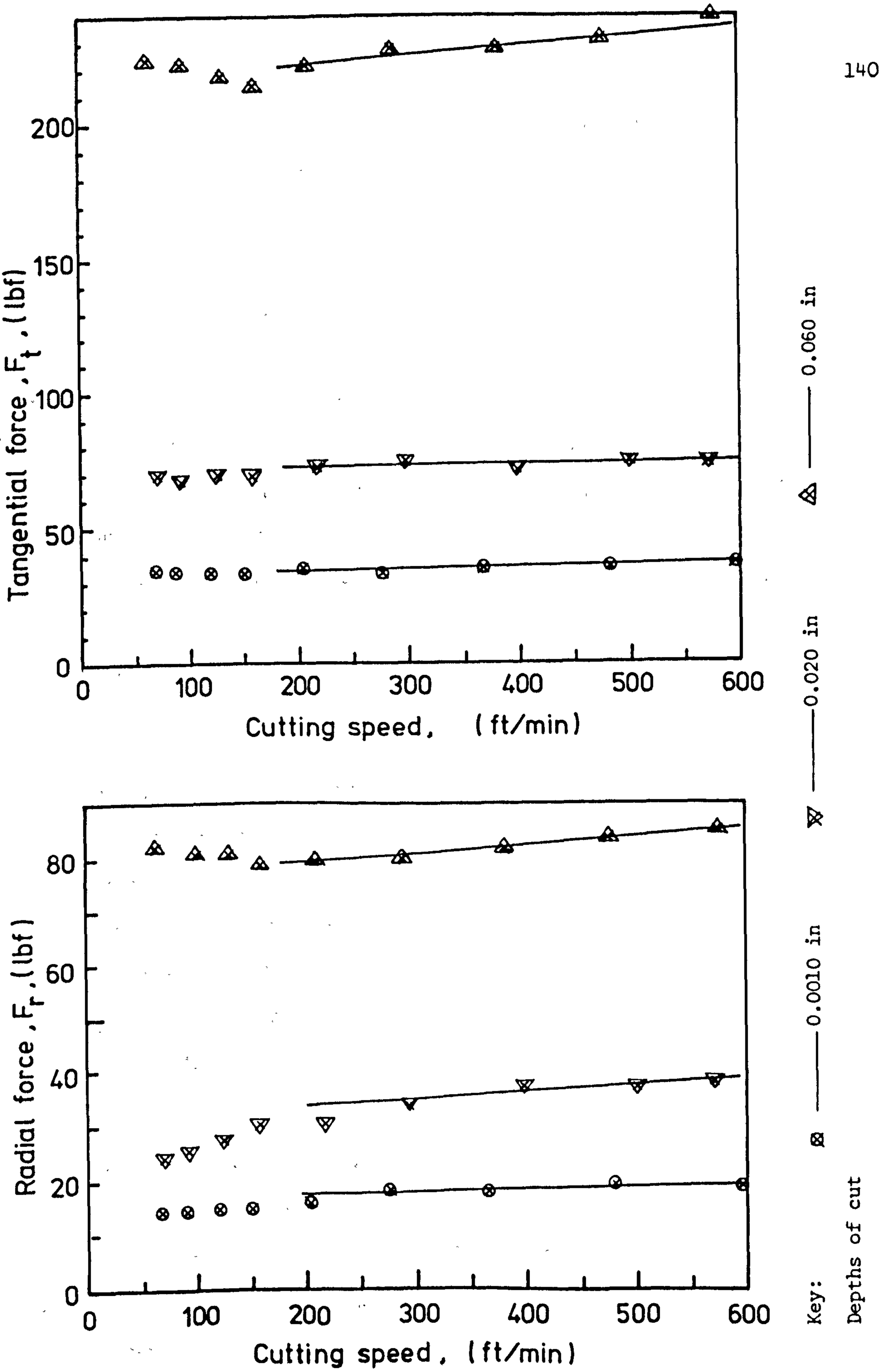

Fig 6.9 Tangential and radial forces versus cutting speed.
Feed = 0.0095 in/rev.

The cutting force data chosen for this purpose are from a cutting speed in the range of 250 ft/min to 350 ft/min. However within reasonable accuracy, the empirical equation is applicable to a range of cutting speeds from 250 ft/min up to 600 ft/min for reasons as explained in the previous section.

Fig. 6.10 shows a set of graphs with F_t plotted against the depth of cut t. Both are drawn to a logarithmic scale. There are five graphs in the set corresponding to the feed rates of 0.003"/rev, 0.0053"/rev, 0.0068"/rev, 0.0095"/rev, and 0.0135"/rev. A little scatter is observed but in general the points fall on a series of straight lines each approximately parallel to each other. Their common slope is equal to a in equation (3.2) and has a value given by,

$$a = \frac{84}{78} = 1.077$$

In Fig. 6.11 are shown a set of graphs with F_t plotted against the feed rate s, both being drawn to a logarithmic scale. Five graphs that correspond to the depths of cut of 0.005", 0.010", 0.020" and 0.040" and 0.060" are shown and they are seen to be linear and parallel to each other. The scatter is small and the common slope of these graphs is equal to b in equation (3.2). Its value is given by

$$b = \frac{57.5}{69} = 0.833$$

The value of A can now be determined from the graph of the tangential cutting force F_t drawn as a function of the quantity $(t^{1.077}\ s^{0.833})$. The graph is shown in Fig. 6.12. The scatter measured in terms of the absolute error increases as the quantity $(t^{1.077}\ s^{0.833})$ increases; but in terms of relative error its order of magnitude is about the same irrespective of the value of $(t^{1.077}\ s^{0.833})$. The slope of this graph is A the value of which is calculated as

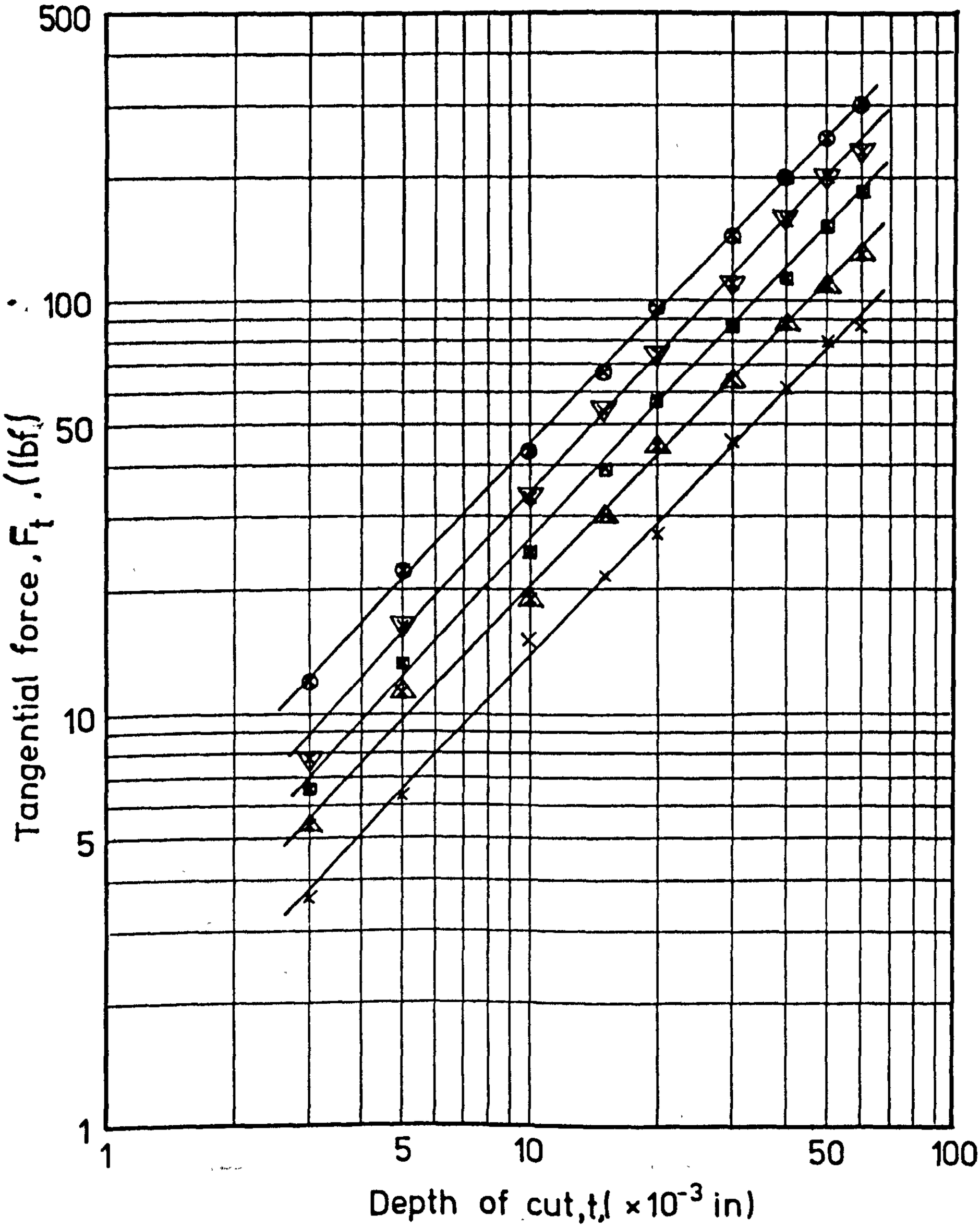

Fig 6.10 Log-log graph of tangential cutting force F_t versus depth of cut t

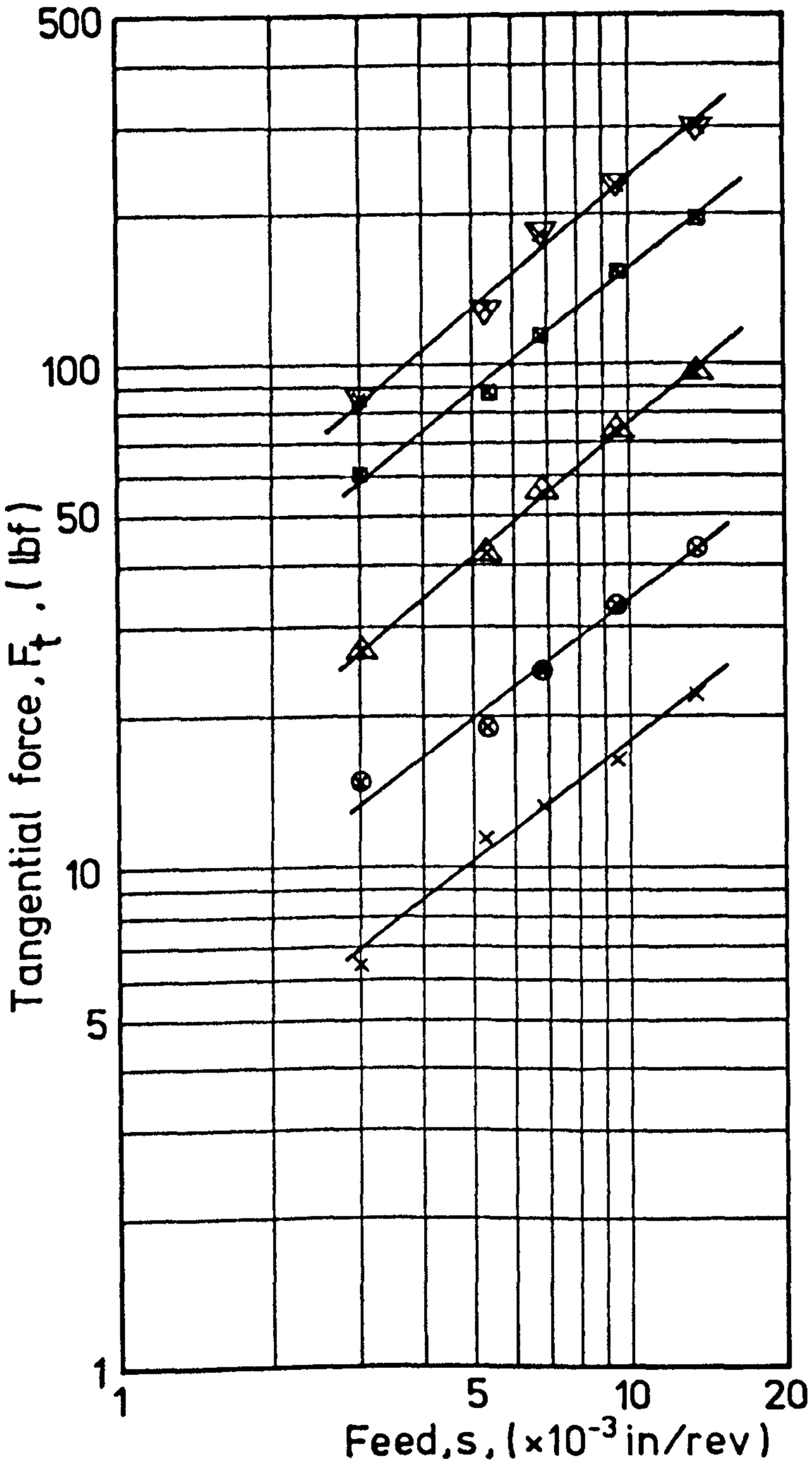

Fig 6.11 Log-log graph of tangential cutting force F_t versus feed s

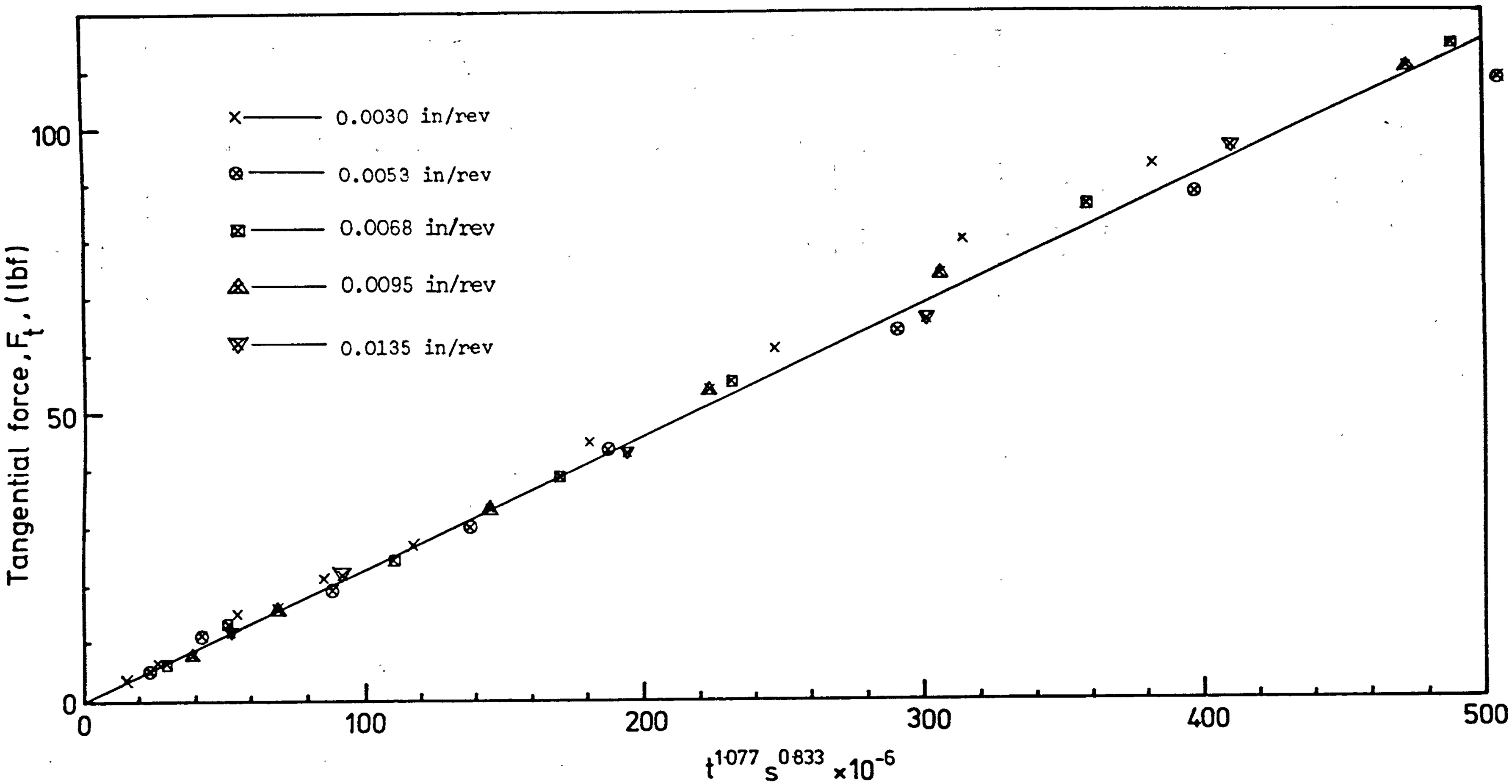

Fig 6.12 Graph of tangential force versus $t^{1.077} s^{0.833}$

$$A = \frac{110}{480 \times 10^{-6}} = 2.292 \times 10^5$$

It follows that the empirical equation for tangential cutting force is

$$F_t = 2.292 \times 10^5 \; t^{1.077} \; s^{0.833} \qquad (6.17)$$

in which the depth of cut t is measured in inches, the feed rates in inches/rev., and the force F_t thus calculated is in lbf.

In S.I. units, equation (6.17) becomes

$$F_t = 2.114 \times 10^3 \; t^{1.077} \; s^{0.833} \qquad (6.18)$$

where t is measured in mm, s in mm/rev., and the force F_t thus calculated is in Newtons.

(ii) Radial cutting force, F_r

The same procedure is used as when the empirical equation for tangential cutting force was determined. The cutting force data that are shown in Fig. 6.13 and 6.14 were obtained at a cutting speed between 250 ft/min and 350 ft/min.

Fig. 6.13 shows a set of graphs with radial force versus the depth of cut, both being drawn to a logarithmic scale. There are five graphs that correspond to the feed rates of 0.003"/rev., 0.0053"/rev., 0.0068"/rev., 0.0095"/rev. and 0.0135"/rev. Considerable scatter is observed but the trend that the points follow a set of approximately straight lines is noticeable. These lines are roughly parallel to each other and their common slope is,

$$a = \frac{95}{120} = 0.792$$

Fig. 6.14 is also a log-log plot with radial force against the feed rate. Five graphs that correspond to the depths of cut of 0.005", 0.010", 0.020", 0.040" and 0.060" are drawn and they are more or less linear and parallel

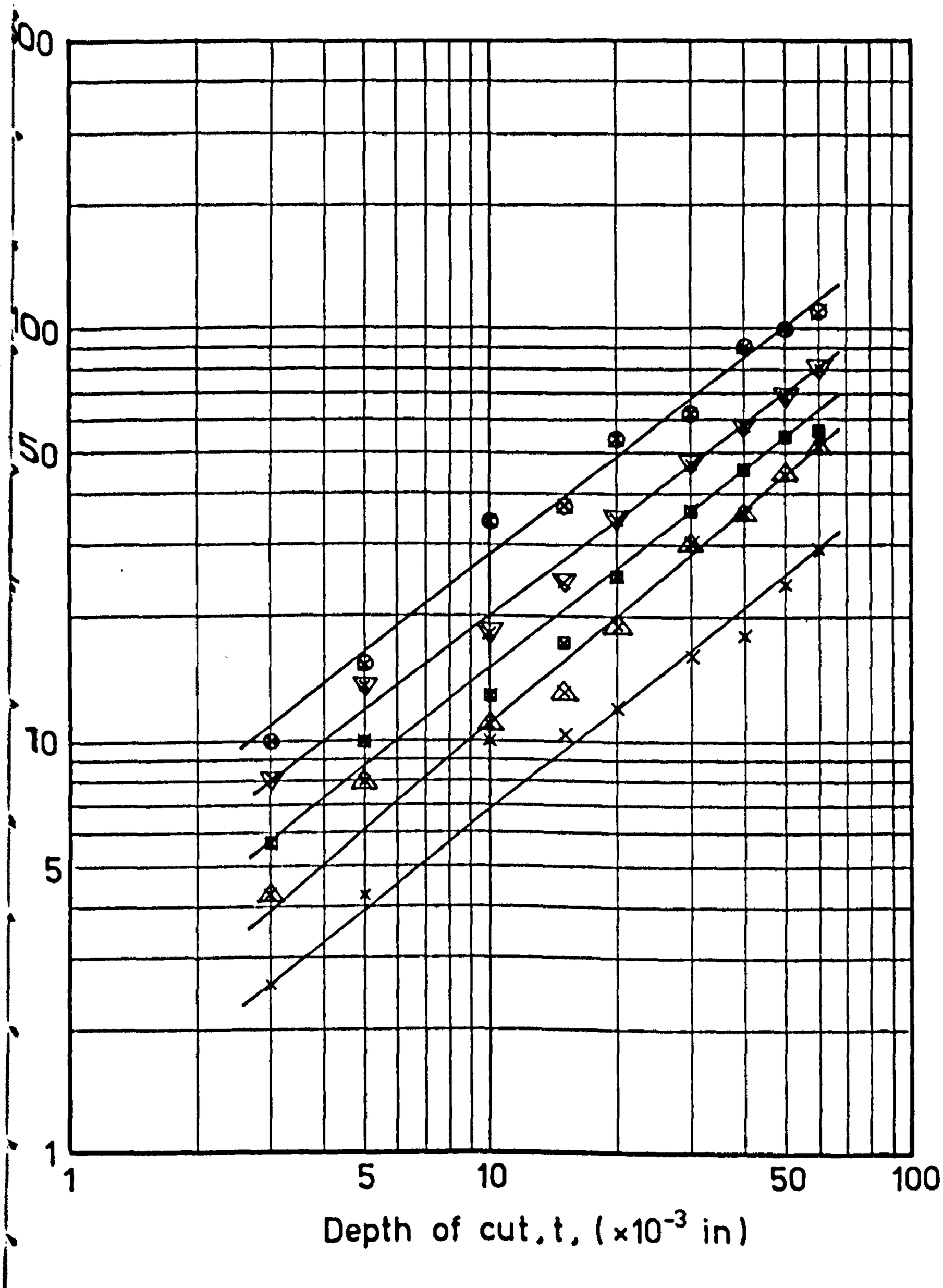

Fig 6.13 Log-log graph of radial cutting force F_r versus depth of cut t

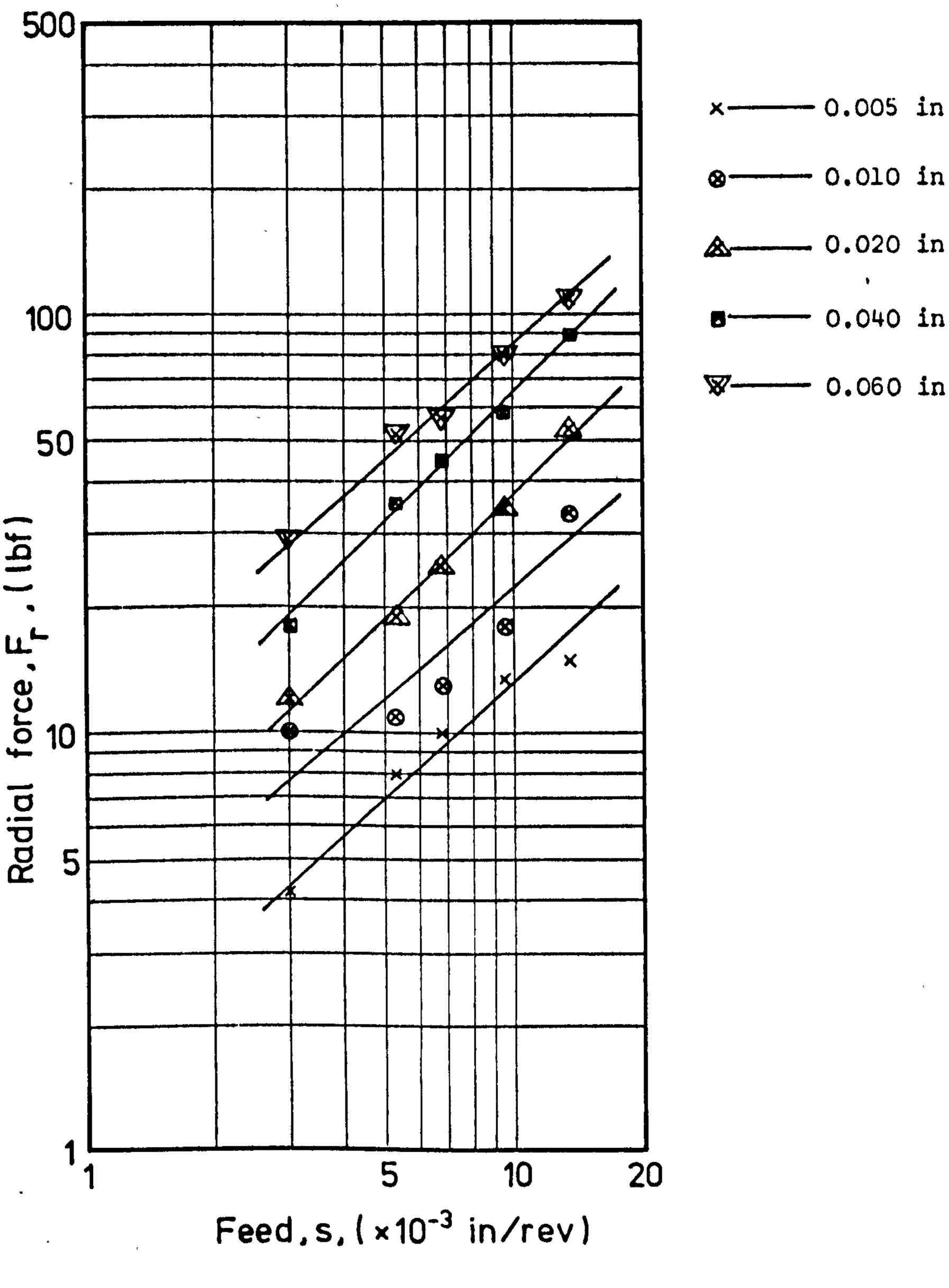

Fig 6.14 Log-log graph of radial cutting force F_r versus feed s

to each other. Scatter is heavier but the trend of the graphs is unmistakeable. The common slope of these graphs is:

$$b = \frac{84}{89} = 0.944$$

Fig. 6.15 shows a graph of radial force F_r as a function of the quantity $(t^{0.792}\ s^{0.944})$. The relationship is linear although there is considerably more scatter than its equivalent in Fig. 6.12. The slope of this line is A and is given by,

$$A = \frac{27.5}{440 \times 10^{-6}} = 6.250 \times 10^4$$

The empirical equation for radial cutting force is, therefore,

$$F_r = 6.250 \times 10^4\ t^{0.792}\ s^{0.944} \qquad (6.19)$$

where t is measured in inches, s in inches/rev., and the force F_r thus calculated is in lbf.

In metric units, equation (6.19) becomes

$$F_r = 1.012 \times 10^3\ t^{0.792}\ s^{0.944} \qquad (6.20)$$

where t is in mm, s in mm/rev., and F_r thus calculated is in Newtons. It is noted that F_t and F_r thus calculated from equations (6.17) and (6.19) are accurate to one decimal place.

6.1.5 Conclusions

The following comments refer to the machining of a rolled EN8 steel with a carbide-tipped tool the geometry of which is shown in Fig. 6.1.

(a) Below 200 ft/min the tangential and radial cutting forces decrease with increasing cutting speed whereas from 250 ft/min to 600 ft/min, cutting forces can be regarded as substantially constant.

(b) The tangential cutting force can be calculated from the empirical equation (6.17)

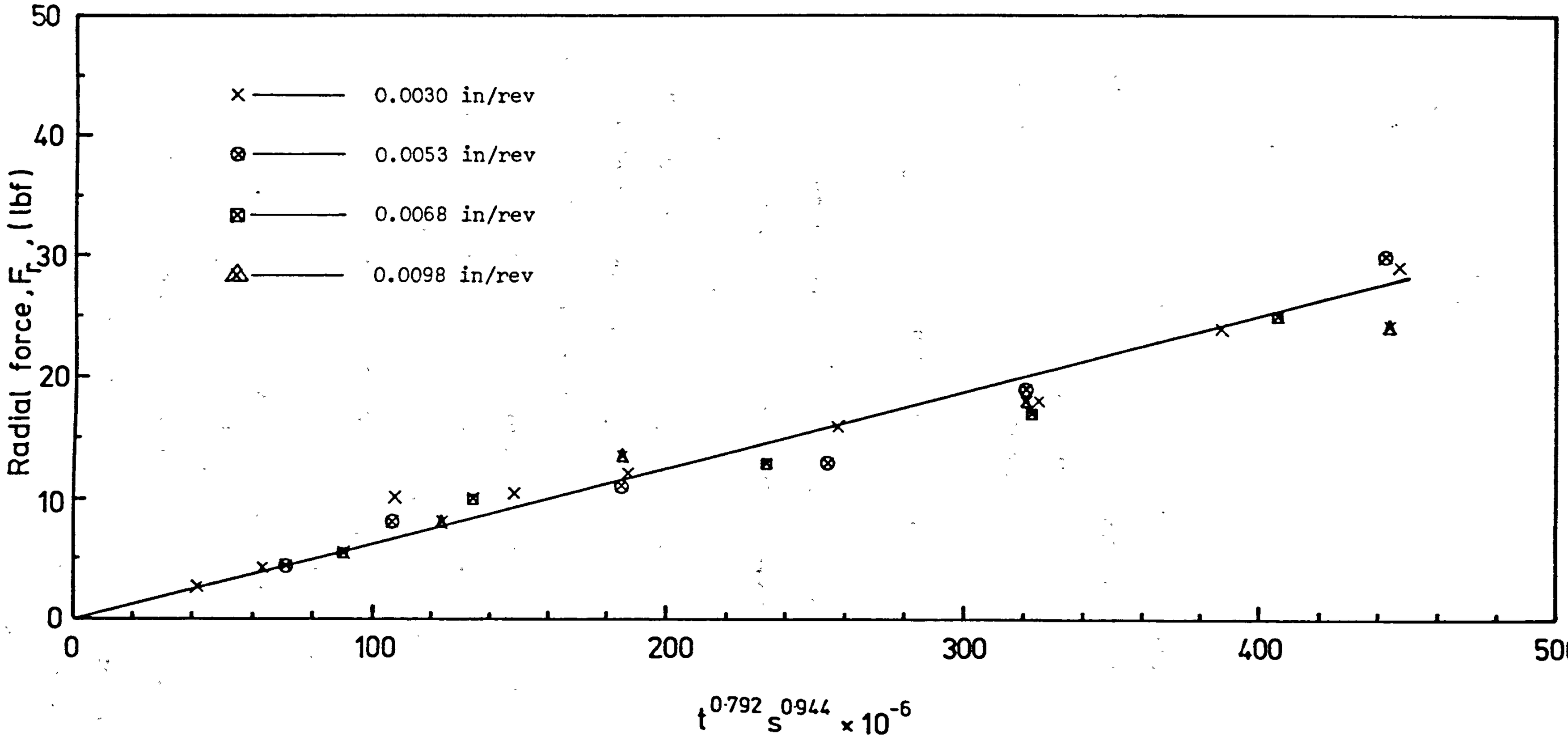

Fig 6.15 Graph of radial force versus $t^{0.792} s^{0.944}$

$$F_t = 2.292 \times 10^5 \, t^{1.077} \, s^{0.833}$$

where F_t is in lbf., t in inches and s in inches/rev.

(c) The radial cutting force can be calculated from the empirical equation (6.19)

$$F_r = 6.250 \times 10^4 \, t^{0.792} \, s^{0.944}$$

where F_r is in lbf., t in inches and s in inches/rev.

(d) Considerable scatter is observed in fitting the radial cutting force empirical equation. Its goodness of fit is inferior to that for the tangential cutting force.

6.2 RADIAL STATIC STIFFNESS OF TUNGSTEN-BUNGED BORING BAR

6.2.1. Object

(1) To determine the equivalent static stiffness of the tungsten-bunged bar in its radial direction when it is mounted on the lathe.

(2) To study the energy dissipation characteristic of the bar in the same direction.

6.2.2. Instrumentation and equipment

(1) Tungsten-bunged bar - details will be found in Section 7.1.

(2) Lathe - Model Sriov by Churchill Denhams. It will be described in more detail in Section 6.3.2.

(3) Dial indicator - made by Verdict, resolution is 0.0005"/div.

(4) Pre-calibration load cell - calibration curve is shown in Fig. 6.16 which is reproduced from Fig. 31 in thesis of Ng [3].

(5) A fixture plate with a loading device - The plate has on its back a spigot which can be gripped by the jaws of the chuck. The loading device is fixed onto the front of the plate and it consists of a metal block with a tapped hole through

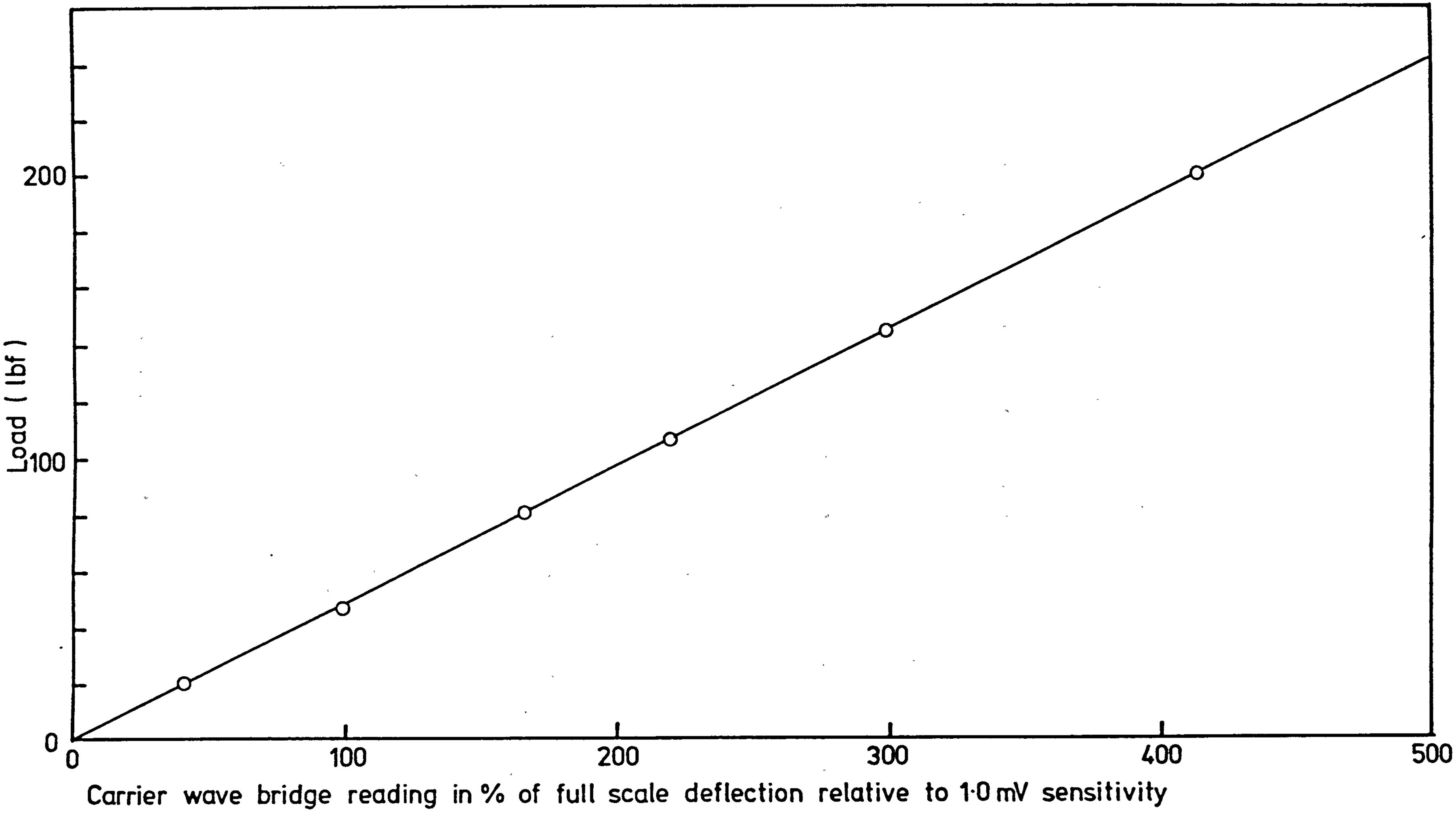

Fig 6.16 Load cell senitivity (reproduced from Fig 31 of Ref 3)

which runs a loading screw.

(6) Carrier Frequency Bridge, Philip PR9307.

6.2.3. Procedure

The tungsten-bunged bar was secured on its bar holder by means of six cap screws on the flange and the holder was bolted onto the cross-slide of the lathe in place of the toolpost and top slide. The fixture plate was clamped onto the chuck such that the loading screw has its axis horizontal. The load was applied by turning the screw which set up a compressive strain on the load cell and an equal magnitude of load would exert on the tool-tip of the dummy tool as shown in the arrangement in Fig. 6.17. The resulting deflection at the free end of the bar was measured by means of a dial indicator positioned diametrically opposite to the load cell. The loading was increased in steps of 50% fsd on the meter of the strain measuring bridge connected to the load cell. The sensitivity setting of the bridge was 1.0mV. 50% fsd corresponds to a static load of 106.55 N, since the load cell has a gain factor of 2.131 N/div which is the slope of the graph shown in Fig. 6.15. The load was increased to a maximum of 400% fsd on the bridge at 1.0mV sensitivity, which is equivalent to 852.4N. Unloading was conducted in a similar manner until zero load was reached. Deflections as indicated on the dial gauge were read at each load increment or decrement.

The above experiment was conducted with the slide at its normal working condition, i.e. there was easy clearance between the slide and the bed.

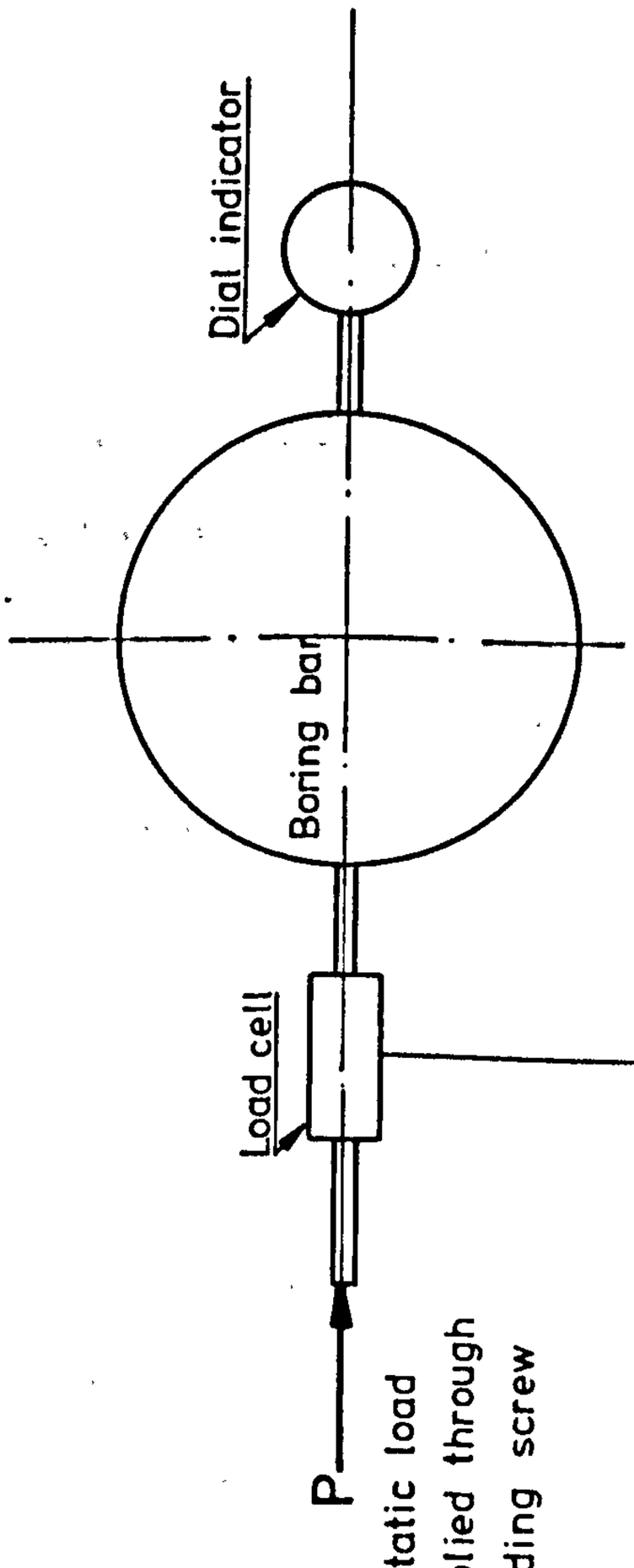

Fig 6.17 Set-up for static-load test

6.2.4. Results and discussion

Fig. 6.16 shows the calibration curve of the load cell, from which the gain factor is calculated as 2.131 N/div[3].

Fig. 6.18 illustrates the load deflection characteristic of the bar in its radial direction. Three features are apparent. First, a hysteretic loop is present indicating that there is some energy loss in the system during the cycle of loading-unloading. Since the internal hysteresis of the bar itself is too small to be of significance, which has been reported by Ng [3] and PERA [4], this energy loss is due to the lathe. Second, the load deflection curve is non-linear during loading as well as unloading. The point at which the slope changes possibly suggests the mechanism of the unlocking of frictional joints on the cross-slide. Third, the curve does not return to the origin when all the loads are removed, but instead a residual deflection is present.

To determine the equivalent radial stiffness of the bar mounted on the lathe is not a straight forward business because the graph does not have a constant slope. Nevertheless, an average value can be calculated but it must be used with caution in future. Thus from Fig. 6.18, the static stiffness in the radial direction at the free end of the bar is,

$$K_e = \frac{400\ \%\ \text{fsd}}{604\ \ \mu\text{m}} \left(\frac{2.131\ \text{N}}{1\%\ \text{fsd}}\right)$$

where the quantity in brackets is the gain factor of the load cell and simplifying,

$$K_e = 1.41\ \text{MN/m}$$

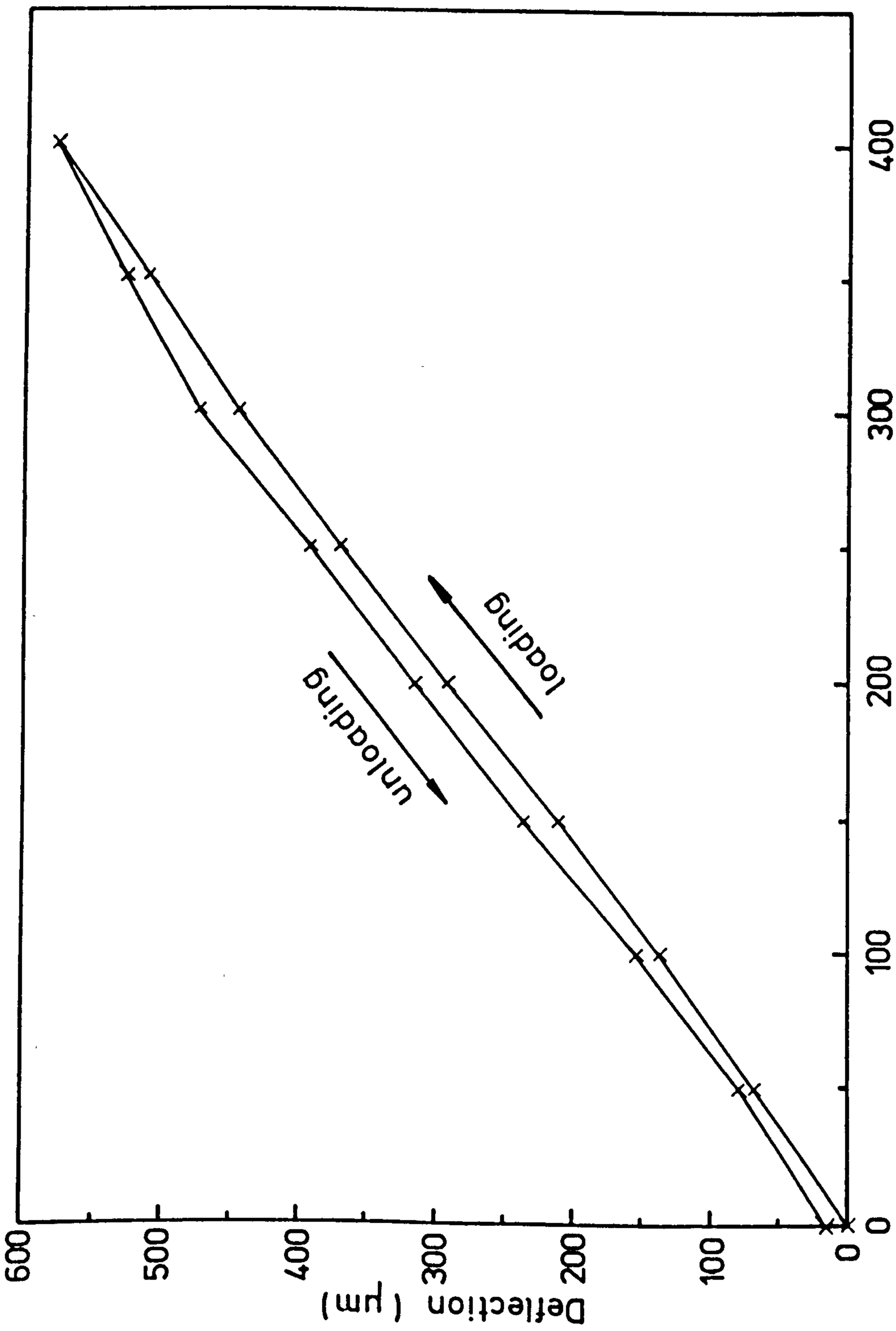

Fig 6.18 Relation between deflection at the tool tip and the percent full-scale deflection of the strain measuring bridge meter

It will be shown in Appendix A that the calculated stiffness of the bar is 1.65 MN/m using the method of Myosotis. The difference is 14.5% of the calculated stiffness.

The energy loss per cycle of loading and unloading is given by the area enclosed in the loop and from Fig 6.18 is estimated to be 15.6 mJ approximately.

6.2.5 Conclusions

1. Within the loading range of 0 to 852.4 N, the average radial stiffness of the tungsten-bunged bar is 1.41 MN/m which is 14.5% lower than the calculated stiffness.

2. The load deflection curve is made up of a number of linear segments pieced together, each having a slightly different slope, hence stiffness. The change in stiffness at some points in the loading or unloading is thought to be due to the unlocking of frictional joints in the cross-slide of the lathe.

3. The relative movements in these frictional joints bring about an energy dissipation, the value of which is 15.6 mJ per cycle for the loading range between 0 and 852.4 N.

6.3 "BELL-MOUTH" ERROR

6.3.1. Object

The experiment was conducted with the tungsten-bunged bar and the bore is concentric with the axis of rotation.

1. To study the general features of the bell-mouth error.
2. To compare the predicted bell-mouth errors with the experimentally measured values.

6.3.2. Instrumentation and equipment

1. Tungsten-bunged bar - details will be found in Section 7.1.
2. Boring tool - Three boring tools will be used:
   (a) Sandvik Coromant circular shank boring tool, tool no. 140 - $\frac{3}{8}$" dia. This is a left-handed tool with a brazed on carbide-tip. Its tool geometry is identical to that which was described in Section 6.1.2 and Fig. 6.1, except that the tool shank is aligned at an angle of 59° to the longitudinal axis of the bar. The nose radius of the tool is 0.010".
   (b) Same as (a) with the exception of the tool geometry which is shown in Fig. 6.19. The nose radius is 0.030". This particular geometry is being used in Rolls Royce Aeronautic factory at Derby.
   (c) Same as (b) except that the nose radius is 0.010".
3. Lathe - Model Sriov by Churchill Denhams. It has a maximum swing of 22 in (559 mm) and a bed length of 8ft.6in. (2.59 mm). The speed range is from 48 - 2000 rpm which can be varied continuously. The feed range is from 0.0011"/rev (0.03mm/rev) to 0.065"/rev. (1.59 mm/rev). The cross-slide was removed and in its place was secured a boring bar holder by means of four bolts.

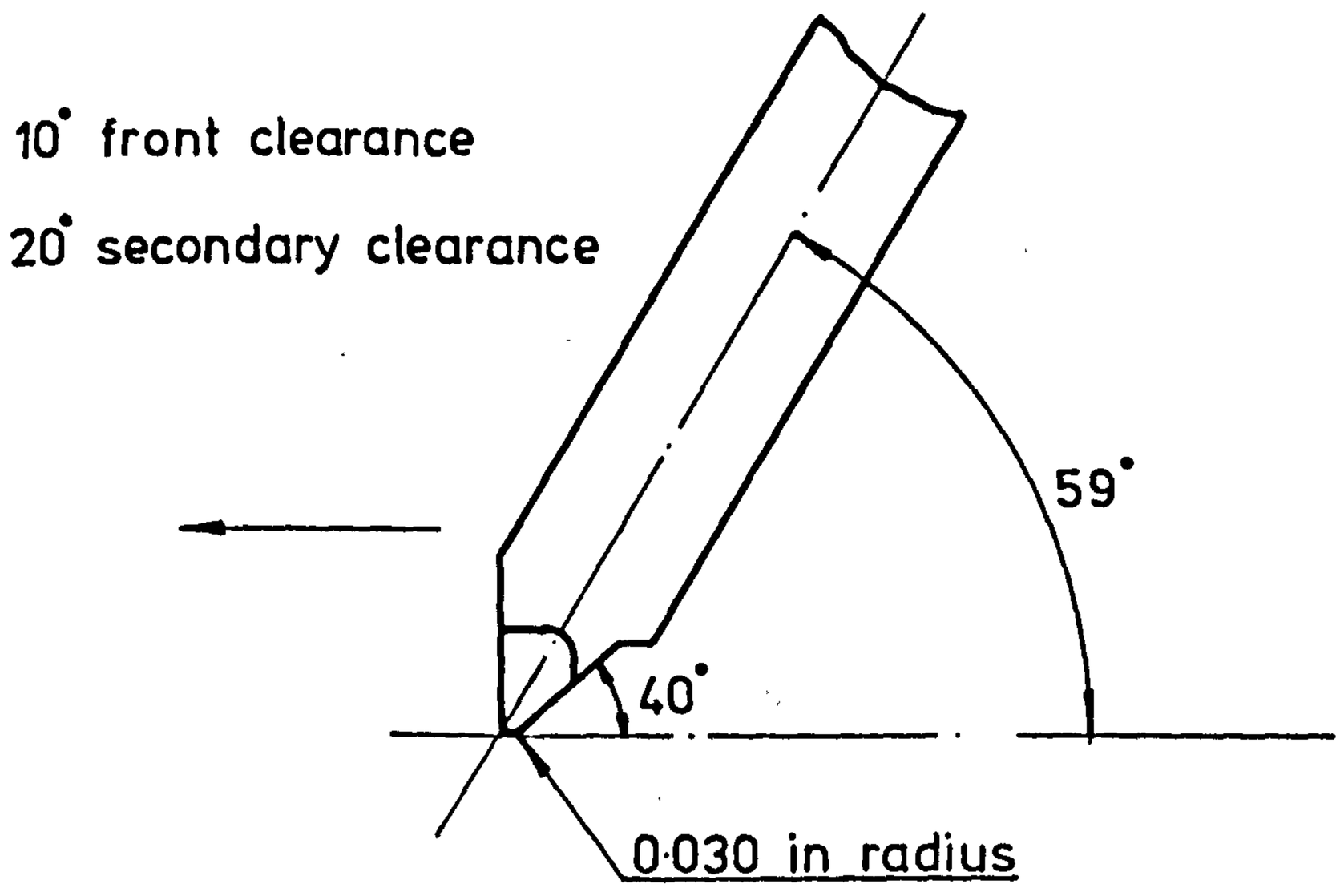

Fig 6.19 Geometry of Rolls Royce tool, designated as the R tool

4. Workpiece - Two types of workpiece will be used:

(a) Steel BS970 : 955 - EN8, which is a 40' normalized carbon steel. The mechanical properties are:

(i) tensile strength - 35 tons/sq.in.min.

(ii) yield stress - 18 tons/sq.in.min.

(iii) elongation - 17% min

(iv) Brinell hardness - 152/207. The average for this batch is 197.

The dimensions of the workpiece are: 4½" O.D. (110 mm), 3" I.D. (75 mm) and a nominal thickness of 1" (25 mm).

(b) Alloy steel supplied from Rolls Royce Aeronautic Ltd., of which the specification code is RR S/HBH steel. It is a 3% chrome molybdenum nitriding steel which has an average Brinell hardness of 395. The general dimension of the workpiece is dictated by the shapes and sizes of the supplies which are rejects failing to meet the required dimensional specifications of the factory. For this batch, the general dimensions are: 4½" O.D. (110 mm), 3" to 3½" I.D. (75 mm to 90 mm) and a nominal thickness of 2" (50 mm).

5. Talysurf 3 - a surface finish measuring equipment by Taylor-Hobson. The stylus used for this particular measurement has a tip radius of 0.0001".

6.3.3. Procedure

Machining tests were conducted on four workpieces: two of EN8 steel and two of alloy steel as specified in Section 6.3.2. The machining conditions will be given in Section 6.3.4., the section of Results and Discussion. The boring bar used was the tungsten-bunged bar optimally tuned with a main slug of 25.299 mm in diameter. No chatter marks were observed on the

cut surface of the workpiece and so the steady-state machining was maintained.

The surface finish of the workpieces was measured using the Talysurf 3. A trace of the surface profile was also obtained while the stylus was made to run across the cut surface at the tool entry region so that any bell-mouth error would be recorded.

In order to calculate the predicted bell-mouth error, it is necessary, as will be explained in Section 6.3.4., that the radial cutting force at the given cutting condition be known. For EN8 steel and cutting with the cutting tool the geometry of which is as in Fig. 6.1., the business of finding the radial cutting force is simple because the force is readily obtained from equation (6.19). However, the radial cutting force that may arise during the machining of the alloy steel has to be determined by means of an experiment which requires the use of the dynamometer. The experiment is very similar to that described in Section 6.1 with the following exception:- since only the radial force at some particular cutting condition was required, the cutting was done at that condition only and the radial force was calculated.

6.3.4. Results and Discussion

1. Work specimen and surface finish

Four workpiece specimens were obtained at the following conditions:-

Specimen 1 - EN8 steel; nose radius 0.010"; depth of cut 0.050"; feed rate 0.0138"/rev., cutting speed 600 ft/min.

Specimen 2 - EN8 steel; nose radius 0.010"; depth of cut 0.060"; feed rate 0.0104"/rev., cutting speed 600 ft/min.

Specimen 3 - RRS/HBH steel; nose radius 0.010"; depth of cut 0.010"; feed rate 0.0104"/rev., cutting speed 200 ft/min.

Specimen 4 - RRS/HBH steel; nose radius 0.030"; depth of cut 0.010"; feed rate 0.0069"/rev., cutting speed 200 ft/min.

Their respective surface finishes measured in CLA are 5.5, 3.2, 3 and 2 μm.

2. Radial cutting force

The radial cutting force that may arise in specimen 1 is calculated from equation (6.19), i.e.

$$F_r = 6.250 \times 10^4 \times 0.050^{0.792} \times 0.0138^{0.944}$$

$$= \underline{102.2 \text{ lbf}}.$$

Similarly for specimen 2 the radial force is

$$F_r = 6.250 \times 10^4 \times 0.060^{0.792} \times 0.0104^{0.944}$$

$$= \underline{90.4 \text{ lbf}}.$$

Also from separate force measurement tests, the radial cutting force for specimen 3 was measured to be 34.2 lbf. and for specimen 4 was 24.5 lbf.

3. Graph of profile

Figures 6.20 to 6.23 show the respective traces of the surface profiles of specimens 1, 2, 3, and 4. The magnification factors in the vertical and horizontal axis are 1000 and 20 respectively. It is immediately obvious

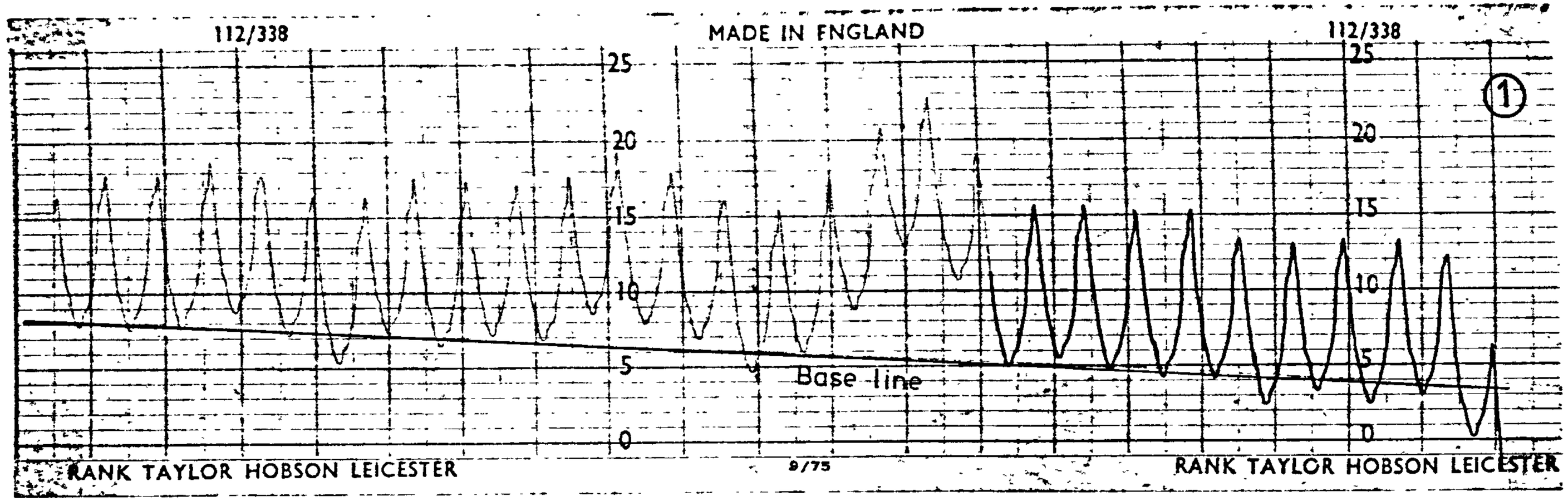

Fig 6.20 Trace of surface profile for specimen 1

Magnification factors: x 20 horizontal, x 1000 vertical

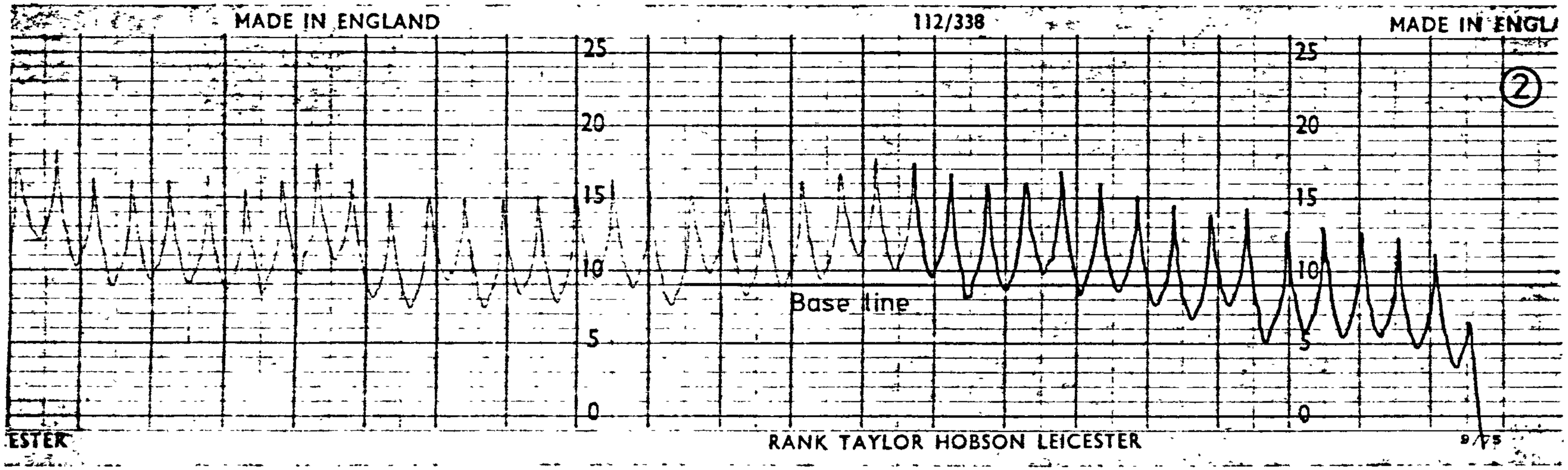

Fig 6.21 Trace of surface profile for specimen 2

Magnification factors: x 20 horizontal, x 1000 vertical

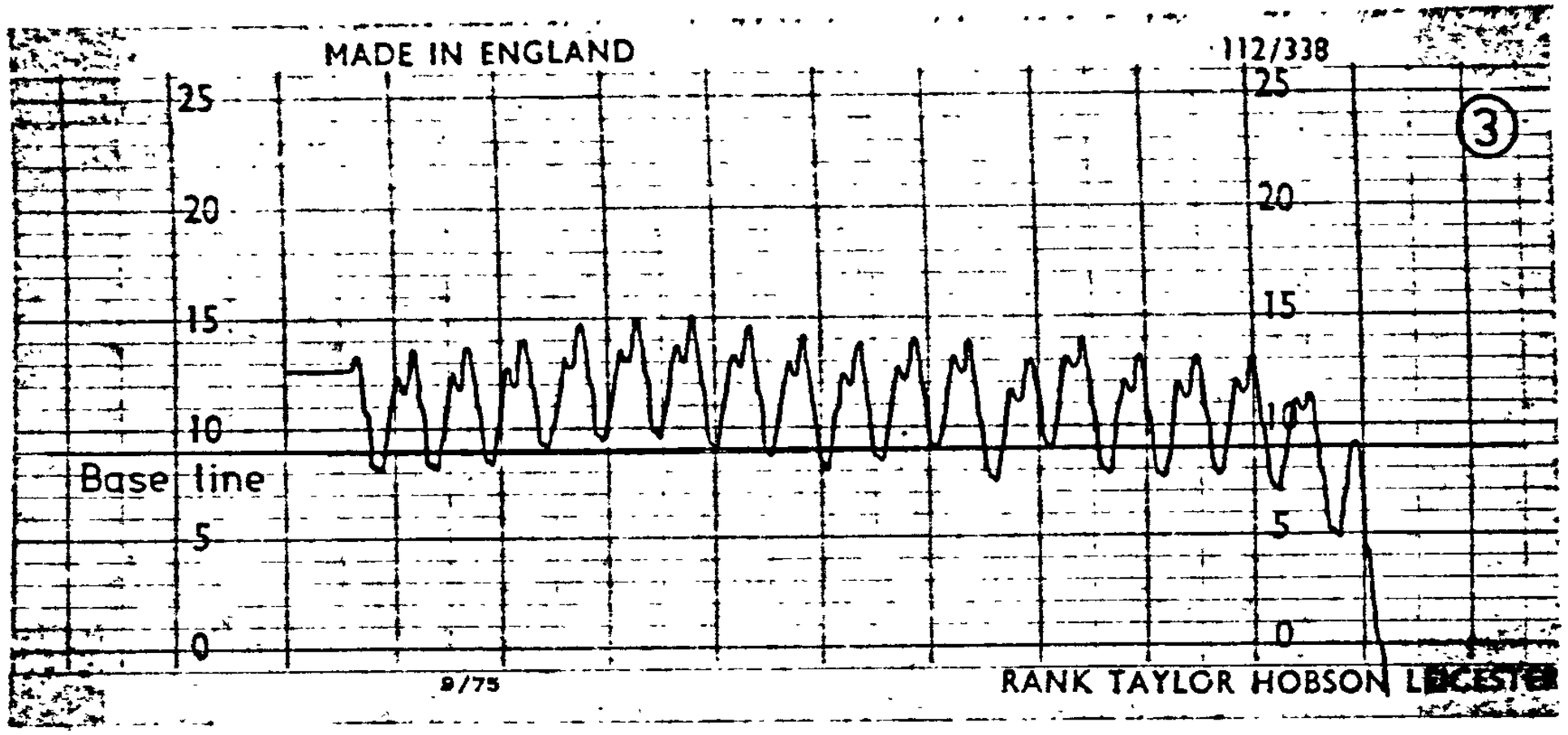

Fig 6.22 Trace of surface profile for specimen 3

Magnification factors: x 20 horizontal, x 1000 vertical

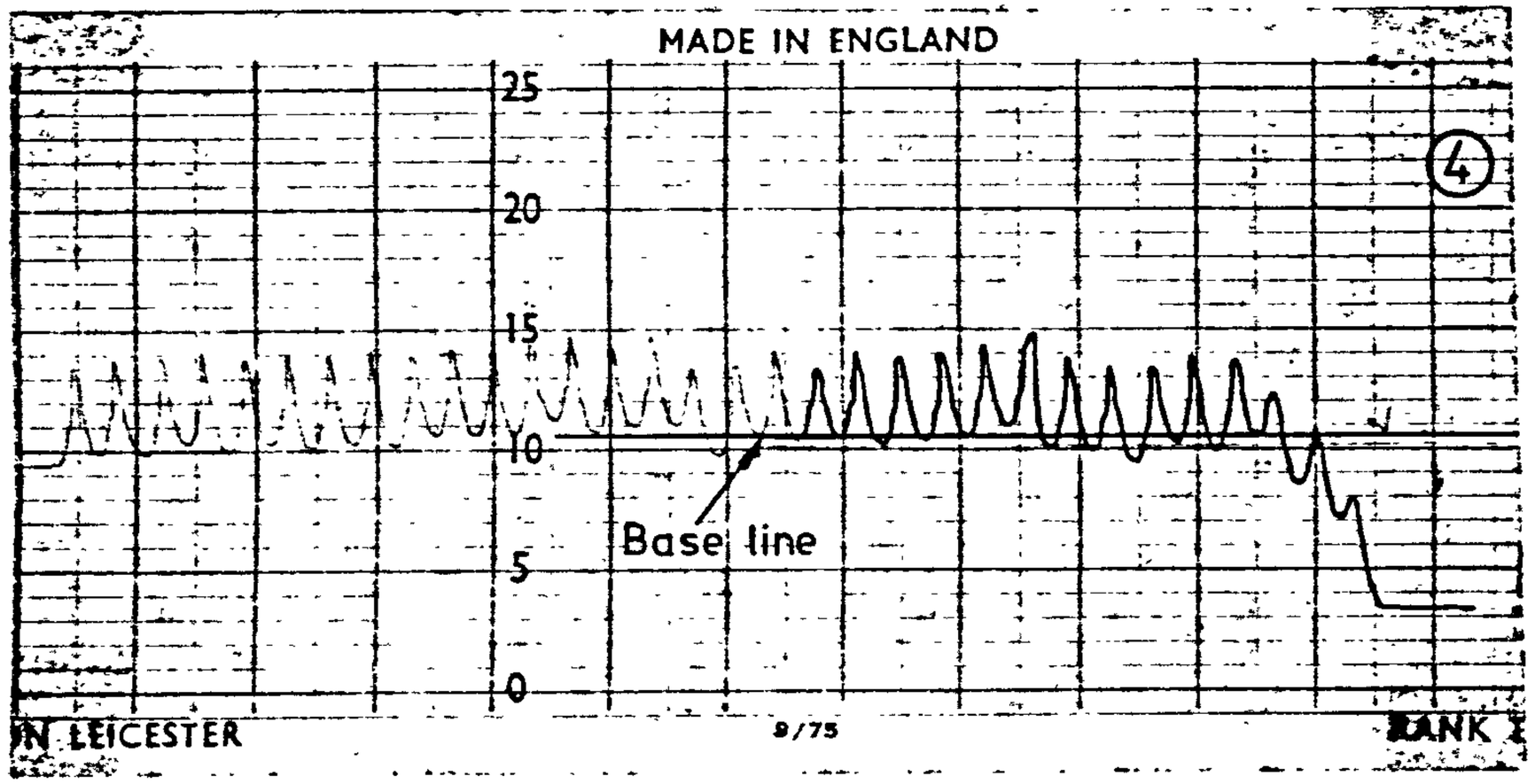

Fig 6.23 Trace of surface profile for specimen 4

Magnification factors: x 20 horizontal, x 1000 vertical

that bell-mouth error indeed occurred on all four specimens.

To facilitate a quantitative comparison between the theory as developed in Section 3.4.1 and the experimental results as shown in Figs. 6.20 to 6.23, the following procedure is thought necessary. Firstly from equation (3.14),

$$X_n = X_1 + \frac{X_1^2 \left(\frac{\mu}{t_o}\right)\left\{1 - \left[X_1\left(\frac{\mu}{t_o}\right)\right]^{n-1}\right\}}{\left\{1 - X_1\left(\frac{\mu}{t_o}\right)\right\}}$$

and equation (3.15)

$$X_\infty = X_1 + \frac{X_1^2\left(\frac{\mu}{t_o}\right)}{\left\{1 - X_1\left(\frac{\mu}{t_o}\right)\right\}}, \quad \text{provided that } \frac{X_1}{t_o} < 1, \text{ which is the case:}$$

Secondly, equation (3.14) is subtracted from equation (3.15) to give

$$X_\infty - X_n = \frac{X_1^2 \frac{\mu}{t_o}}{\left\{1 - X_1\left(\frac{\mu}{t_o}\right)\right\}}\left[X_1\left(\frac{\mu}{t_o}\right)\right]^{n-1}$$

from which

$$r_n = \frac{X_\infty - X_n}{X_1} = \frac{X_1\left(\frac{\mu}{t_o}\right)^n}{1 - X_1\left(\frac{\mu}{t_o}\right)}$$

In particular, when n = 1,

$$r_1 = \frac{X_\infty - X_1}{X_1} = \frac{X_1\left(\frac{\mu}{t_o}\right)}{\left\{1 - X_1\left(\frac{\mu}{t_o}\right)\right\}}$$

and the ratio of the successive r's will be

$$\frac{r_n}{r_{n-1}} = \ldots = \frac{r_3}{r_2} = \frac{r_2}{r_1} = \left(\frac{X_1}{t_o}\mu\right)$$

It follows that

$$\frac{r_n}{r_1} = \left(\frac{X_1}{t_o}\mu\right)^{n-1} \qquad (6.21)$$

in which $X_1 = \dfrac{\beta_r t_o s_o}{(1 + \beta_r s_o)}$ as equation (3.7) and

$$\beta_r = \frac{Rr}{K_r} = \frac{Fr}{t_o s_o K_r} \qquad (6.21a)$$

The radial forces F_r have been determined in the last section, t_o and s_o are the depth of cut and feed rate, both of which are known for each specimen; and the radial static stiffness K_r has been determined in Section 6.2.

Finally, the surface profiles from Figs. 6.20 to 6.23 have to be converted to a form compatible with equation (6.21). This is carried out as follows:

From the definition of r_n, $r_n = \dfrac{X_\infty - X_n}{X_1}$ and

so $r_1 = \dfrac{X_\infty - X_1}{X_1}$. It follows that the ratio $\dfrac{r_n}{r_1} = \dfrac{(X_\infty - X_n)}{(X_\infty - X_1)}$

(6.22)

Both $(X_\infty - X_n)$ and $(X_\infty - X_1)$ can be measured from the figures 6.20 to 6.23. Take, for example, Fig. 6.20. A base line corresponding to X_∞ is drawn averaging the troughs at large n. The amount of deviation of each successive trough from the base line is then measured. The first trough gives $(X_\infty - X_1)$ and the subsequent troughs give $(X_\infty - X_n)$ as n is increased from 2 onwards. Finally, the ratio r_n is determined by using equation (6.22).

The following tabulations refer to the four specimens and include entries calculated from Figs. 6.20 to 6.23 as well as entries calculated from equation (6.21) which provides the theoretical $\frac{r_n}{r_1}$ values. It is assumed that the overlapping factor $\mu = 1$. The radial static stiffness of the tungsten-bunged bar is 1.41 MN/m as obtained from Section 6.2. To calculate $\frac{X_1}{t_o}$ in equation (6.21) we need to use equation (3.7) and (6.21a).

(a) Specimen 1 - The graph of profile is shown in Fig. 6.24a in which the entries in the second last column are indicated by crosses and entries in the last column are joined by a smooth curve.

Cut no. n.	$(X_\infty - X_n)$ x 1000 mm.	$\frac{(X_\infty - X_n)}{(X_\infty - X_1)}$	$r_n = \left[\frac{X_1}{t_o}\mu\right]^{n-1}$
1	7.2	1	1
2	1.8	0.25	0.203
3	3.0	0.42	0.41
4	1.6	0.22	0.008
5	4.0	0.56	0.002
6	0.7	0.10	0
7	1.0	0.14	0
8	0.4	0.06	0
9	-0.8	-0.11	0
10	0.3	0.04	0

(b) Specimen 2 - The graph is shown in Fig. 6.24b.

Cut no. n.	$(X_\infty - X_n) \times 1000$ mm	$\frac{(X_\infty - X_n)}{(X_\infty - X_1)}$	$r_n = \left[\frac{X_1}{t_o}\mu\right]^{n-1}$
1	11.2	1	1
2	8.6	0.77	0.158
3	6.8	0.61	0.025
4	7.1	0.63	0.004
5	6.3	0.56	0
6	7.7	0.69	0
7	2.6	0.23	0
8	4.6	0.41	0
9	2.7	0.24	0
10	0.8	0.07	0

(c) Specimen 3 - The graph is shown in Fig. 6.24c.

Cut no. n	$(X_\infty - X_n) \times 1000$ mm	$\frac{(X_\infty - X_n)}{(X_\infty - X_1)}$	$r_n = \left[\frac{X_1}{t_o}\mu\right]^{n-1}$
1	8.2	1	1
2	3.9	0.48	0.298
3	2.1	0.26	0.089
4	2.6	0.32	0.026
5	2.1	0.26	0.008
6	0	0	0.002
7	2.7	0.33	0.001
8	0	0	0
9	0.8	0.10	0
10	1.2	0.15	0

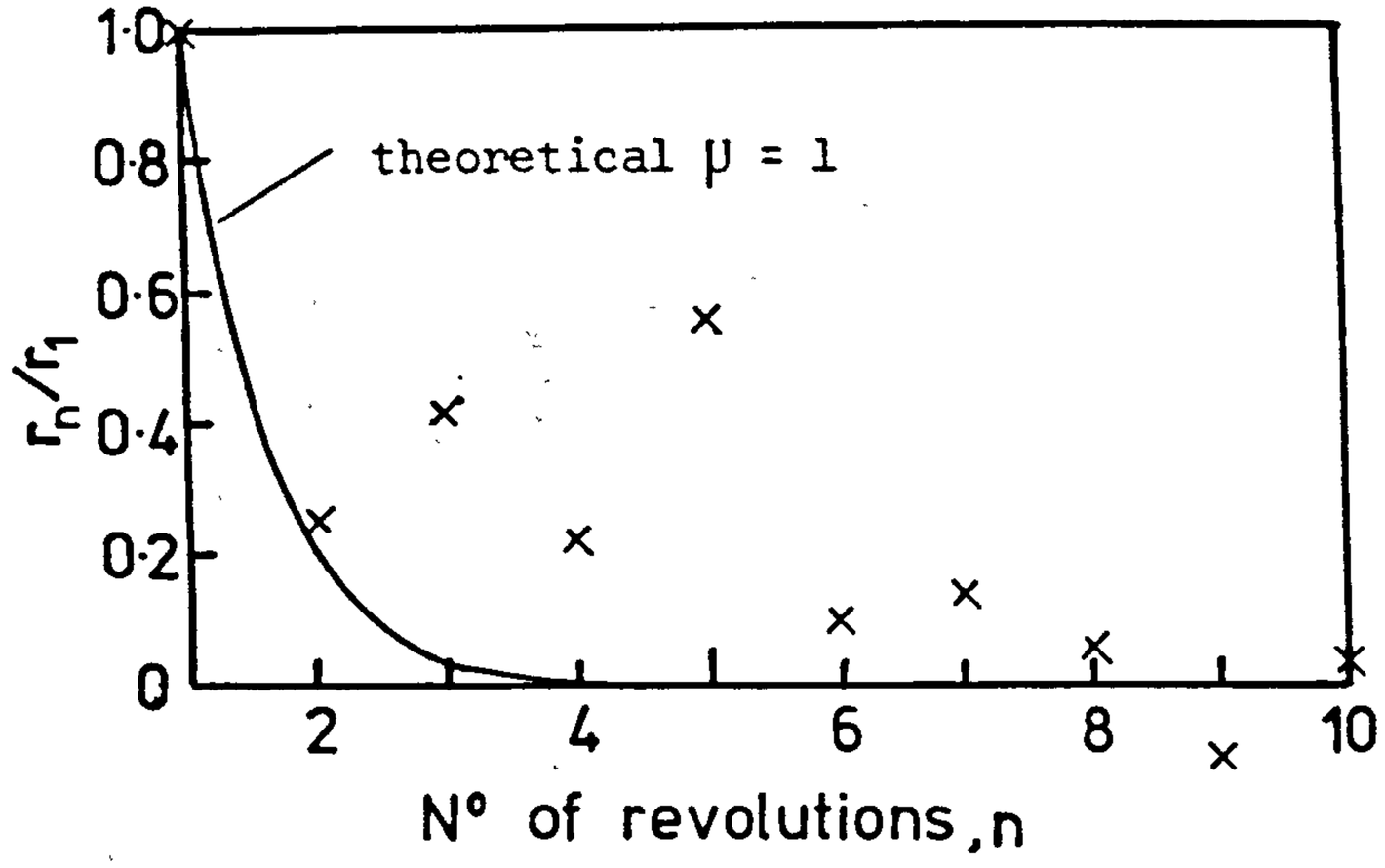

a) Specimen No 1

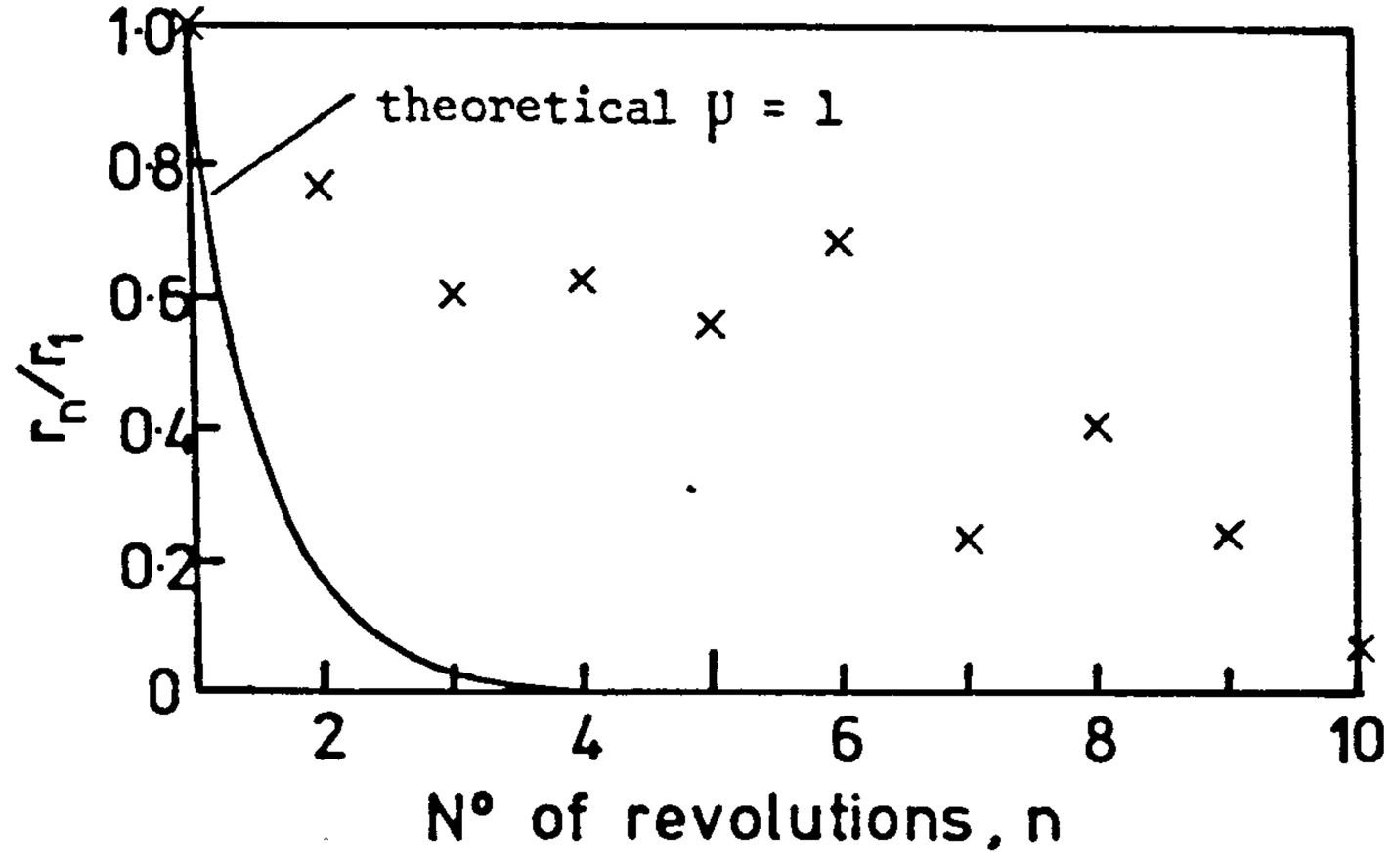

b) Specimen No 2

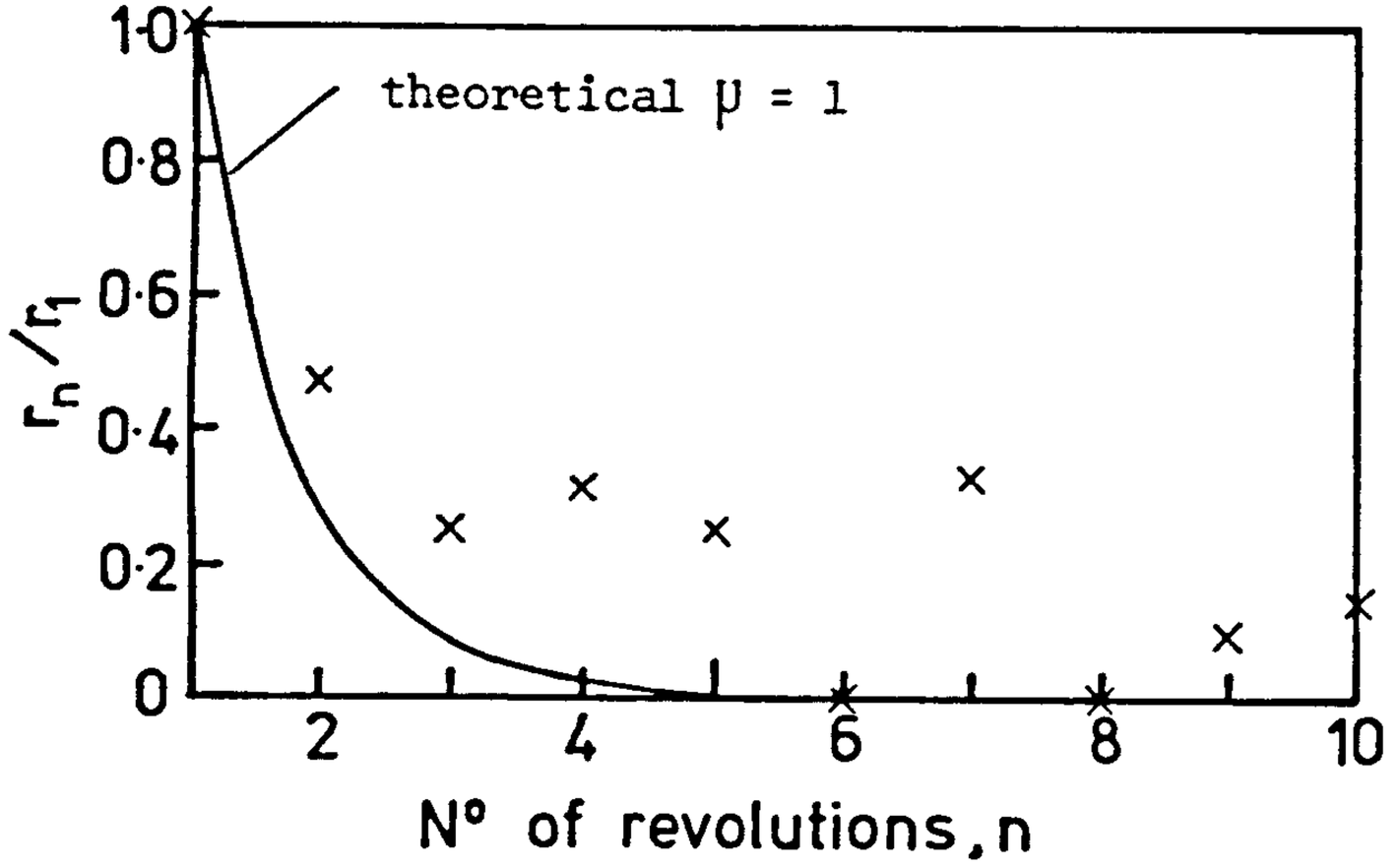

c) Specimen No 3

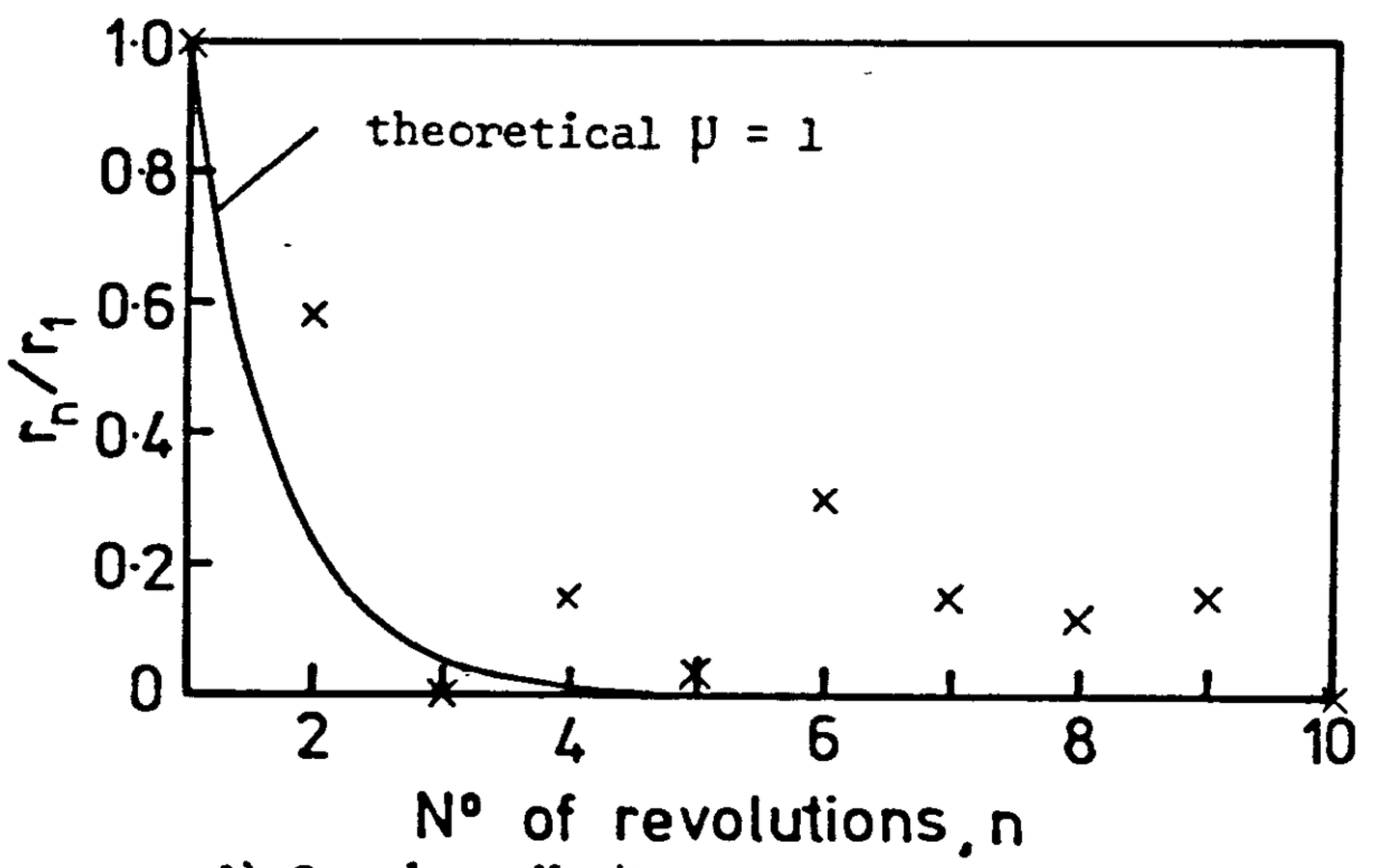

d) Specimen No 4

Fig 6.24 Graphs of profiles for the four specimens

(d) Specimen 4 - The graph of profile is shown in Fig. 6.24d.

Cut no. n	$(X_\infty - X_n) \times 1000$ mm	$\frac{(X_\infty - X_n)}{(X_\infty - X_1)}$	$r_n = \left[\frac{X_1}{t_o}\mu\right]^{n-1}$
1	6.7	1	1
2	3.9	0.58	0.233
3	0	0	0.054
4	1.0	0.15	0.013
5	0.2	0.03	0.003
6	2.0	0.30	0.001
7	1.0	0.15	0
8	0.8	0.12	0
9	-1.0	-0.15	0
10	0	0	0

From the four diagrams in Figs 6.24, it is obvious that the agreement between the theory and the results is very poor. The theory always predicts a sharper rate of decrease in r_n as the number of cuts n increases. There are two different causes. First, the theory as developed in Section 3.4.1 is very crude in that the overlapping factor μ is not an accurate representation of the real situation. It was also said that μ cannot exceed unity. Referring to Figs 6.24, if μ were made to exceed unity, the theoretical curve would have fitted the experimental points better. However, $\mu > 1$ does not seem to stand to reason. Second, the experiment design itself may possess some inherent errors, which renders the calculated experimental points suspicious. It is remembered that in an effort to measure $(X_\infty - X_n)$,

a base line is required to be drawn across all the troughs except for those when n is small. Drawing this line is highly arbitrary and this is one possible source of error. Another possible source of error stems from the nature of the cutting process and of the surface measuring equipment. It is true that radial force can be calculated by means of the equation (6.19) or measured from an experiment designed for that purpose. However, the instantaneous value of the radial force may vary up to $\pm$ 1 lbf or even more simply because the metal being cut is non-homogeneous. Taking an error bound of $\pm$ 1 lbf, we can show that it will result in a deflection on the tool tip of,

$$\pm \frac{1 \times 4.448 \times 39.37}{1.41 \times 10^6} = \pm 1.242 \times 10^{-4} \text{ in}$$

which in metric unit is $\pm$ 3.155 x 10^{-3}mm. When magnified a thousand times on the trace, it gives a deviation of $\pm$ 3.155 mm which is of quite a significant proportion compared with the entries in the second column of the tables.

6.3.5 Conclusions

(1) The experiments confirm the existence of the bell-mouth error that occurs in the first few revolutions of cut on the workpiece.

(2) The theory as developed in Section 3.4.1 can only predict the general trend the error takes but is not able to provide a quantitative prediction.

(3) The attempt to measure bell-mouth errors is complicated by:-

(i) the inability to determine the instantaneous value of radial cutting force at the position of profile measurement, and

(ii) the fact that a small error in the radial force will be magnified to produce a considerable shift on the profile trace and hence a large scatter is introduced on a profile graph such as Figs. 6.24.

6.4. "COPYING" ERROR

6.4.1 Object

(1) To study the "copying" error in the machining of EN8 steel with the tungsten-bunged boring bar.

(2) To compare the predicted "copying" error with that obtained from experiments.

6.4.2 Instrumentation and equipment

(1) Tungsten-bunged bar - The bar is optimally tuned with a main slug of 25.299 mm in diameter. Details can be found in Section 7.1.

(2) Boring tool - This is the same as that described in 2(a) of Section 6.3.2.

(3) Lathe - This is the same as that described in Section 6.3.2.

(4) Workpiece - The material is EN8 steel, the details of which are given in Section 6.3.2.

(5) Dial indicator by Verdict, with resolution of 0.0005"/div. Also a support stand with a magnetic base was needed.

6.4.3. Procedure

The main aim of this experiment is to test the goodness of fit of equation (3.25) in which the "copying" error u is related to a parameter K as,

$$u = \frac{1}{1 + K} \qquad (3.25)$$

$$\text{where } K = \frac{K_r t^{(1-a)}}{a A_r s^b} \qquad (3.26)$$

According to equation (3.24a),

$$u = \frac{e_f}{e_r} \qquad (3.24a)$$

where e_f = eccentricity of the finished bore

and e_r = eccentricity of the pre-finished bore

The two eccentricity values, e_f and e_r, are the objects to be measured.

In designing the experiment, a rough check using equations (3.25) and (3.26) indicates that u is likely to be very small and so from equation (3.24a) e_r has to be reasonably large in order that e_f becomes measurable. Nevertheless, a large e_r in comparison with the mean depth of cut t will violate the assumption made in arriving at the equation (3.25). The assumption is that the ratio e_r/t is reasonably less than unity. Furthermore, the mean depth of cut t cannot be in excess of the limiting depth of cut at which the chatter sets in, which in turn restricts the range of e_r which can be used in the experiment.

In view of this, the initial eccentricity was chosen to be 0.020" nominal while the exact value was measured on each workpiece during the experiment. The cutting conditions adopted are illustrated in

the next section and the cutting speed was 450 ft/min on all workpieces. There are five stages in which the experiment was conducted:-

(1) To ensure a circular concentric bore at the start, the workpiece that was held in a three-jaw chuck was bored through with a short rigid boring bar. This bar shared the same holder as, but was mounted oppositive to, the tungsten-bunged bar.

(2) A shim of thickness 0.030" - how this was worked out is shown in the next section - was inserted in between the outside diameter of the workpiece and one of the jaws. This would produce an eccentricity, e_r, of 0.020" nominal on the bore.

(3) The actual eccentricity, e_r, was measured by means of a dial indicator set up on the stand with a magnetic base, hence providing a secured foundation for relative measurements. The first reading on the dial face was taken when the stylus rested at a point on the bore in line with the jaw with the inserted shim. The second reading was taken after the chuck was rotated through 180°. The actual eccentricity, e_r, is then half the difference of the two readings.

(4) The bar holder was rotated through 180° such that the tungsten-bunged bar was in position for cutting. The cutting was performed according to the conditions adopted.

(5) To measure the eccentricity, e_f, on the finished bore, stage (3) was repeated.

6.4.4 Results and Discussion

(1) Determining the thickness of the shim

Fig. 6.25a shows a schematic diagram of a circular workpiece mounted on the jaws. O is the centre of rotation of the chuck. C is the centre of the workpiece relative to its external circumference. The amount of eccentricity is e and the outer radius of the workpiece is r. R is the radial distance of the jaw tip from the centre of rotation O.

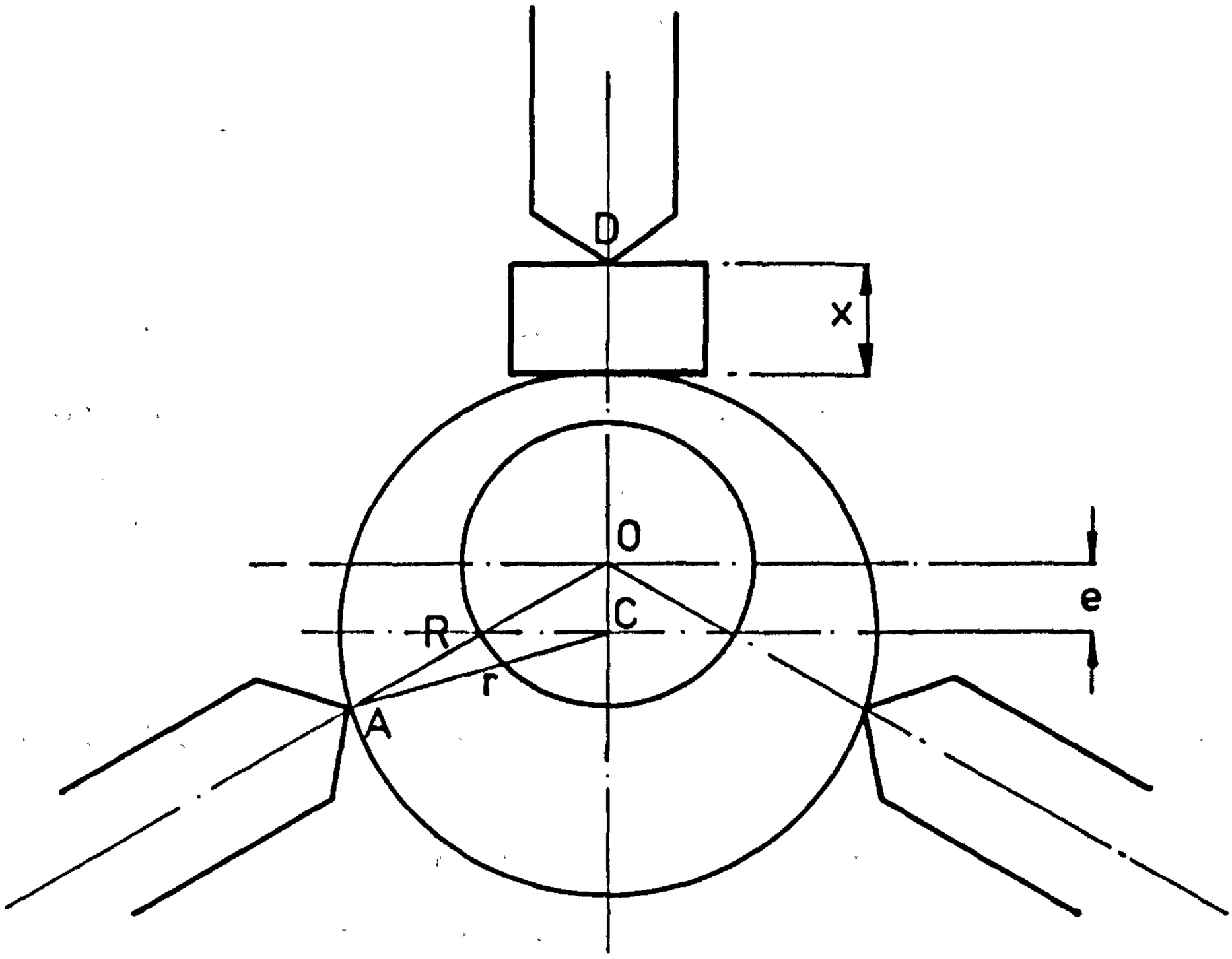

Fig 6.25a Determining the thickness x of the shim for an eccentricity e

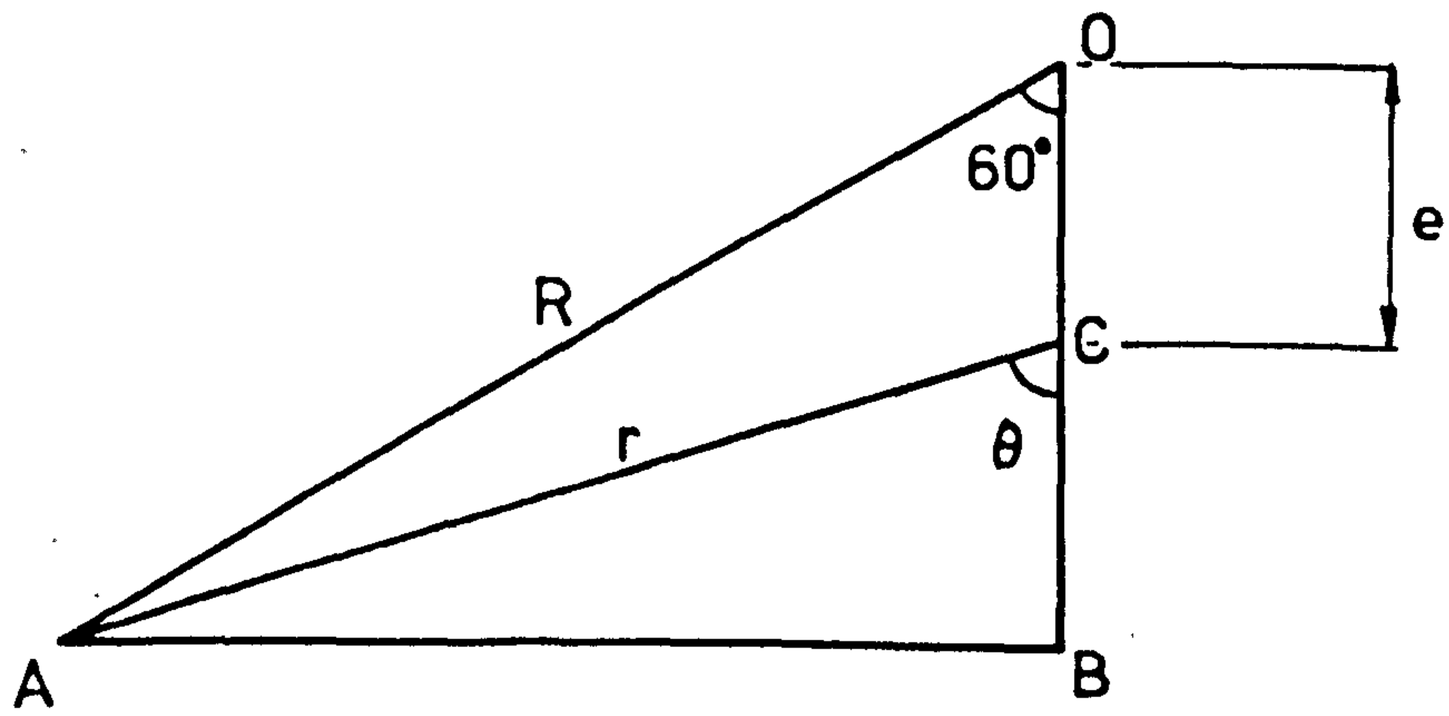

Fig 6.25b Enlarged view of the triangle OCA in Fig 6.25a

x is the thickness of the shim to be determined.

From Fig. 6.25a, DO + OC = R + e = r + x.

from which $x = R + e - r$ (6.23)

Fig. 6.25b is an enlarged view of the triangle OCA in Fig. 6.25a. OC is extended to meet a perpendicular from A at B. Referring to Fig. 6.25b, and using the cosine formula,

$$R^2 = e^2 + r^2 - 2er \cos (180^\circ - \theta)$$

which gives

$$R^2 = e^2 + r^2 + 2er \cos \theta \quad (6.24)$$

But CB = OB - OC, and CB = r cos θ, OB - OC = R cos 60° - e

Hence, $r \cos \theta = R \cos 60^\circ - e = \frac{R}{2} - e$

Substitute this into equation (6.24) $R^2 = e^2 + r^2 + 2e\ (\frac{R}{2} - e)$

$$= r^2 - e^2 + eR$$

Since $r = \frac{d}{2}$ where d is the outside diameter of the workpiece, then

$$R^2 = (\frac{d}{2})^2 - e^2 + eR$$

from which the following quadratic equation is obtained,

$$R^2 - eR + (e^2 - \frac{d}{4}^2) = 0$$

The solution for R is

$$R = \frac{e \pm \sqrt{e^2 - 4\ (e^2 - \frac{d^2}{4})}}{2}$$

which can be simplified to

$$R = \frac{e + \sqrt{d^2 - 3e^2}}{2}$$

where the negative sign before the radical is dropped.

Substitute this value of R into equation (6.23), the thickness of the shim is

$$x = \frac{e + \sqrt{d^2 - 3e^2}}{2} + e - \frac{d}{2}$$

$$\text{i.e. } x = \frac{3e - d + \sqrt{d^2 - 3e^2}}{2} \qquad (6.25)$$

In this case, diameter of the workpiece d = 4.501" and the eccentricity required is e = 0.020". Using equation (6.25), the resulting thickness of the shim is

$$x = \frac{3 \times 0.020 - 4.501 + \sqrt{4.501^2 - 3 \times 0.020^2}}{2}$$

$$= \underline{0.0299"}$$

(2) Comparing experimental results with theory

To facilitate comparison between the experimental results and the theoretical predictions, the former was converted as follows. Corresponding to each depth of cut t and feed rate s, the parameter K was calculated using equation (3.26) and K_r = 1.41MN/m. The theoretical "copying" error u was then determined using equation (3.25). The experimental "copying" error u was obtained from equation (3.24a) i.e.

$$u = \frac{e_f}{e_r}$$

The following table illustrates the results and the associated conversions.

		Experimental			Theoretical	
t(in	s(in/rev)	e_r(in)	e_f(in)	$u = \frac{e_f}{e_r}$	u	K
0.050	0.0044	0.0205	0.0014	0.0683	0.0640	14.63
0.050	0.0069	0.0194	0.0016	0.0825	0.0946	9.57
0.050	0.0104	0.0201	0.0025	0.1244	0.1334	6.50
0.060	0.0044	0.0210	0.0014	0.0667	0.0567	16.63
0.060	0.0069	0.0208	0.0020	0.0962	0.0914	9.94
0.060	0.0104	0.0205	0.0025	0.1220	0.1291	6.75

Fig. 6.26 shows a curve of the "copying" error u as a function of the parameter K. The experimentally determined u's were also drawn as crosses, the values of which correspond to the entries in the third last and last columns of the table. It can be observed from this figure that for K > 6, the formula of "copying error

$$u = \frac{1}{1 + K} \qquad (3.25)$$

conforms with the experimental evidence. It is, however, dangerous to speculate that for K < 6, equation (3.25) still holds. As have been explained in Section 6.4.3. there are considerable difficulties to design an experiment to operate in the region of 0 < K < 6, mainly because of the possible onset of chatter if, in an effort to decrease K, the radial static stiffness K_r is lowered or if a harder material and hence higher A_r is used. Any attempt to lower K will inevitably bring about a higher radial force F_r, and there is a limit to which this can be increased. Fortunately, for most practical situations, K is unlikely to be less than 6.

6.4.5. Conclusions

(1) The experiments confirm the existence of the "copying" error that occur on a bore with some initial eccentricity.

(2) The "copying" error can be predicted by using equation (3.25),

$$u = \frac{1}{1 + K}$$

where $K = \frac{K_r t^{(1-a)}}{a A_r s^b}$, when the condition K >6 is met.

(3) When K < 6, equation (3.25) must be used with caution since the experiments do not cater for this possibility. Fortunately, K < 6 hardly arises in most practical machining situations in which there is no chatter.

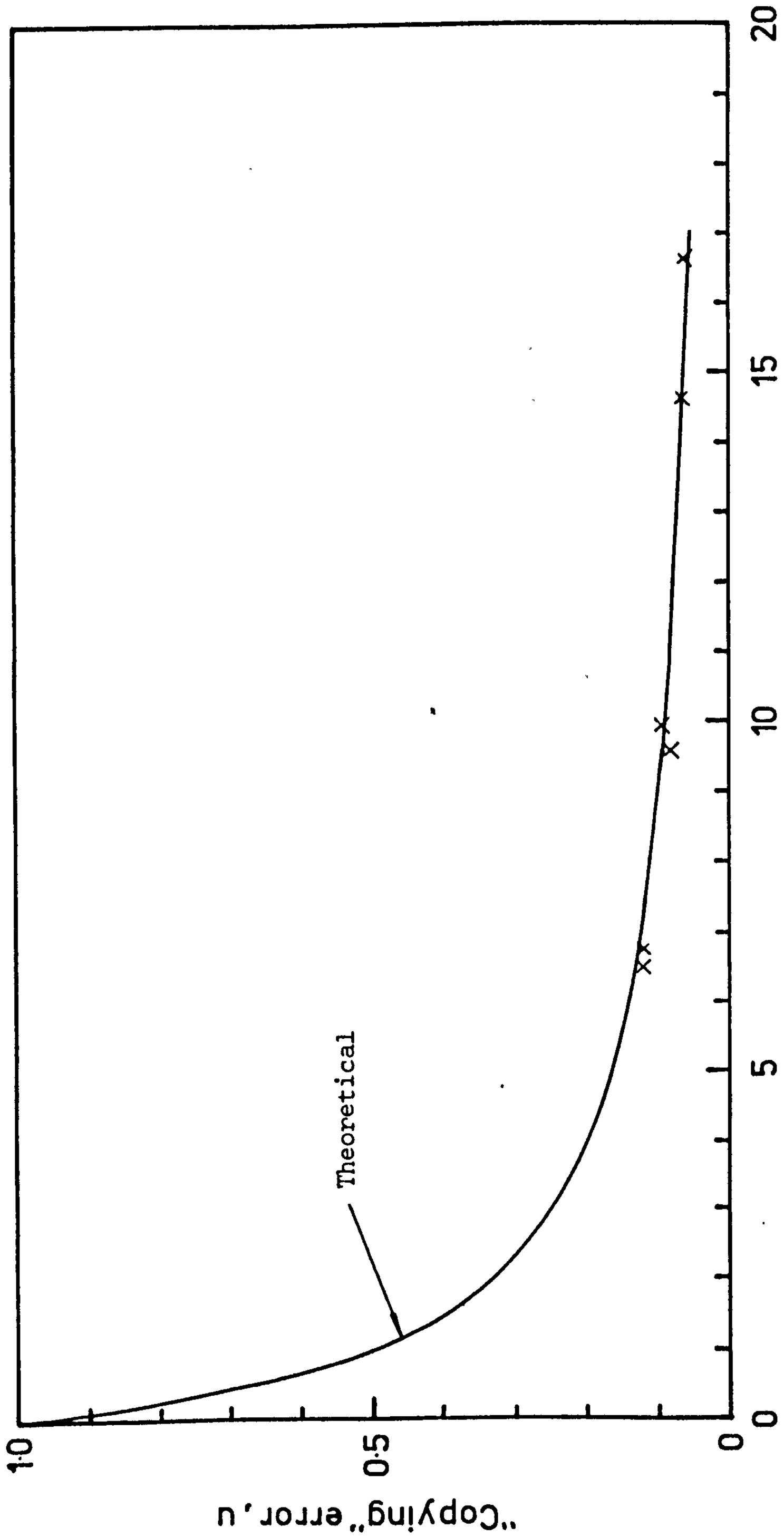

Fig 6.26 Graph of "copying" error u in relation to the cutting parameter K

References for Chapter 6

1. PERA No. 90 "Steady State Cutting Forces and their Measurement - Part 2 - Investigation into Overhung Boring Bars", August 1961

2. KOENIGSBERGER, F. "Design Principles of Metal-cutting Machine Tools", Pergamon Press, 1964, pp. 5 and 6.

3. NG, K. W. "Overhung Boring Bars - Part I - Dynamic Behaviour of New Designs of Damped Boring Bars under forced Vibratory Conditions".
Ph.D. Thesis, Dept. of Production Technology, Brunel University, October, 1977.

4. PERA No. 78 "Investigation into Overhung Boring Bars - Part I Static Load Tests - The Behaviour of a Boring Bar mounted on a Test Bed and on a Lathe Saddle".

7. FREQUENCY RESPONSE EXPERIMENTS

In this chapter are presented results of the frequency response experiments that were conducted on the test bars fitted with different slug dampers as described in sections 7.1 and 7.2. The term "frequency response" is used to refer to the amplitude and phase measurements at the tool tip of the bar mounted on the lathe in response to a sinusoidal force input that varies within a frequency range of interest, namely 50 Hz to 300 Hz. Since the frequency response experiments were conducted on the lathe, the dynamic characteristic obtained necessarily included the dynamics of the bar as well as of the lathe. The dynamics of the latter were small in comparison with those of the bar and hence quite often ignored. Based on this assumption, an attempt was made to evaluate the goodness of fit of the mathematical model of the bar developed in Chapters 5 and 6 based on the equivalent mass, stiffness and damping coefficient.

The goodness of fit is considered to be reasonable as will be discussed in section 7.6, but in order to predict the stability limit during boring, the mathematical model needs refinement. For this reason, the stability theory in Appendix E was developed. Using this theory, it will be shown in Chapter 8 that stability limits in terms of the depth of cut can be estimated provided that the frequency response of the bar measured at the tool tip at the time of boring is known. Obviously such a requirement is difficult to realise in practice. A practical alternative is to measure the response of the bar mounted as before on the lathe but having the lathe inoperative. The difference between the two responses is believed to be small. It is this alternative that was adopted for the experiments.

7.1 BORING BAR DESIGN

Four types of boring bars were used in the experiments. They all had an overhung length of 381 mm and a diameter of 38 mm, equivalent to 10 to 1 overhang ratio.

(1) Solid bar - This bar, as shown schematically in Fig. 7.1, was machined in one piece from EN8 steel. It served as a reference in relation to which the performance of other bars was assessed.

(2) Recessed bar - The bar is shown in Fig. 7.2. Aside from a round hole bored out close behind the toolpost to accommodate a slug damper, the recessed bar was in every respect identical to the solid bar.

(3) Steel-bunged bar - The bar is shown in Fig. 7.3. The term "steel-bunged" refers to the particular design in which a steel bung was fitted into a tubular shank. As illustrated in Fig. 7.3, the steel bung terminated at a fraction of the maximum allowable length. This was to ensure a reasonable measure of stiffness to be achieved whilst substantially reducing the effective mass of the boring bar, so enabling a high μ ratio, i.e. ratio of absorber mass to effective mass of boring bar, to be achieved. The contact pressure between the bung and the surrounding shank was designed to be 14 MN/m^2 (2000lb f/in^2). Both the bung and shank were made of EN8 steel. Like the recessed bar, the steel-bunged bar was similarly recessed to accommodate a slug damper. In addition, to enhance machining performance, a second but much shorter slug in a capsule could be fitted to the free end of the bar if desired. Whilst such a bar would not be suitable for use in "blind" boring, i.e. up to the bottom of a cavity, it could be used for through boring and profiling operations.

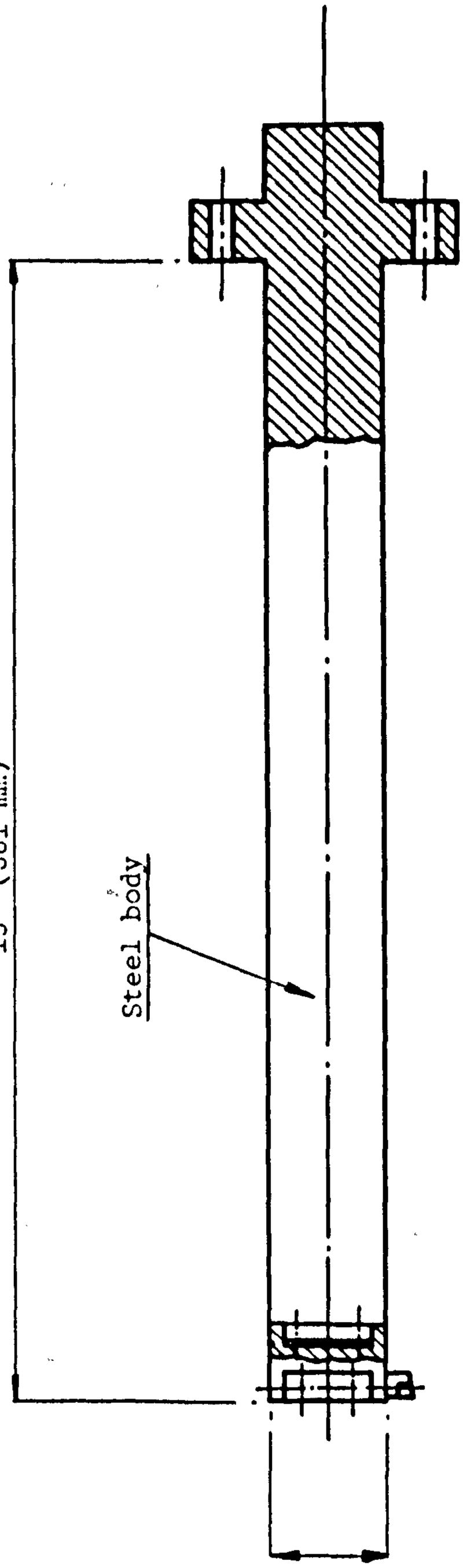

Schematic diagram showing a plain solid bar at 10:1 overhang ratio

Fig 7.1

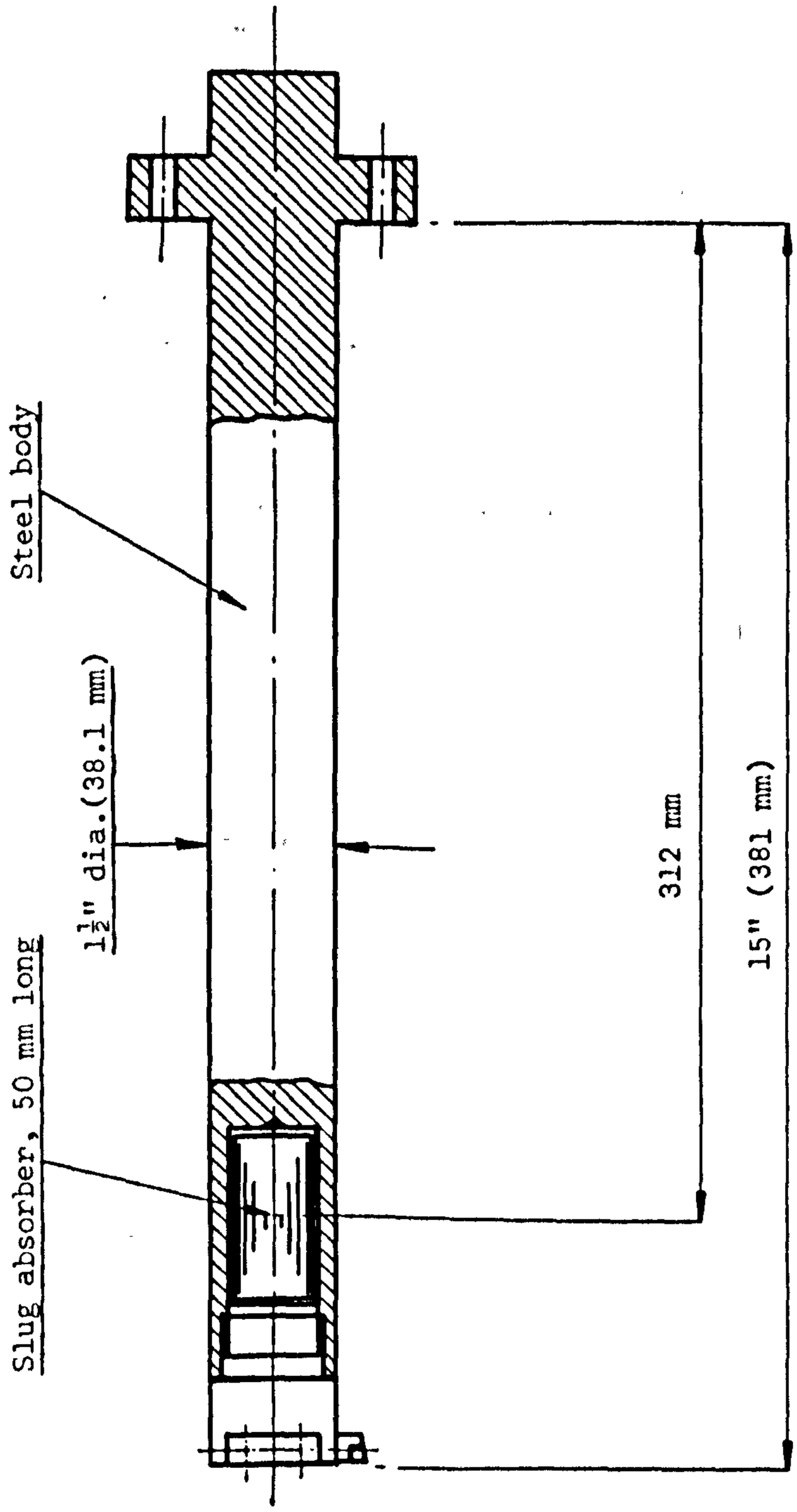

Fig 7.2 Schematic diagram showing a single-slug recessed bar at 10:1 overhang ratio

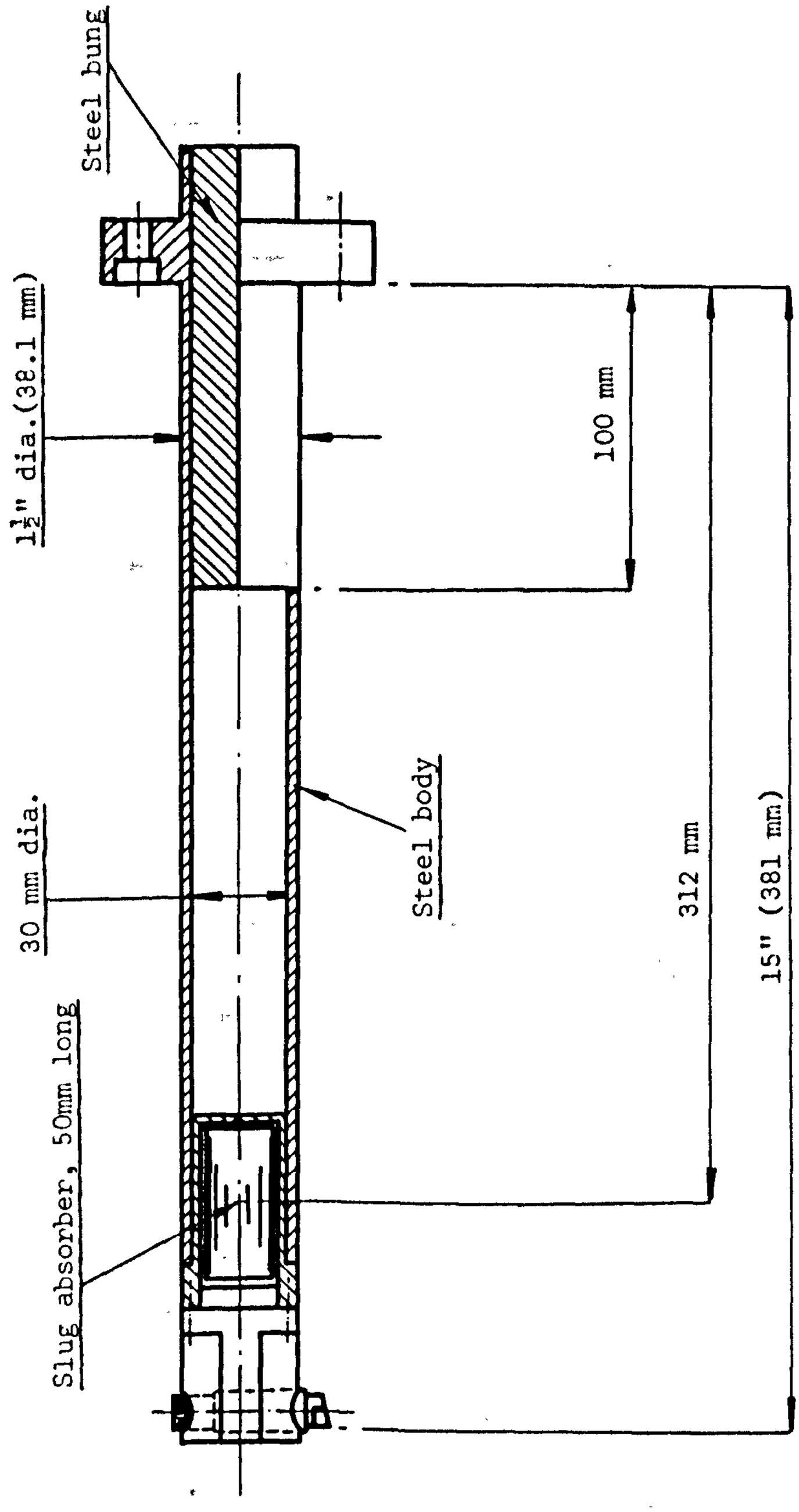

Fig 7.3 Schematic diagram showing a single-slug steel-bunged bar at 10:1 overhang ratio

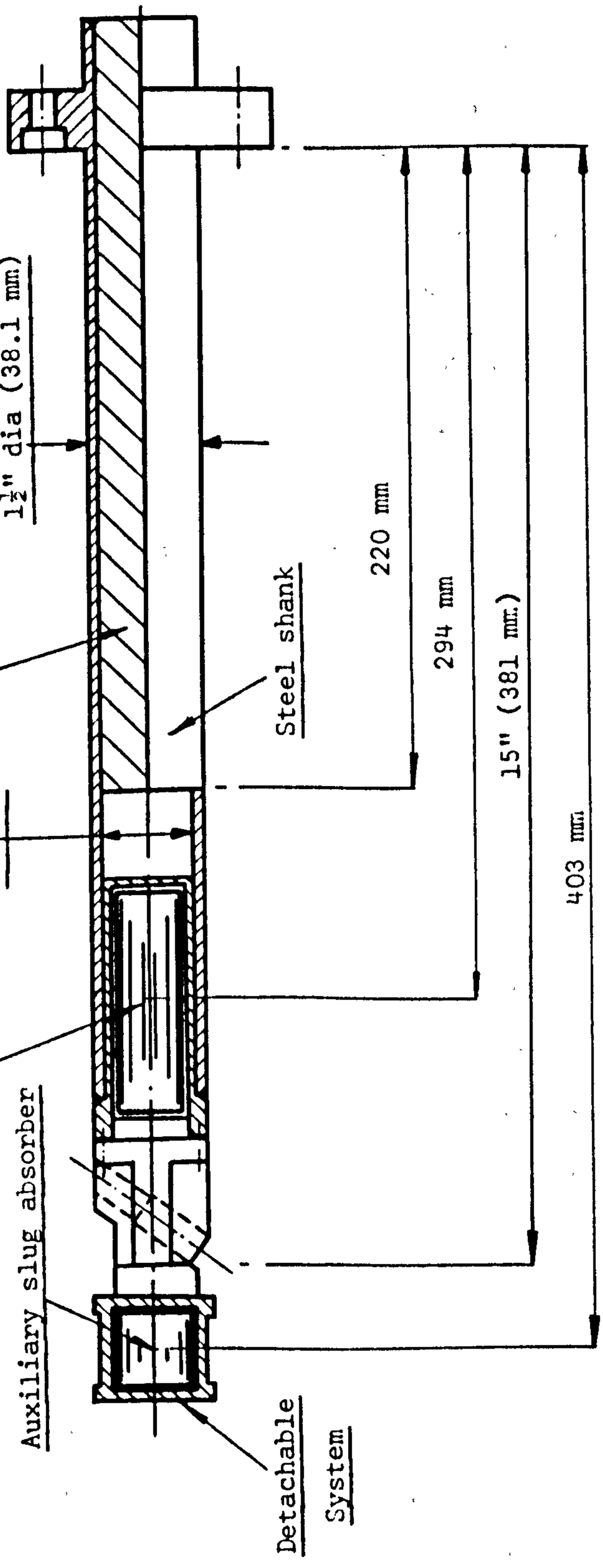

Fig 7.4 Schematic drawing showing a twin-slug tungsten-bunged bar at 10:1 ratio

(4) Tungsten-bunged bar - The bars, as shown in Fig. 7.4, had the same appearance as the steel-bunged bar. However, there were two important differences:-

(i) the bung length of the bar had been optimized using the theory described in Section 4.5 and the method described in Appendix C;

(ii) the bung was made of tungsten carbide which has a modulus of elasticity of 534 MN/m^2, that is 2.67 times that of steel.

Similar to the steel-bunged bar, an auxiliary slug damper could be fitted to the free end of the bar.

The four bars just described were fitted with a flange and spigot mounting whereby the bars were tightened to the bar-holder by means of six Allen screws that were evenly spaced on the flange face. The reason for choosing this type of end fixing, and hence a fixed overhang, was to ensure a constant rigidity of the mounting to facilitate experimental and analytical work.

The bungs in (3) and (4) were finely ground to close tolerances before assembly so as to provide the desired mating pressure of $14MN/m^2$. To aid assembly, the bung was refrigerated whilst the shank was heated in an oven so as to produce enough clearance for them to slip into one another. Finally, the bung was brazed to the spigot at the exposed end.

7.2 SLUG DAMPER DESIGN

Slugs were made from a GEC heavy metal alloy with a density of 16.8 Mg/m^3 (0.607 lb/in^3). The slug dampers were cylindrical in shape and had a nominal diameter slightly under 25.4 mm (1 in.). The actual diameters varied so as to produce different clearances between themselves and the accommodating holes. There were three groups of slug dampers as

illustrated below:

(1) Main slug damper (length 52.4 mm) - There were six slug dampers, used in either the recessed bar or the steel-bunged bar. Their masses are tabulated alongside their diameters as follows:

Diameter (mm)	Slug mass (kg)
25.222	0.434
25.243	0.432
25.268	0.435
25.293	0.435
25.321	0.437
25.347	0.438

The mass variation was mainly due to the varying diameter, but slight inconsistencies were caused by variations in the threaded hole at one end of the slug. This threaded hole was to aid the slug removal from the damper hole.

(2) Main slug damper (length 76 mm). - These were used exclusively in the tungsten-bunged bar. Diameters and masses are presented in the following table:

Diameter (mm)	Slug mass (kg)
25.278	0.6379
25.299	0.6364
25.318	0.6410
25.350	0.6415

(3) Auxiliary slug damper (length 25.6 mm) - These were used in the tungsten-bunged and steel-bunged bars. Diameters and masses are shown in the following table:

Diameter (mm)	Slug mass (kg)
25.226	0.209
25.250	0.209
25.282	0.210
25.302	0.210
25.322	0.210
25.356	0.211

7.3 INSTRUMENTATION AND EQUIPMENT

7.3.1 Lathe for Frequency Response Experiment

Particulars of the lathe were presented in section 6.3.2.

7.3.2 Bar Holder

Fig. 7.5 shows the bar holder mounted on the saddle of the lathe. For the case of frequency response measurement, the bar under test was mounted onto one face of the bar-holder. For machining tests, the bar holder also allowed a stumpy boring bar to be mounted end-to-end with the boring bar under test. The function of this stumpy boring bar was to produce a standard chatter free surface prior to any test cut. Indexing of the two bars into their cutting position was achieved by allowing the bar holder to rotate about an axis normal to its base and by tightening after indexing the bar holder to the cross slide with bolts located in the four corners of the base.

7.3.3 Frequency Response Measurement

The way in which the instruments were connected for the frequency response measurement is shown in the block diagram of Fig. 7.6. Functionally the instruments fall into three groups as follows:

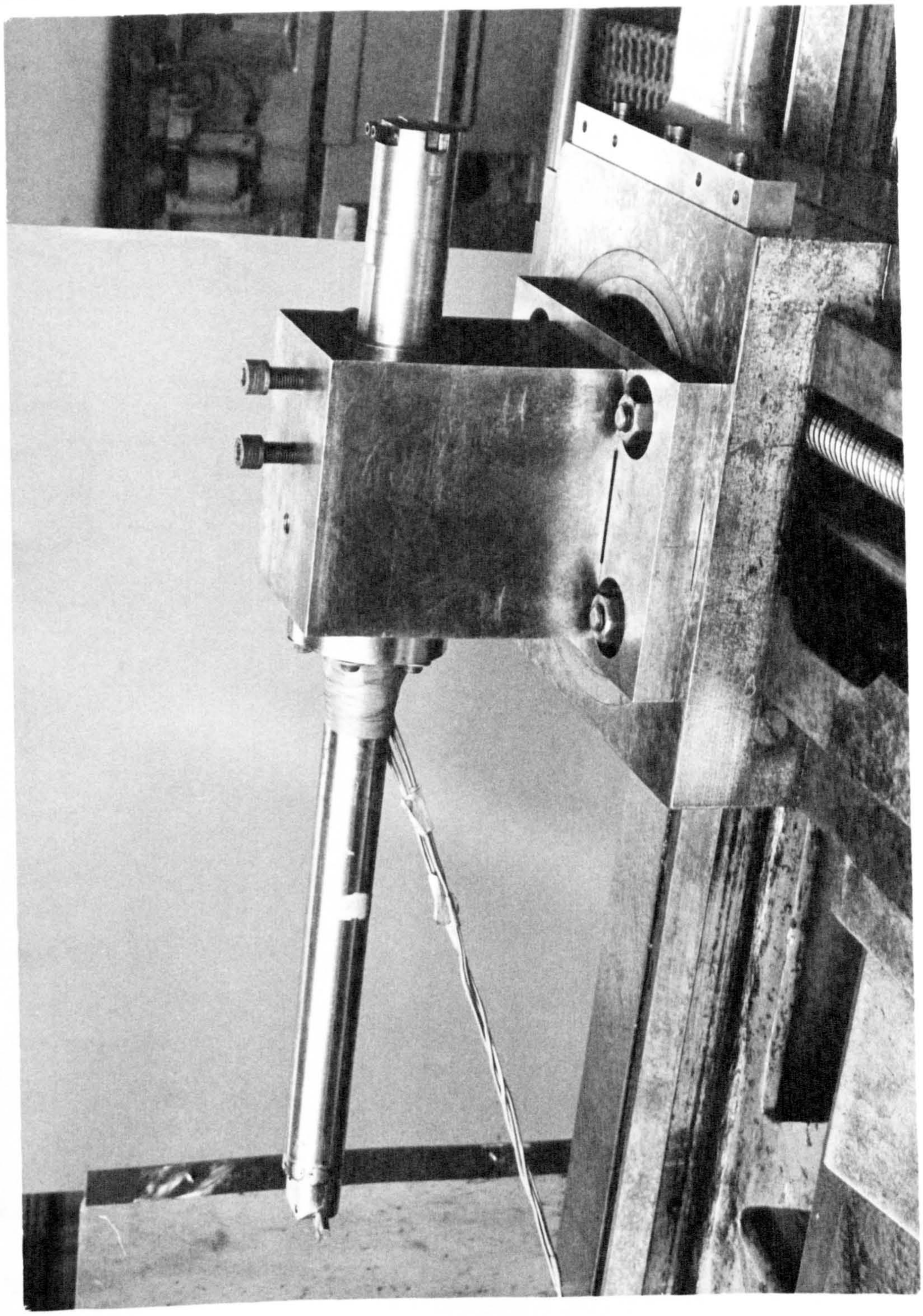

Fig 7.5 Close-up view of bar holder mounted on the cross-slide of the lathe

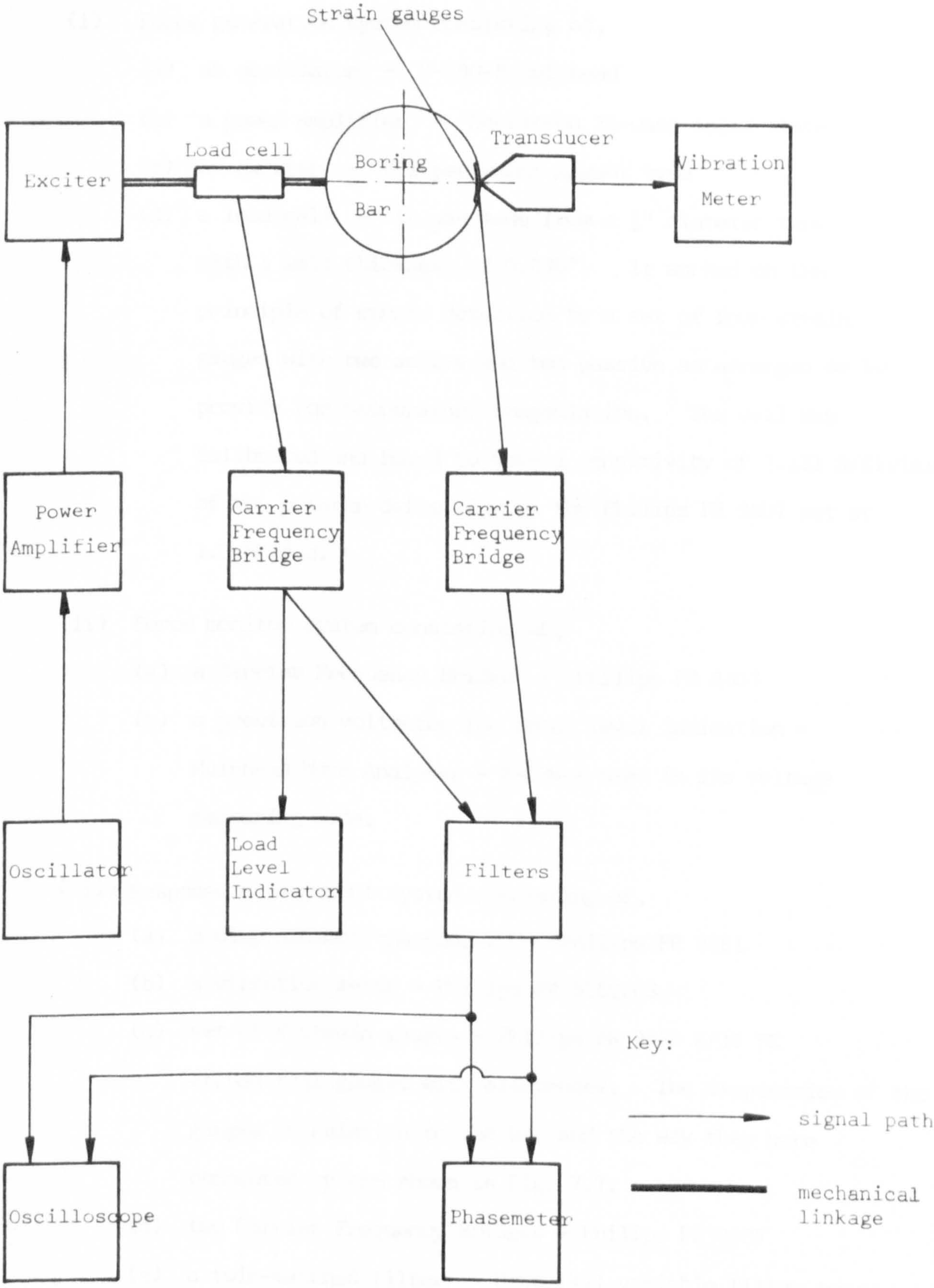

Fig 7.6 Block diagram of instrumentation for frequency response measurements of boring bars

(i) Force generation system consisting of,

(a) an oscillator - D-890-B Muirhead

(b) a power amplifier - Derritron 25-wass solid-state

(c) an exciter - VP2 permanent magnet type

(d) a load cell - it was made from a ½" diameter tube with a wall thickness of 0.030". It worked on the principle of strain detection by a set of four strain gauges with two active and two passive so arranged as to provide for temperature compensation. The cell was calibrated and found to have a sensitivity of 2.131 N/division of the pointer deflection on the Philips PR 9307 set at 1.0 mV/fsd.

(ii) Force monitor system consisting of,

(a) a Carrier Frequency Bridge - Philips PR 9307

(b) a precision voltmeter for force level indication - Muirhead Wave Analyser - K-134-A used in its voltage measuring mode.

(iii) Response measurement system consisting of,

(a) a displacement transducer - Philips PR 9261

(b) a vibration meter - Philips PR 9252/03

(c) set of 8 strain gauges - Philips PR 9832 K/10 FE etched foil gauges with electrodes. The disposition of the gauges in relation to the bar and the way they were connected up are shown in Fig. 7.7.

(d) two Carrier Frequency Bridges - Philips PR 9307

(e) a twin-matched filter - Dawe 1471 variable filter type. This instrument consisted of two identical filters which could be operated independently with a common power supply. For the frequency response experiment, it was used as a

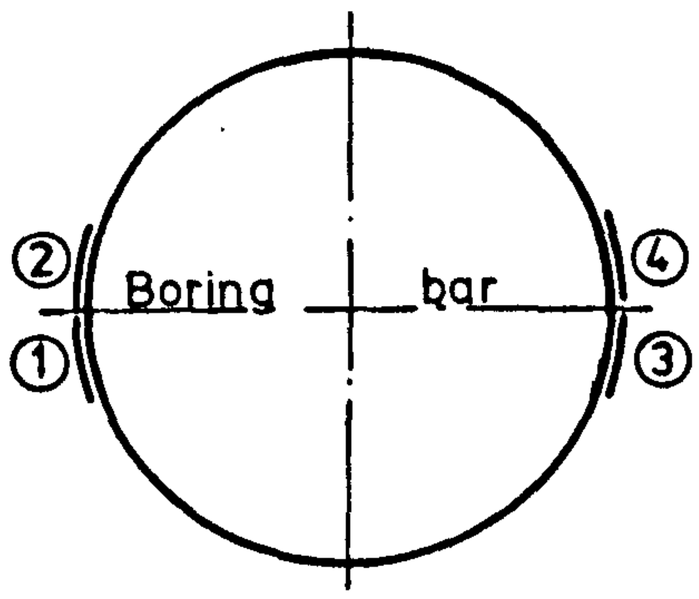

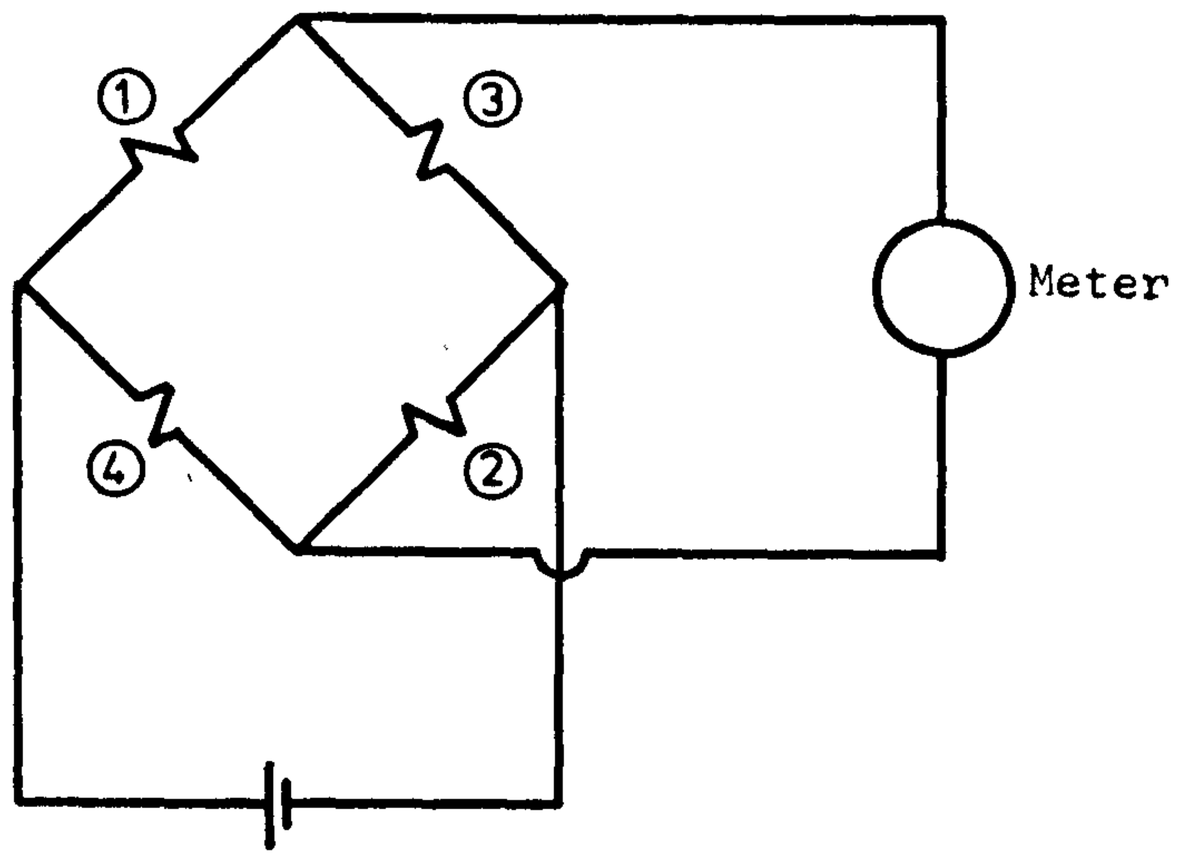

Strain gauges are labelled as ① , ② , ③ , and ④ .

Fig 7.7 Bridge circuit of strain gauges mounted on boring bar for strain detection in horizontal plane

pair of low pass filters to remove the high frequency contents of the force and displacement voltage signals before the phase difference between their main components was measured.

(f) a phase meter - Wiltron 351 differential input model.

(g) an oscilloscope - Medelec 4 - channel fibre-optic recording oscilloscope.

7.4 OBJECTS

(1) To measure the amplitude and phase responses of the solid bar, the recessed bar, the steel-bunged bar and the tungsten-bunged bar.

(2) To measure the amplitude and phase responses of the recessed bar, the steel-bunged bar and the tungsten-bunged bar when fitted with different sizes of slug dampers.

(3) To determine the optimum slug dampers for the recessed bar, the steel-bunged bar and the tungsten-bunged bar in terms of their minimum amplitude response at resonance.

(4) To assess the goodness of fit of the mathematical model for the case of single-slug damped bars.

(5) To assess the dynamic influence of the Model Sriou lathe on the frequency response of the bar measured.

(6) To compare the theoretical stiffness with the experimental stiffness of the bar.

(7) To establish an empirical relation between the damping ratio in the model and the radial clearance of the damper in the real system.

7.5 PROCEDURE

The set-up is illustrated in Figs. 7.6 and 7.8. The exciter and the transducer were mounted diametrically opposite to each other sandwiching, in between them, the bar whose response was to be measured. The exciter delivered a harmonic force, whose magnitude was monitored by a load cell, to the tip of the dummy tool seated and secured in the toolpost of the bar. The amplitude response was picked up by the transducer which sent the signal onwards to the vibration meter for visual display.

The term "phase response" is taken to mean the phase lag of the amplitude response signal in relation to the input force signal. The signal for amplitude response was derived from the strain gauges mounted at the root end of the bar whereas the signal for the input force was taken from the load cell. These two signals were then sent through the two identical filters so as to remove their higher frequency components and finally into the phase-meter from which a phase lag reading was obtained.

Response measurements were taken in both the horizontal and vertical planes relative to the lathe. The frequency range was 50-300 Hz and the input force was maintained at a magnitude of 4.448N (1 lbf) peak-to-zero.

7.6 RESULTS AND DISCUSSION

7.6.1 Frequency response of bar

The frequency response curves for various bars either on their own or fitted with slug dampers are shown in the figures whose numbers are indicated in Table 7.1. The common direction in which both the force

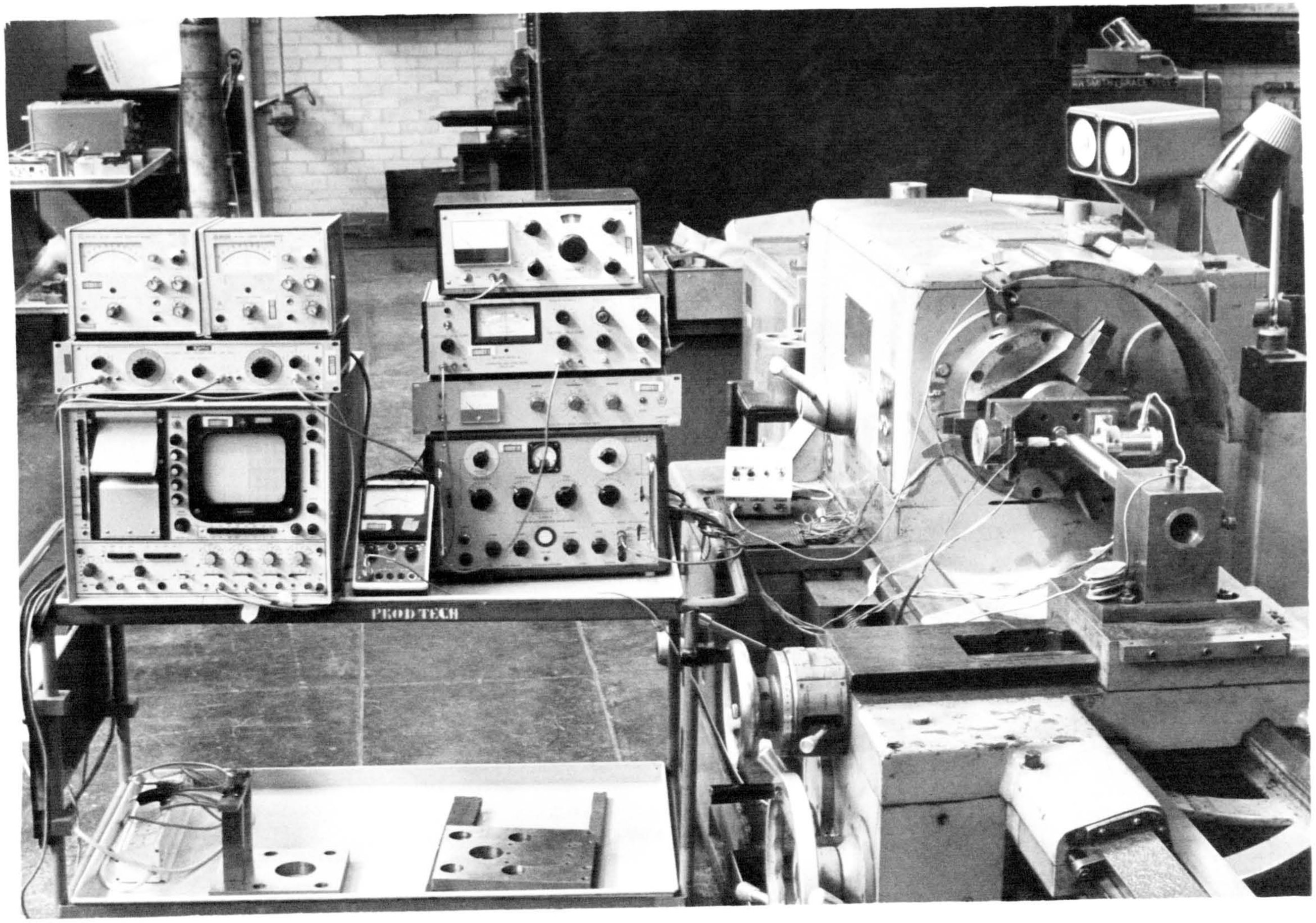

Fig 7.8 Set-up for frequency response experiment

was applied and the amplitude was measured is shown in column 3. Also shown are the slug sizes and their radial clearances whenever it is appropriate.

TABLE 7.1

Fig. No.	Bar	Direction	Slug (mm)		Rad.clearance		Remark
			Main	Aux.	Main	Aux.	
7.9	Solid	Horizontal	-	-	-	-	-
7.10	Solid	Vertical	-	-	-	-	-
7.11	Recessed	Horizontal	-	-	-	-	-
7.12	Recessed	Vertical	-	-	-	-	-
7.13	Recessed	Horizontal	25.268	-	0.0735	-	Optimum
7.14	Recessed	Vertical	25.268	-	0.0735	-	Optimum
7.15	Steel-bunged	Horizontal	25.293	-	0.071	-	Optimum
7.16	"	Vertical	25.293	-	0.071	-	Optimum
7.17	"	Horizontal	25.293	25.250	0.071	0.081	Optimum
7.18	"	Vertical	25.293	25.250	0.071	0.081	Optimum
7.19	Tungsten-bunged	Horizontal	-	-	-	-	-
7.20	"	Vertical	-	-	-	-	-
7.21	"	Horizontal	25.299	-	0.067	-	Optimum
7.22	"	Vertical	25.299	-	0.067	-	Optimum
7.23	"	Horizontal	25.299	25.282	0.067	0.065	Optimum
7.24	"	Vertical	25.299	25.282	0.067	0.065	Optimum

In general, it is noted that ordinary boring bars which were not fitted with dampers had an amplitude response curve with a very pronounced peak corresponding to a substantial amplitude of vibration at resonance.

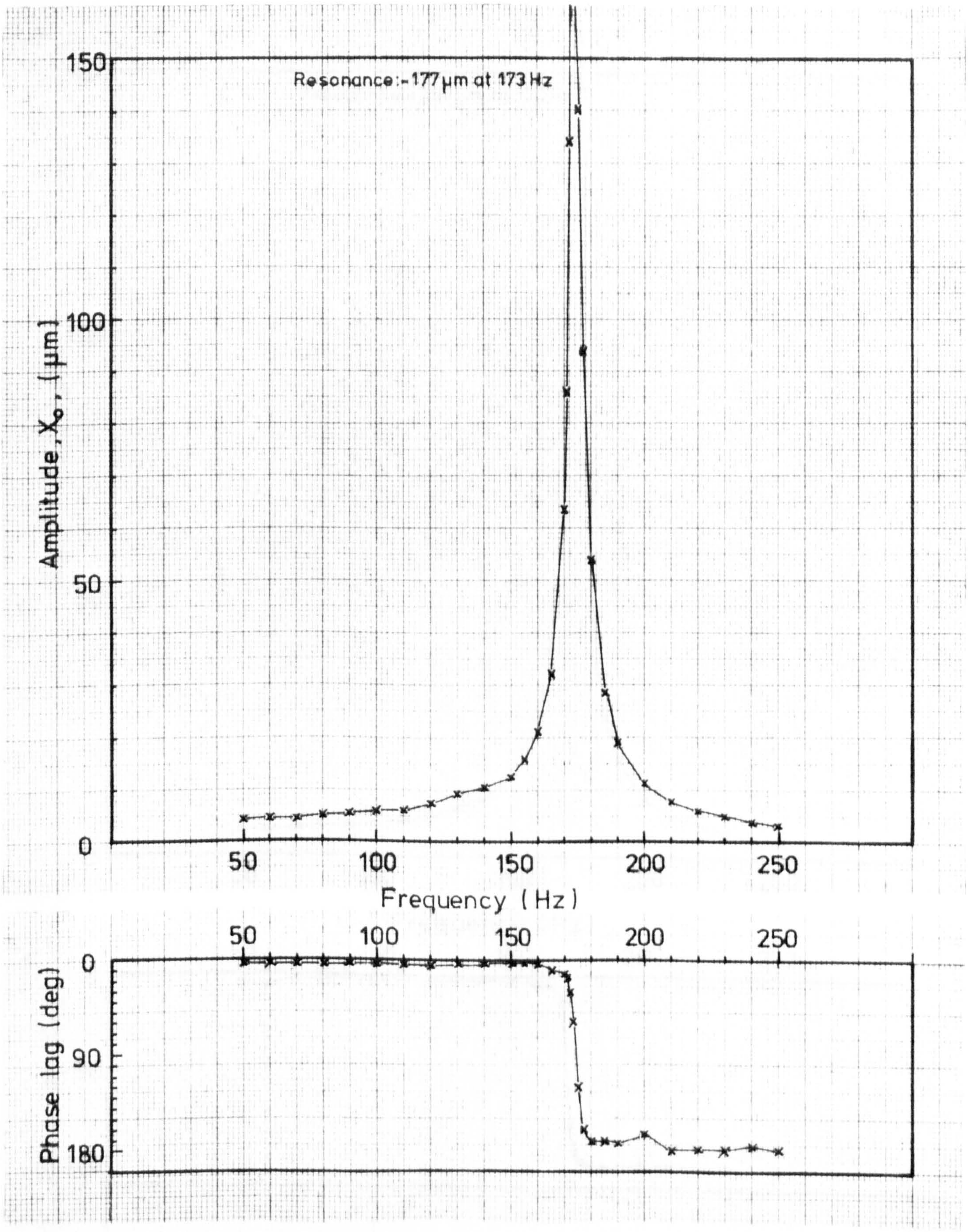

Fig 7.9 Horizontal frequency response of solid bar

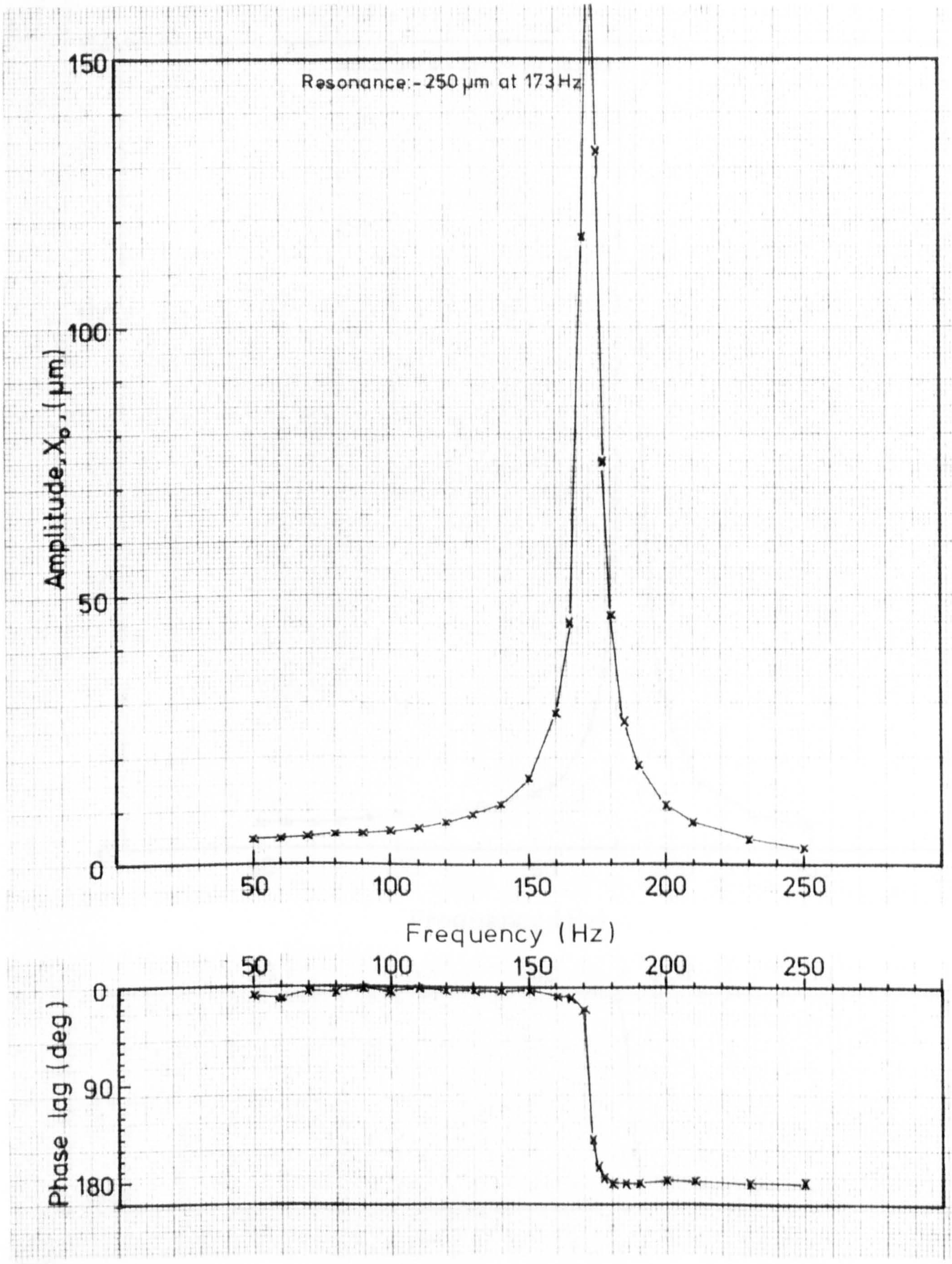

Fig 7.10 Vertical frequency response of solid bar

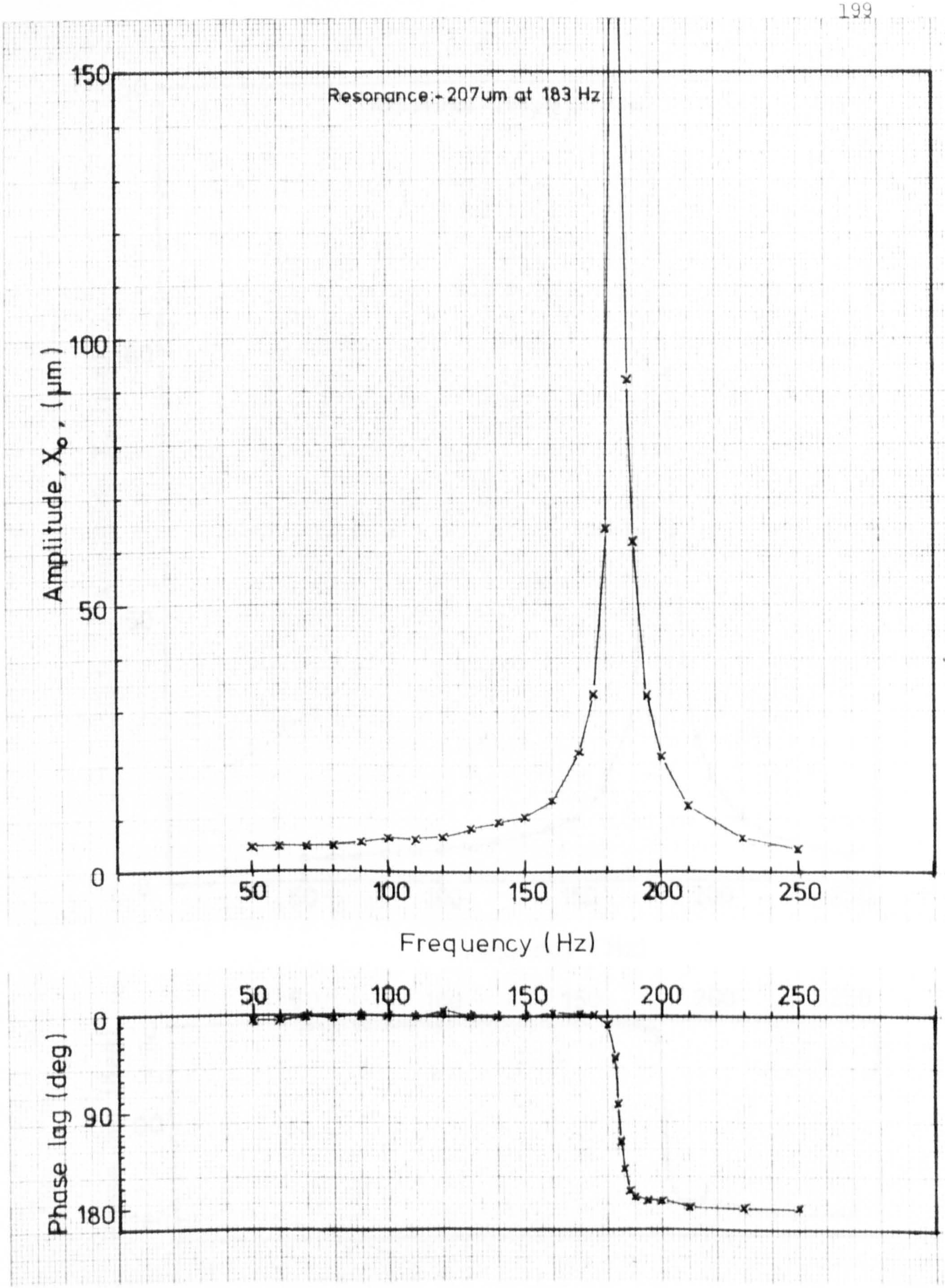

Fig 7.11 Horizontal frequency response of recessed bar

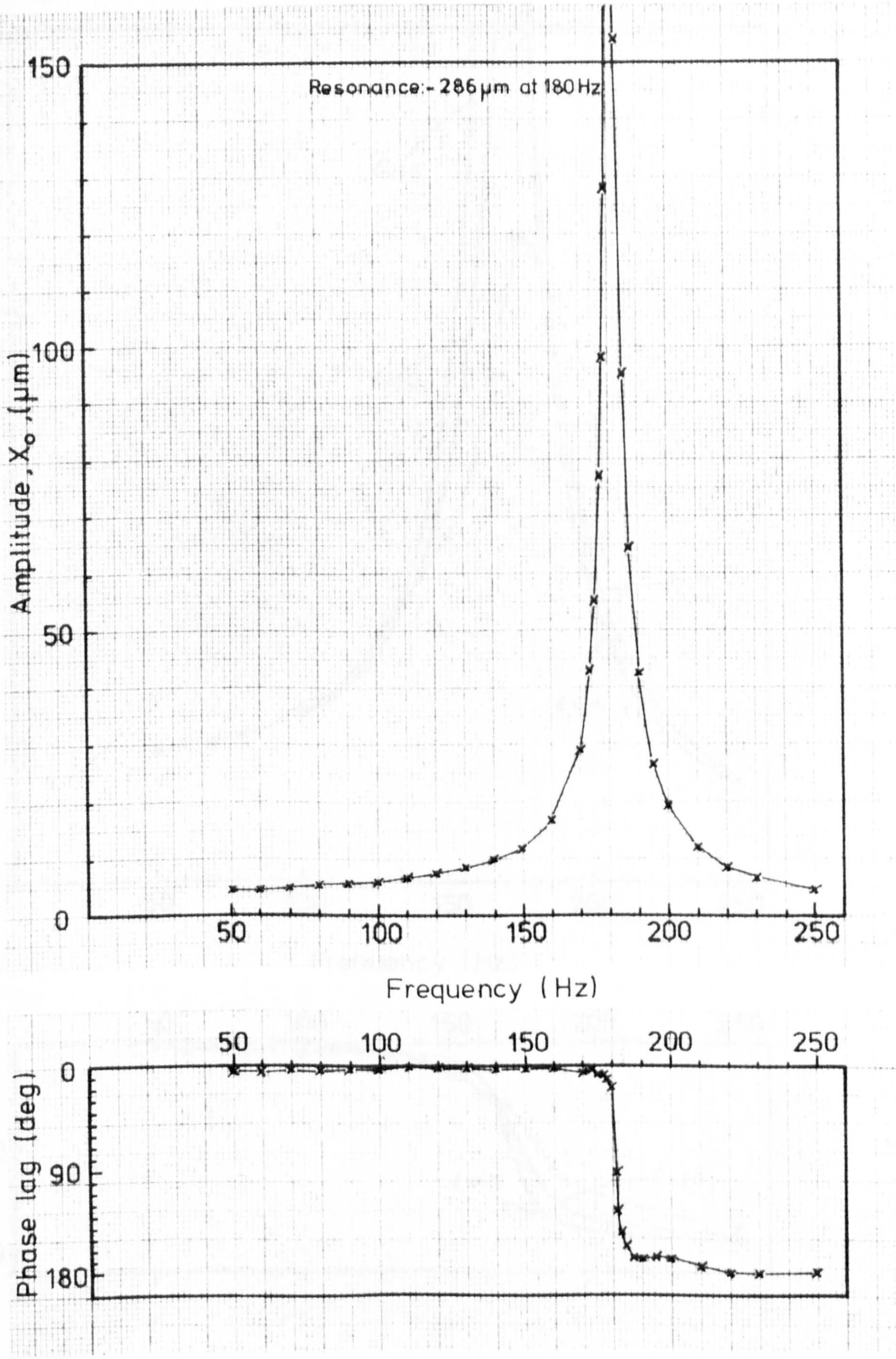

Fig 7.12 Vertical frequency response of recessed bar

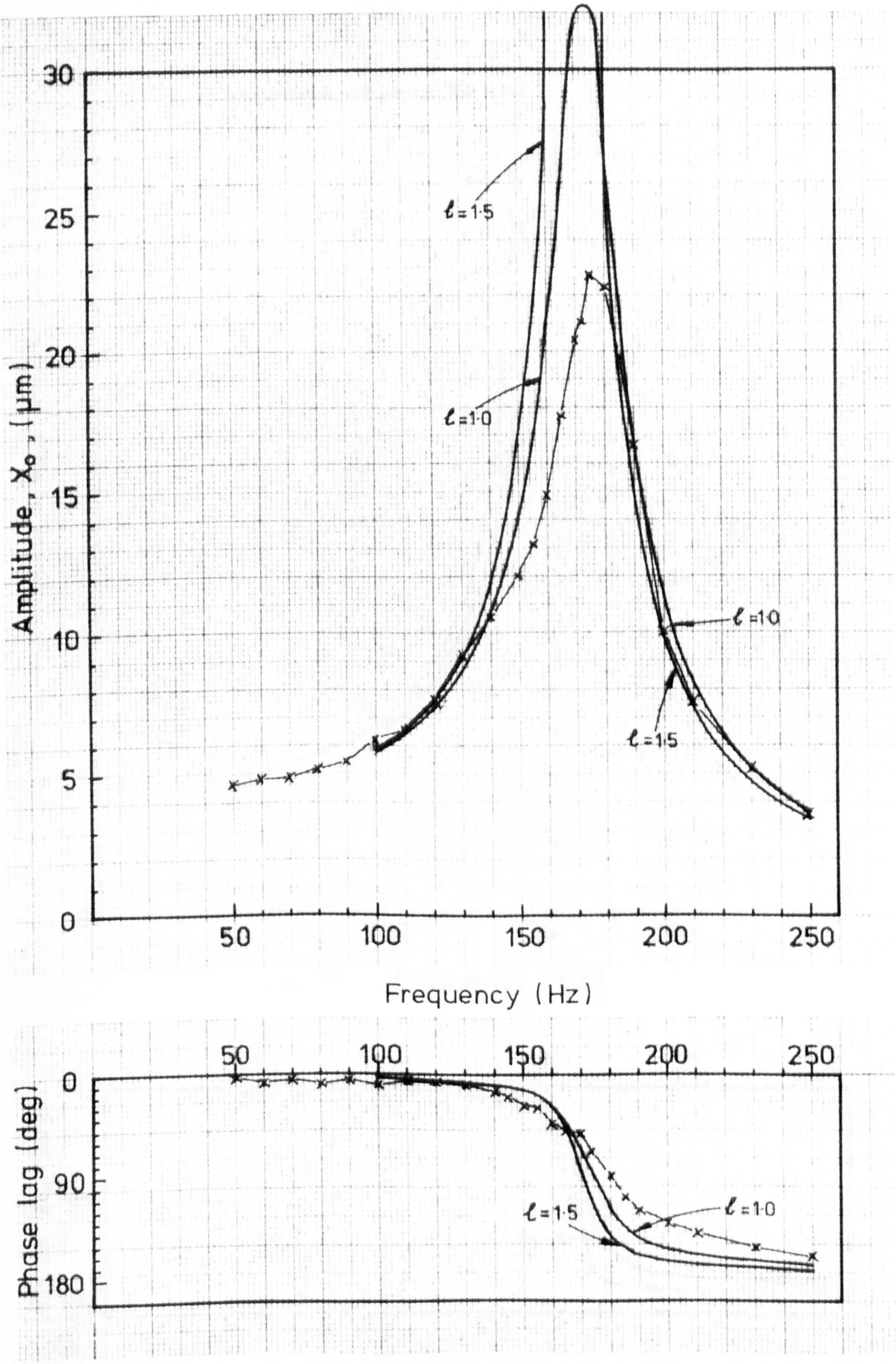

Fig 7.13 Horizontal frequency response of optimally tuned main-slug recessed bar

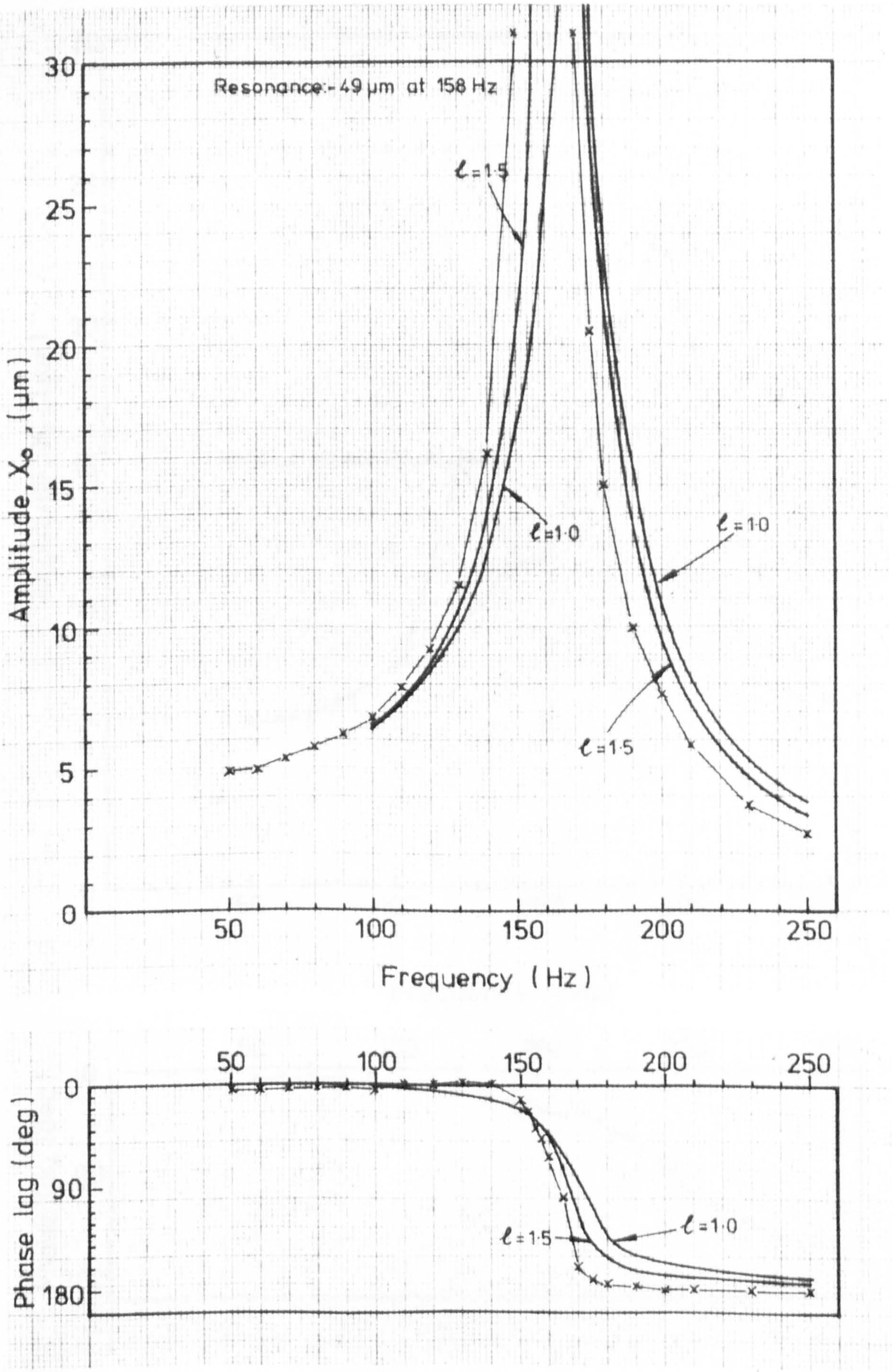

Fig 7.14 Vertical frequency response of optimally tuned main-slug recessed bar

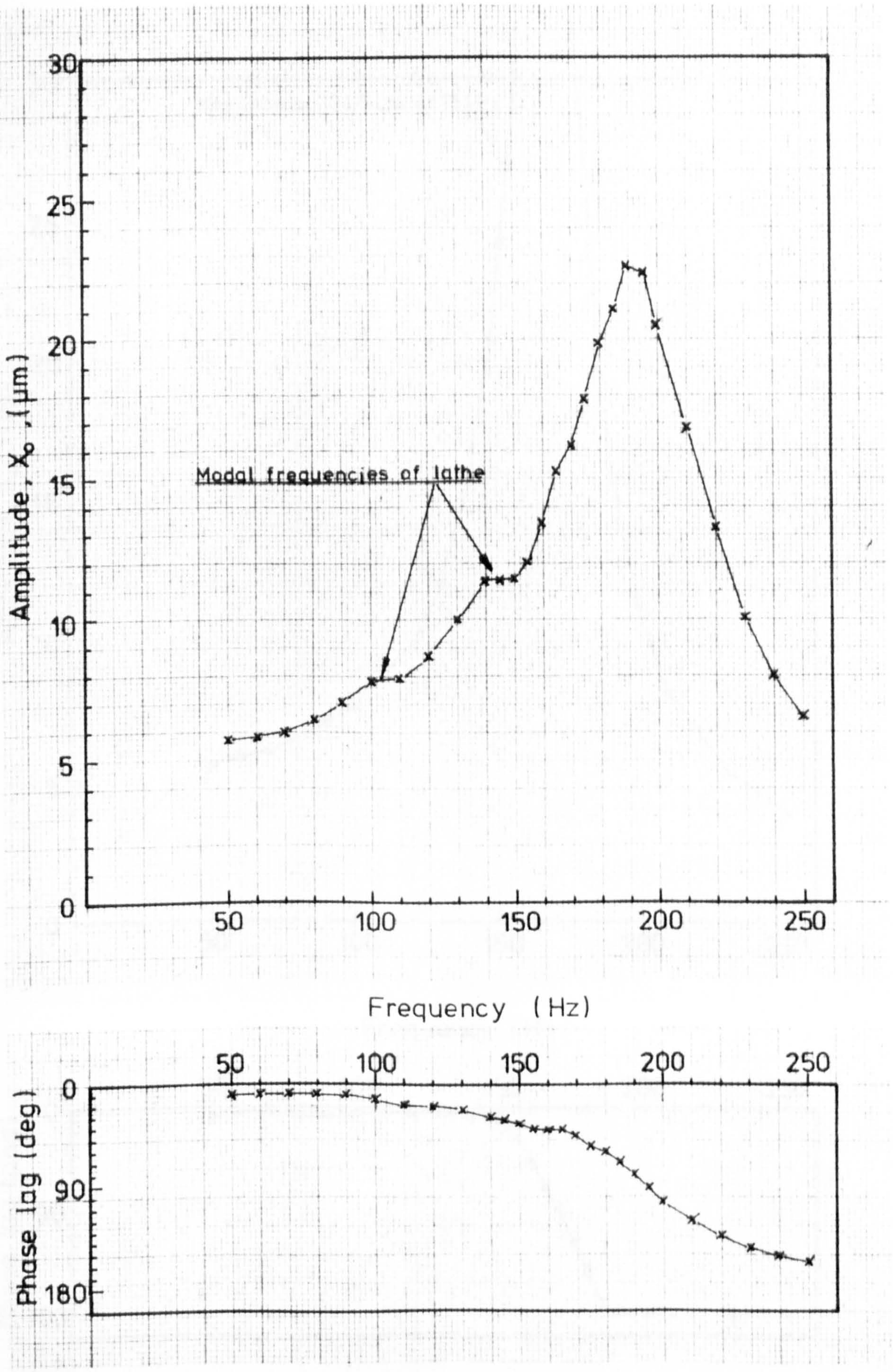

Fig 7.15 Horizontal frequency response of optimally tuned main-slug steel-bunged bar

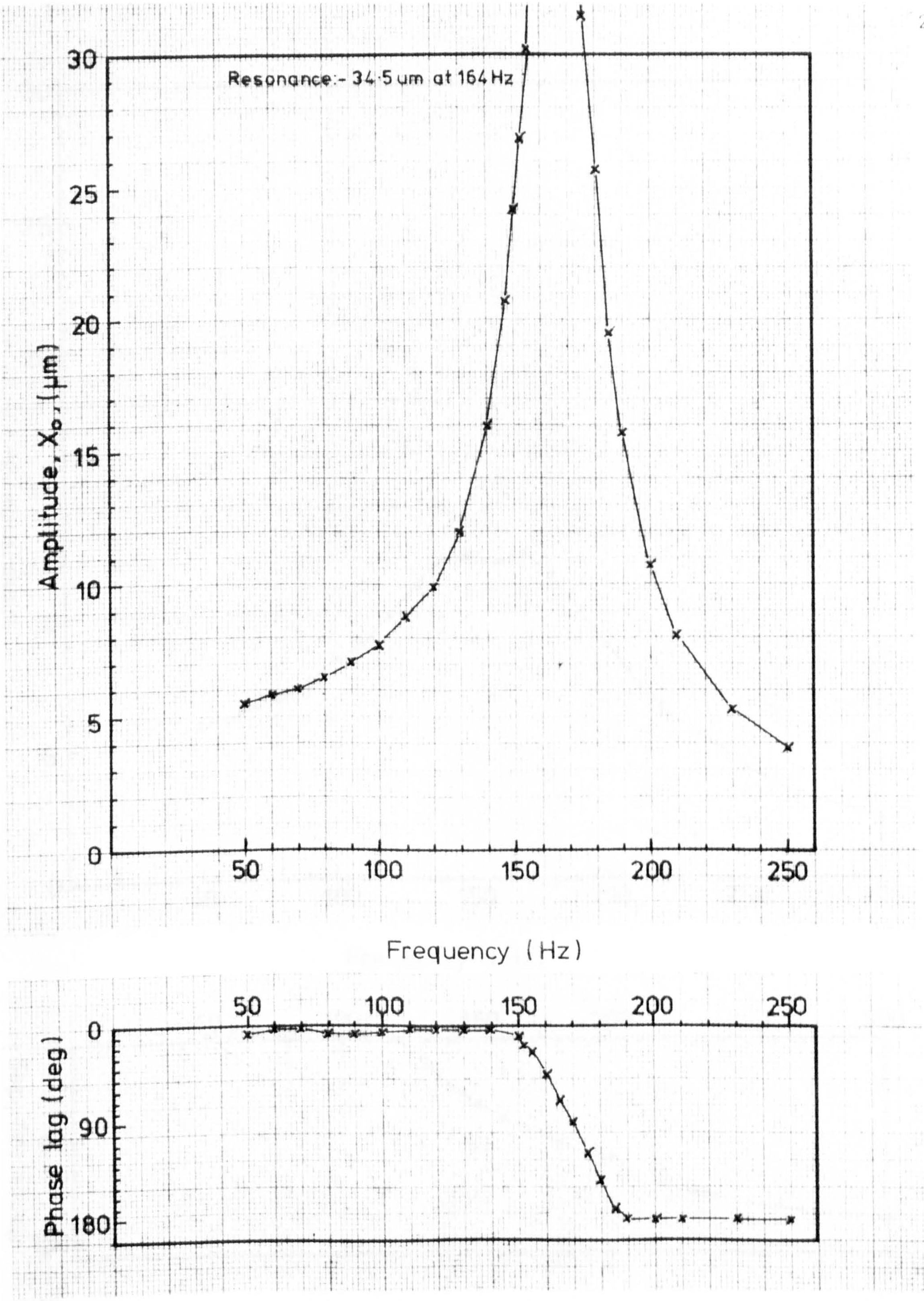

Fig 7.16 Vertical frequency response of optimally tuned main-slug steel-bunged bar

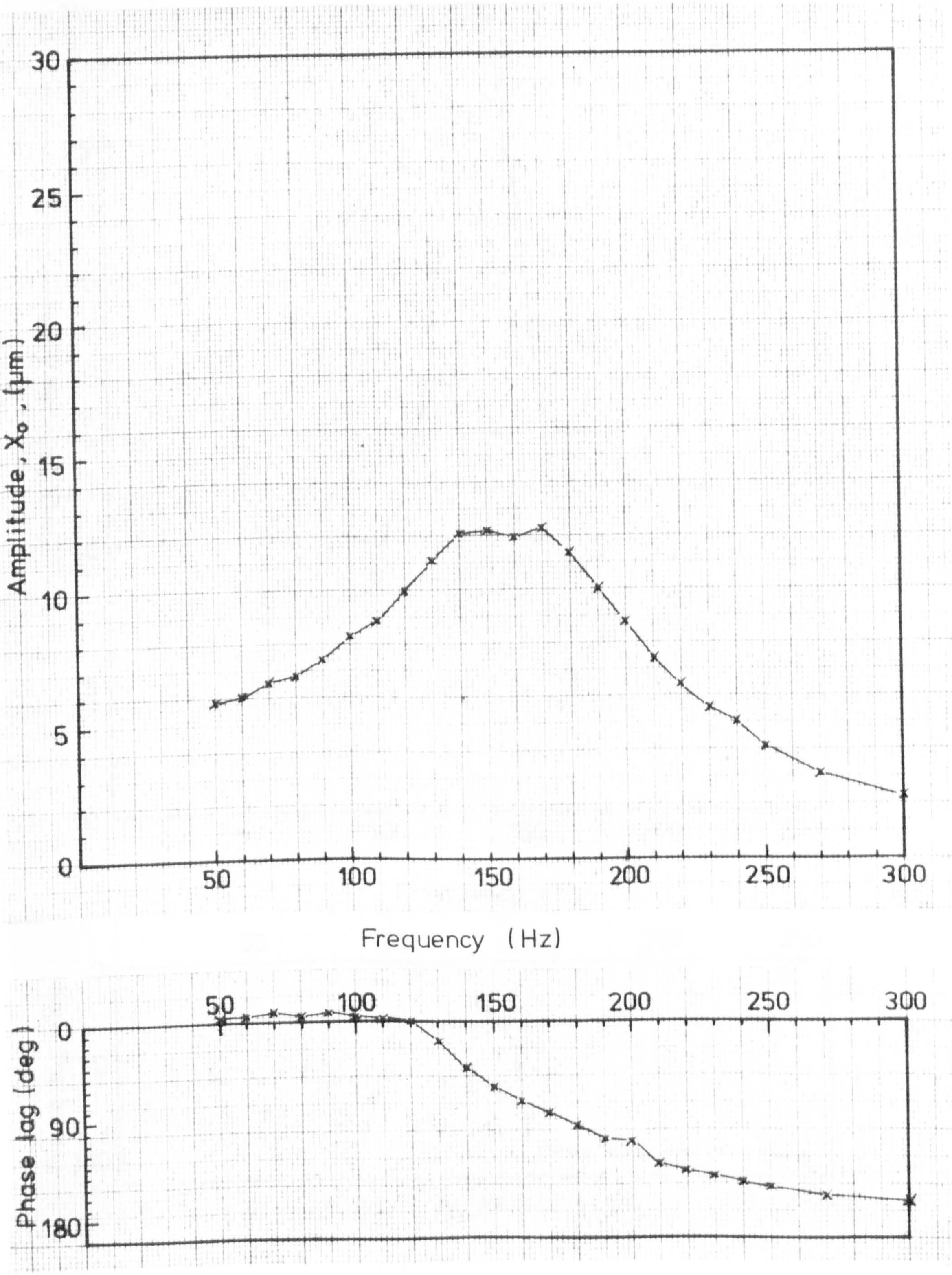

Fig 7.17 Hortizontal frequency response of optimally tuned twin-slug steel-bunged bar

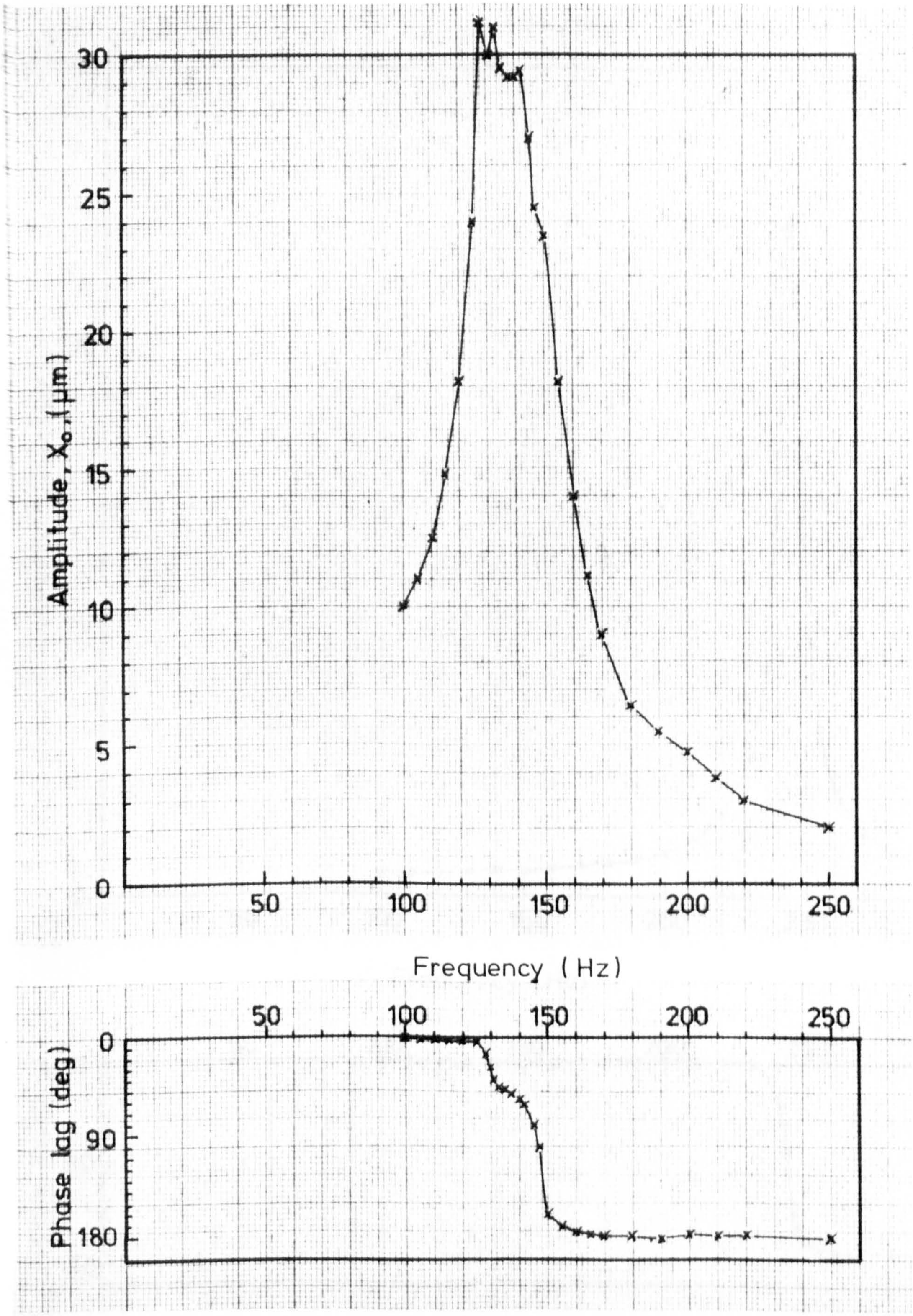

Fig 7.18 Vertical frequency response of optimally tuned twin-slug steel-bunged bar

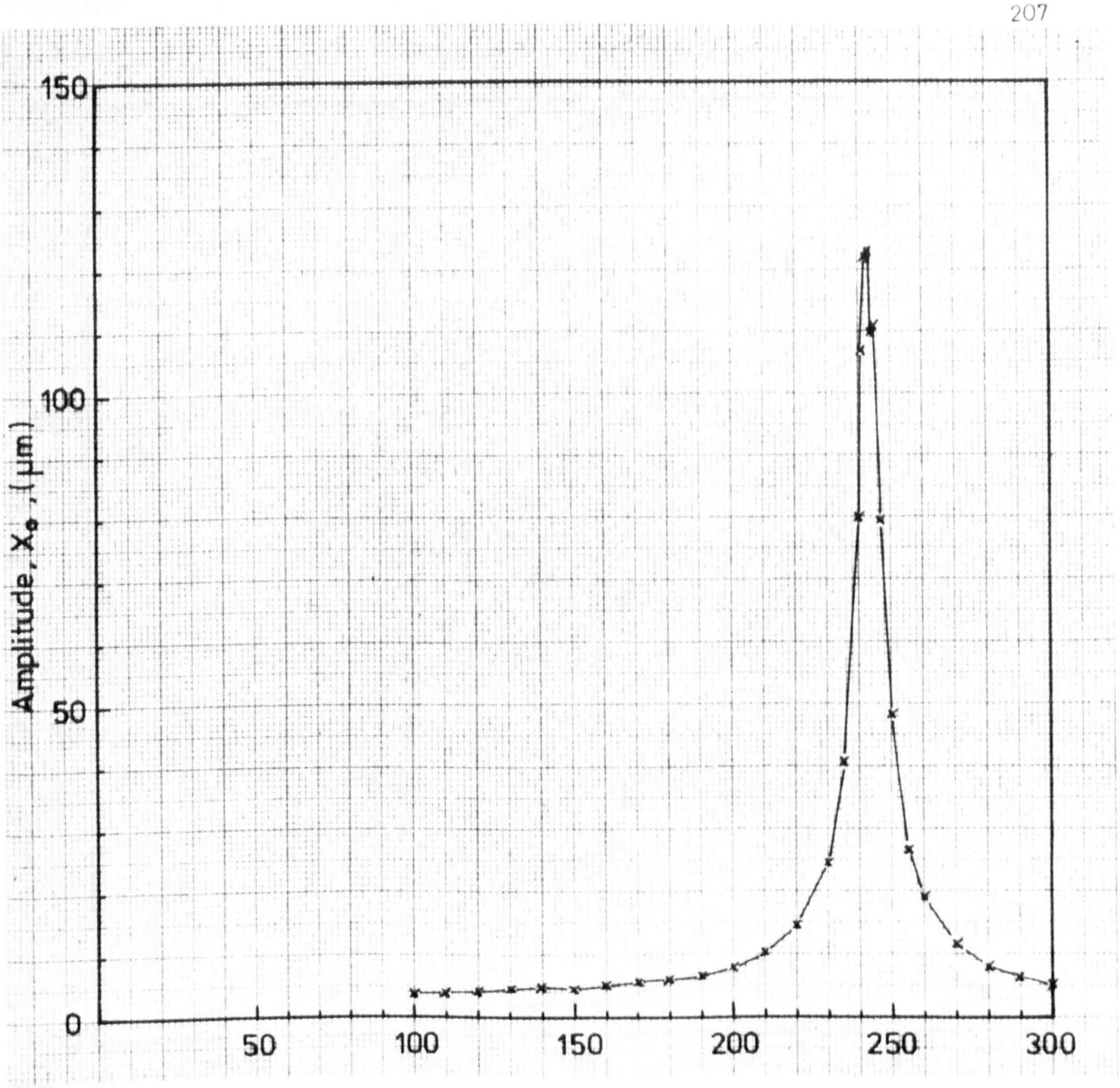

Fig 7.19 Horizontal frequency response of tungsten-bunged bar without slug

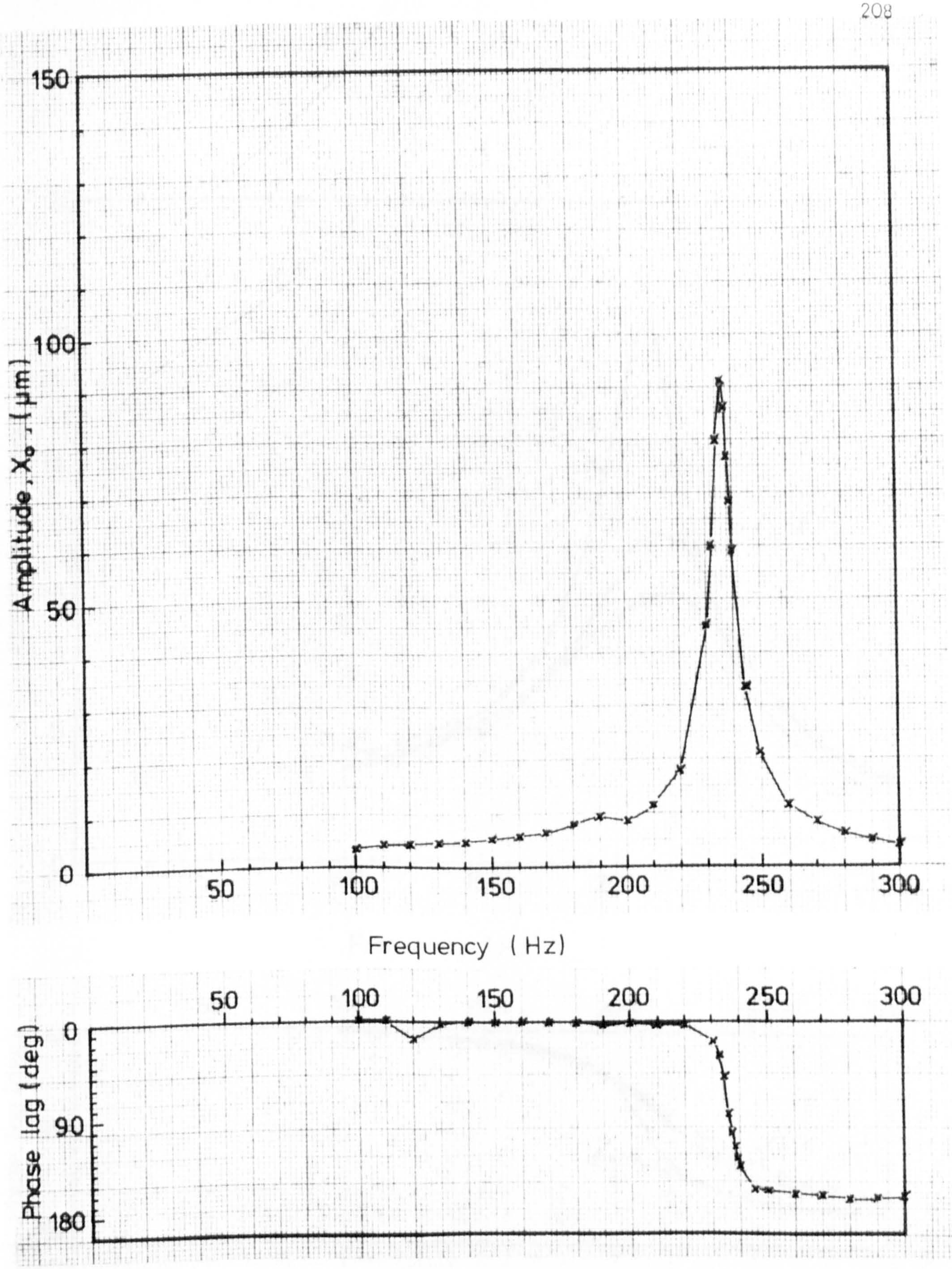

Fig 7.20 Vertical frequency response of tungsten-bunged bar without slug

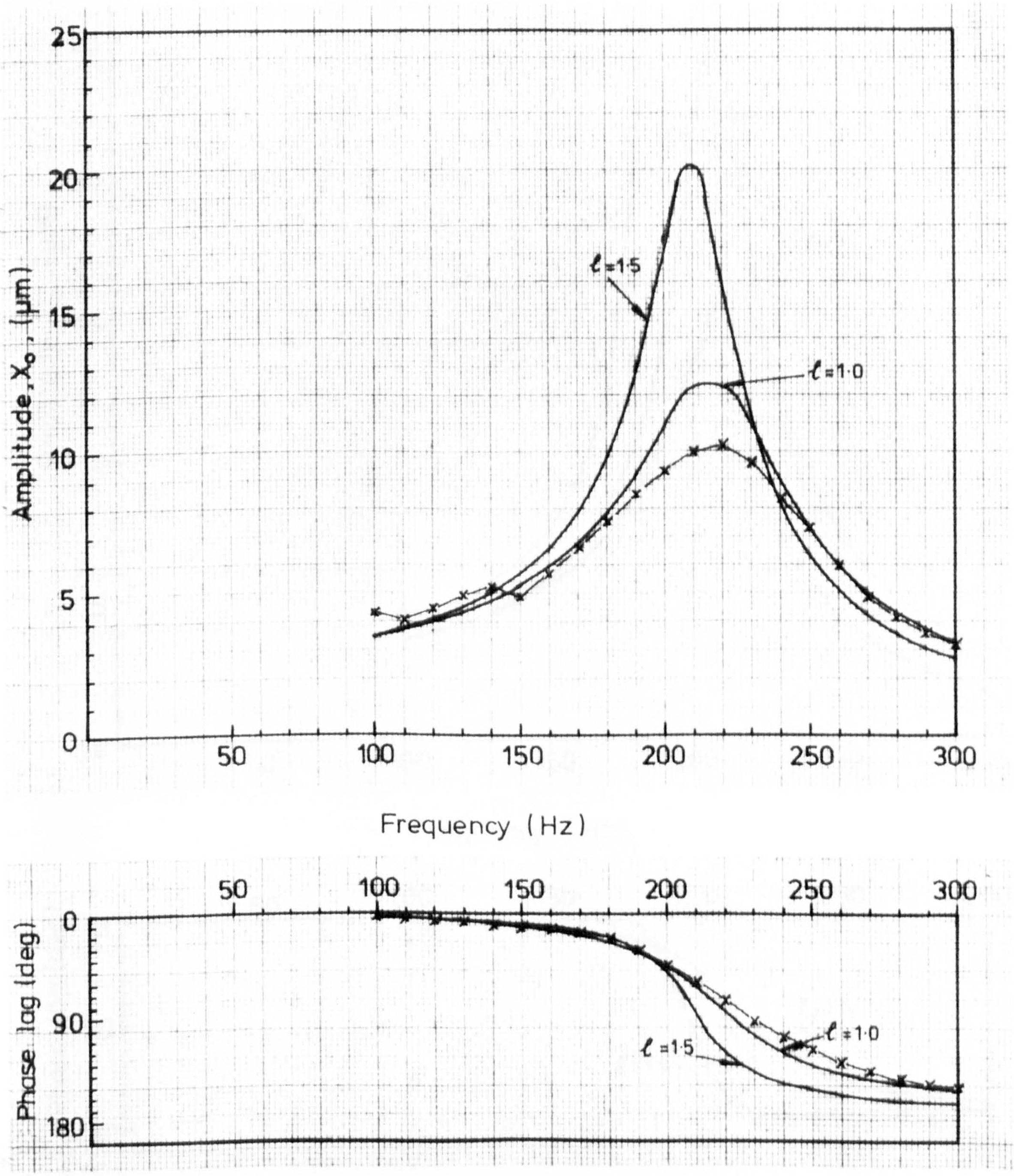

Fig 7.21 Horizontal frequency response of optimally tuned main-slug tungsten-bunged bar

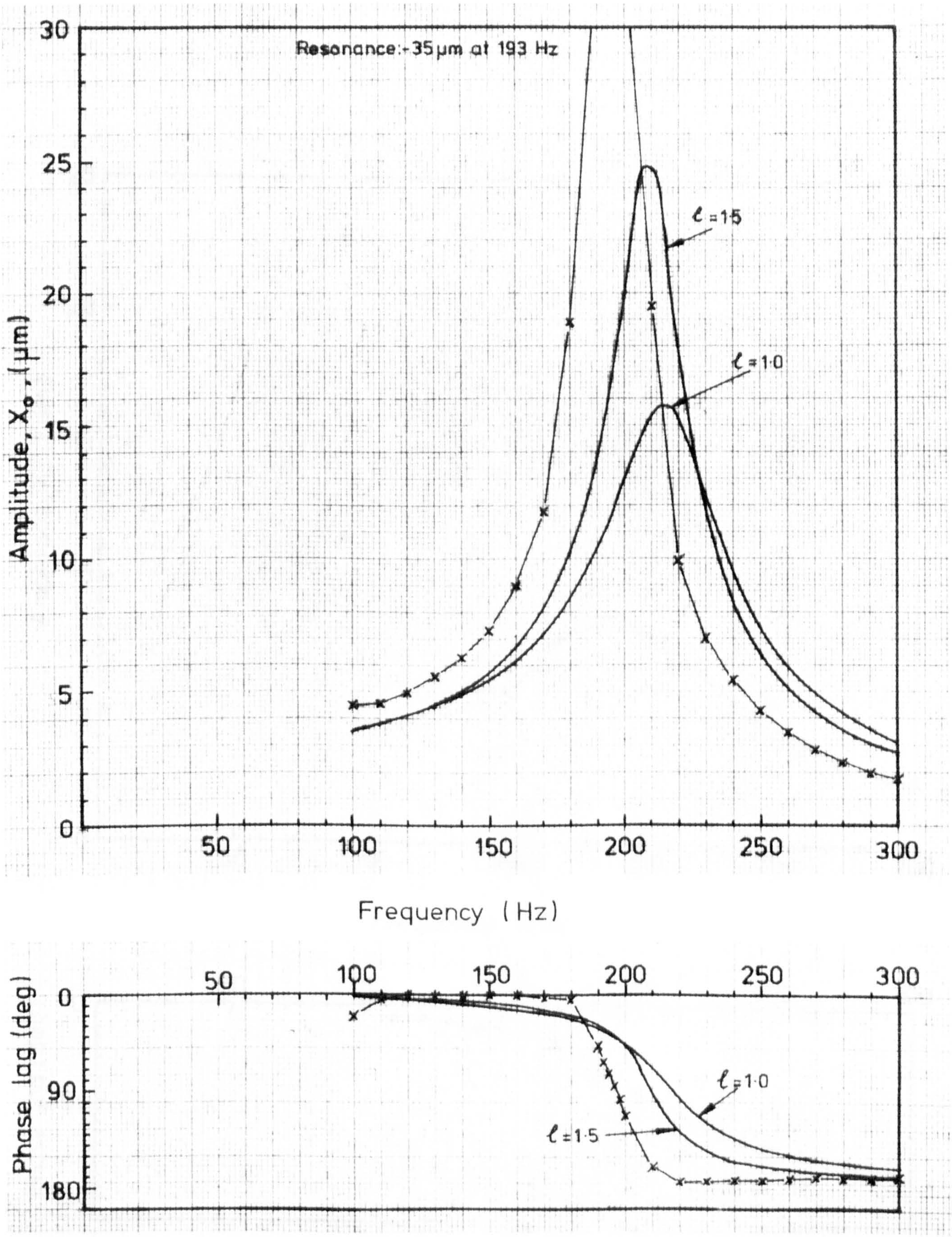

Fig 7.22 Vertical frequency response of optimally tuned main-slug tungsten-bunged bar

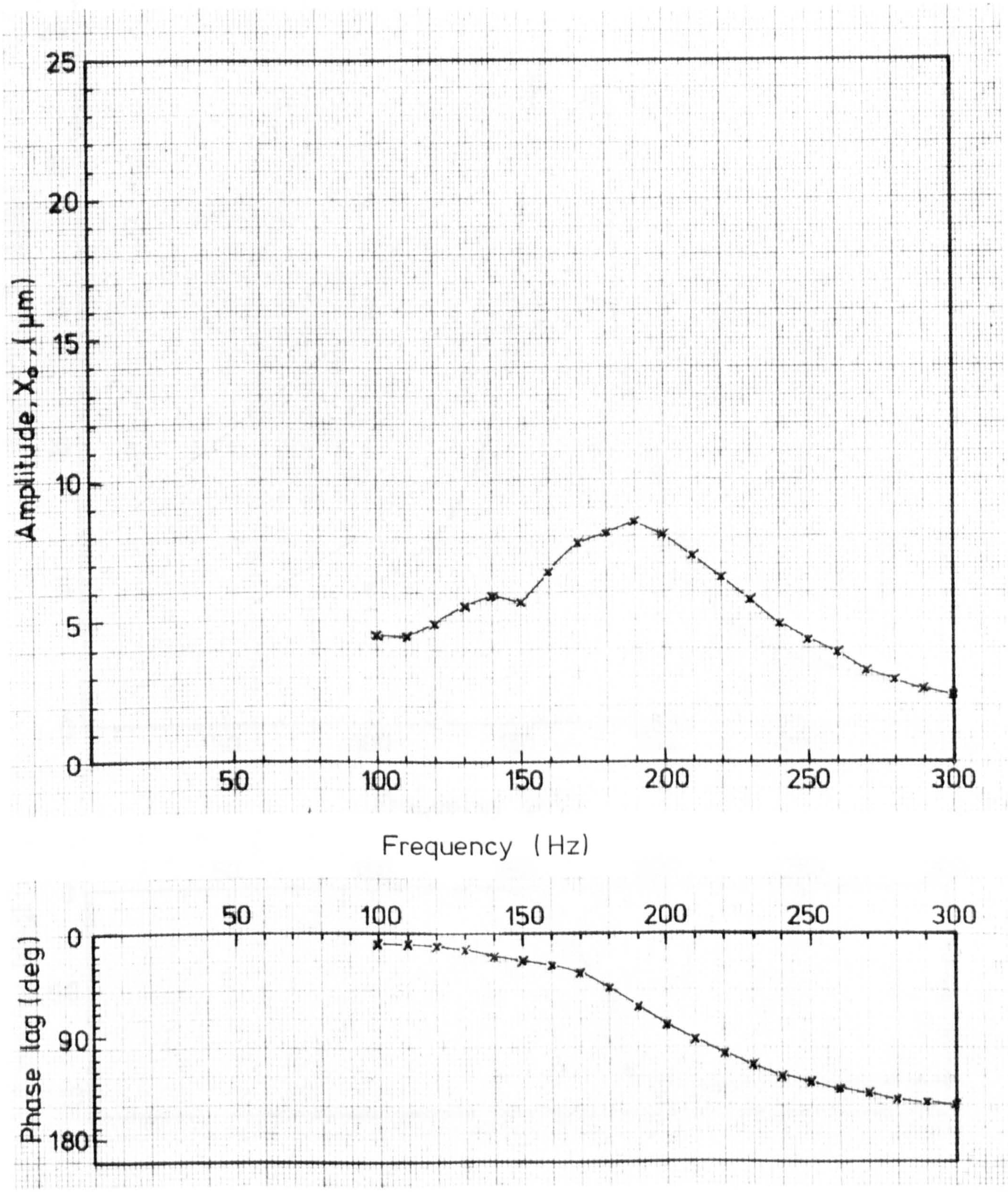

Fig 7.23 Horizontal frequency response of optimally tuned twin-slug tungsten-bunged bar

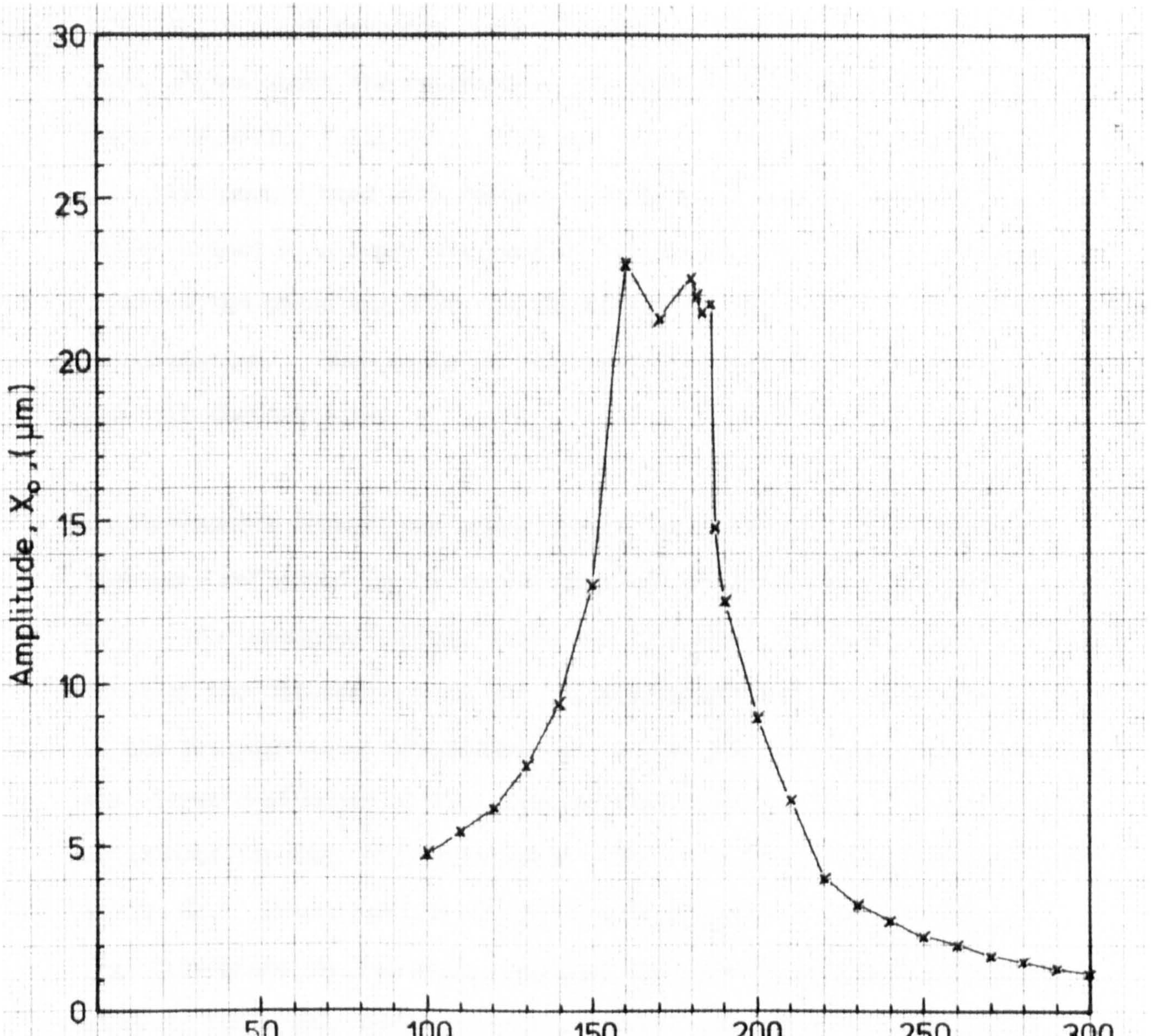

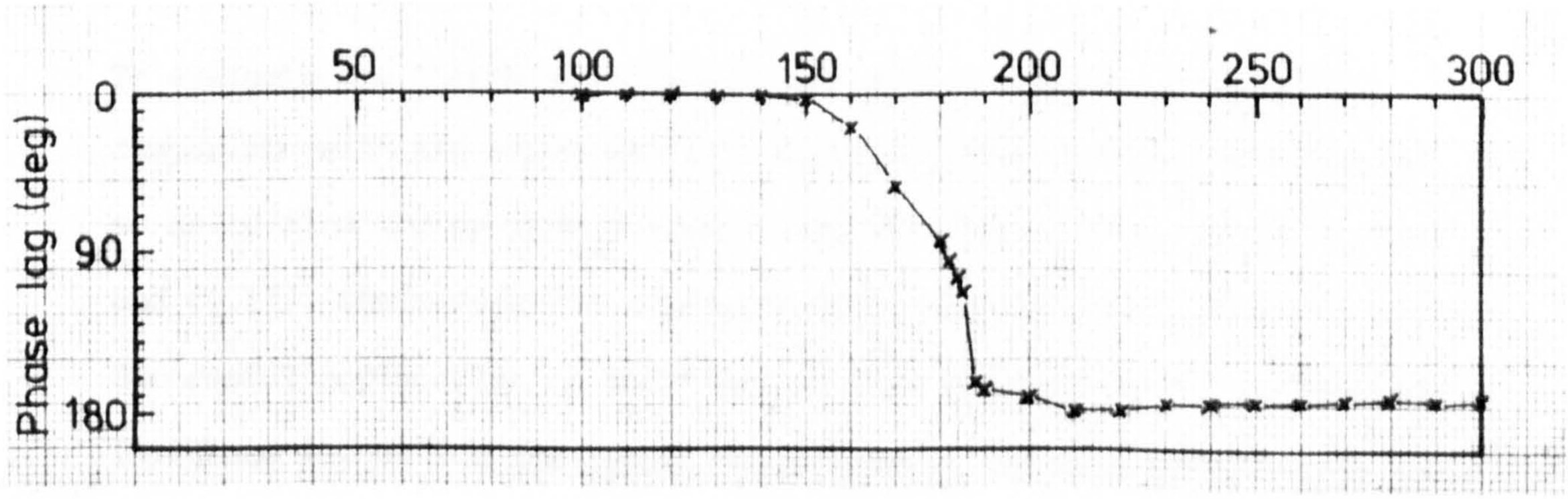

Fig 7.24 Vertical frequency response of optimally tuned twin-slug tungsten-bunged bar

Also, their phase response curves indicate a very rapid change in phase angles about the resonance. Examples can be found in Figs. 7.9, 7.10, 7.11, 7.12, 7.19 and 7.20. In contrast, boring bars that were fitted with dampers possessed an amplitude response characterised by a dome-like peak at resonance; and a phase response in which the phase angle change was more gradual with respect to the frequency of excitation. Such examples are found in Figs. 7.13 through 7.18 and 7.21 through 7.24.

The horizontal vibrational modes of the lathe occurred at frequencies that were reflected in the amplitude response curves shown in Figs. 7.15 and 7.21. For example, in Fig. 7.15, the otherwise smooth amplitude response curve of the optimally-tuned main slug steel-bunged bar shows two kinks at the frequencies of 100 Hz and 140 Hz indicating the occurrence of the vibrational modes of the lathe at these frequencies. In addition, as is noted in Fig. 7.20, the lathe has one vertical vibrational mode at 190 Hz. The influence of this vertical mode was also present in Fig. 7.24 where the resonant frequency of the bar happened to fall very close to the modal frequency of the lathe. As a result, the amplitude response curve at resonance became very irregular.

To evaluate the theoretical frequency response curves to facilitate comparison with the experimental results, equation (4.39) was employed so as to find the optimum damping ratio at which, by equations (4.16) and (4.17), the respective amplitude and phase responses were calculated. Successful application of these equations and others such as equations (4.38) and (4.40) for the respective frequency and amplitude at resonance

at this optimum damping condition requires a knowledge of the following parameters:

(a) G for tungsten-bunged bar = 0.6995 (see Section 7.6.5)

(b) G for recessed bar = 0.726 (from K.W.Ng[1])

(c) Horizontal natural frequency of tungsten-bunged bar,

f_{no} = 196 Hz (see Fig. 7.19)

(d) Horizontal natural frequency of recessed bar,

f_{no} = 183 Hz (see Fig. 7.11)

(e) Vertical natural frequency of tungsten-bunged bar,

f_{no} = 236 Hz (see Fig. 7.20)

(f) Vertical natural frequency of recessed bar

f_{no} = 181 Hz (see Fig. 7.12)

(g) Mass correction factor for the case of slug rolling,

ℓ = 1.5 approx.

(h) Mass correction factor for the case of slug sliding or floating

ℓ = 1 approx.

(i) Horizontal static deflection of tungsten-bunged bar

(See Section 7.6.2 or Table 7.2)

X_{st} = 2.683 μm

(j) Horizontal static deflection of recessed bar,

(See Section 7.6.2 or Table 7.2)

X_{st} = 3.742 μm

(k) Vertical static deflection of tungsten-bunged bar

(See Section 7.6.2 or Table 7.2)

X_{st} = 2.720 μm

(l) Vertical static deflection of recessed bar,

(see Section 7.6.2 or Table 7.2)

X_{st} = 4.099 μm

(m) Horizontal equivalent mass of tungsten-bunged bar

(see Section 7.6.5)

m = 0.708 kg

(n) Horizontal equivalent mass of recessed bar,

(see Section 7.6.5)

$$m = 0.890 \text{ kg}$$

(o) Vertical equivalent mass of tungsten-bunged bar

(see Section 7.6.5)

$$m = 0.744 \text{ kg}$$

(p) Vertical equivalent mass of recessed bar

(see Section 7.6.5)

$$m = 0.839 \text{ kg}$$

The theoretical amplitude and phase responses for the case of optimum damping were calculated using, as mentioned earlier, equations (4.39), (4.16), and (4.17). The calculated results were joined by a smooth curve and were presented as shown in Figs. 7.13, 7.14, 7.21 and 7.22 alongside the experimental results. In general, the agreement between the theory and experimental results was not satisfactory suggesting further refinements of the mathematical model were needed. Nevertheless, the existing model serves adequately in indicating the trend the response followed as the frequency was varied. A possible cause of the discrepancy will be discussed in Section 7.6.5.

Using equations (4.38), (4.39) and (4.40), it was possible to calculate the respective values of damping ratio, the amplitude at resonance and the resonant frequency at the optimum damping for any single slug-damped boring bar. The following table shows these values for the single slug-damped recessed bar and the single slug-damped tungsten-bunged bar.

In column 5 of the following table, the mass correction factor takes on the value $\ell = 1$ when it is assumed that the slug is in either a sliding or floating mode; whereas $\ell = 1.5$ when the slug is in a rotational mode.

Invariably, it is noted that in terms of minimum amplitude at resonance, a slug operating in a rotational mode is the least efficient.

Fig. No.	Bar	Direction	Mass ratio μ	Mass correction factor ℓ	Damping ratio $(\frac{c}{c_c})_{opt}$	Amplitude at res. $(X_o)_{opt}$ (μm)	Resonant freq. f_{opt}(Hz)
7.13	Recessed	Horizontal	0.2576	1	0.4706	32.79	173.2
7.14	Recessed	Vertical	0.2733	1	0.4690	34.10	169.8
7.13	Recessed	Horizontal	0.2576	1.5	0.7220	51.06	170.0
7.14	Recessed	Vertical	0.2733	1.5	0.7205	53.19	164.5
7.21	Tungsten-bunged	Horizontal	0.5444	1	0.4435	12.54	216.0
7.22	Tungsten-bunged	Vertical	0.4185	1	0.4547	15.72	214.6
7.21	Tungsten-bunged	Horizontal	0.5444	1.5	0.6983	20.15	208.6
7.22	Tungsten-bunged	Vertical	0.4185	1.5	0.7079	24.94	208.6

The mass ratio μ in column 4 of the table was calculated using the relation $\mu = G^2 \frac{m_s}{m}$, where the numerical values for G, m_s and m were taken from the list of data supplied preceding the last table.

Frequency responses were also measured on bars fitted with slug dampers other than the optimum ones that have been reported in Table 7.1. To present these responses in a compact manner, three features that may be regarded as being characteristic of the frequency response are chosen to be reported, namely:

(1) the frequency at which the amplitude lags behind the input force by 90°, termed for short the "90°-frequency";

(2) the amplitude at the 90°- frequency, termed the "90°- amplitude", and

(3) the amplitude at resonance.

These features are related to the slug size and the slug clearance. We shall consider five different cases in respect of the three features as follows:

(a) Steel-bunged bar fitted with main and auxiliary slug dampers and excited horizontally. The diameters of the main slug hole and auxiliary slug hole were measured to be 25.435 mm and 25.412 mm respectively. The main slug of diameter 25.293 mm was used, hence giving a main slug radial clearance of 0.071 mm. Based on the auxiliary slug diameters supplied in Section 7.2.3, it is also possible to work out the auxiliary slug radial clearance. The 90°-frequency, 90°-amplitude and the amplitude at resonance can then be plotted against the radial clearance as shown in Fig. 7.25a.

(b) Same as (a) except that the force was applied and the amplitude was measured in the vertical direction. Variations of these features in relation to the radial clearance are presented in Fig. 7.25b.

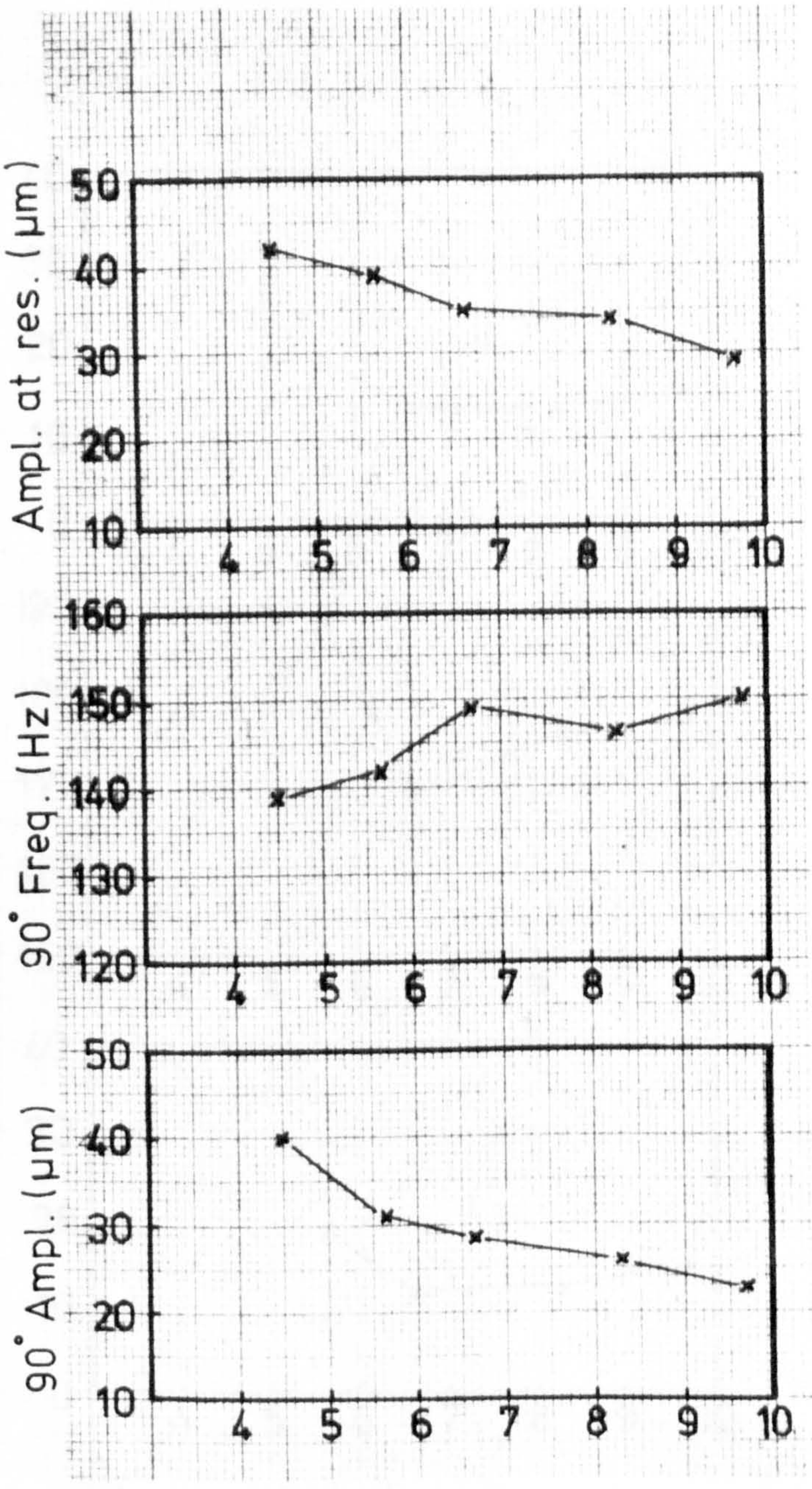

Fig 7.25a Variations of (i) amplitude at resonance, (ii) 90°- frequency, and (iii) 90°- amplitude in the horizontal direction in relation to auxiliary radial clearance of steel-bunged bar fitted with main and auxiliary slugs. Main radial clearance is 0.071 mm.

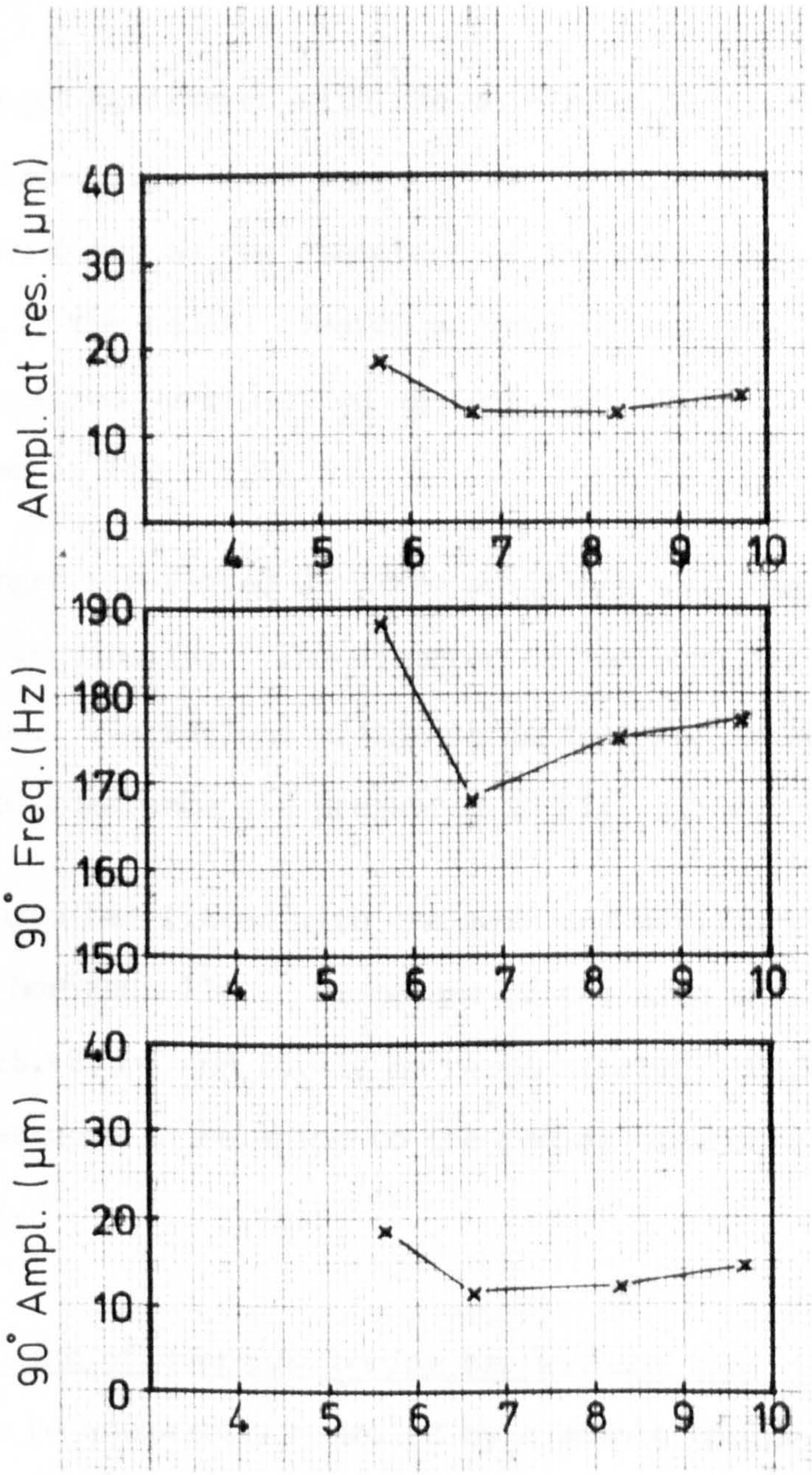

Fig 7.25b Variations of (i) amplitude at resonance, (ii) 90°- frequency, and (iii) 90°- amplitude in the vertical direction in relation to auxiliary radial clearance of steel-bunged bar fitted with main and auxiliary slugs. Main radial clearance is 0.071 mm.

(c) Tungsten-bunged bar fitted with the main slug damper only and excited horizontally. The diameter of the main slug hole was 25.433 mm and based on the diameters of the main slugs given in Section 7.2.2, the radial clearances were worked out. As before, the three features were plotted against the radial clearance and this is shown in Fig. 7.26a.

(d) Tungsten-bunged bar fitted with the auxiliary slug damper only and excited vertically. The diameter of the auxiliary slug hole was 25.412 mm. Variations of the three features in relation to the radial clearance are presented in Fig. 7.26b.

(e) Tungsten-bunged bar fitted with the main and auxiliary slug dampers and excited horizontally. Diameters of the main and auxiliary slug holes were 25.433 mm and 25.412 mm respectively. Variations of the three features in relation to the radial clearance are presented in Fig. 7.27.

7.6.2 Stiffness and damping of overhung boring bar without slug damper

The solid bar can be adequately modelled by a simple spring-mass-damper system. With the slug-dampers removed, the recessed bar, the steel-bunged bar and the tungsten-bunged bar are no different from the solid bar dynamically and hence can also be similarly modelled. From the textbook on vibrations, for a system with mass m, spring constant k, and a damping coefficient c, and subjected to a sinusoidal force P at the frequency ω, the amplitude response X_o can be expressed as

$$X_o = \frac{X_{st}}{\sqrt{\left[1-\left(\frac{\omega}{\omega_n}\right)^2\right]^2 + \left[2\frac{c}{c_c}\frac{\omega}{\omega_n}^2\right]}} \qquad \ldots (7.1)$$

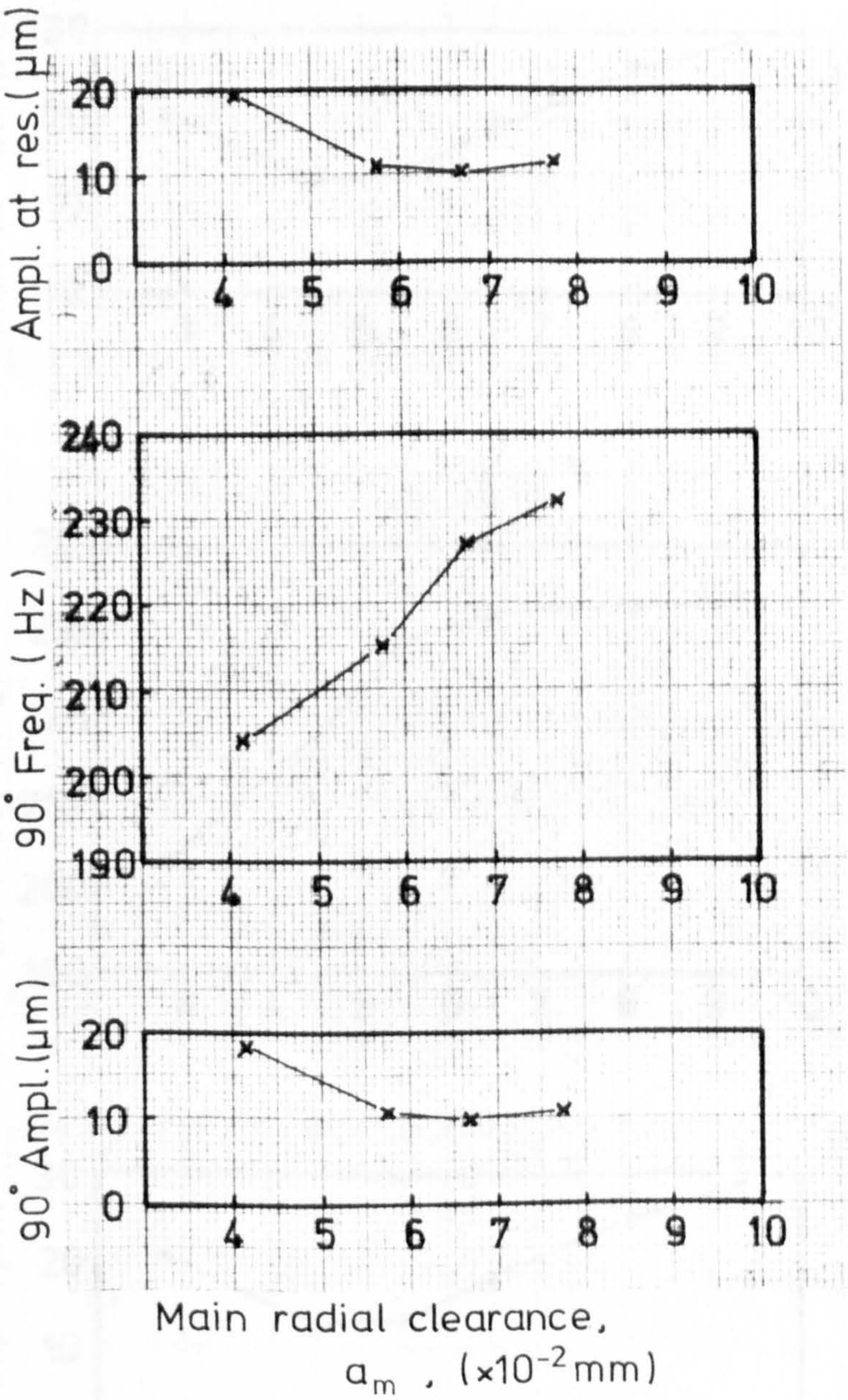

Fig 7.26a Variations of (i) amplitude at resonance, (ii) 90°- frequency and (iii) 90°- amplitude in the horizontal direction in relation to main radial clearance of tungsten-bunged bar fitted with main slug only

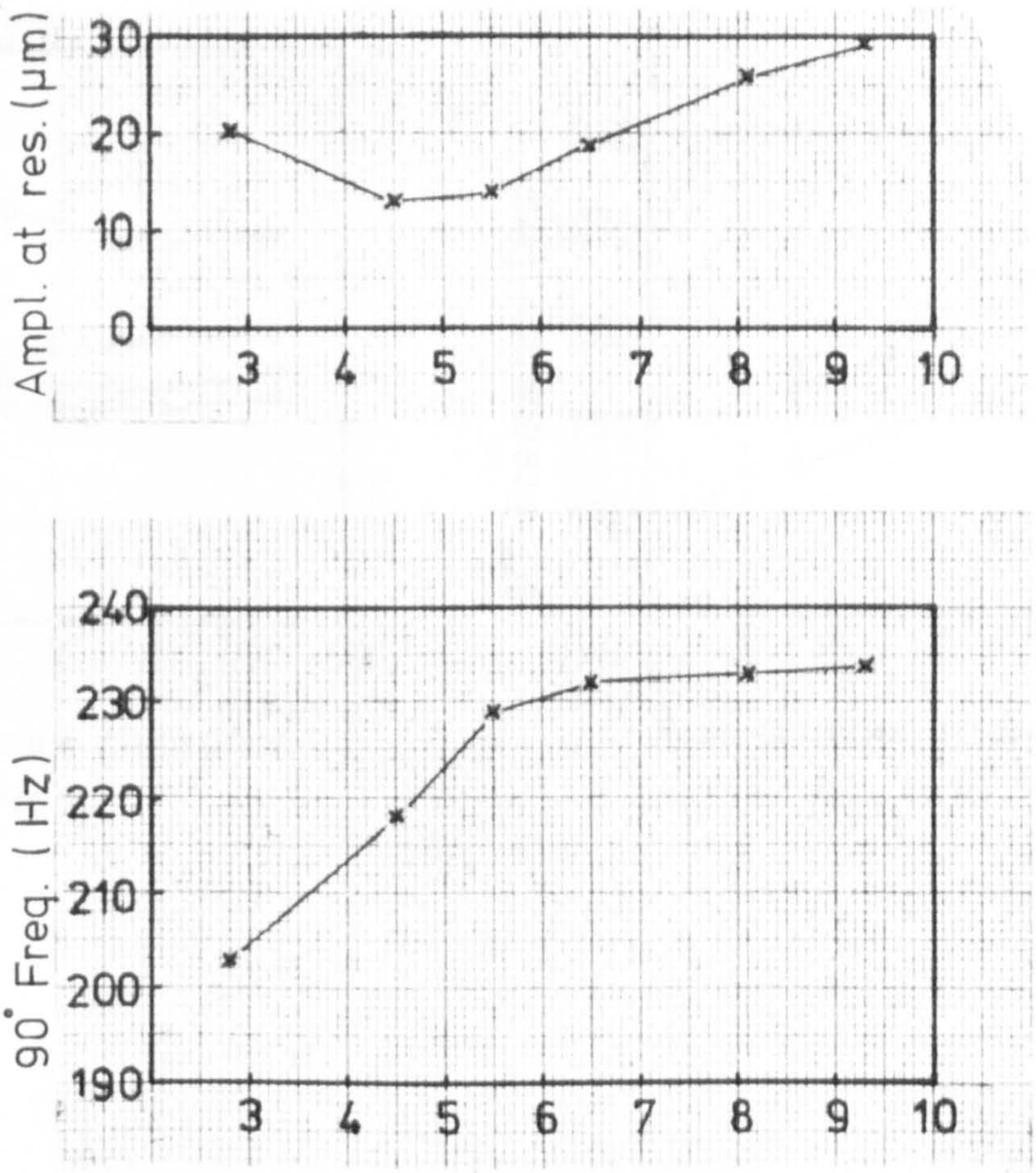

Fig 7.26b Variations of (i) amplitude at resonance, (ii) 90°- frequency, and (iii) 90°- amplitude in the vertical direction in relation to auxiliary radial clearance of tungsten-bunged bar fitted with auxiliary slug only

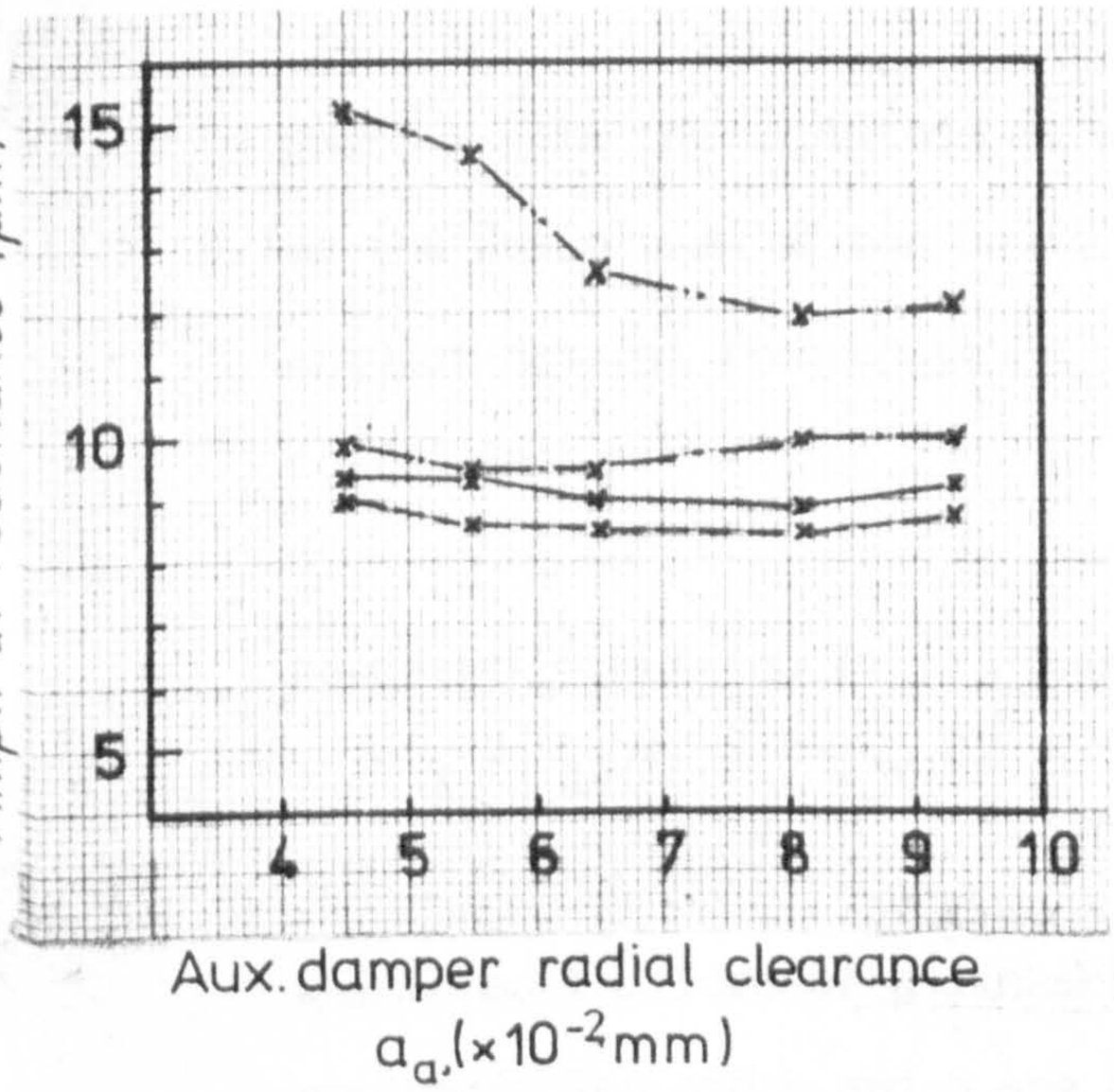

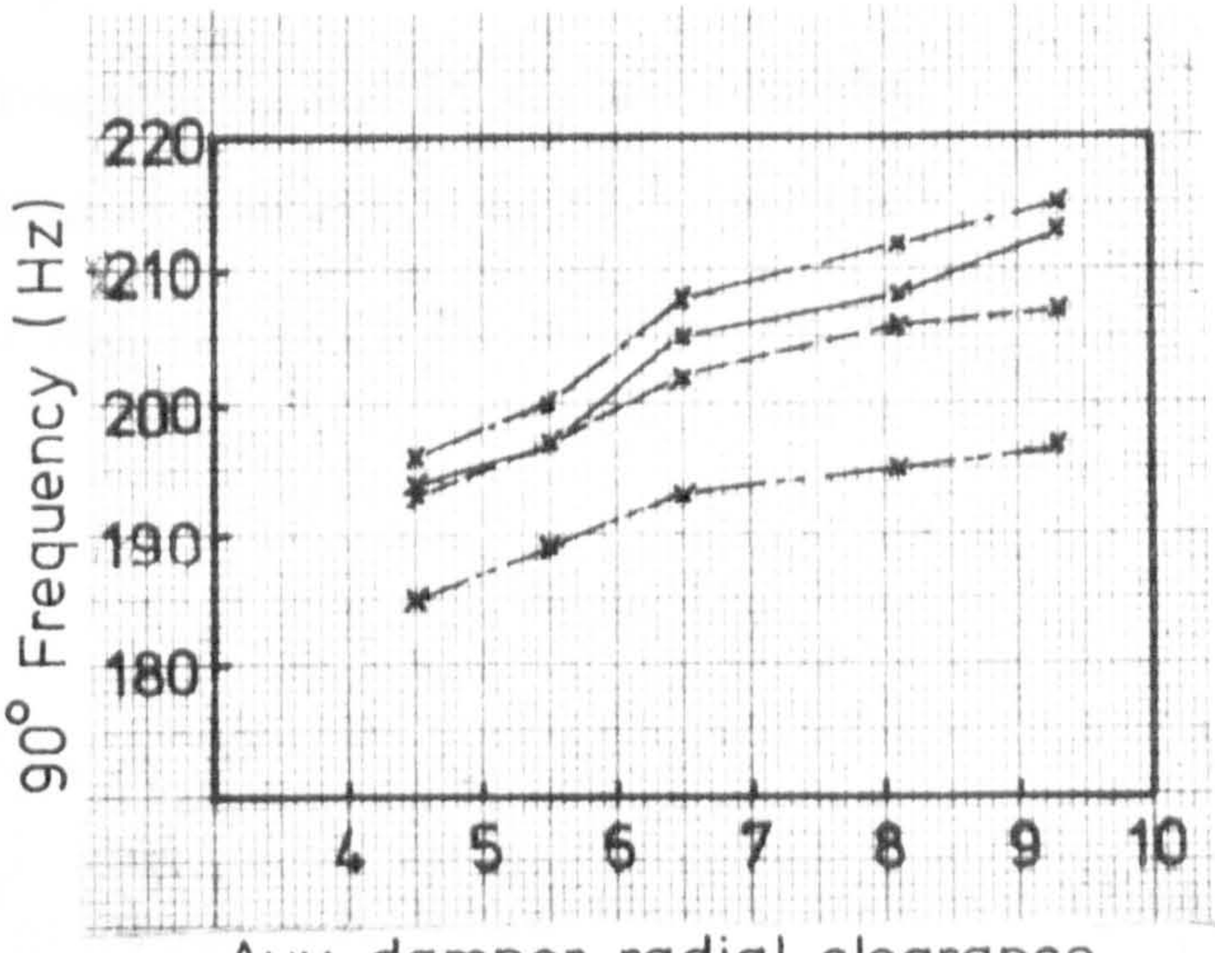

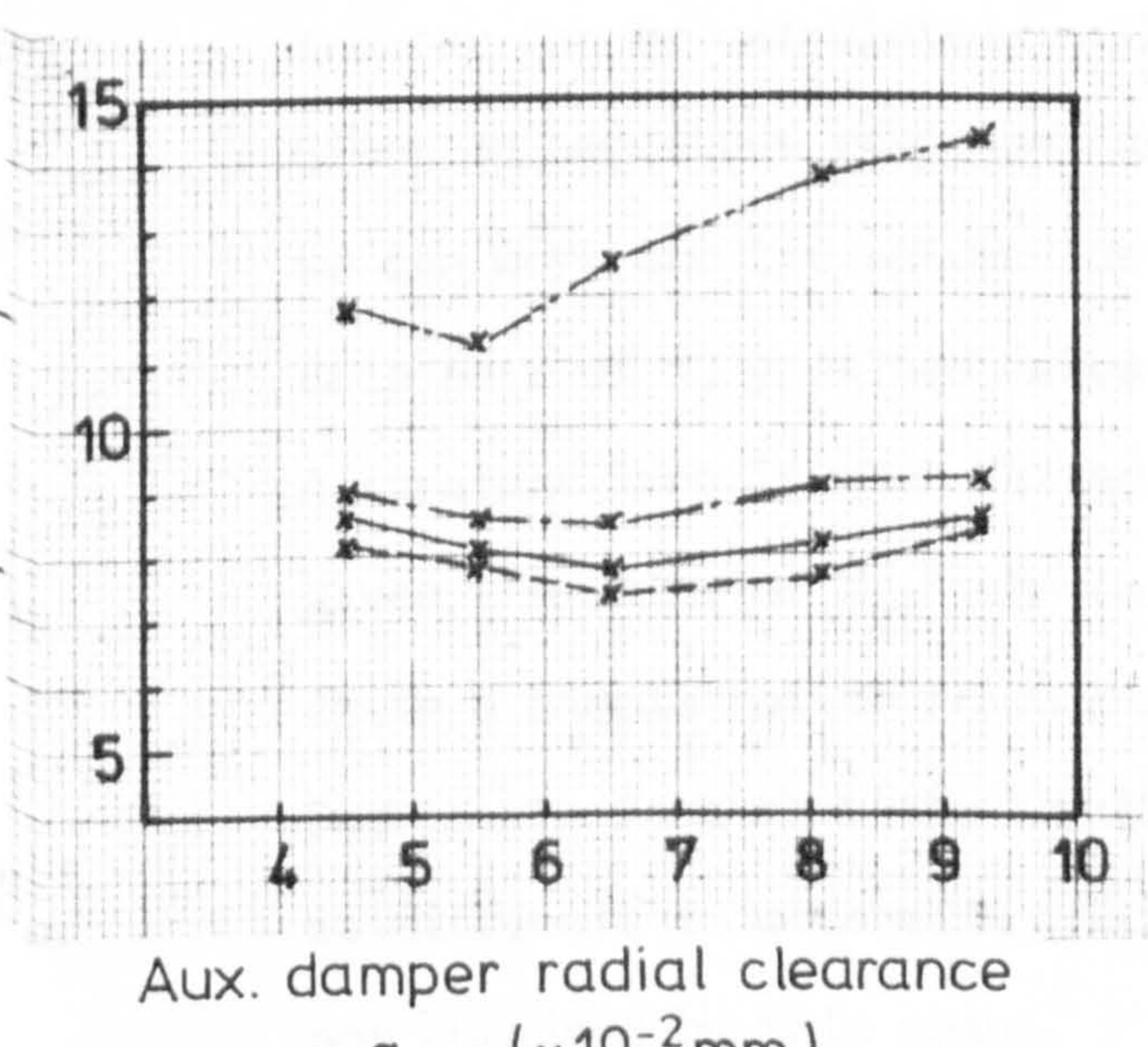

Key:

	Main damper radial clearance
———	0.0775 mm
– – – – –	0.067 mm
—·—·—·—	0.0575 mm
—··—··—	0.0415 mm

Fig 7.27 Variations of (i) amplitude at resonance, (ii) 90°- frequency, and (iii) 90°- amplitude in relation to radial clearance in horizontal direction of tungsten-bunged bar fitted with main and auxiliary slugs

where X_{st} is the amplitude at zero frequency, and it may be regarded as the deflection of bar under the static force P; $\omega_n = \sqrt{\frac{k}{m}}$ is the angular natural frequency; $c_c = 2 m\omega_n$ is the critical damping coefficient.

Re-writing equation (7.1) gives

$$X_o^2\left[1-(\frac{\omega}{\omega_n})^2\right]^2 + X_o^2\left[2\frac{c}{c_c}\frac{\omega}{\omega_n}\right]^2 = X_{st}^2 \qquad \ldots (7.2)$$

which has the form of a linear equation, y + bx = d, where y and x are variables and b and d are constants, if we identify

y to $X_o^2\left[1-(\frac{\omega}{\omega_n})^2\right]^2$, x to $X_o^2\left[\frac{\omega}{\omega_n}\right]^2$, b to $(2\frac{c}{c_c})^2$ and d to X_{st}^2.

Equation (7.2) suggests a method whereby the stiffness and damping of the bar can be calculated. The method is explained as follows.

Given an amplitude response curve of the bar obtained from experiment, we can work out the values for y and x at each frequency of excitation ω. Each pair of x, y values makes up a point on the rectangular coordinates. A straight line is then fitted through the set of points. The y-intercept gives the value of X_{st}^2 whereas the slope is $-(2\frac{c}{c_c})^2$. Since $X_{st} = \frac{P}{K}$, it is a simple matter to calculate the stiffness K from this relation. Due to the fact that the amount of scatter of the set of points makes it difficult to determine the slope reliably, the damping ratio $\frac{c}{c_c}$ is not obtained by this means.

Figs. 7.28(a) and (b) are examples of the results obtained from applying this method to the tungsten-bunged bar excited in the respective horizontal and vertical directions. Similar graphs which are not shown here can also be drawn for determining the stiffness k of other bars.

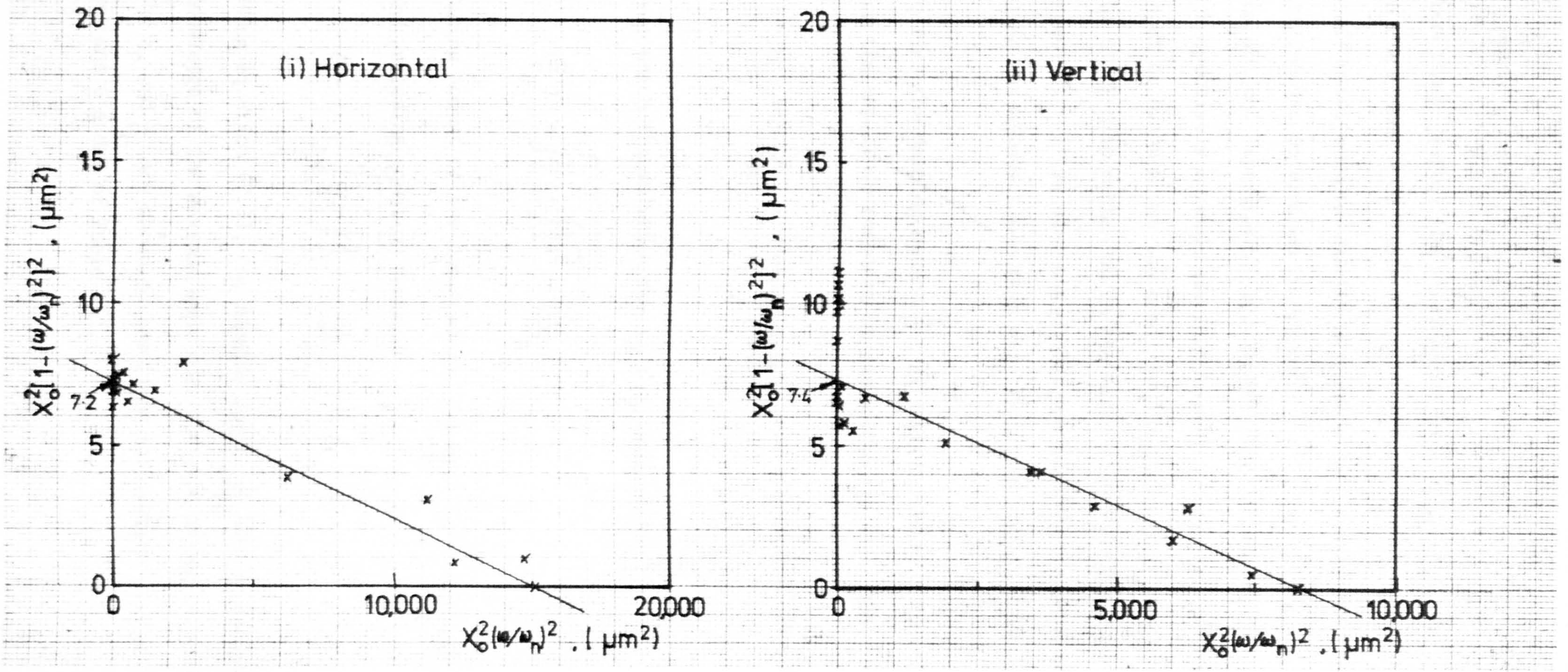

Fig 7.28 Linear graphs for finding the equivalent stiffness in (i) horizontal and (ii) vertical directions of tungsten-bunged bar

From these graphs, the stiffnesses were calculated and were entered in the column 4 of Table 7.2. The values of X_{st} from which the stiffnesses were calculated are given in column 3 and the theoretical stiffnesses determined in Appendix A are shown in column 5. On comparison, experimental and theoretical stiffnesses in columns 4 and 5 respectively agreed remarkably well. Since the sinusoidal force input of 4.448 N was too small to initiate any possible operation of the stick-slip mechanism in the machine tool, the agreement was to be expected. It is also noted that experimental stiffness in the vertical plane was always lower than that in the horizontal plane.

To find the damping ratio $\frac{c}{c_c}$, it is preferable to use the expression for the amplitude response at resonance $X_p^{(2)}$. That is

$$M_p = \frac{X_p}{X_{st}} = \frac{1}{2\frac{c}{c_c}\sqrt{1-(\frac{c}{c_c})^2}} \qquad \begin{cases} 0 \leqslant \frac{c}{c_c} \leqslant 0.707 \\ M_p \geqslant 1 \end{cases}$$

from which the solution for $(\frac{c}{c_c})$ is obtained as

$$(\frac{c}{c_c}) = \sqrt{\frac{1}{2} \pm \sqrt{(\frac{1}{2})^2 - \frac{1}{4M_p}}}$$

Taking acount of the constraints $0 \leqslant \frac{c}{c_c} \leqslant 0.707$ and $\frac{X_p}{X_{st}} \geqslant 1$ the preceding equation becomes

$$(\frac{c}{c_c}) = \sqrt{\frac{1}{2} - \sqrt{(\frac{1}{2})^2 - \frac{1}{4M_p}}} \qquad \ldots (7.3)$$

Using equation (7.3), the damping ratio $\frac{c}{c_c}$ can be calculated from a knowledge of the maximum amplitude ratio M_p derived from experiment. The X_p and $\frac{c}{c_c}$ are shown as the first six entries in the respective columns 6 and 7 of Table 7.2.

Bar	Direction	Static Deflection X_{st} (μm)	Expt.Stiffn. K (MN/m)	Theo.Stiffn. K (MN/m)	Max.Ampl. X_p (μm)	Damping Ratio c/c_c	P.O.(%)
Solid	Horizontal Vertical	3.742 4.111	1.189 1.082	1.110 1.110	177 250	0.01057 0.00822	96.73 97.45
Recessed	Horizontal Vertical	3.742 4.099	1.189 1.085	1.107 1.107	207 286	0.00904 0.00717	97.20 97.77
Tungsten-bunged	Horizontal Vertical	2.683 2.720	1.658 1.635	1.652 1.652	123 91	0.01091 0.01495	96.63 95.41
Recessed & opt. slug	Horizontal Vertical	3.742 4.099	1.189 1.085	1.107 1.107	22.7 49	0.08270 0.04186	77.05 87.67
Steel-bunged & main opt. slug	Horizontal Vertical	6.16* 6.16*	- -	0.722 0.722	22.6 34.5	0.13850 0.09022	64.45 75.23
Steel-bunged & main & aux opt. slugs	Horizontal Vertical	6.16* 6.16*	- -	0.722 0.722	34 12.1	0.09156 0.26575	74.91 42.06
Tungsten-bunged & main opt. slug	Horizontal Vertical	2.683 2.720	1.658 1.635	1.652 1.652	10.2 35.1	0.13271 0.03878	65.66 88.52
Tungsten-bunged & main & aux opt. slugs	Horizontal Vertical	2.683 2.720	1.658 1.635	1.652 1.652	8.5 22.5	0.15990 0.06056	60.12 82.62

* X_{st} is calculated from the theoretical stiffness 0.722 MN/m

Expt. - experimental stiffn. - stiffness theo. - theoretical max.ampl. - maximum amplitude
opt. - optimum aux. - auxiliary

TABLE 7.2

7.6.3 Damping of overhung boring bar with slug damper

From a control point of view [2], the roots of the characteristic equation that are located nearest the imaginary axis have a predominant influence on the transient behaviour of higher-order systems. Thus, the transient behaviour of an overhung boring bar with one or more slug dampers, which is obviously governed by a higher-order characteristic equation than two, may be approximated by a second-order system and the concept of damping ratio may be used to describe the transient behaviour of this higher-order system. It must, however, be emphasized that the term "damping ratio" is different from that which models the damping action of the slug damper in Fig. 4.1. The damping ratio for a higher-order system is simply an approximate measure of its transient behaviour. The damping ratios calculated using equation (7.3) for overhung boring bars with slug dampers are entered from the seventh entry downwards in columns 6 and 7 of Table 7.2.

7.6.4 Percent maximum overshoot as a measure of damping

A typical system response of a second-order system to a step-input is shown in Fig. 7.29. Various specifications indicative of the damping action in the transient behaviour of the system are possible. We shall choose as our specification, the percent maximum overshoot which, according to Raven [3], is defined as 100 times the maximum amount by which the response overshoots its final steady-state value divided by the final steady-state value.

For a second-order system, it can be shown [3] that the percent maximum overshoot, deisgnated as P.O. is

$$P.O. = 100\, e^{-\frac{c}{c_c}\pi \Big/ \sqrt{1-\left(\frac{c}{c_c}\right)^2}} . \qquad \ldots (7.4)$$

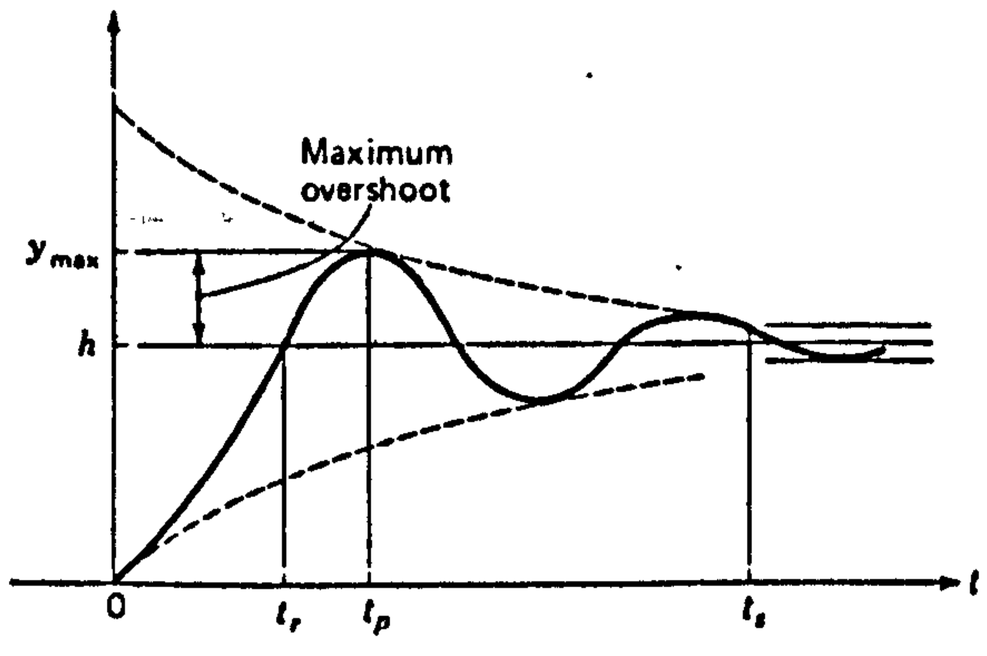

Fig 7.29 System response to a step input

Using equation (7.4), the P.O. for each bar was calculated and the results are entered in column 8 of Table 7.2.

7.6.5 Damping ratio and mass correction factor of slug damper

According to the dynamic theory developed in Chapter 4, for the case of a boring bar fitted with a single slug damper, its mass correction factor ℓ and the damping ratio $\frac{c}{c_c}$ can be determined from equations (4.21) and (4.22) that are repeated here as follows:

$$\ell = \frac{\left(\frac{X_o}{X_{st}}\right)^2 (h^2-1)\,\mu\, h^2}{(1+\mu)\left[1+(h^2-1)^2\left(\frac{X_o}{X_{st}}\right)^2\right]} \qquad \ldots (4.21)$$

and $$\frac{c}{c_c} = \frac{h}{2}\left[\frac{\ell\,\mu\,h^2}{(1+\mu)\,(h^2-1)} - \ell^2\right]^{\frac{1}{2}} \qquad \ldots (4.22)$$

where the symbols are as defined in nomenclature 4.1.

Both equations are applicable to steady-state vibrations in the horizontal as well as vertical directions. It must be noted that ℓ and $\frac{c}{c_c}$, thus calculated, are related to a particular frequency ω at which the vibrational displacement lags the impressed force by 90^o, i.e. the 90^o-frequency. Despite the assumption that $\frac{c}{c_c}$ and ℓ are to be constant in the theory, it may be possible that they will vary as ω is varied. For this reason, other means are needed to validate or disprove this particular assumption.

By definition, the natural frequency of the bar itself, f_{no}, is given by

$$f_{no} = \frac{1}{2\pi}\sqrt{\frac{K}{m}}$$

in which K is the stiffness of the bar, the value of which had already been determined as in column 4 of Table 7.2. By re-arranging this equation, the equivalent mass of the bar is obtained. Thus,

$$m = \frac{K}{(2\pi f_{no})^2} \qquad \ldots (7.6)$$

Using equation (7.6) and substituting the numerical values for K as in column 4 of Table 7.2 and for f_{no} from the amplitude response curves, the equivalent mass is calculated. The results are tabulated as follows.

BAR	DIRECTION	NATURAL FREQ. f_{no} (Hz)	EQUIV. MASS m(kg)
Recessed	Horizontal	184	0.890
Recessed	Vertical	181	0.839
Tungsten-bunged	Horizontal	244	0.708
Tungsten-bunged	Vertical	236	0.744

By definition, the natural frequency of the bar fitted with an integral slug, i.e. a slug that is not allowed to move relative to its slug hole, is given by

$$f_n = \frac{1}{2\pi}\sqrt{\frac{K}{m(1+\mu)}} \qquad \ldots (7.7)$$

where $\mu = \frac{G^2 m_s}{m}$ in which m_s is the mass of the slug damper and G the amplitude ratio as defined in Appendix B. There are two different ways of calculating G :- one is based on the static deflection theory of cantilever and the other is derived from experimental measurements. They are discussed sequentially as follows.

First, the theoretical method assumes that the overhung boring bar can be modelled by a cantilever which is subjected to a concentrated load W at a point distant ℓ_s from the fixed end as shown in the following diagram. The overall length of the cantilever is ℓ_1.

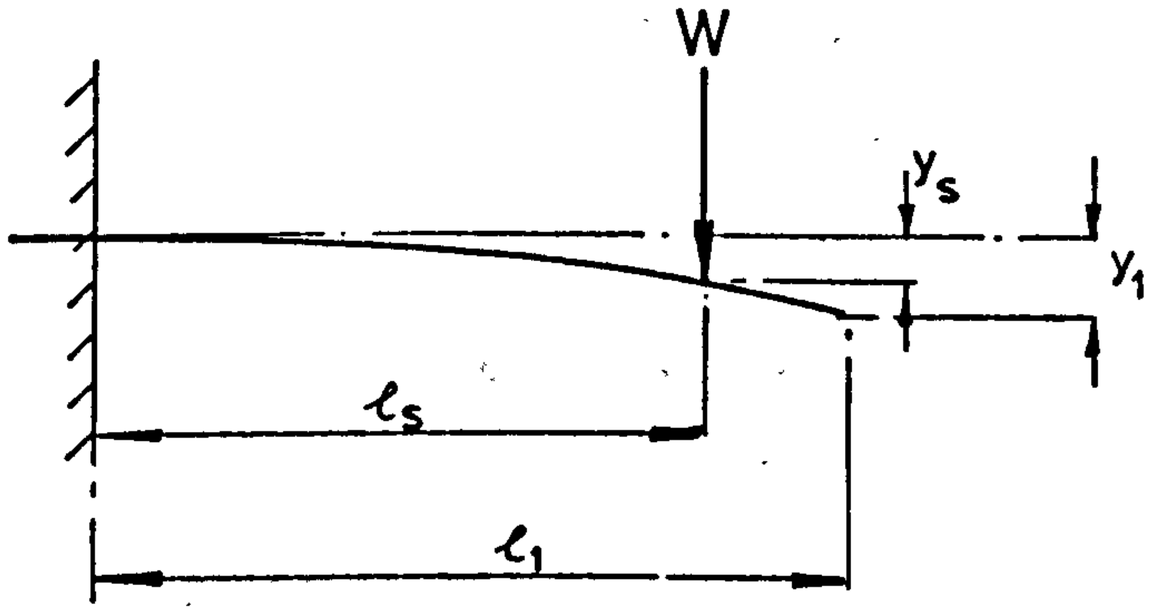

From the theory on cantilever deflections, it is noted that the displacement y_s and the slope $\left.\frac{dy}{dx}\right|_{x = \ell_s}$ at the point of application of the load W are respectively

$$y_s = \frac{W\ell_s^3}{3EI} \quad \text{and} \quad \left.\frac{dy}{dx}\right|_{x = \ell_s} = \frac{W\ell_s^2}{2EI}$$

The deflection at the free end is

$$y_1 = y_s + \left.\frac{dy}{dx}\right|_{x = \ell_s} \cdot (\ell_1 - \ell_s)$$

which can be simplified to

$$y_1 = y_s - \frac{(3\ell_1 - \ell_s)}{2\ell_s}$$

By the definition of G,

$$G = \frac{y_s}{y_1} = \frac{2\ell_s}{3\ell_1 - \ell_s} \qquad \ldots (7.8)$$

From Fig. 7.1 for the tungsten-bunged bar,

$$\ell_s = 294 \text{ mm} \quad \text{and} \quad \ell_l = 381 \text{ mm}$$

Hence, by equation (7.8), $G = \frac{2 \times 294}{3 \times 381 - 294} = 0.6926$

Next, the experimental method is employed. It is based on the amplitude response measurements conducted on a test-bed so as to simulate as closely as possible the ideally rigid end-fixing condition. Two horizontal amplitude response curves of the tungsten-bunged bar were obtained at the applied sinusoidal force of 0.919 N peak-to-zero for the cases of (a) no slug and (b) integral slug. They are as shown in Fig. 7.30 from which it is noted that:

(a) the natural frequency with no slug is $f_{no} = 244.6$ Hz, and

(b) the natural frequency with an integral slug is $f_n = 203.5$ Hz.

That is, $$f_{no} = \frac{1}{2\pi}\sqrt{\frac{K}{m}} = 244.6$$

and $$f_n = \frac{1}{2\pi}\sqrt{\frac{K}{m(1+\mu)}} = 203.5$$

Combining both equations gives $$\sqrt{1 + \mu} = \frac{244.6}{203.5}$$

from which $$\mu = \left(\frac{244.6}{203.5}\right)^2 - 1 = 0.4447$$

By definition, $\mu = \frac{G^2 m_s}{m}$ where $m_s = 0.6435$ kg for the integral slug obtained by actual weighing, and $m = 0.708$ kg for vibrations in the horizontal plane, it follows that

$$G = \sqrt{\frac{\mu m}{m_s}} = \sqrt{\frac{0.4447 \times 0.708}{0.6435}} = 0.6995$$

By comparison, the theoretical G is different from its experimental G by 1.00%. The error in the theoretical G^2 is understandably higher and is 2.00% which is acceptable. From now on, let it be agreed that

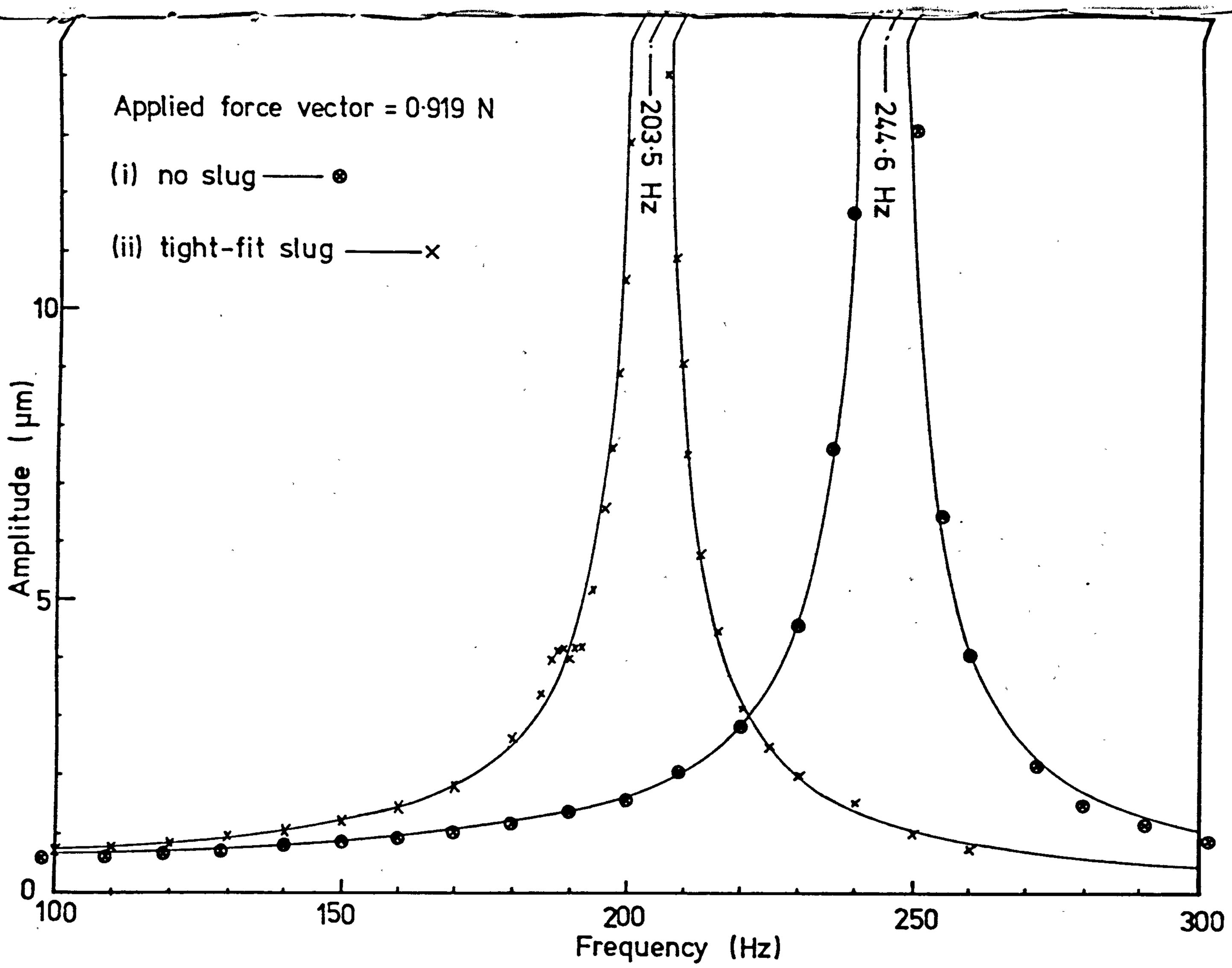

Fig 7.30 Amplitude response of tungsten-bunged bar on test-bed for the cases of (i) no slug; and (ii) tight-fit slug

G = 0.6995 in further calculations.

Two cases will be considered for the calculation of the mass correction factor ℓ and the damping ratio $\frac{c}{c_c}$:-

(a) For the case of the tungsten-bunged bar fitted with various main slugs and excited horizontally, the values of ℓ and $\frac{c}{c_c}$ are calculated using equations (4.21) and (4.22) for each size of the slug damper. As an example, we shall illustrate in detail the calculations involved for this bar fitted with an optimum slug whose size and mass are respectively 25.299 mm and 0.6364 kg.

By measurement, the diameter of the main slug hole in the tungsten-bunged bar is 25.433 mm. Hence the radial clearance, a_m, is (25.433 - 25.299)/2 = 0.067 mm.

From Fig. 7.21, the 90°-amplitude, which is designated as X_o in equation (4.21), is X_o = 9.8 μm; the 90°-frequency, $f_{90°}$ = 227 Hz.

Since G = 0.6995, and the equivalent mass of the tungsten bunged bar in the horizontal direction is m = 0.708 kg, the mass ratio μ can be calculated. Thus,

$$\mu = \frac{G^2 m_s}{m} = \frac{(0.6995)^2 \times 0.6364}{0.708} = 0.4398$$

The natural frequency of the tungsten-bunged bar fitted with an integral slug is

$$f_n = \frac{1}{2\pi}\sqrt{\frac{K}{m(1+\mu)}} = \frac{1}{2\pi}\sqrt{\frac{1.658 \times 10^6}{0.708 \times (1+0.4398)}}$$

$$= 203.0 \text{ Hz.}$$

and it follows that the frequency ratio

$$h = \frac{f_{go}}{f_n} = \frac{227}{203} = 1.1182$$

From Table 7.2, the static deflection of the tungsten-bunged bar under a load of 4.448 N (1 lbf) in the horizontal direction is X_{st} = 2.683 μm.

Using equation (4.21)

$$\ell = \frac{(\frac{9.8}{2.683})^2 (1.1182^2 - 1) \times 0.4\ 398 \times 1.1182^2}{(1 + 0.4398)\left[1 + (1.1182^2-1)^2 \times (\frac{9.8}{2.683})^2\right]}$$

$$= 0.6948$$

And using equation (4.22)

$$\frac{c}{c_c} = \frac{1.1182}{2} \left\{\frac{0.6948 \times 0.4398 \times 1.1182^2}{(1 + 0.4398)(1.1182^2-1)} - 0.6948^2\right\}^{\frac{1}{2}}$$

$$= 0.4247$$

Similar calculations can be performed for the tungsten-bunged bar fitted with slug dampers other than the one mentioned in the example. The results of the calculations are presented in Table 7.3. Variations of ℓ and $\frac{c}{c_c}$ in relation to the radial clearance a_m are shown in Fig. 7.31.

(b) For the case of the tungsten-bunged bar fitted with the auxiliary slug only and excited vertically, the values for ℓ and $\frac{c}{c_c}$ may be calculated in the same manner as those presented in (a). Since the centre position of the auxiliary slug is different from that of the main slug, the value of G is expected to be different. From experiment the value of G is found to be 1.0814. The results calculated are presented in Table 7.4.

Main Radial clearance a_m(mm)	90^o-Ampl. (μm)	90^o Freq. (Hz)	Slug Mass m_s(kg)	Mass ratio μ	f_n	ℓ	$\frac{c}{c_c}$
0.0775	10.8	232	0.6379	0.4409	202.9	0.7872	0.3637
0.067	9.8	227	0.6364	0.4398	203.0	0.6948	0.4247
0.0575	10.4	215	0.6410	0.4430	202.8	0.5221	0.5760
0.0415	18.2	204	0.6415	0.4433	202.7	0.1828	1.0539

TABLE 7.3

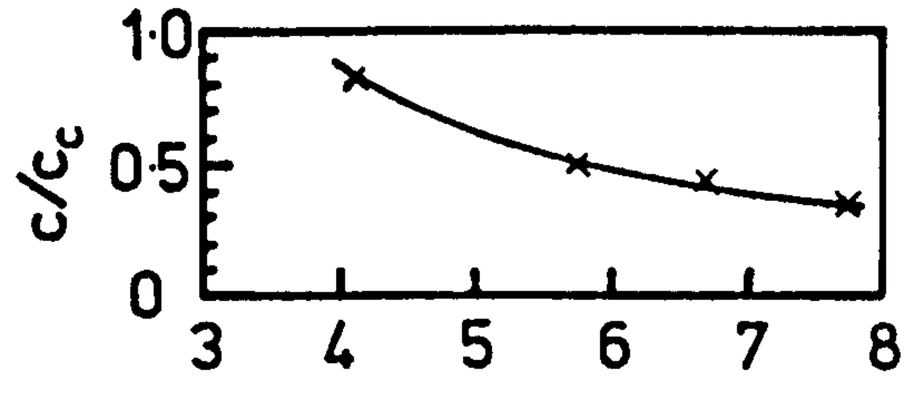

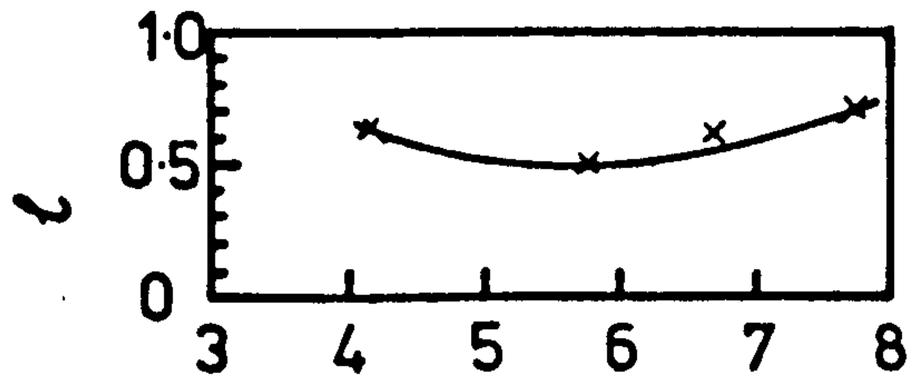

Fig 7.31 Variations of c/c_c and ℓ in relation to main damper radial clearance, a_m, of tungsten-bunged bar excited horizontally

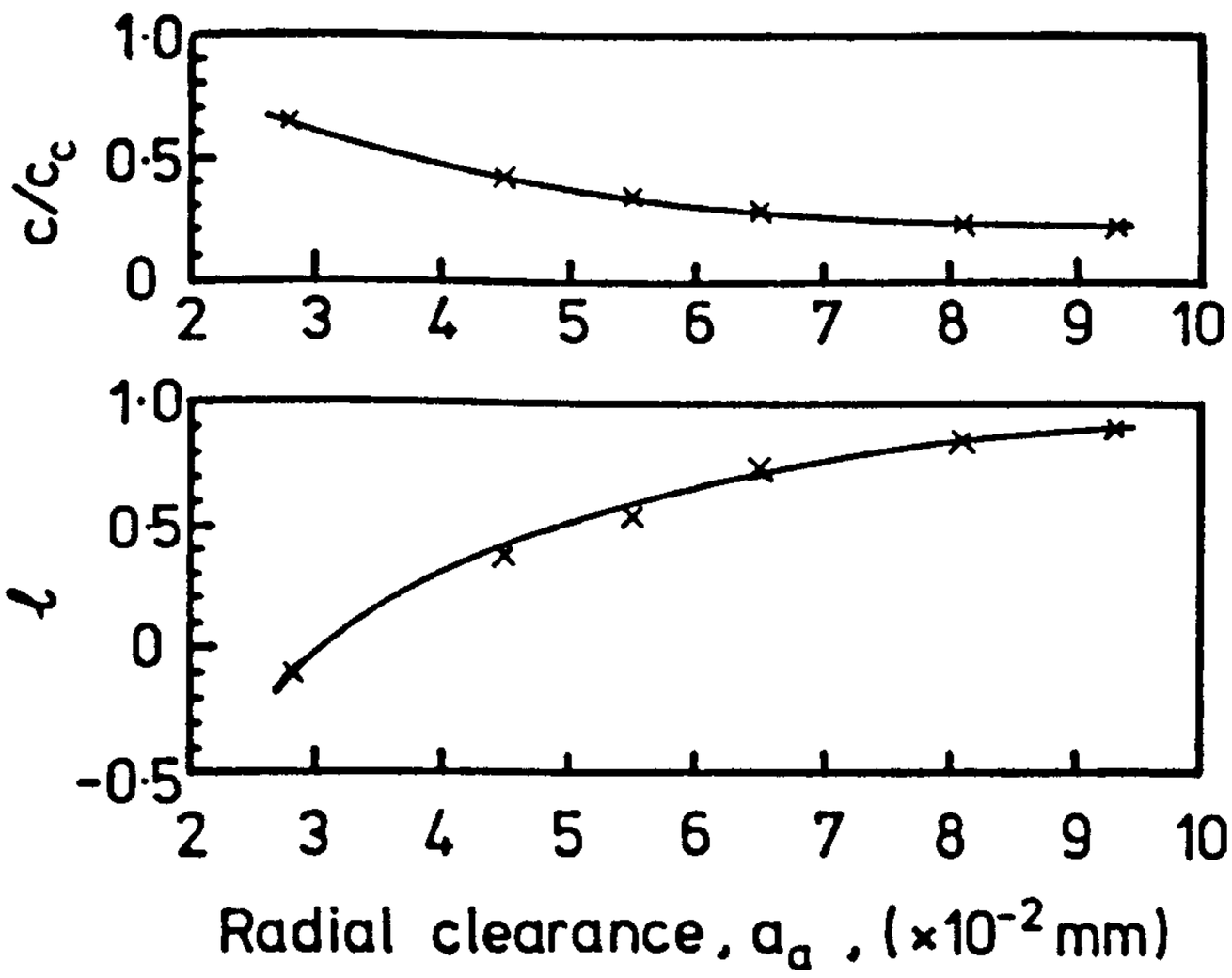

Fig 7.32 Variations of c/c_c and ℓ in relation to auxiliary damper radial clearance, a_a, of tungsten-bunged bar excited vertically

Aux. rad. clearance a_a (mm)	90^o-Ampl. (μm)	90^o Freq. (Hz)	Slug Mass m_s (kg)	Mass Ratio μ	f_n	ℓ	$\frac{c}{c_c}$
0.093	28.7	234	0.209	0.3285	204.7	0.9616	0.1698
0.081	24.8	233	0.209	0.3285	204.7	0.9526	0.2011
0.065	18.3	232	0.210	0.3301	204.6	0.8789	0.2592
0.055	13.5	229	0.210	0.3301	204.6	0.7521	0.3356
0.045	12.9	218	0.210	0.3301	204.6	0.6073	0.5043
0.028	20.2	203	0.211	0.3317	204.5	-0.1955	0.8942

TABLE 7.4

Entries for ℓ and $\frac{c}{c_c}$ are plotted against the radial clearance a_a as shown in Fig. 7.32.

If the curves in Figs. 7.31 and 7.32 are plotted in a log-log scale as shown in Figs. 7.33 and 7.34 respectively, a linear relationship becomes obvious. It follows that the damping ratio $\frac{c}{c_c}$ can be related to the radial clearance a_i (where i = m or a) by an empirical equation such as,

$$\frac{c}{c_c} = \alpha\, a_i^{\beta} \qquad \ldots (7.9)$$

where α and β are constants to be calculated from the log-log graphs.

(a) For the tungsten-bunged bar fitted with different sizes of main slugs and excited horizontally, the empirical equation is calculated to be

$$\frac{c}{c_c} = 4.5976 \times 10^{-3}\, a_m^{-1.6977} \qquad \ldots (7.10)$$

where $0.0415 \text{ mm} \leqslant a_m \leqslant 0.0775 \text{ mm}$

Extreme caution must be exercised when using equation (7.10) outside the limits specified for a_m.

(b) For the same bar but fitted with different sizes of auxiliary slugs and excited vertically, the empirical equation is

$$\frac{c}{c_c} = 6.4831 \times 10^{-3}\, a_a^{-1.3764} \qquad \ldots (7.11)$$

where $0.028 \text{ mm} \leqslant a_a \leqslant 0.093 \text{ mm}$

Referring to Figs. 7.33 and 7.34, it is noted that the linear approximations are good. The coefficient α and the index β in equations (7.10) and (7.11) are seen to be different. This is caused by the different locations of the slug dampers and the different directions of the damping action in these two cases.

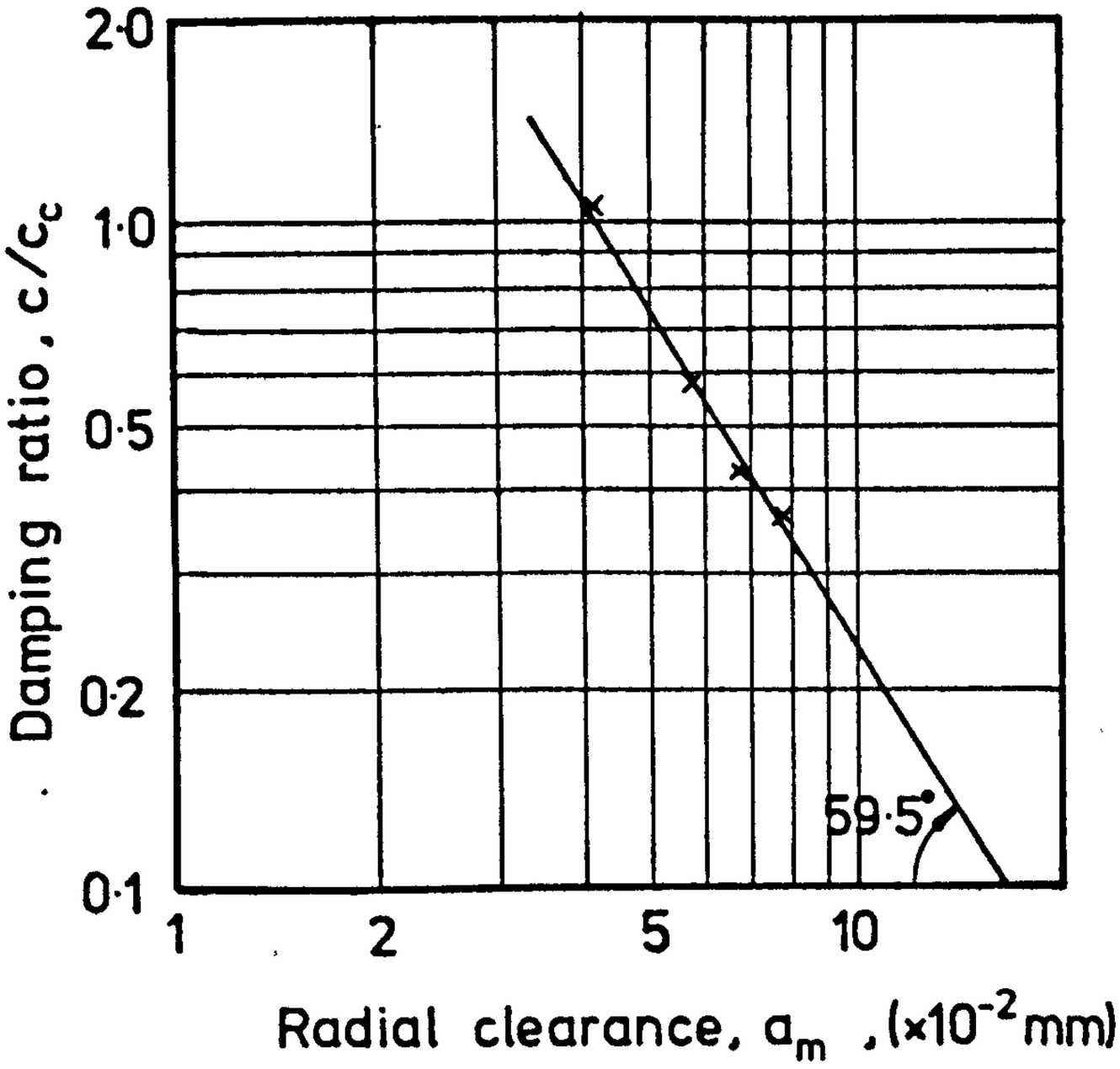

Fig 7.33 Log-log graph of damping ratio c/c_c versus radial clearance a_m in Fig 7.31

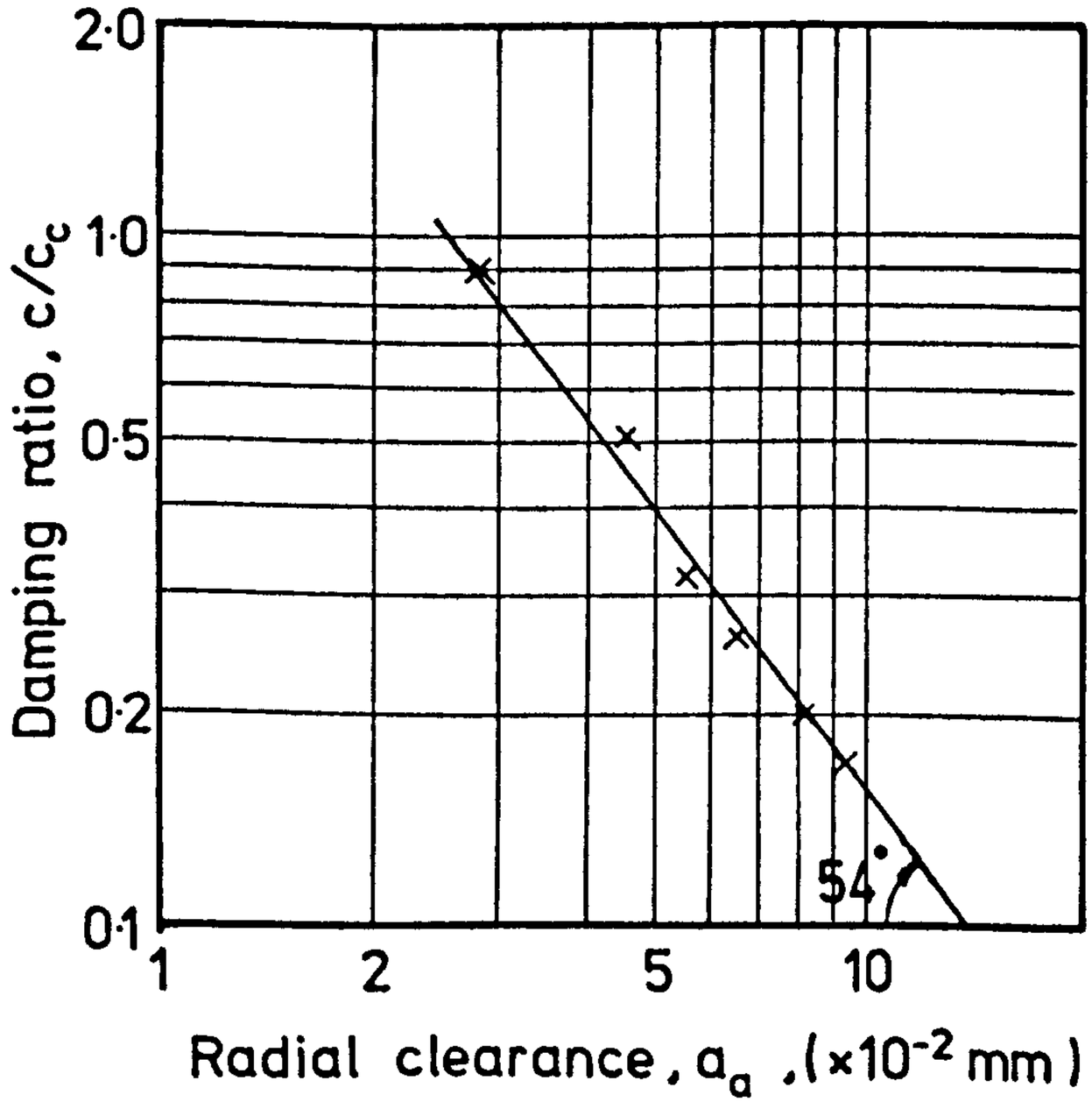

Fig 7.34 Log-log graph of damping ratio c/c_c versus radial clearance a_a in Fig 7.32

It is noted in Tables 7.3 and 7.4 that the mass correction factor ℓ, contrary to what is expected, namely $\ell = 1 + \frac{\lambda^2}{R_2^2} + \frac{m_f}{m_s}\beta_c$ hence $\ell \geq 1$, turns out to be always less than unity.

The discrepancy is better understood if it is recognised that the fluid film surrounding the slug possesses not only the damping characteristic as has been taken into account by the damping coefficient c in the mathematical analogue, but also an elasticity characteristic which may be modelled by a spring constant k_f connected in parallel with the dashpot of the analogous system shown in Fig. 4.1. Mathematically, the spring force term caused by the spring constant k_f will appear in conjunction with the inertia term and the former will have an opposite sign to that of the latter. Thus, taking account of the elasticity effect due to the fluid film, equations (4.6) and (4.7) are modified to become respectively

$$-\left[\omega^2\left(\frac{m}{G^2} + m_s\frac{\lambda^2}{R_2^2} + m_f\beta_c - \frac{k_f}{\omega^2}\right) + j\omega c + \frac{K}{G^2}\right]X_1$$

$$-\left[-\omega^2\left(m_s\frac{\lambda^2}{R_2^2} + m_f\beta_c - \frac{k_f}{\omega^2}\right) + j\omega c\right]X_2 = \frac{P_o}{G} \qquad \ldots (4.6a)$$

and

$$-\left[-\omega^2\left(m_s\frac{\lambda^2}{R_2^2} + m_f\beta_c - \frac{k_f}{\omega^2}\right) + j\omega c\right]X_1 + \left[-\omega^2\left(m_s + m_f\beta_c - \frac{k_f}{\omega^2}\right) + j\omega c\right]X_2 = 0 \qquad (4.7a)$$

Previously, ℓ was defined as $\ell = 1 + \frac{\lambda^2}{R_2^2} + \frac{m_f}{m_s}\beta_c$.

If now we introduce ℓ' to replace ℓ so that

$$\ell' = 1 + \frac{\lambda^2}{R_2^2} + \frac{m_f}{m_s}\beta_c \text{ and redefine } \ell \text{ such that } \ell = \ell' - \frac{k_f}{m_s\omega^2}$$

to account for the elasticity effect of the film, then two observations of ℓ can be made:-

(a) ℓ is now a variable, being a function of k_f, ω and m_s; and

(b) it can become negative if $\frac{k_f}{m_s\omega^2} > \ell'$

Due to the fact that the 90^o-frequency always occurs ahead of the resonant frequency, provided that k_f remains constant, the value of ℓ increases as the frequency is increased from the 90^o-frequency to the resonant frequency. It follows that ℓ at resonance will be larger than the corresponding entries suggested in Tables 7.3 or 7.4. In particular, for the optimum radial clearance, namely, 0.067 mm for the main slug and 0.065 mm for the auxiliary slug, the values of ℓ at resonance will be larger than 0.6948 and 0.8789 respectively. In view of this, the errors that may occur in the assumption that the slug slides or floats around resonance, i.e. $\ell = 1$, are not as significant as it appears at first sight. We shall not attempt to pursue any further the refinement of ℓ here apart from the remark that investigations along this line are being conducted by M. Twumasi-Boateng [4] in the Department.

Another source of error which may cause ℓ to deviate from unity stems from the fact that the frequency response was measured with the overhung boring bar mounted on the lathe. Owing to the flexibility in the elements that make up the lathe, the frequency response thus measured includes the effects of the bar as well as of the lathe. This source of error is believed to be small in comparison with that caused by the elasticity effect mentioned earlier.

7.7 CONCLUSIONS

All subsequent conclusions are made in respect of the frequency responses obtained with the applied sinusoidal force of 4.448N peak-to-zero.

1. The optimum damper for the recessed bar, the steel-bunged bar and the tungsten-bunged bar are presented in the following table

BAR	SLUG SIZE (mm)		RADIAL CLEARANCE (mm)	
	MAIN	AUXILIARY	MAIN	AUXILIARY
Recessed	25.268	-	0.0735	-
Steel-bunged	25.293	-	0.071	-
Steel-bunged	25.293	25.245	0.071	0.083
Tungsten-bunged	25.299	-	0.067	-
Tungsten-bunged	25.299	25.245	0.067	0.065

2. In the frequency range of 100 to 300 Hz, the lathe possesses
   (a) two horizontal modes of vibration at 100 and 140 Hz; and
   (b) one vertical mode of vibration at 190 Hz.

3. The experimental stiffness of the bar is in good agreement with its theoretical stiffness. The experimental stiffness is lower in the vertical plane than is the case in the horizontal plane.

4. The goodness of fit between the theoretical and experimental frequency response curves at the optimum damping condition is in general poor. But the general trend of the frequency response is adequately predicted by the theory.

5. In terms of the percent maximum overshoot (P.O. in the last column of Table 7.2) taken as a measure of the reluctance of the overhung boring bar to return to its equilibrium position after some initial disturbances, the relative performance of the boring bars can be assessed. The boring bars are listed in the ascending order of P.O. in the horizontal direction as follows:

   (a) Tungsten-bunged bar fitted with optimally-tuned main and auxiliary slug dampers.

   (b) Steel-bunged bar fitted with optimally-tuned main slug damper.

   (c) Tungsten-bunged bar fitted with optimally-tuned main slug damper.

   (d) Steel-bunged bar fitted with optimally-tuned main and auxiliary slug dampers.

   (e) Recessed bar fitted with optimally-tuned single slug damper.

   (f) Tungsten-bunged bar without damper.

   (g) Solid bar without damper.

   (h) Recessed bar without damper.

6. For the tungsten-bunged bar fitted with different sizes of main slug dampers and excited horizontally, the variation of $\frac{c}{c}$ in relation to the radial clearance a_m is given by the empirical equation

$$\frac{c}{c_c} = 4.5976 \times 10^{-3} \, a_m^{-1.6977} \qquad \ldots (7.10)$$

where $0.0415 \text{ mm} \leqslant a_m \leqslant 0.0775 \text{ mm}$.

7. For the tungsten-bunged bar fitted with different sizes of auxiliary slug dampers and excited vertically, the variation

of $\frac{c}{c_c}$ in relation to the radial clearance a_a is given by

$$\frac{c}{c_c} = 6.4831 \times 10^{-3} \; a_a^{\,-1.3764} \qquad \ldots (7.11)$$

where $0.028 \text{ mm} \leq a_a \leq 0.093 \text{ mm}.$

8. The mass correction factor ℓ is observed to be lower than unity, which is inconsistent with the assumption of ℓ. Two sources of error are suggested:

   (a) that the elasticity effect of the fluid film is significant and has to be accounted for properly, and

   (b) that the dynamics of the lathe modify the frequency response of the overhung boring bar measured and hence the mass correction factor ℓ thus calculated is affected.

REFERENCES FOR CHAPTER 7

1. NG, K.W., and NEW, R.W. "Dynamic behaviour of new designs of damped boring bars under forced vibratory conditions", S.R.C. Research Report BB1, October 1977, Department of Production Technology, Brunel University.

2. RAVEN, F.H., "Automatic Control Engineering", 3rd edition, McGraw Hill, pp. 416-417.

3. RAVEN, F.H., "Automatic Control Engineering", 3rd edition, McGraw Hill, pp. 178-181.

4. TWUMASI-BOATENG, M., "The Slug Damper: Mechanism of Operation and Squeeze Film Effects of a Compressible Damping Fluid", Ph.D. Thesis, 1980, Department of Production Technology, Brunel University.

8. BORING STABILITY TESTS

There are three objectives to be fulfilled in this chapter, namely,

(a) to elucidate the considerations undertaken in the design stage of the boring tests,

(b) to report on the test results of various boring bars with reference to their stability behaviour during boring, and

(c) to assess the goodness of fit of the stability model developed in Appendix E.

8.1 DESIGN OF EXPERIMENTS

As was reviewed in section 2.2, vibrations in cutting, known as chatter, are caused by:

(1) the cutting process dynamics,

(2) the machine tool dynamics at the tool point where cutting forces are generated, and

(3) the mutual directional orientation of the preceding two factors.

Despite the analytical complexities of the cutting process dynamics, some major influencing parameters may be readily identifiable, namely, the work material, tool geometry, tool wear, tool material, workpiece temperature, cutting speed, feed and depth of cut. With the exception of the workpiece temperature and tool wear, all parameters are readily controllable in the design stage, or during the course of the test. Invariably, any test will have to be such designed that some or all of the controllable parameters are varied independently of each other and their effects on machining stability will be observed. Tool wear and workpiece temperature, owing to their possible effects on the cutting process dynamics, hence the machining stability, will have to be

monitored within close limits so that their effects can be regarded as constant. On account of the time constraint, we chose to experiment on two different workpiece materials with tools of two different tool geometry. Detailed investigation was conducted, however, on one of these two workpiece materials, specifically the EN8 steel, and with one of the tools. The cutting speed, having noted to have less influence on machining stability compared with other parameters, was made to vary in large discrete steps whereas the feed and depth of cut were made to vary in finer discrete steps that were within the practical range of profile boring.

The dynamics of the machine tool at the tool point can be considered to be the vectorial sum of the dynamics of individual elements that make up the machine tool at the tool point. In the case of boring, the boring bar itself possesses dynamics - commonly represented by its frequency response curve - whose contribution towards the overall dynamics is extremely significant. The overall dynamics can also be modified substantially if the workpiece to be machined is flexible. Since the objective of the investigation is mainly to assess the machining behaviour of different designs of boring bar, elements other than the boring bar within the system must be made relatively rigid so that their resulting dynamics is small in comparison with that of the bar. For this reason and the other reason that the flow of chip during boring must not be restricted, the shape of the workpiece takes the form of a collar as described in Section 6.1.2 and Section 8.2.

The criterion of stability is based on the absence of chatter marks on the machined surface. Very often, this is good enough. However, surface irregularities that can sometimes be mistaken as chatter marks can also occur as a consequence of a phenomenon known as forced vibration

as discussed in Section 2.2. Usually on a lathe, forced vibrations arise from elements that have to undergo periodic motions and if these elements are not properly balanced, centrifugal forces will be set up and will leave their marks of a periodic nature on the machined surface. In view of this, before the test was started, possible causes of forced vibrations on the lathe were identified and eliminated.

Machining stability results were obtained using the tungsten-bunged boring bar whose bung length was optimised using the theories developed in Chapters 3 and 4. Specifically, the theory in Chapter 3 provides the optimum length in terms of the maximum dynamic stiffness at resonance that can be achieved; whereas the theory in Chapter 4 gives the optimum length in terms of the maximum stability limit against chatter. Appendices C and D show respectively the methods for calculating the optimum bung length based on the theories presented in Chapters 3 and 4. It is noted that both methods give roughly the same value for the optimum bung length, namely 220 mm, according to which the tungsten-bunged bar was manufactured for test purposes. Ideally in order to test the validity of the theories, one needs to experiment with a series of tungsten-bunged bar, each having a different bung length. Unfortunately, owing to the cost incurred in this alternative option, we have to be satisfied with only one tungsten-bunged bar. It follows that the results can in no way indicate that the bar is of the optimum bung length although comparison with other designs in respect of their machining capability still holds.

8.2 INSTRUMENTATION AND EQUIPMENT

Details of the boring bars, the slug dampers, the bar-holder and the lathe on which the boring tests were conducted are presented in Sections 7.1 through 7.4.

1. Boring tool

Although a number of boring tools were tried, basically the results to be reported and discussed were obtained from the use of two tools of the same tool material but of different tool geometry. For brevity they are labelled as:

(a) University specification tool, designated as the U tool - Sandvik Coromant circular shank left-handed boring tool tool No. 140-3/8" dia., with a brazed-on carbide tip. The tool geometry is as shown in Fig. 8.1 in which it is noted that the tool shank is at an angle of 59^{o} measured from the longitudinal axis of the bar. Nose radii of 0.010" and 0.030" were used.

(b) Rolls Royce specification tool, designated as the "R tool" - Also a Sandvik Coromant circular shank left-handed tool as in (a). Nevertheless, the tool geometry is different and is as shown in Fig:6.19. Nose radius of 0.030" was used.

2. Workpiece

Two different workpiece materials were used, namely:

(a) Steel BS970: 955-EN8, a 40' normalized carbon steel. Details of its mechanical properties can be found in Section 6.3.2. Nominal dimensions of the workpiece are: 5" O.D. (127 mm), $3\frac{1}{2}$" I.D. (89 mm) and a thickness of 1" (25 mm).

(b) 3% Chrome molybdenum nitriding steel, designated as RRS/HBH steel by Rolls Royce Ltd. which was the supplier of this steel for test purposes. The average Brinell hardness of this batch was measured to be 395. Dimensions of the workpiece are: $4\frac{1}{2}$" O.D. (110 mm), 3" to $3\frac{1}{2}$" I.D. (75 to 90 mm), and a thickness of 2" (50 mm).

Type:- Coromant circular shank no.140-3/8 in dia.

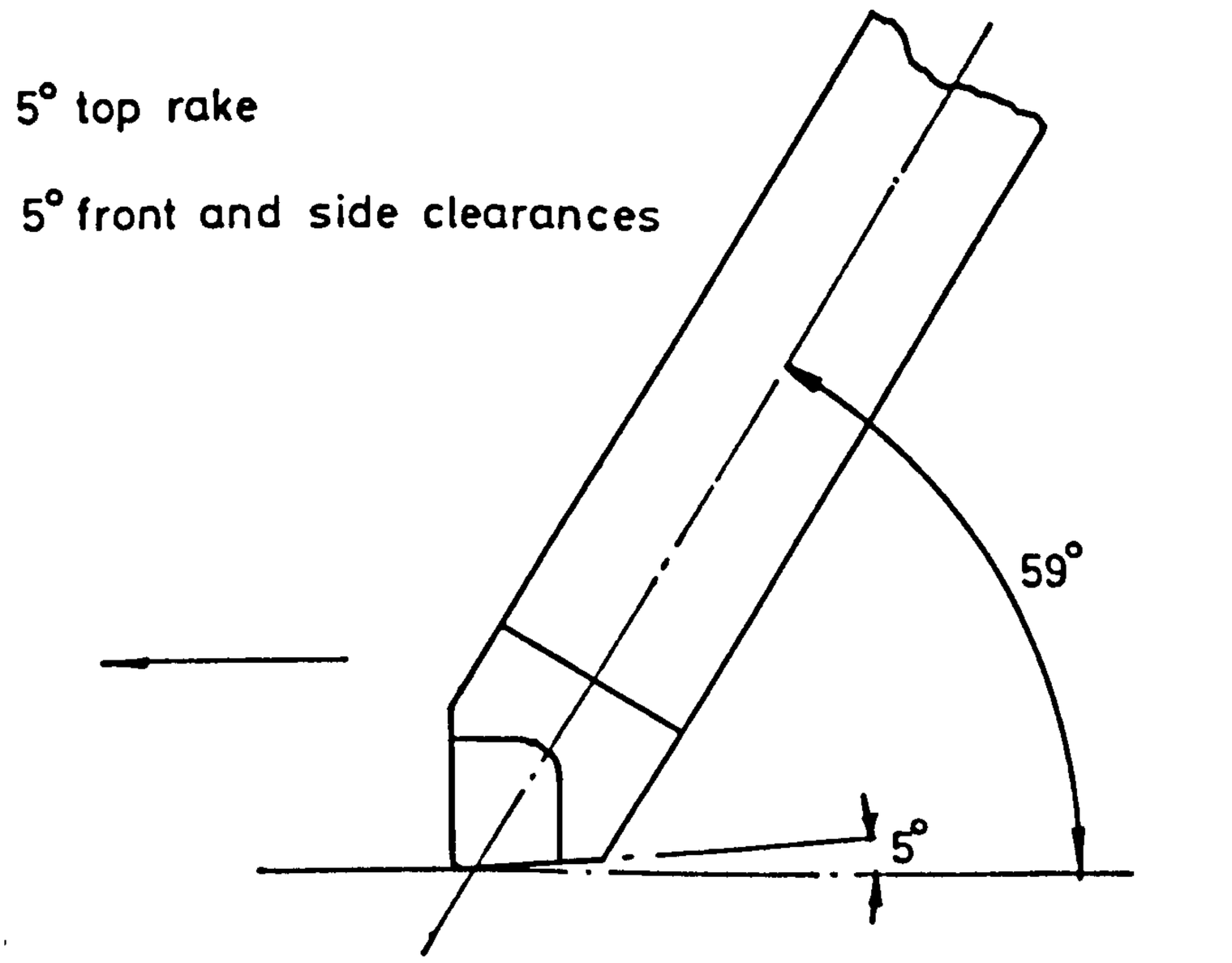

Nose radius:-0·010 or 0·030 in

Fig 8.1 Nomenclature and geometry of the U tool used in the stability test

Other instruments employed in the tests include:

(a) Tachometer for measuring the spindle speed of the lathe, from which the actual cutting speed can be calculated if desired.

(b) Carrier frequency bridges - Philips PR9307

(c) Set of 8 strain gauges - Philips PR9832 K/10FE etched foiled gauges with electrodes. Their arrangement in relation to the boring bar and their connection in the bridge circuit are shown in Fig. 7.7.

8.3. OBJECTS

(1) To study the effect of cutting speed, depth of cut and feed on machining stability.

(2) To compare the machining capability of different boring bars in respect of their maximum depth of cut before the occurrence of chatter.

(3) To assess the goodness of fit of the stability theory presented in Appendix E.

8.4. PROCEDURE

The set-up is shown in the photograph of Fig. 8.2. It is noted that a stumpy boring bar is mounted end to end with the boring bar under test. To ensure a consistent chatter-free finish of high quality on the surface to be bored, and a pre-test bore concentric with the axis of rotation, the stumpy boring bar was employed to prepare such a surface prior to any test cut. Indexing of the two bars into their cutting position was achieved by allowing the bar holder to rotate about an axis normal to its base by securing after indexing the bar holder to the slide with four bolts located in the four corners of the base.

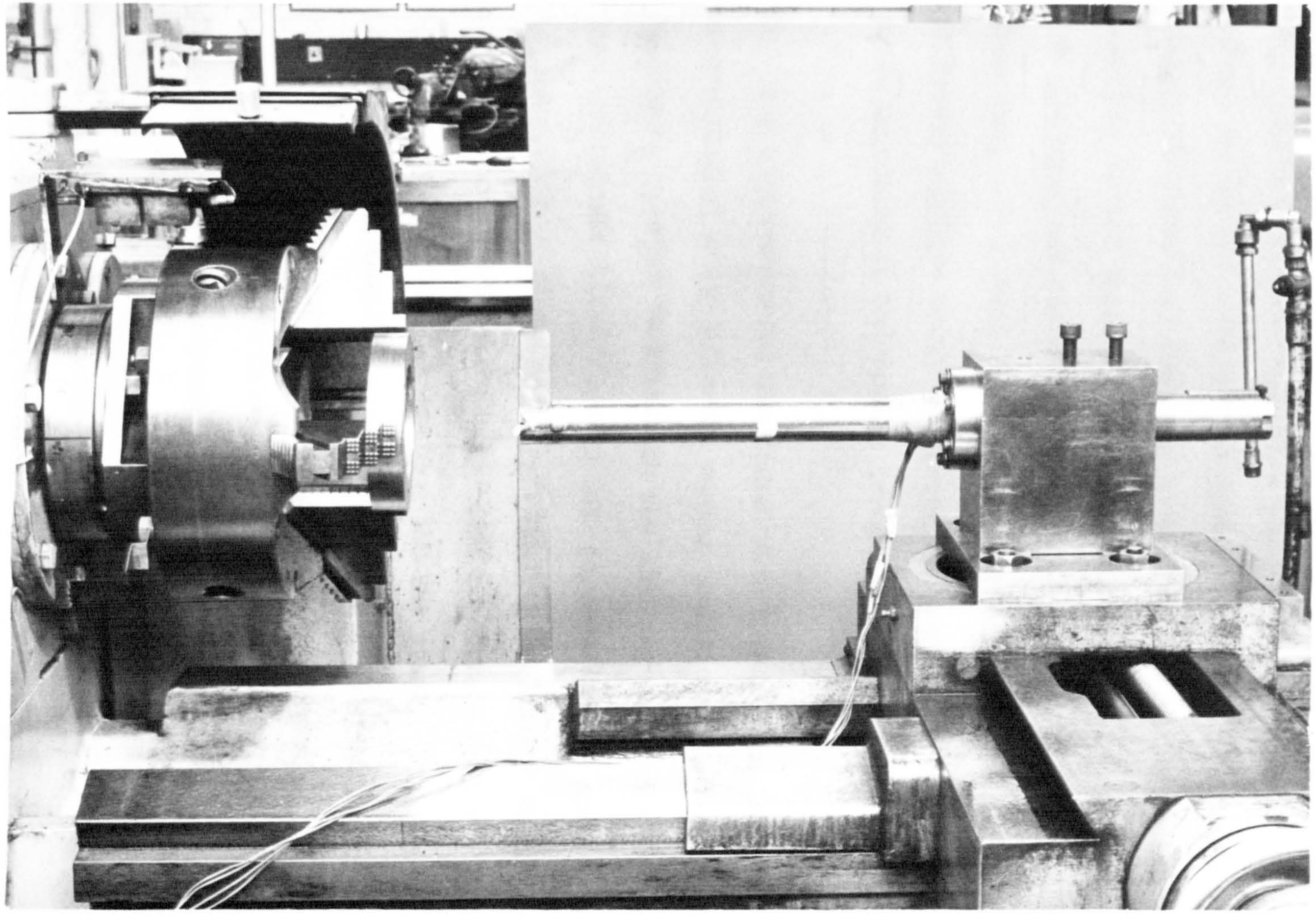

Fig 8.2 Set-up for boring stability test

The cutting tool tip on the boring bar under test was carefully adjusted so that, without any cutting load, it was 0.005" (0.127 mm) above the horizontal plane through the spindle axis. The workpiece was clamped on a three-jaw chuck and was bored first of all with a stumpy boring bar using a fine feed to obtain a good finish. The boring bar under test was then indexed to its boring position and a cut of a certain depth was taken. To economize on the workpiece material, two and sometimes three cuts of different depths were taken on the same workpiece. From time to time, attempts were made to cut into the chattered surfaces using the boring bar under test at a light cut so as to determine if the surface irregularities could be removed.

For the tungsten-bunged bar fitted with a main slug, some boring tests were conducted using different tuning conditions, i.e. different slug diameters, in order to establish the limiting depth of cut when the feed adopted was 0.0065"/rev (0.1651 mm/rev) and the spindle speed was 500 rpm on a bore diameter of $3\frac{1}{2}$", that is equivalent to a cutting speed of 458 ft/min or 140 m/min. In terms of surface quality, this condition was found to be around the optimum for EN8 steel. The tests were limited in number for it was found that repeatedly fixing and removing the boring head to allow the slug to be changed caused a loosening in the fit between the head and the bar. In consequence, the rigidity of the boring bar at the tool point deteriorated.

The main difficulty encountered in setting the depth of cut was to establish the initial reference at which the boring tool just began to contact the bore surface. The difficulty was overcome with the help of the strain gauge signals derived from the strain gauges cemented at the root end of the bar. With the carrier frequency bridge set to the most sensitive range, this initial reference was taken to be

the reading on the dial for depth of cut at which the pointer on the meter of the bridge began to deflect.

8.5 RESULTS AND DISCUSSION

Since the lathe on which the machining tests were conducted indicates feed and depth of cut readings in imperial units, it will be convenient to adopt in this report the units of inch/rev for feed and inch for depth of cut. Whenever a feed or depth of cut value is first encountered, it will be expressed in both the imperial unit and metric unit, the latter being enclosed in brackets. Any subsequent reference of the same quantity will be in imperial units only. The depth of cut was the set value as indicated on the dial of the lathe; the actual depth of cut is obviously lower.

8.5.1 Boring EN8 Steel

The following results were obtained from boring with a 0.010" (0.254 mm) nose radius U tool and are presented according to the boring bar with which the tests were conducted.

(1) Solid bar - apart from one stable cut at a depth of 0.003" (0.0762 mm), feed of 0.0065"/rev (0.1651 mm/rev), and a speed of 500 rpm, chatter always occurred under any condition. The stable cut observed, however, was not always repeatable. An example of the type of chattered surface obtained is shown in Fig. 8.14.

(2) Tungsten-bunged bar without slug - Only depths of cut below 0.007" (0.1778 mm) in the feed range of 0.0044"/rev. (0.1118 mm/rev) to 0.0104"/rev. (0.2642 mm/rev) and speed range of 400 rpm to

700 rpm could be achieved with chatter-free finish. Repeatability of results was not satisfactory, dependent significantly on the boring tool finish.

(3) Optimally-tuned main-slug recessed bar - Fig 8.3 shows the effect of depth of cut and feed on stability at the speed of 500 rpm, equivalent to 458 ft/min for a bore diameter of 3½". The stability borderline that separated the stable from the unstable cuts, ie the full dots from the circles in Fig 8.3, was difficult to locate. However, the general trend was obvious, namely, the limiting depth increased as the feed increased until the depth reached 0.025" (0.635 mm) at the feed of 0.0044"/rev and 0.0065"/rev, for heavier feeds up to 0.0104"/rev, the limiting depth decreased slightly. As can be seen from Fig 8.3 at some light depths of cut of 0.005" (0.127 mm), partly chattered surface was obtained. It seems reasonable to suggest that at these light cuts, the slug damping mechanism was not operating effectively.

(4) Optimally-tuned main-slug steel-bunged bar - Fig 8.4 shows the effect of speed on the limiting depth of cut at the feed of 0.0044"/rev. The stability borderline gradually lowered towards the high speed end of 900 rpm. At the lower speed of 250 rpm, at times difficulties arose when deciding if the surface unevenness was the consequence of instability or of the inherent poor surface finish due to the low cutting speed. Some of these results were not repeatable, as is indicated by the presence of more than one symbol

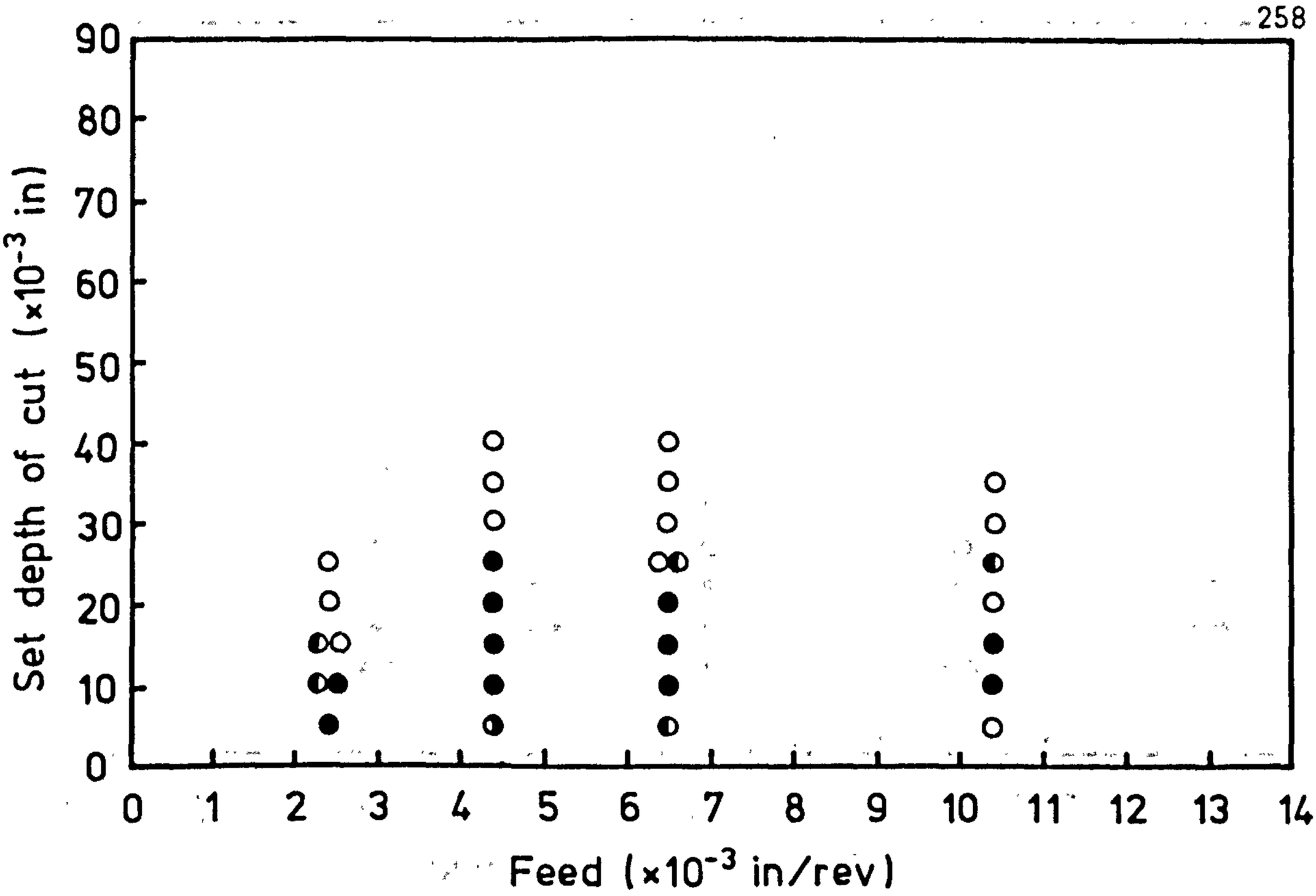

Key: ● stable

○ unstable

◐ partly stable

Material: EN8 steel

Tool: U tool 0.010" nose radius

Spindle speed: 500 rpm

Fig 8.3 Effect of depth of cut and feed on stability of optimally-tuned recessed bar

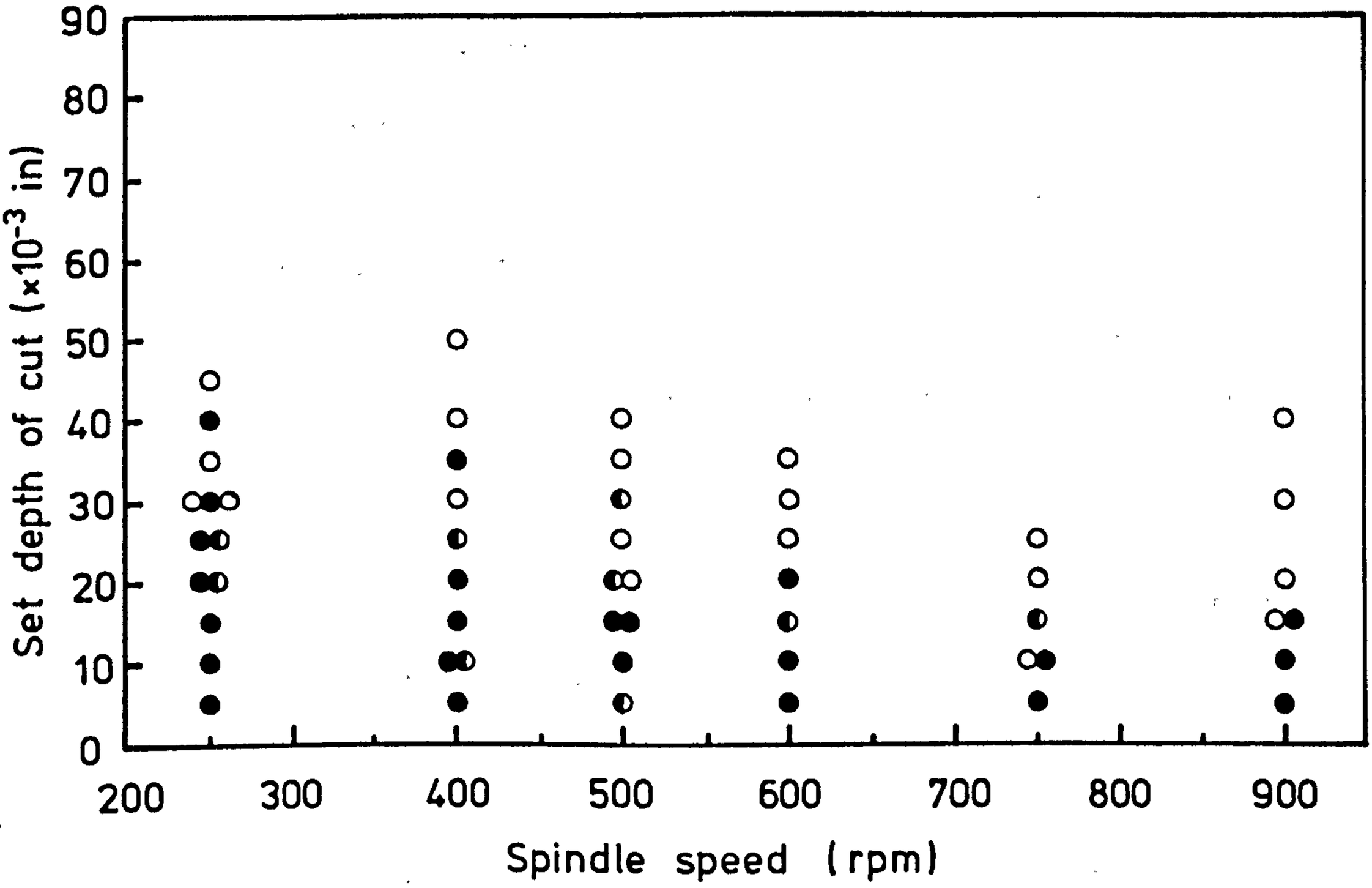

Material: EN8 steel

Feed: 0.00 44"/rev

Tool: U tool 0.010" nose radius

Fig 8.4 Effect of depth of cut and speed on stability of optimally-tuned main-slug steel-bunged bar

in Fig 8.4 at the same boring condition. Non-repeatability of performance is believed to be caused by the wear condition of the boring tool and the formation of built-up edge at low cutting speeds. At light cuts, slight tool wear was proved to be beneficial for it improved stability. The improvement was probably the result of additional damping produced by the wear land rubbing on the surface.

Fig 8.5 shows the variations of limiting depth of cut in relation to the feed when cutting at the spindle speed of 500 rpm. As the bore diameter varied slightly around the nominal value of $3\frac{1}{2}$", the real cutting speed would change within an interval whose width was acceptable since the cutting speed had little effects on the limiting depth of cut. From Fig 8.5, the maximum limiting depth of cut was somewhere between 0.025" (0.635 mm) and 0.030" (0.762 mm) at the feed of 0.0065"/rev. The stability borderline shows the same pattern of variations as that in Fig 8.3.

(5) Optimally-tuned twin-slug steel-bunged bar - Fig 8.6 shows the relation between the limiting depth of cut and feed at the speed of 500 rpm. Due to the operation of the additional slug damper, the maximum limiting depth was increased to somewhere between 0.050" (1.27 mm) and 0.060" (1.524 mm).

(6) Optimally-tuned main-slug tungsten-bunged bar - Fig 8.7 shows the effect of depth of cut and speed on stability when the feed was kept at 0.0065"/rev. It is noted that the limiting depth decreased as the cutting speed increased. At the lower cutting speed of 250 rpm, due to the formation of built-up edge, the surface finish

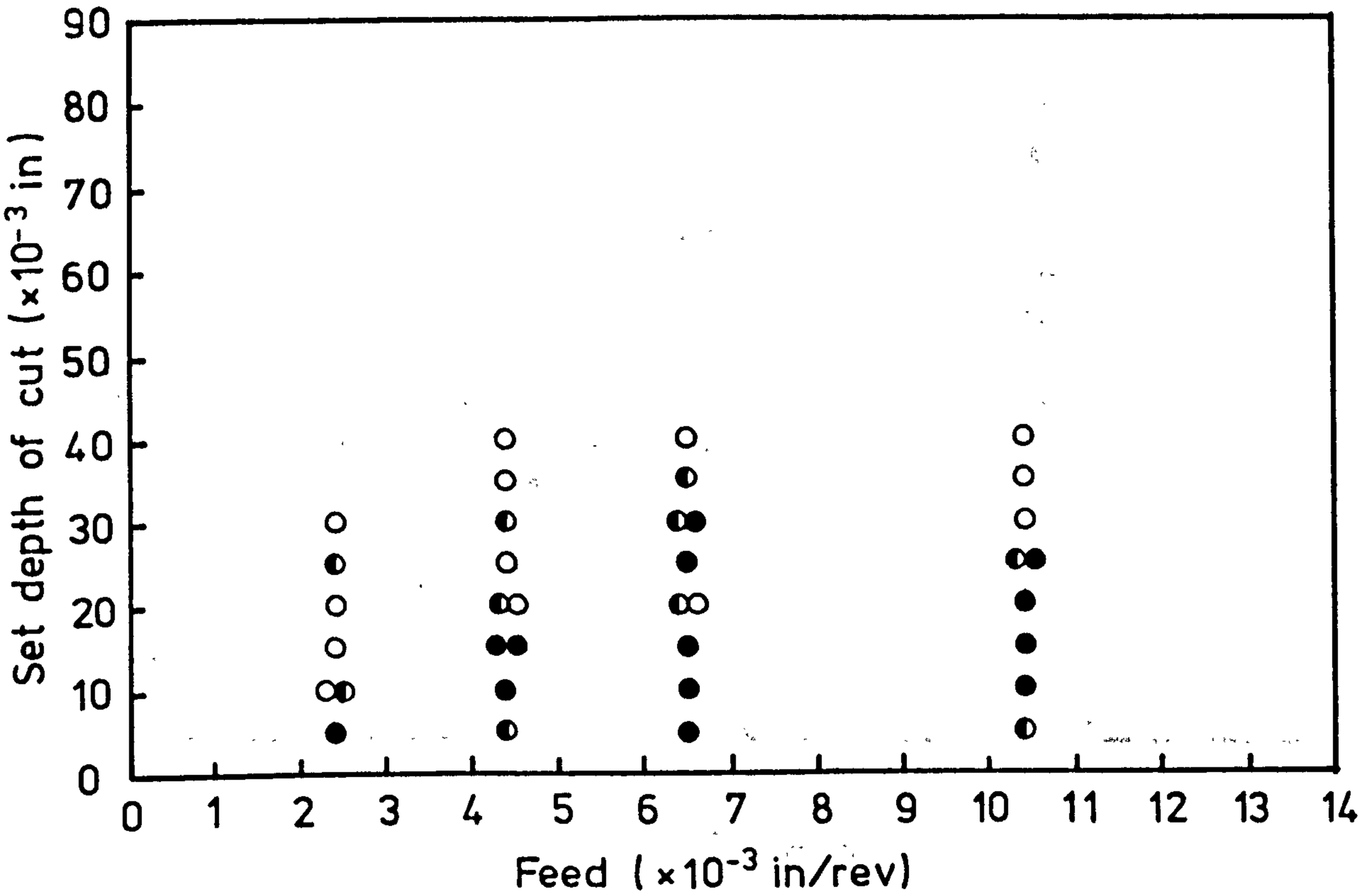

Material: EN8 steel

Tool: U tool 0.010" nose radius

Spindle speed: 500 rpm

Fig 8.5 Effect of depth of cut and feed on stability of optimally-tuned main-slug steel-bunged bar

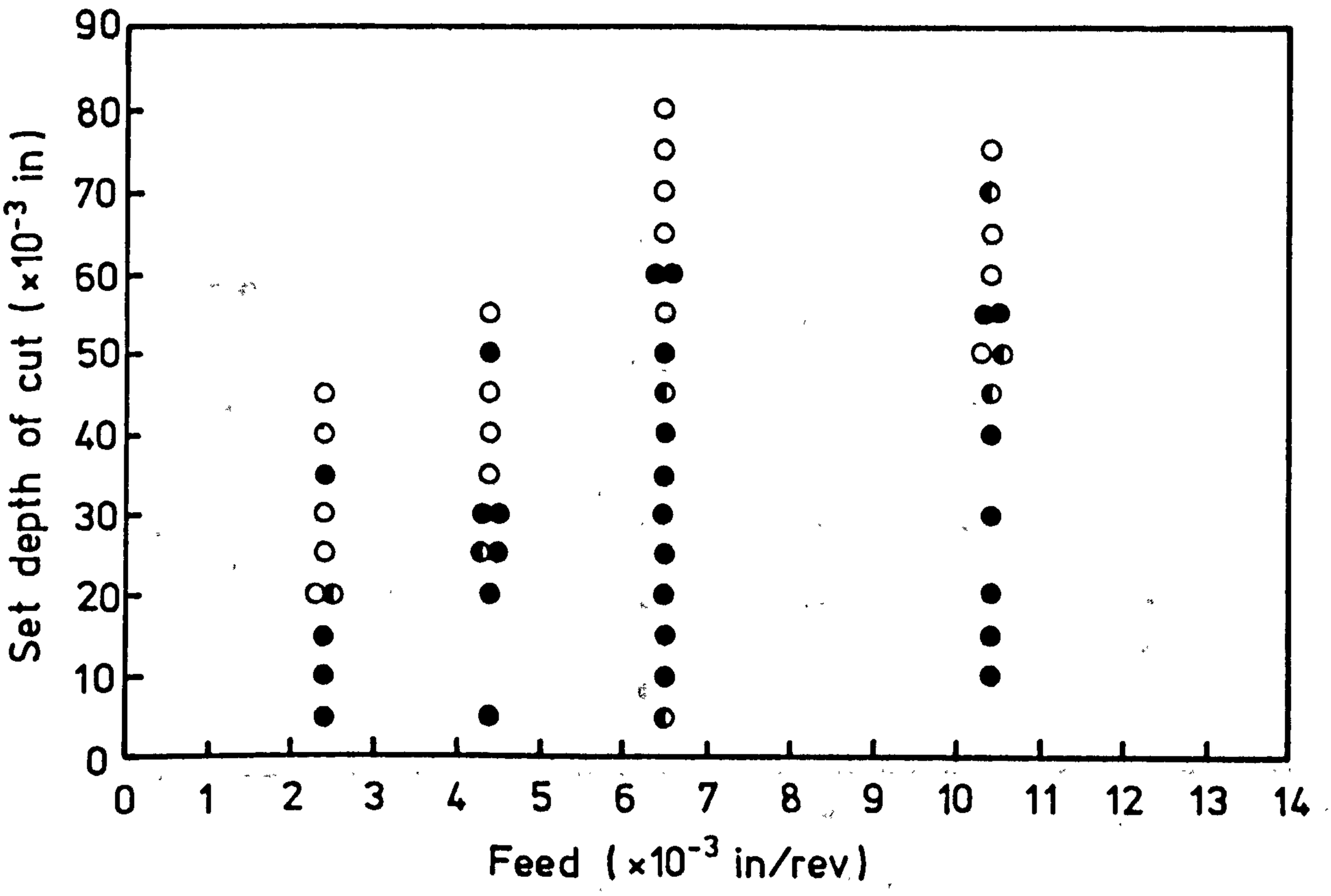

Key:
- ● stable
- ○ unstable
- ◐ partly stable

Material: EN8 steel

Tool: U tool 0.010" nose radius

Spindle speed: 500 rpm

Fig 8.6 Effect of depth of cut and feed on stability of optimally-tuned twin-slug steel-bunged bar

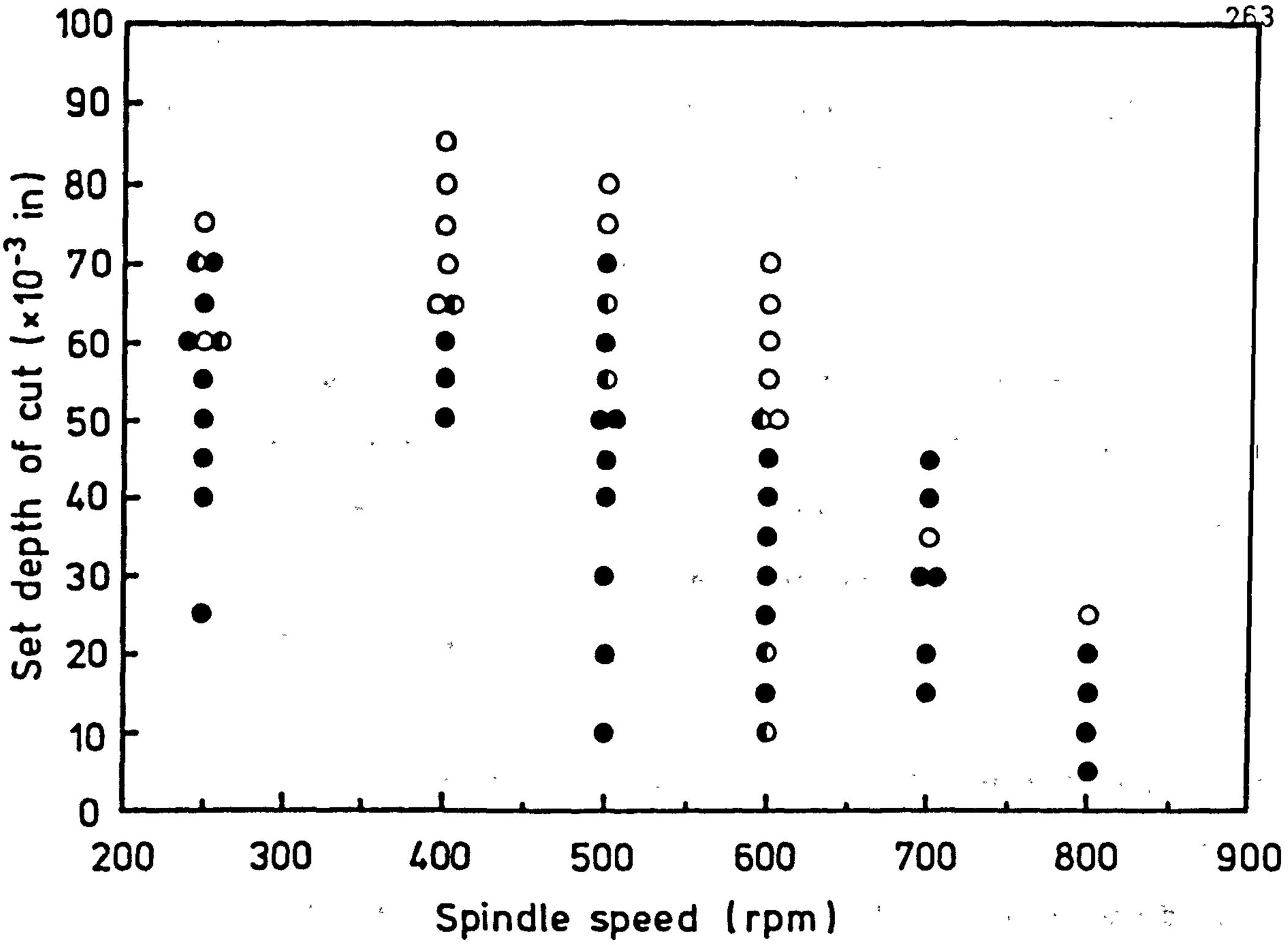

Material: EN8 steel

Tool: U tool 0.010" nose radius

Feed: 0.0065"/rev

Fig 8.7 Effect of depth of cut and speed on stability of optimally-tuned main-slug tungsten-bunged bar

produced was poor. In consequence, there was some difficulty in deciding the occurrence of chatter by way of inspecting the bored surface for chatter marks.

Fig 8.8 shows the limiting depth of cut variation relative to the feed at the constant spindle speed of 500 rpm. The pattern of variation is similar to that shown in Figs 8.3, 8.5 and 8.6. The maximum limiting depth was somewhere between 0.060" (1.524 mm) and 0.070" (1.778 mm).

Fig 8.15 is a photograph showing some typical finishes obtained for three different depths of cut at the feed of 0.0065"/rev and the speed of 500 rpm. The depths of cut at the top, middle, and bottom of the workpiece are 0.020", 0.030" and 0.070" respectively. Chatter-free surfaces were obtained under these three conditions. There was some scoring on each finish, but the worst was observed on the heaviest depth. The problem of scoring is a significant feature in boring with the damped tungsten-bunged bar, either of single-slug or twin-slug configuration. The subject will be taken up later.

Some "tuning" was performed on the tungsten-bunged bar by means of a limited number of boring tests using slug dampers of different diameters. At the speed of 500 rpm, and the feed of 0.0065"/rev, the limiting depths for different slug dampers were found to be as follows.

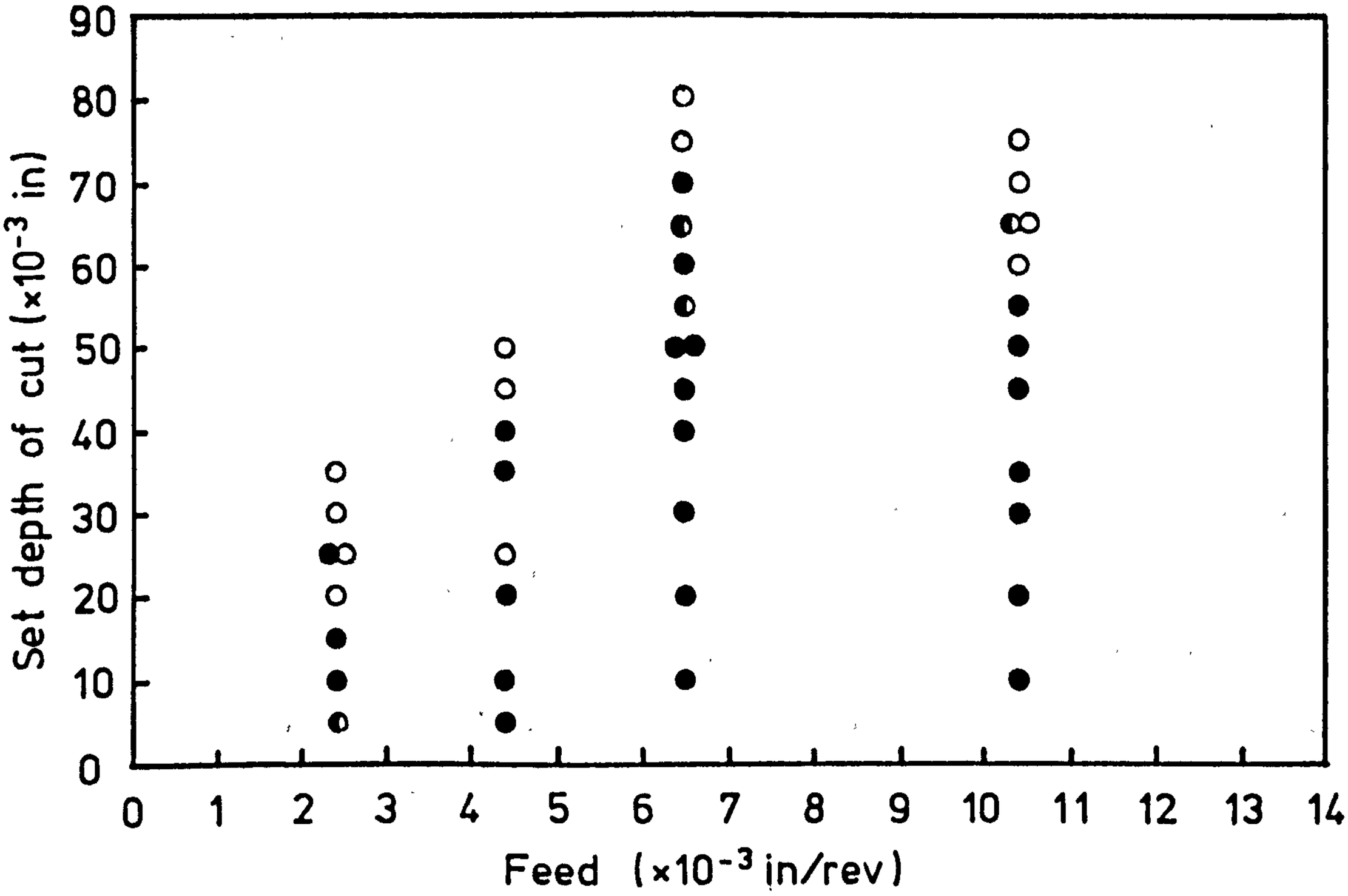

Key: ● stable
○ unstable
◐ partly stable

Material: EN8 steel
Tool: U tool
Spindle speed: 500 rpm

Fig 8.8 Effect of depth of cut and feed on stability of optimally-tuned main-slug tungsten-bunged bar

Main slug dia.(mm)	Rad. clear.(mm)	Limit. depth (in)
25.278	0.0775	0.055
25.299	0.067	0.060-0.070
25.318	0.0575	0.060
25.350	0.0415	0.035

(7) Optimally-tuned twin-slug tungsten-bunged bar - Fig 8.9 shows the effect on stability of depth of cut and feed at the speed of 500 rpm. The pattern of variation of the limiting depth of cut is very similar to that in the other diagrams such as Figs 8.3, 8.5, 8.6 and 8.8. Owing to the additional slug damper, the maximum limiting depth was increased to between 0.105" (2.667 mm) and 0.110" (2.794 mm).

The photograph in Fig 8.16a shows two finishes obtained with the optimally-tuned twin-slug tungsten-bunged bar. The surface at the top of the photograph was produced at a depth of cut of 0.010", a feed of 0.0065"/rev and a speed of 500 rpm, which is the typical finishing cut in boring practice. The surface at the bottom was produced at a heavier cut, namely 0.020" whilst other conditions were identical. Aside from some scoring, the finish is satisfactory and it is definitely chatter-free. Better finishes could sometimes be achieved when the chip produced were neatly conducted away from the cutting region.

The photograph in Fig 8.16b shows some finishes obtained when taking much heavier depths of cut. The surface finish in the middle was obtained with the stumpy boring bar and was regarded as the standard surface on which the two other cuts were taken. Obviously the finish is of high quality by virtue of the high rigidity of the stumpy bar. The surface at the top was produced at a depth of cut of 0.030" and

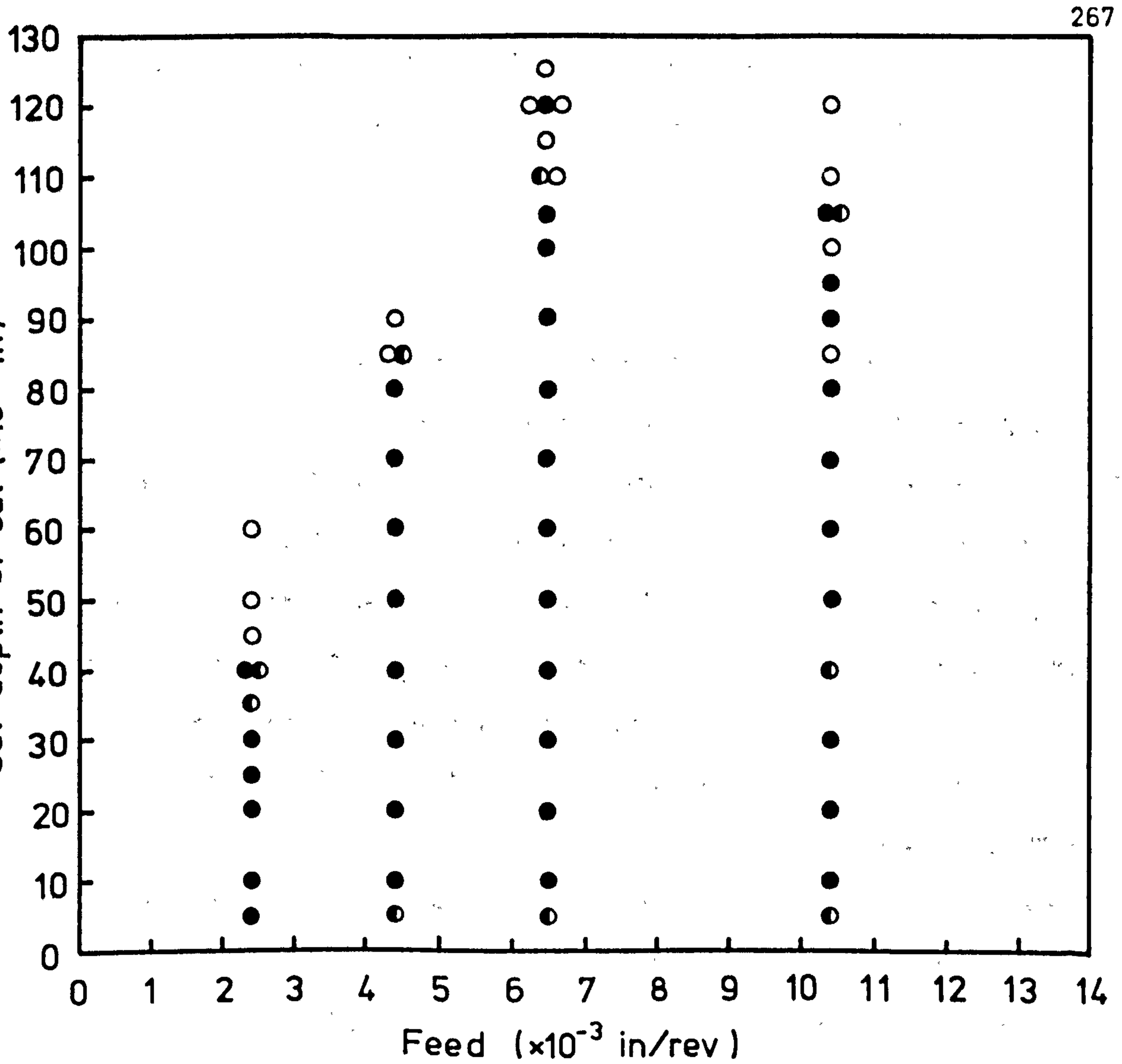

Key: ● stable
○ unstable
◐ partly stable

Material: EN8 steel
Tool: U tool 0.010" nose radius
Spindle speed: 500 rpm

Fig 8.9 Effect of depth of cut and feed on stability of optimally-tuned twin-slug tungsten-bunged bar

that at the bottom at 0.070". Finishes are slightly inferior to the standard in the middle; nevertheless, they are chatter-free.

8.5.2 Boring RRS/HBH steel

A few boring tests were performed on the RRS/HBH steel to find the limiting depth of cut at various feeds when the speed was kept at 190 rpm, using a 0.010" nose radius U tool. Results of these tests were presented graphically as shown in Figs 8.10 and 8.11, in which the limiting depth of cut is plotted against the feed for the cases of boring with the optimally-tuned tungsten-bunged bar fitted with the main slug and with the twin slug. The twin-slug arrangement brought about a marginally higher limiting depth of cut. Since the RRS/HBH steel is of much greater strength than EN8 steel, the reduction in the limiting depth is something to be expected. The photograph in Fig 8.17a shows the surface finishes obtained from boring depths of cut of 0.030" (top) and 0.020" (bottom) with the twin-slug tungsten-bunged bar at a feed of 0.0104"/rev and a speed of 190 rpm. Despite the chatter-free finish, both surfaces show unevenness of yet another kind as a result of chip scoring and of the flexibility of the boring bar. Better finishes can always be obtained if a light cut, for example, 0.005" is taken. The finish at the top of the photograph in Fig 8.17b shows such a finish. The finish at the bottom was obtained from the stumpy boring bar.

A problem peculiar to this type of boring at higher depths of cut is that the boring bar vibrated at two component frequencies. While one component frequency was close to the natural frequency of the boring bar; the other had a value very much higher. These component frequencies were measured

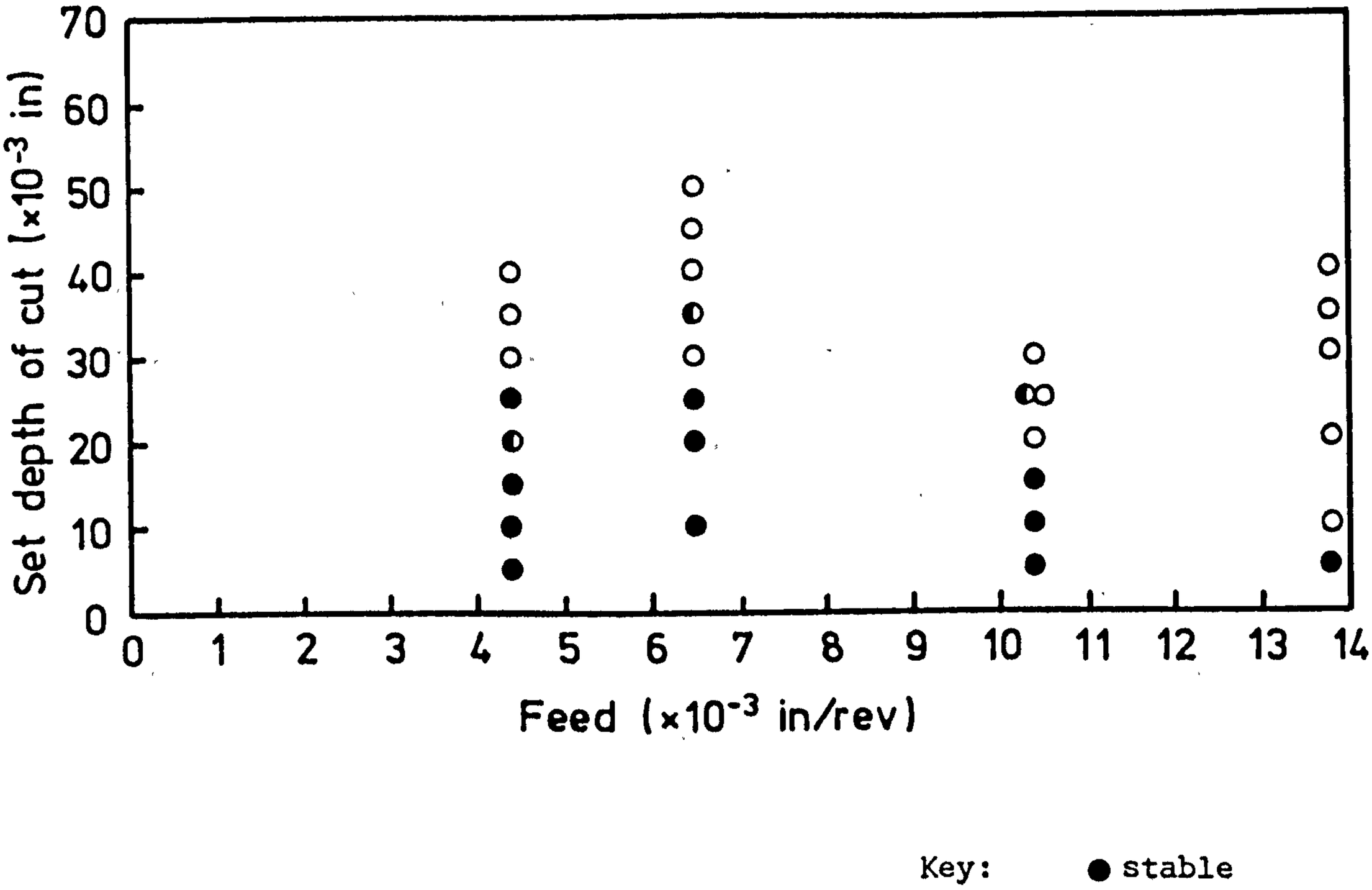

Material: RRS/HBH

Tool: U tool 0.010" nose radius

Spindle speed: 190 rpm

Fig 8.10 Effect of depth of cut and feed on stability of optimally-tuned main-slug tungsten-bunged bar

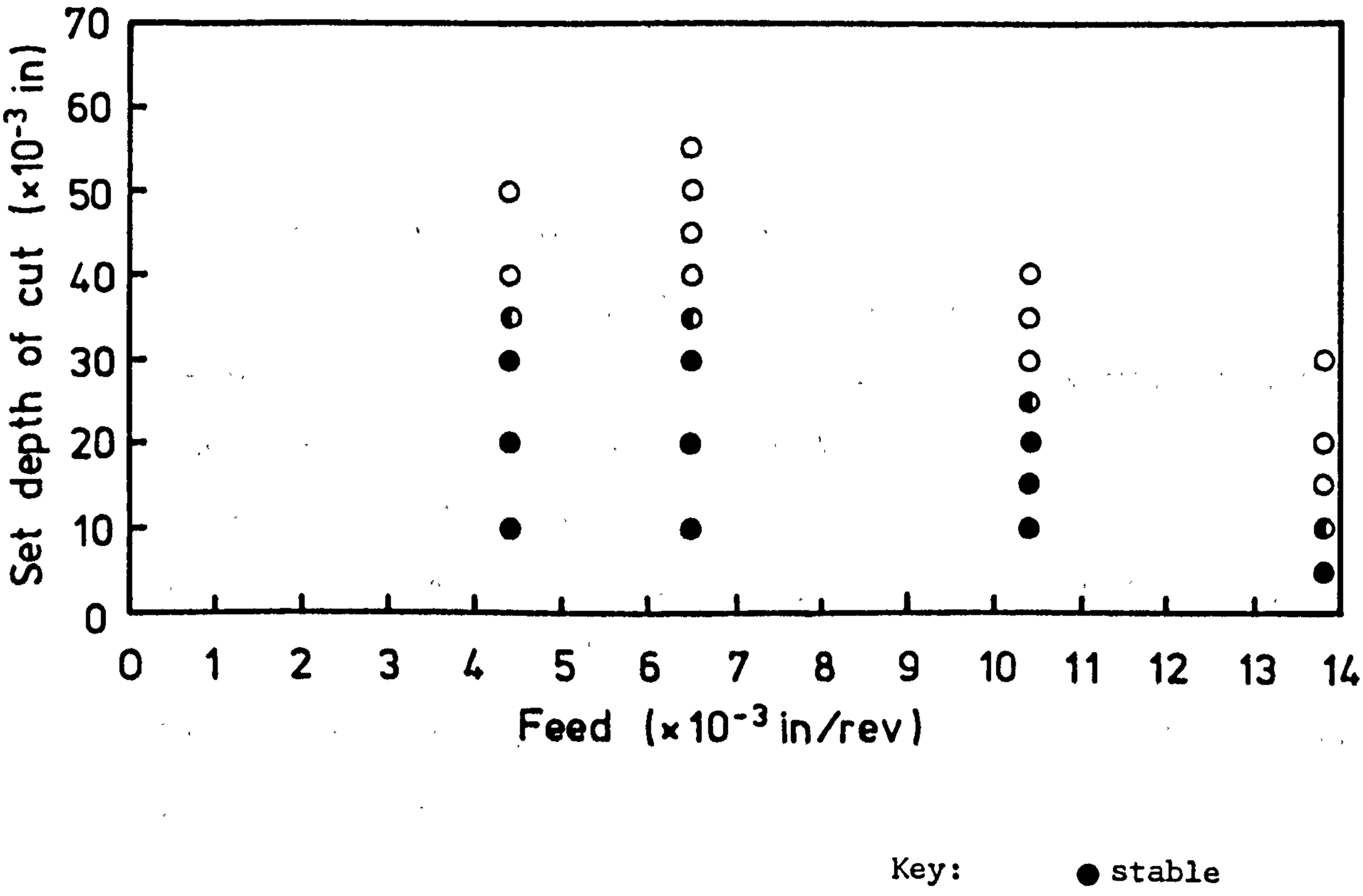

Material: RRS/HBH

Tool: U tool 0.010" nose radius

Spindle speed: 190 rpm

Fig 8.11 Effect of depth of cut and feed on stability of optimally-tuned twin-slug tungsten-bunged bar

when the optimally-tuned main-slug tungsten-bunged bar was used to remove a depth of 0.040" at the feed of 0.0044"/rev and the speed of 190 rpm, and their values were respectively 168 Hz and about 2690 Hz, the latter being 16 times the former.

8.5.3 Ability to remove surface irregularities

For the optimally-tuned tungsten-bunged bar whether it be of single-slug or twin-slug configuration, it was always possible to remove the surface irregularities from a previously chattered surface by means of a finishing cut having the specification:

(a) for EN8 steel, depth of cut 0.010" to 0.030", feed 0.0044"/rev to 0.0104"/rev, and cutting speed 500 rpm to 700 rpm.

(b) for RRS/HBH steel, depth of cut 0.010" to 0.015", feed 0.0065"/rev and cutting speed 190 rpm to 200 rpm.

8.5.4 Boring with the 0.030" nose radius U and R tools

A few boring tests were carried out using the U and R tools that had the nose radius of 0.030". In general, it was observed that the limiting depth of cut achieved for the EN8 steel was some 0.010" to 0.020" lower than that using the 0.010" nose radius tools under the otherwise identical boring condition. For the RRS/HBH steel, the limiting depth of cut was about 0.005" to 0.010" lower.

8.5.5 Surface roughness

Measurements of the surface roughness values on finishes obtained with the 0.010" and 0.030" nose radius tools varied from 0.5μm to 6μm. Variability depended on the tool wear condition, the tool nose radius, the feed and to some extent the cutting speed. The lowest value for surface roughness was

recorded on the RRS/HBH steel for the 0.010" nose radius U tool, but, on average, the value would be in the range of 1 to 2 μm. Better finishes were almost always obtained using a tool with the smaller nose radius, in this case, 0.010".

8.5.6 Problems in boring stability tests

A number of problems was encountered in the boring tests and are identified as below.

(1) Repeatability - It was at times difficult to determine the state of the surface finish that fell on the stability borderline due to the fact that it was not always repeatable. Non-repeatability was caused in the main by the amount of tool wear and to a lesser extent by the built-up edge formation at low cutting speeds. In general, chatter occurred with a freshly ground tool, and at light cuts, slight tool wear was found to improve stability. To alleviate this difficulty associated with a freshly ground tool, the cutting edges were dulled by a fine grade of oil stone before the tool was employed to take any cut.

(2) Chip disposal - For the EN8 steel and at small depths of cut the problem of chip disposal hardly arose. Nevertheless, at heavier depths such as obtainable with the optimally-tuned tungsten-bunged bar, the proper delivery of the chip away from the cutting zone presented a formidable problem. The same problem was also encountered when boring high duty alloy steel such as the RRS/HBH steel in which, although the limiting depth of cut was smaller than was the case for EN8, the chips formed were of much higher strength and hence difficult to shape or break.

Quite often, such chips emerged from the tool tip in the form of a large-coil continuous spiral which would wrap round anything that was in its path. As a result, the machined surface was scored by virtue of the numerous cutting edges presented by the chips in contact with the surface; and equally undesirably the tool would break under the excessive cutting load.

Some tentative solutions by way of chip-breaking and chip-shaping were experimented. Initially a chip-breaker in the form of a 0.020" high by 0.020" wide step measured from the cutting edge was adopted. This chip-breaker succeeded in breaking the chip into shorter segments that were then carried away by means of a stream of pressurized air. However, the resulting periodic fluctuation in the cutting load exerting on a flexible element such as the boring bar caused the surface finish to show periodic irregularities. In the second stage of the development, a chip-breaker was designed, not to break chips, but rather to conveniently curl the chip into one long and continuous closely-coil spiral so that it could be led away from the cutting zone. Preliminary results proved that the method was satisfactory; and further investigation are now being conducted in this direction.

(3) Chattered surface - In general, it was simple matter to decide if the boring bar bored stably or not by examining the surface finish produced. Chatter marks such as those shown in the photograph of Fig 8.14 clearly indicates instability. However, there were situations, particularly when light depths of cut were attempted, where the chatter marks became extremely fine and could be missed easily if the surface in question was not scrutinized in a well-lit environment.

For obvious reason, the whole problem was aggravated by the chip disposal problem discussed in the last section.

Aside from the problem elucidated, it is worthy of mention that there is another class of problem with which we were not concerned in the boring stability tests, and yet it significantly affects the quality of profile boring using long overhung boring bars. These are the problems of geometric form error and are dealt with in Chapters 2 and 6.

8.5.7 Comparison between stability theory and results.

The theory referred to is the one presented in Appendix E. The reason why Appendix E is preferred to that developed in Chapter 5 is expounded in the opening paragraph of the appendix.

Essentially, it is suggested in Appendix E that a boring process can be considered to be under closed-loop control in which the cutting process dynamics interacts with the machine tool dynamics at the tool point as shown in the block diagram of Fig E1. For primary chatter, the cutting process dynamics can be regarded to have a transfer function $a - jf_1\omega$ where a is the rate of change of radial force with respect to the depth of cut and $- f_1$ is the negative viscous damping coefficient which provides the hypothetical source of instability. For regenerative chatter, the cutting process dynamics has a transfer function $a' - jf_2$ where a' is similarly defined as a (see section 5.3.2 for details) and $- f_2$ is the negative hysteretic damping coefficient. For the closed-loop system as depicted in Fig E1, the stability borderline can be specified in terms of f_1 as a function of a for the case of primary chatter as shown graphically

in Fig E6; and in terms of f_2 as a function of a' for the case of regenerative chatter as shown graphically in Fig E7. From these figures, it is observed that as a and a' decrease, the respective f_1 and f_2 decrease but level off eventually at some constant values which for brevity are termed the asymptotic values. Physically, being related to the cutting force slope, a and a' decrease as the depth of cut increases, until when the depth exceeds the nose radius on the boring tool, a and a' will then settle at a small yet constant value. As an example, for boring mild steel with tools of nose radii of 0.010", 0.020", 0.030" and 0.040", the cutting force slope values as shown in Fig 5.2 for these tools are all observed to level off at 80 lbf/in, equivalent to 14kN/m for a. By the reasoning presented in section 5.3.2, the value for a' is less than 3a, ie 42 kN/m. For the optimally-tuned main-slug tungsten-bunged bar, it can be seen from Fig E7 that at a = 14 kN/m, f_1 is at its asymptotic value of 317 Ns/m and from Fig E8 that at a' < 3a = 42 kN/m, the value of f_2 lies in the interval 452 to 456 kN/m, the lower limit being the asymptotic value. Without much loss of accuracy, it can be assumed that f_2 takes on its asymptotic value whenever a' is less than 3a, ie 42 kN/m in this example. Following this line of reasoning, it can be deduced that whenever the limiting depth of cut is in excess of the nose radius (which is the case for most practical machining processes) and by virtue of the fact that asymptotic f_1 or f_2 corresponds to when the closed-loop system in Fig E1 becomes just unstable, both asymptotic f_1 and f_2 can be related uniquely to the limiting depth of cut attainable with a particular boring bar when other factors such as tool geormtry, workpiece material, feed and speed are maintained constant. The asymptotic values for f_1 and f_2 were calculated as explained in the numerical example in Appendix E.

The following table shows the asymptotic values for f_1 and f_2 for each boring bar under test. These values were calculated in the same manner as the numerical example shown in Appendix E.

BAR	ASYMPTOTIC f_1 (Ns/m)	ASYMPTOTIC f_2(kNs/m)
Solid	23	25
Opt. damped recessed	176	199
Opt. main-slug steel-bunged	163	199
Opt. twin-slug steel-bunged	337	371
Tungsten-bunged	24	36
Opt. main-slug tungsten-bunged	317	452
Opt. twin-slug tungsten-bunged	452	585
Main-slug tungsten-bunged with slug diameter:		
1) 25.278 mm	289	422
2) 25.299 mm (optimum)	317	452
3) 25.318 mm	316	429
4) 25.350 mm	198	255

For the case of primary chatter, Fig 8.12 shows the relation between the limiting depth of cut and the negative viscous damping coefficient f_1 when boring EN8 steel with a 0.010" nose radius U tool at the feed of 0.0065"/rev and speed of 500 rpm. Similarly, for the case of regenerative chatter, the limiting depth of cut and the negative hysteretic damping coefficient f_2 can be related as shown in Fig 8.13. Both curves have a shape that can be represented by a logarithmic function as will be discussed later. Extreme care, however, must be exercised in interpreting the results

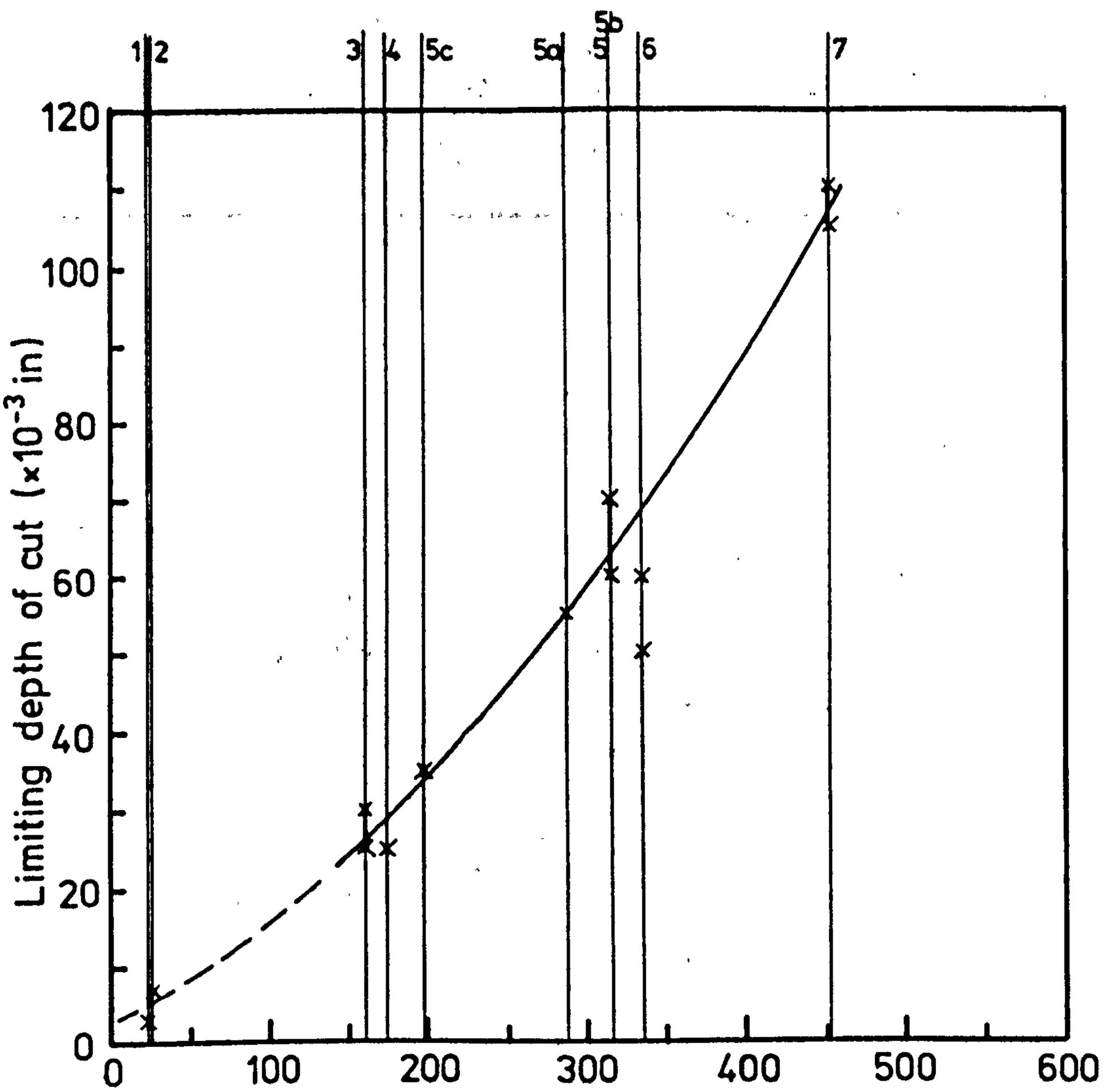

Key: Common to both Figs 8.12 and 8.13

1 - Solid bar

2 - Tungsten-bunged bar without slug

3 - Optimally-tuned main-slug steel-bunged bar, 0.025" to 0.030" depth of cut

4 - Optimally-tuned single-slug recessed bar, 0.025" depth of cut

5 - Optimally-tuned main-slug tungsten-bunged bar (0.067 mm radial clearance), 0.060" to 0.070" depth of cut

5a - Main-slug tungsten-bunged bar (0.0775 mm radial clearance)

5b - Main-slug tungsten-bunged bar (0.0575 mm radial clearance), 0.060" depth of cut

5c - Main-slug tungsten-bunged bar (0.0415 mm radial clearance)

6 - Optimally-tuned twin-slug steel-bunged bar

7 - Optimally-tuned twin-slug tungsten-bunged bar

Fig 8.12 Relation between the limiting depth of cut and the asymptotic negative viscous damping coefficient, f_1

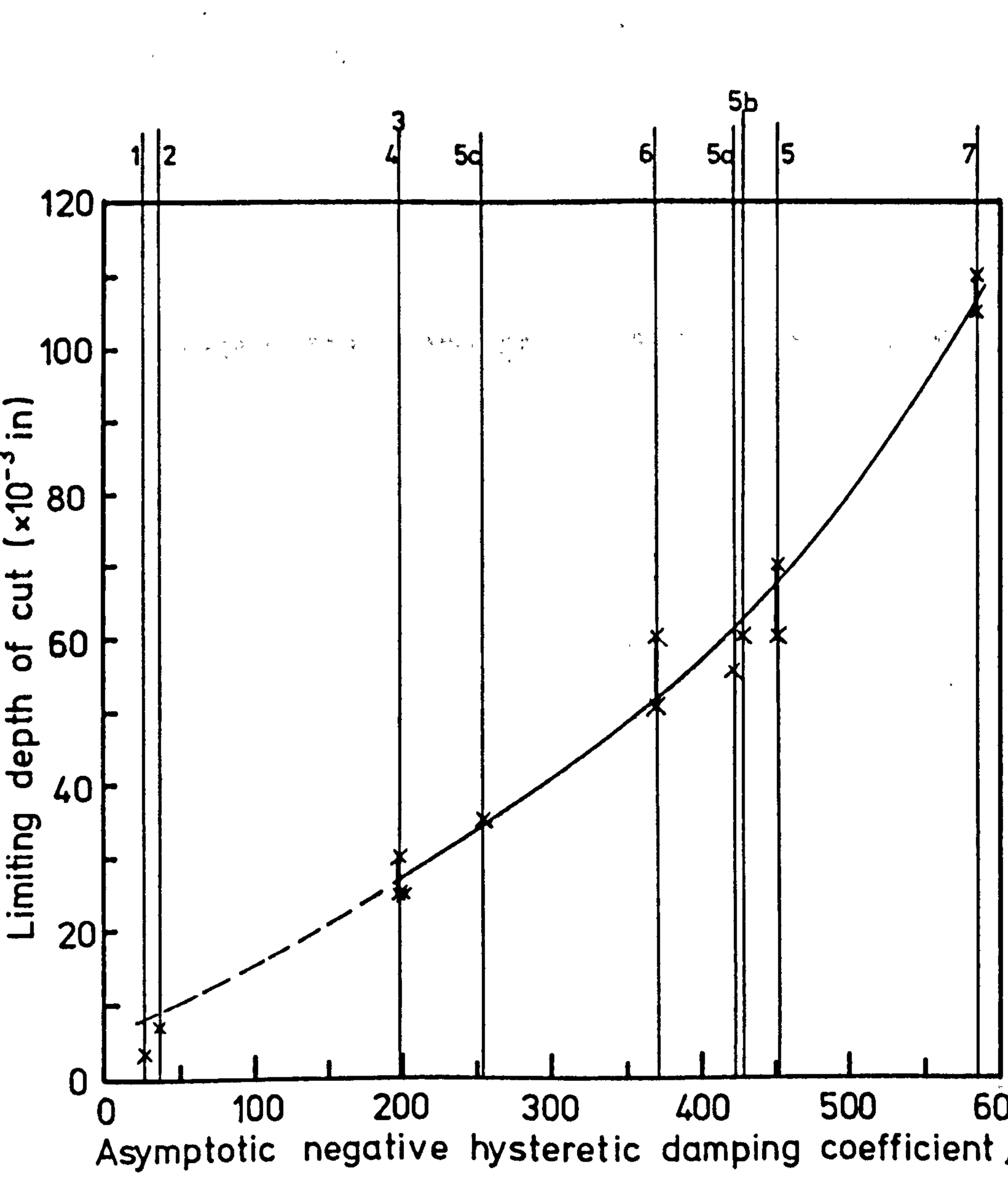

Key: See Fig 8.12

Fig 8.13 Relation between the limiting depth of cut and the asymptotic negative hysteretic damping coefficient, f_2

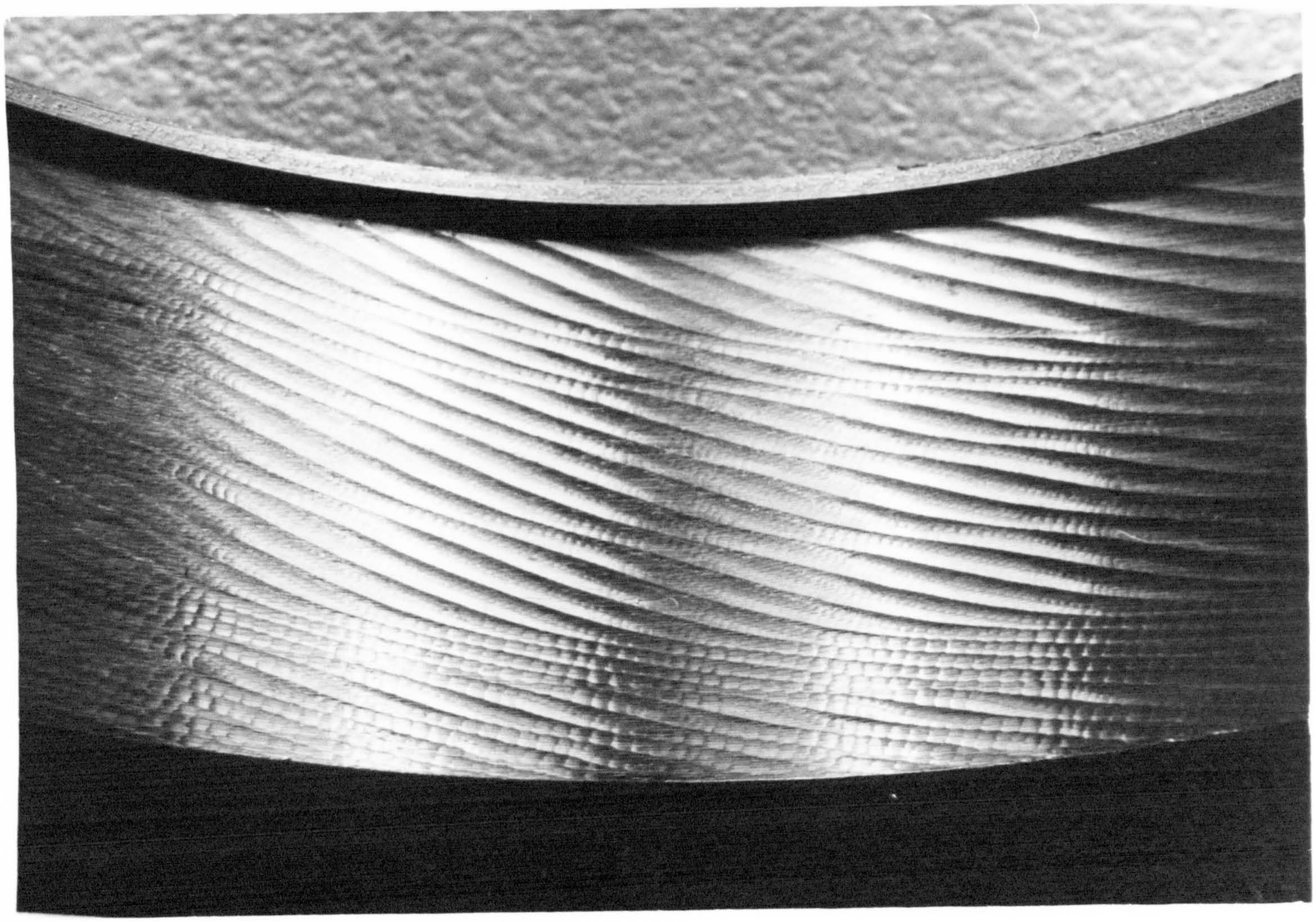

Fig 8.14 Surface finish obtained with the solid bar

Depth of cut: 0.030" Feed: 0.0065 in/rev

Material: EN8 steel Speed : 500 rpm on $3\frac{1}{2}$" diameter bore

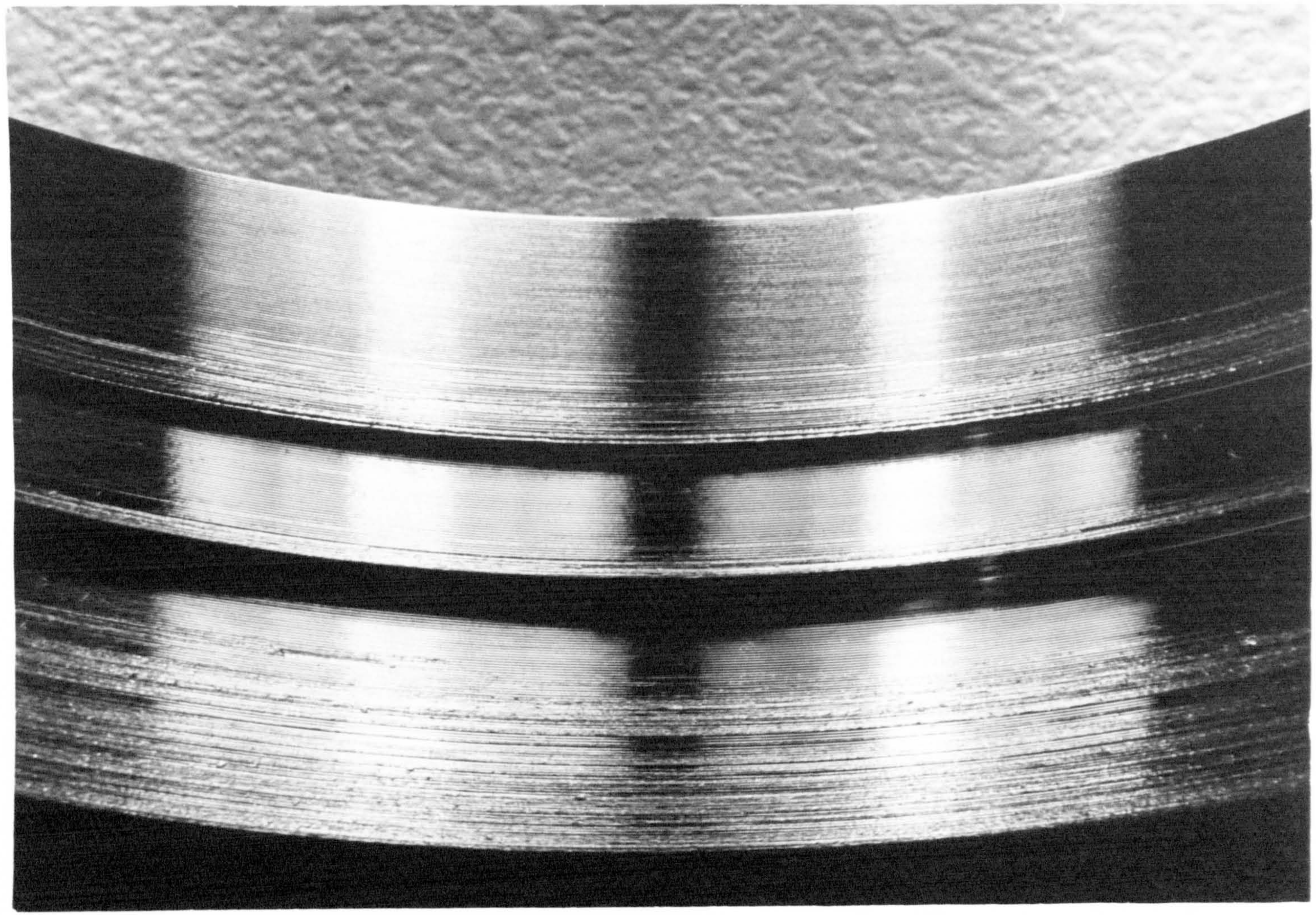

Top

Middle

Bottom

Fig 8.15 Surface finishes obtained with the optimally-tuned main-slug tungsten-bunged bar

Depths of cut: 0.020" (top)
0.030" (middle)
0.070" (bottom)

Material: EN8 steel
Feed: 0.0065 in/rev
Speed: 500 rpm on $3\frac{1}{2}$" diameter bore

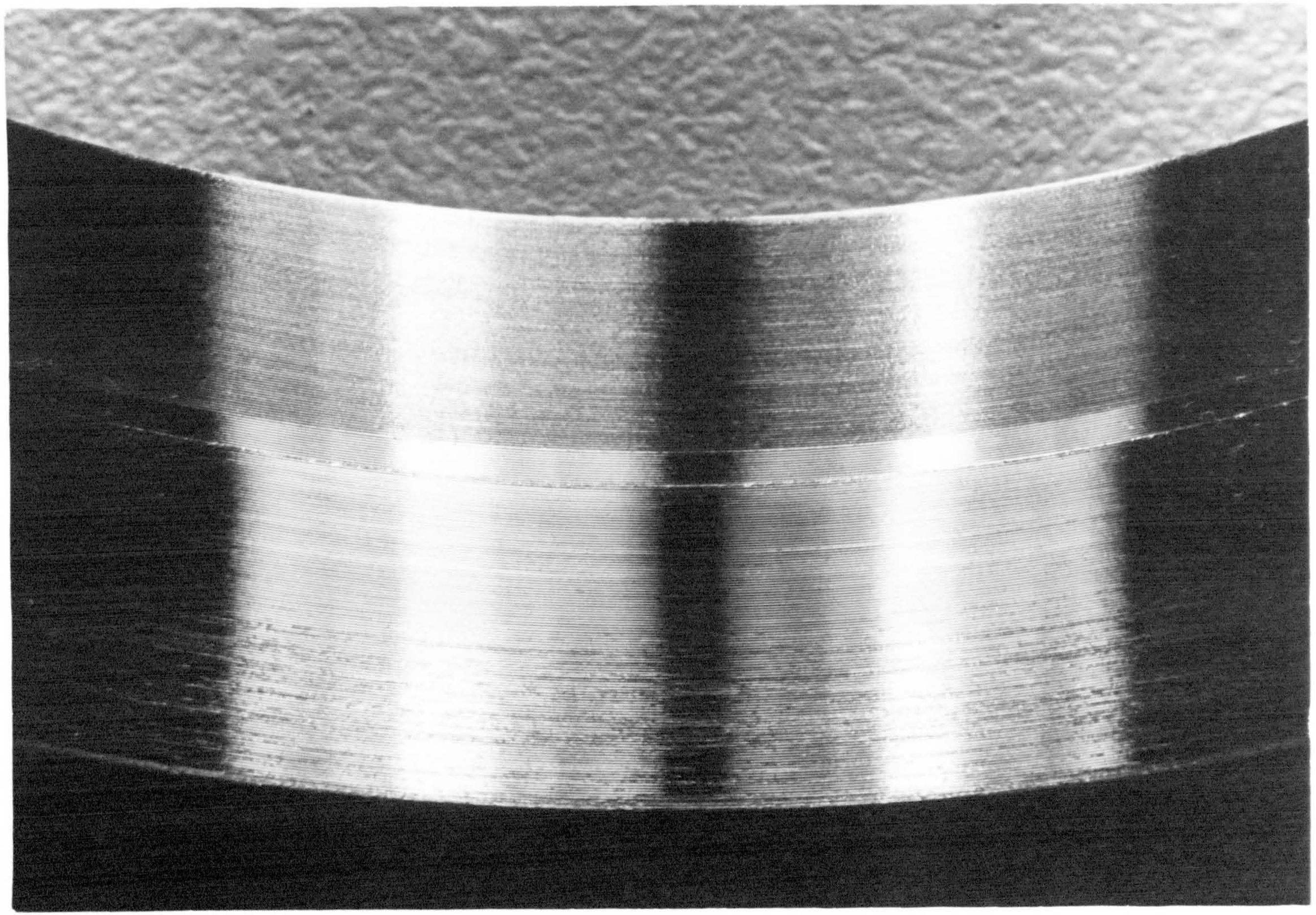

Top

Bottom

Fig 8.16a Surface finishes obtained with the optimally-tuned twin-slug tungsten-bunged bar

Depths of cut: 0.010" (top), 0.020" (bottom) Material: EN8 steel

Speed: 500 rpm on $3\frac{1}{2}$" diameter bore Feed: 0.0065 in/rev

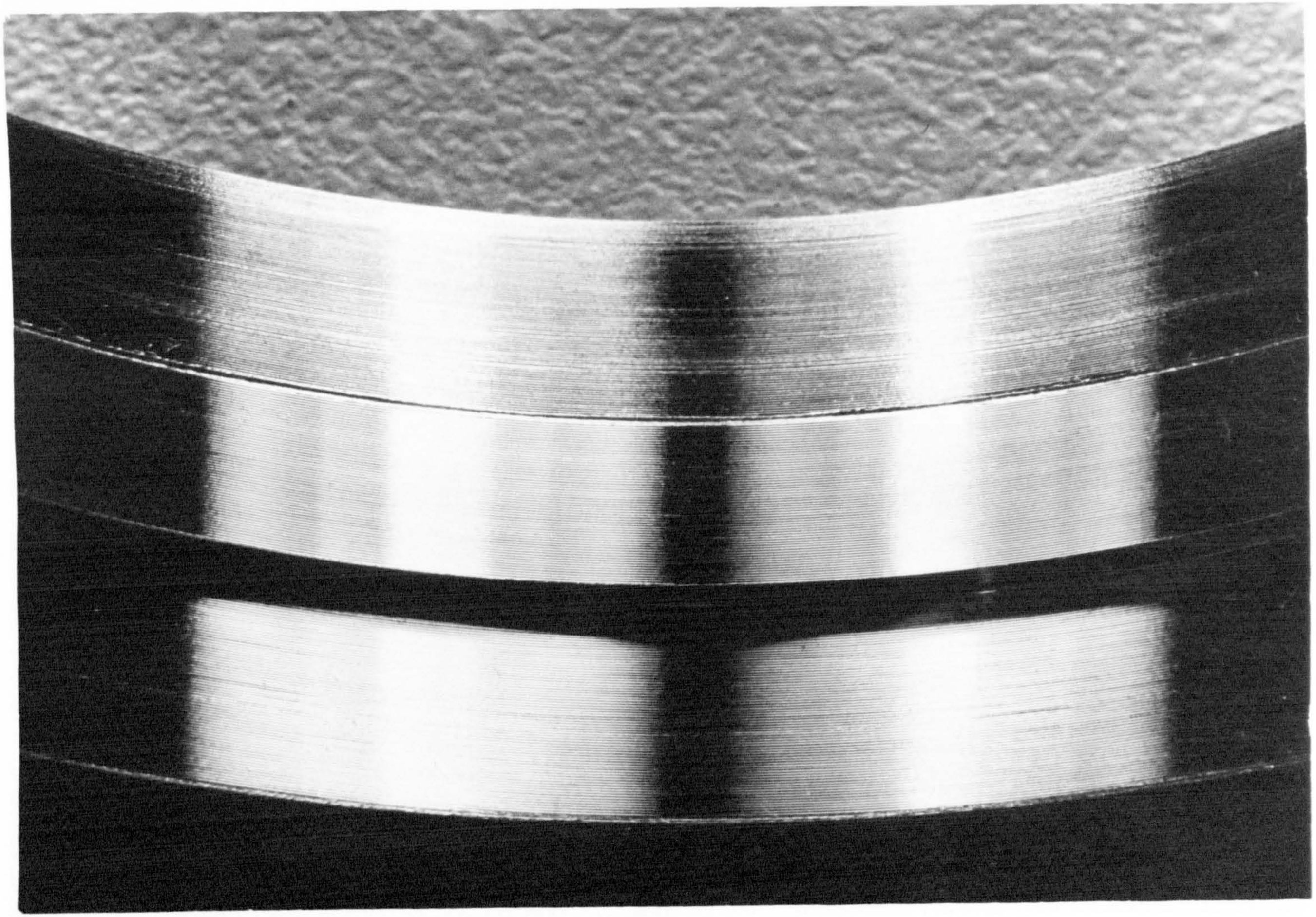

Fig 8.16b Surface finishes obtained with the optimally-tuned twin-slug tungsten-bunged bar.

Depths of cut: 0.030" (top), 0.070" (bottom) Material: EN8 steel
Speed: 500 rpm on $3\frac{1}{2}$" diameter bore Feed: 0.0065 in/rev
The finish in the middle is the standard finish obtained with the stumpy bar.
The other two cuts were measured relative to this standard surface.

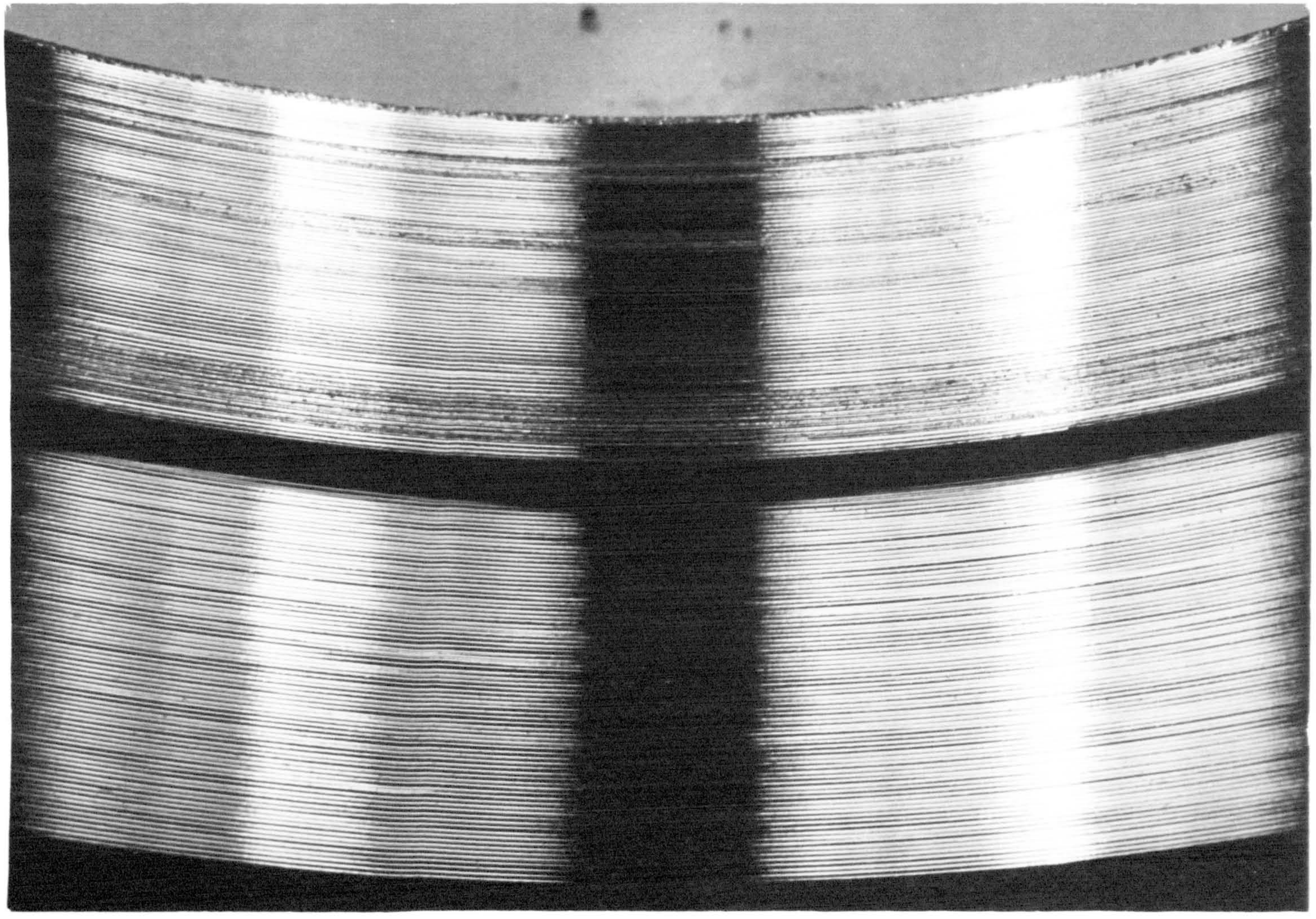

Top

Bottom

Fig 8.17a Surface finishes obtained with the optimally-tuned twin-slug tungsten-bunged bar

Depths of cut: 0.030" (top), 0.020" (bottom) Material: RRS/HBH

Speed: 190 rpm on 3¼" diameter bore Feed: 0.0104 in/rev

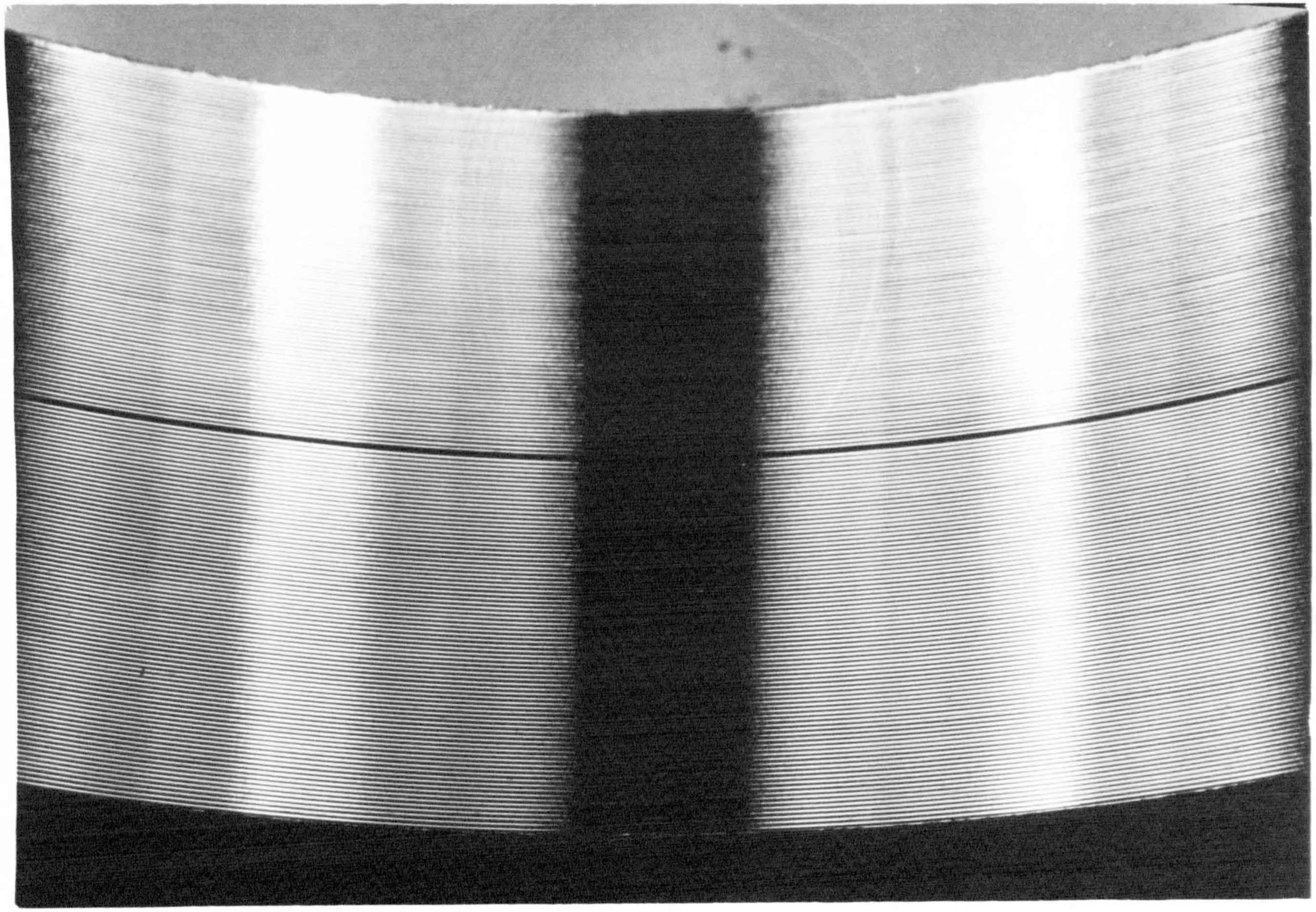

Top

Bottom

Fig 8.17b Surface finishes obtained with the optimally-tuned twin-slug tungsten-bunged bar

Depth of cut: 0.005" (top) Feed: 0.0104 in/rev
Material: RRS/HBH steel Speed: 190 rpm on $3\frac{1}{4}$" diameter bore

Finish at bottom is the standard finish obtained with the stumpy bar.

shown by the dashed part of curve in Figs 8.12 and 8.13, since the results obtained from using the solid bar and the tungsten-bunged bar without slug correspond to effective depths of cut being less than the nose radius of 0.010" and hence a and a' may have values greater than their minimum. For this reason, f_1 and f_2 thus calculated as being the asymptotic values are not strictly valid. Some amount of scatter is observed in both curves of Figs 8.12 and 8.13, but since the boring tests results are not exactly repeatable due to factors as explained in section 8.5.6, such errors are tolerated.

To establish the empirical relation between f_1 and the limiting depth of cut, Fig 8.12 is redrawn as Fig 8.18 with the limiting depth of cut, designated as d, plotted to a logarithmic scale whilst f_1 is plotted to a linear scale as before. By virtue of the linear relationship, the empirical expression may take the form:

$$\log d = Af_1 + B \qquad \ldots\ldots\ldots\ldots\ldots\ldots \quad (8.1)$$

where A and B are constants to be evaluated.

Let the depth of cut have the unit of mm and f_1 the unit of Ns/m, then at d = 0.020" = 0.508 mm hence log d = -0.2941, and from Fig 8.18, f_1 = 90Ns/m.

Substituting these into eqt. (8.1) gives

$$-0.2941 = 90A + B \qquad \ldots\ldots\ldots\ldots\ldots\ldots \quad (8.2)$$

Similarly, at another point on the graph, say, d = 0.100" = 2.54 mm, hence log d = 0.4048, f_1 = 435 Ns/m, which when substituted into eqt. 8.1 gives

$$0.4048 = 435A + B \qquad \ldots\ldots\ldots\ldots\ldots\ldots \quad (8.3)$$

Sovling eqts. (8.2) and (8.3) simultaneously gives

$A = 2.026 \times 10^{-3}$ and $B = -0.4764$

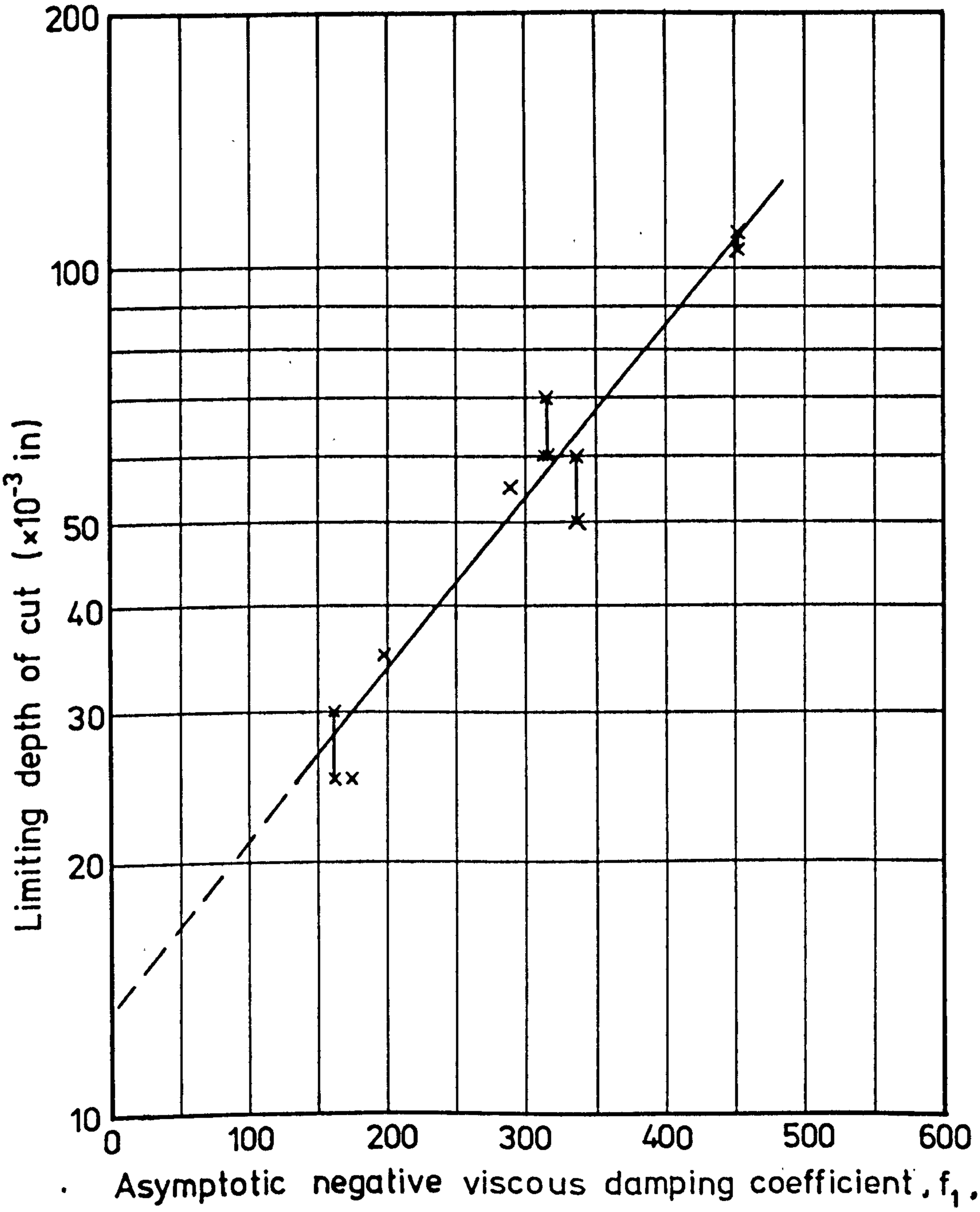

Fig 8.18 Finding the empirical relation between limiting depth of cut and asymptotic negative viscous damping coefficient f_1

Hence the empirical equation for Fig 8.18 is

$$\log d = (2.026 \times 10^{-3})f_1 - 0.4764 \quad \ldots\ldots\ldots\ldots \quad (8.4)$$

For ease in utilising eqt. 8.4, d is preferred to log d and the alternative equation can be shown to be

$$d = (1.00468^{f_1})/2.9952 \quad \ldots\ldots\ldots\ldots\ldots\ldots \quad (8.4a)$$

where d is in mm and f_1 in Ns/m.

It is noted that the base of f_1 in the numerator is expressed to 5 decimal places, which is necessary if accuracy in d is to be maintained when the practical range of f_1 falls in the interval $150 \leqslant f_1 \leqslant 450$ Ns/m as in Fig 7.18. Obviously any error in the base of 1.00468 will be magnified by virtue of the high power f_1.

For the case of regenerative chatter, a similar empirical expression to eqts (8.4) or (8.4a) can be established. In particular, for boring EN8 steel with the 0.010" nose radius U tool at the feed of 0.0065"/rev and the speed of 500 rpm, Fig 8.13 can be redrawn as Fig 8.19 and the empirical relation is found to be

$$\log d = 1.5379 \times 10^{-3} f_2 - 0.4641 \quad \ldots\ldots\ldots\ldots \quad (8.5)$$

or $$d = (1.00355^{f_2})/2.9112 \quad \ldots\ldots\ldots\ldots \quad (8.5a)$$

where d is the limiting depth of cut in mm; and f_2 the negative hysteretic damping coefficient in kNs/m.

The advantages in using the stability model presented in Appendix E and the two empirical formulae, namely eqts (8.4) and (8.5) or their alternatives, eqt (8.4a) or (8.5a) are significant. First, from the evidence obtained as demonstrated in Figs 8.12 and 8.13 specifically that there is a one-to-one correspondence between the limiting depth of cut and the negative damping

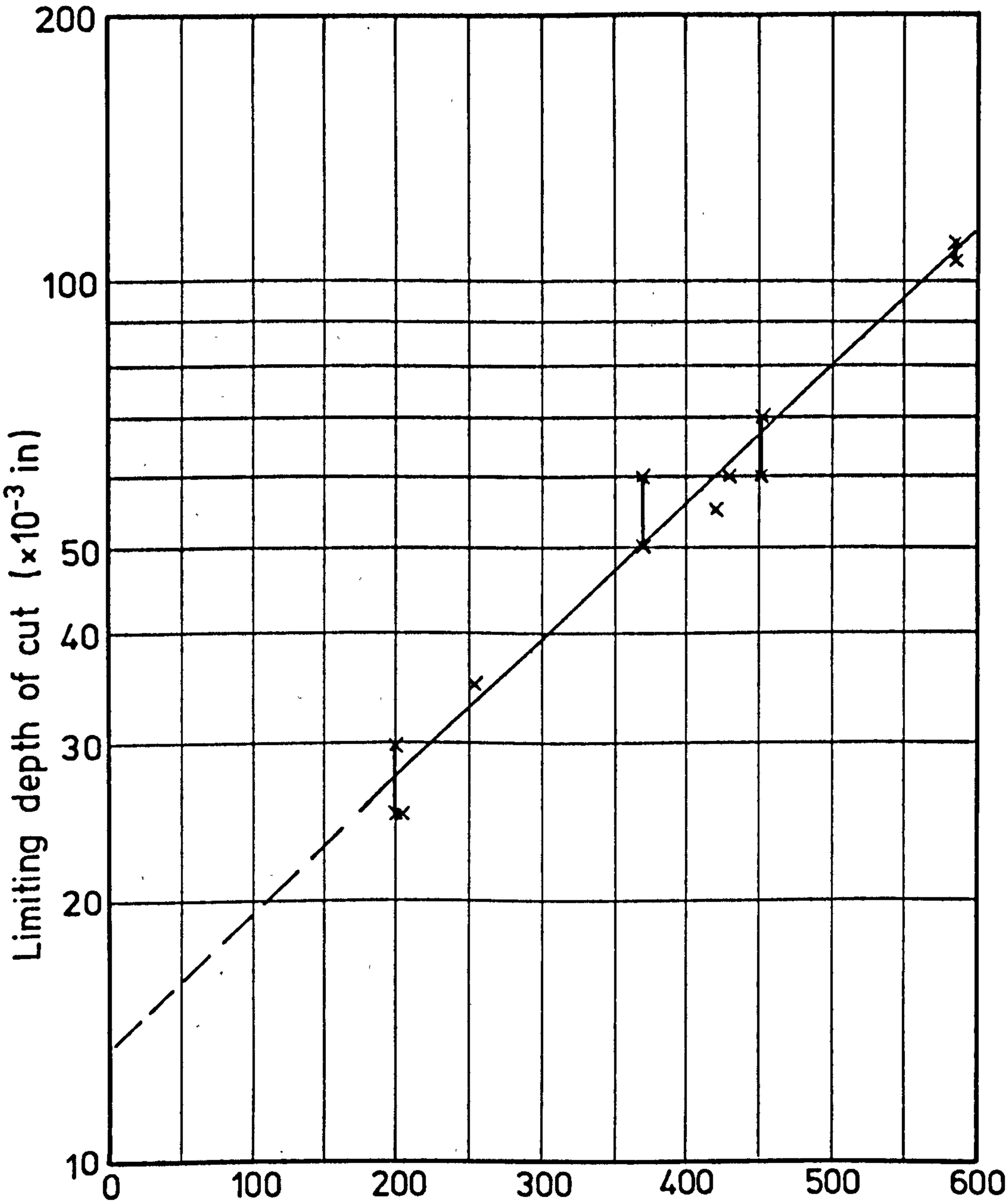

Fig 8.19 Finding the empirical relation between limiting depth of cut and asymptotic negative hysteretic damping coefficient f_2

coefficients, the stability model enables us to rate the machining performance of different boring bars employed in the boring tests in terms of their limiting depths of cut achieved. Second, the limiting depth of cut, when other conditions are fixed, can be calculated from the empirical formulae such as eqts (8.4) and (8.5), once the asymptotic value for f_1 or f_2 of a particular boring bar has been obtained from the stability model. Third, provided enough cutting tests are done to cover the practical range of machining, from which formulae like eqts (8.4) and (8.5) are derived, it is in principle possible to predict the limiting depth of cut of any machine tool system whose frequency response characteristics are known. Finally, the process of limiting depth of cut prediction can be quickened with the aid of cheap programming facilities that are made available by the applications of microcomputers on the shop floor in the vicinity of the machine tool concerned.

8.6 CONCLUSIONS

(1) For boring EN8 steel with the 0.010" nose radius U tool, the limiting depth of cut decreased as the cutting speed increased.

(2) For boring EN8 and RRS/HBH steels with a 0.010" nose radius U tool at the respective speeds of 500 and 190 rpm, the limiting depth of cut increased with the feed rate until the latter reached 0.0044"/rev to 0.0065"/rev before the limiting depth decreased slowly as the feed increased further.

(3) Arranged in the order of decreasing limiting depths of cut, the different boring bars are listed together with the limiting depths

of cut achieved as follows (also see Figs 8.13 or 8.14):

a) Optimally-tuned twin-slug tungsten-bunged bar	0.105" - 0.110"
b) Optimally-tuned main-slug tungsten-bunged bar	0.060" - 0.070"
c) Optimally-tuned twin-slug steel-bunged bar	0.050" - 0.060"
d) Optimally-tuned main-slug steel-bunged bar	0.025" - 0.030"
e) Optimally-tuned single slug recessed bar	0.025"
f) Tungsten bunged bar without slug	0.007"
g) Solid bar	0.003"

(4) It was possible to remove all traces of badly chattered surface in one cut with conditions as specified in section 8.5.3.

(5) Below the limiting depths of cut, when boring EN8 steel at a heavy cut or RRS/HBH steel at a lighter cut, there was the problem of badly scored surface finish caused by the long and unruly chips that wrapped round the cutting tool. Some success was achieved by introducing a chip-breaker to the tool.

(6) The stability theory developed in Appendix E succeeded in sorting out the order of machining performance of different boring bars employed in the tests in terms of the limiting depths of cut achieved purely from the asymptotic values of the negative damping coefficient.

(7) A one-to-one correspondence exists between the limiting depth of cut and the asymptotic value of the negative damping coefficient.

(8) With the help of the theory in Appendix E and the empirical formulae

such as eqt (8.3) and (8.4), or their alternatives, (8.3a) and (8.4a), it is possible to predict the limiting depth of cut of any machine tool system whose frequency response characteristics are known.

9. OVERALL CONCLUSIONS AND AREA FOR FURTHER WORK

9.1 Overall Conclusions

(1) For machining with boring bars under stable conditions, both theories and experiments indicate the existence of two types of geometric form errors, namely the "bell-mouth" errors and the "copying" errors. "Bell-mouth" errors occur on the entry of boring tool into the work-piece and the theory did not seem to fit the results well. "Copying" errors are defined as the ratio of the final eccentricity error to the initial eccentricity error and as such are related to both the initial eccentiricity of the bore and the flexibility of the overhung boring bar. The theory on "copying" errors agreed remarkably well with the experimental results when the initial eccentricity was small compared with the depth of cut.

(2) The dynamical behaviour of the slug-damped boring bar in terms of frequency response curves was characterised by a lumped-parameter model in which the respective masses of the bar and of the slug-damper were linked together by a linear dashpot and a linearized fluid inertia coupler. This formulation was found to be a significant improvement over the model of Hahn[1] in that the inertia effect of the air film surrounding the slug was taken into account.

(3) The theoretical frequency response curves calculated using the lumped-parameter model were not in close agreement with the experimental curves. It was reasoned that were the compressibility effects of the air film around the slug considered, a better fit could be expected.

Despite this simplification, the model revealed the possibility of design improvements. In consequence, the prototype optimally-tuned slug-damped tungsten-bunged bar was developed and tested.

(4) Based on the lumped-parameter model, an optimization method was devised whereby the bung length for the minimum amplitude response at resonance could be determined. A similar method was also devised for the case of maximum resistance to machining chatter. Both methods gave the same optimum bung length for the prototype tungsten-bunged boring bar. Results demonstrated that this bar was far superior to other bars under test in respect of the dynamic and machining behaviour.

(5) The stability borderline expressed in terms of the negative damping coefficient - as a source of instability - and of the cutting force slope was derived from the lumped-parameter model. However, since the model was not exact and hence accuracies of the stability borderline thus calculated would suffer, a more precise stability model based on the theory of closed-loop control was suggested. The procedure involved was graphical, and the main advantage was the representation of the dynamical characteristics of a boring bar by means of its frequency response curves instead of the lumped-parameters in the model.

(6) When the limiting depths of cut exceeded the nose radius of the boring tool, the cutting force slope became very small and the negative damping coefficient approached its asymptote. A one-to-one correspondence was found to exist between the asymptotic negative damping coefficient and the limiting depth of cut. It is, therefore, possible

in principle to predict the limiting depth of cut of any machine tool system whose frequency response characteristics are known.

(7) Compared with other bars tested, the prototype optimally-tuned tungsten-bunged boring bar was found to possess the best dynamic and machining characteristics. When machining EN8 steel at the feed of 0.0065"/rev (0.165 mm/rev) and the speed of 500 rpm on a 3½" bore (140m/min), the boring bar would readily remove depths of cut up to 0.110" (2.79 mm) without any signs of chatter. Even when machining high duty alloy steel such as the RRS/HBH, chatter free finishes could always be obtained at depths of cut under 0.030" (0.762 mm), feeds between 0.0044"/rev and 0.0104"/rev (0.112 mm/rev and 0.264 mm/rev) and a speed of 190 rpm on a 3¼" diameter bore (49 m/min).

9.2 Area for Further Work

The optimally-tuned tungsten-bunged boring bar has been found to be able to take heavier depths of cut than other designs of boring bars under test without the occurrence of chatter. However, this causes two problems to rise to significance.

(1) Geometric form error - It occurs as a result of the heavier cutting load and of the flexible nature of the boring bar. The analyses presented in Chapter 2 are only approximate as reflected in the discrepancies between the experimental and theoretical results. A more exact analysis will be needed if one is to obtain a more satisfactory model from which the geometric form errors can be predicted in a quantitive manner and hence corrective actions that

may be in the form of adaptive control can be taken for its elimination. This work has initiated an investigation now being conducted in the Department.

(2) Chip disposal - It is a problem common in profile boring in which the chip flow passage is necessarily restricted by the geometry of the bore and of the boring bar. The problem is further aggravated by the increased metal removal rate by virtue of the heavier depths of cut now attainable. By a suitable choice of cutting conditions and tool geometry, it is possible to control the chip flow such that it does not impinge on the cutting process. There is scope for development into the chip flow characteristics and the effective chip removal.

The damping mechanism of the slug damper as modelled by a linear damping coefficient and an inertia coefficient is clearly not adequate. The squeeze film[2] surrounding the slug has been found to have a significant effect on the damping behaviour. To a first approximation, this effect can be represented by a spring element. As a result, the optimization method whereby the optimum bung length is derived may have to be refined to give a more precise design basis.

The stability theories developed in Chapter 6 and Appendix E made use of the concept of negative damping as being a source of instability. In Chapter 8, it was found that the asymptotic negative damping coefficient was related uniquely to the limiting depth of cut, which can be represented by an empirical function. If enough of this relation is established, it is in principle possible to predict the limiting depth of cut for any machine tool system once its dynamic

characteristics in the form of frequency response curves are known. Further research in this area may bring fruitful results.

REFERENCES FOR CHAPTER 9

1. Hahn R S "Metal cutting chatter and its elimination" Trans ASME 75, 1953, p1073

2. TWUMASI-BOATENG M "The slug-damper; mechanisms of operation and squeeze film effects of a compressible damping fluid" PhD Thesis 1980, Department of Production Technology, Brunel University

APPENDIX A CALCULATING EQUIVALENT STATIC STIFFNESS OF OVERHUNG BAR

The overhung boring bar is assumed to have an infinitely rigid end-fixing and hence is analogous to a cantilever with an encastre end. To determine the equivalent stiffness, it is a prerequisite to know the amount of deflection under the point of application of the load at the free end. The Myosotis Method[1] is employed to calculate the static deflection and hence the static stiffness explained as follows.

Consider a general composite bar which will account for all of the different designs of boring bars that are discussed in this thesis. The bar consists of four parts of unequal flexural rigidities, namely E_1I_1, E_2I_2, E_3I_3, and E_4I_4, as shown in Fig A1. A load P is applied at the free end and the deflection under the point of load application is denoted by δ . The Myosotis Method is based on the principle of superposition which asserts that the deflection curve of the bar in Fig A1 is the algebraic sum of the deflection curves of the individual section of the bar with other sections assumed to have infinite flexural rigidities. Thus, for instance, when the E_1I_1 section is considered, the rest of the bar is assumed to be infinitely rigid and the deflection curve caused by the load P will be as shown in Fig A2. The end deflection under P is seen to consist of two components: a deflection δ_1 at point A, and a deflection $\delta_2=\psi(\ell_4-\ell_1)$ which is the linear extrapolation of the slope ψ at A. Other sections will be considered similarly.

With reference to Fig A1, at section A-A, the shear force is P and the bending moment is $P(\ell_4-\ell_1)$. The loading P causes a deflection $\frac{P\ell_1^3}{3E_1I_1}$, whilst the bending moment $P(\ell_4-\ell_1)$ causes a deflection $\frac{P(\ell_4-\ell_1)\ell_1^2}{2E_1I_1}$. The slope at section A-A caused by P is $\frac{P\ell_1^2}{2E_1I_1}$ and by $P(\ell_4-\ell_1)$ is $\frac{P(\ell_4-\ell_1)\ell_1}{E_1I_1}$. Thus, the deflection at the free end, ie section D-D, is:

$$\delta_A = \frac{P\ell_1^3}{3E_1I_1} + \frac{P(\ell_4-\ell_1)\ell_1^2}{2E_1I_1} + (\ell_4-\ell_1)\left[\frac{P\ell_1^2}{2E_1I_1} + \frac{P(\ell_4-\ell_1)\ell_1}{E_1I_1}\right] \quad \ldots\ldots \quad (A1)$$

At section B-B, the shear force is P and the bending moment is $P(\ell_4 - \ell_2)$. The deflection at B-B, assuming E_1I_1, E_3I_3, and E_4I_4 as infinitely large, is

$$\frac{P(\ell_2-\ell_1)^3}{3E_2I_2} + \frac{P(\ell_4-\ell_2)(\ell_2-\ell_1)^2}{2E_2I_2}$$

the first term being the deflection caused by the load P and the second term the deflection caused by the bending moment $P(\ell_4 - \ell_2)$.

The slope at B-B relative to the tangent line at A-A is

$$\frac{P(\ell_2-\ell_1)^2}{2E_2I_2} + \frac{P(\ell_4-\ell_2)(\ell_2-\ell_1)}{E_2I_2}$$

where the first and second terms arise from the respective load P and the bending moment $P(\ell_4 - \ell_2)$.

It follows that the deflection at the free end is

$$\delta_B = \frac{P(\ell_2-\ell_1)^3}{3E_2I_2} + \frac{P(\ell_4-\ell_2)(\ell_2-\ell_1)^2}{2E_2I_2} + (\ell_4-\ell_2)\left[\frac{P(\ell_2-\ell_1)^2}{2E_2I_2} + \frac{P(\ell_4-\ell_2)(\ell_2-\ell_1)}{E_2I_2}\right] \quad (A2)$$

At section C-C, the shearing force is P and the bending moment is $P(\ell_4 - \ell_3)$.

The deflection at C-C, assuming E_1I_1, E_2I_2, and E_4I_4 as infinitely large, is

$$\frac{P(\ell_3-\ell_2)^3}{3E_3I_3} + \frac{P(\ell_4-\ell_3)(\ell_3-\ell_2)^2}{2E_3I_3}$$

and the slope at C-C relative to the tangent line at B-B is

$$\frac{P(\ell_3-\ell_2)^2}{2E_3I_3} + \frac{P(\ell_4-\ell_3)(\ell_3-\ell_2)}{E_3I_3}$$

Thus, the deflection at the free end is

$$\delta_C = \frac{P(\ell_3-\ell_2)^3}{3E_3I_3} + \frac{P(\ell_4-\ell_3)(\ell_3-\ell_2)^2}{2E_3I_3} + (\ell_4-\ell_3)\left[\frac{P(\ell_3-\ell_2)^2}{2E_3I_3} + \frac{P(\ell_4-\ell_3)(\ell_3-\ell_2)}{E_3I_3}\right] \quad (A3)$$

Finally at the free end, ie, section D-D, the shearing force is P but there is no bending moment. Assuming flexural rigidities, except E_4I_4, as infinitely large, the deflection is simply,

$$\delta_D = \frac{P(\ell_4-\ell_3)^3}{3E_4I_4} \quad (A4)$$

The deflection δ under the load P for this composite bar is the sum of eqts(A1) to(A4), ie

$$\delta = \delta_A + \delta_B + \delta_C + \delta_D \qquad \text{(A5)}$$

By definition, the static equivalent stiffness is given by

$$K = \frac{P}{\delta} \qquad \text{(A6)}$$

Static stiffness calculation

(1) Solid bar

$l_1 = l_2 = l_3 = l_4 = 0.381$ m

$E_1I_1 = E_2I_2 = E_3I_3 = E_4I_4 = \frac{\pi}{64} \times (0{\cdot}038)^4 \times 200 \times 10^9 = 20{\cdot}471 \times 10^3$ Nm^2

From eqt(A6), the static stiffness K = 1.110 MN/m

(2) Recessed bar

$l_1 = l_2 = 0.287$ m

$l_3 = 0.337$ m

$l_4 = 0.381$ m

$E_1 = E_2 = E_3 = E_4 = 200$ GN/m^2

$I_1 = I_2 = I_4 = \frac{\pi}{64} \times (0{\cdot}038)^4 = 102{\cdot}354 \times 10^{-9}$ m^4

$I_3 = \frac{\pi}{64} \times (0{\cdot}038^4 - 0{\cdot}0254^4) = 81{\cdot}922 \times 10^{-9}$ m^4

From eqt(A6), the static stiffness K = 1.107 MN/m

(3) Steel-bunged bar

$l_1 = 0.100$ m

$l_2 = 0.287$ m

$l_3 = 0.337$ m

$l_4 = 0.381$ m

$E_1 = E_2 = E_3 = E_4 = 200$ GN/m^2

$I_1 = I_4 = \frac{\pi}{64} \times (0{\cdot}038)^4 = 102{\cdot}354 \times 10^{-9}$ m^4

$I_2 = \frac{\pi}{64} \times (0.038^4 - 0.030^4) = 62.593 \times 10^{-9} m^4$

$I_3 = \frac{\pi}{64} \times (0.038^4 - 0.0254^4) = 81.922 \times 10^{-9} m^4$

From eqt(A6), the static stiffness K = 0.722 MN/m

(4) Tungsten-bunged bar

$l_1 = 0.220$ m

$l_2 = 0.256$ m

$l_3 = 0.332$ m

$l_4 = 0.381$ m

$E_1 I_1 = (EI)_t + (EI)_s = 2.67 \times 200 \times 10^9 \times \frac{\pi}{64} \times (0.030^4) + 200 \times 10^9 \times \frac{\pi}{64} \times (0.038^4 - 0.030^4)$

$= 33.751 \times 10^3 Nm^2$

where $(EI)_t$ is the flexural rigidity of the tungsten bung and $(EI)_s$ is the flexural rigidity of the steel hollow sleeve.

$E_2 I_2 = 200 \times 10^9 \times \frac{\pi}{64} \times (0.038^4 - 0.030^4) = 12.519 \times 10^3 Nm^2$

$E_3 I_3 = 200 \times 10^9 \times \frac{\pi}{64} \times (0.038^4 - 0.0254^4) = 16.384 \times 10^3 Nm^2$

$E_4 I_4 = 200 \times 10^9 \times \frac{\pi}{64} \times (0.038^4) = 20.471 \times 10^3 Nm^2$

From eqt(A6), the static stiffness K = 1.652 MN/m

Reference

(1) Den Hartog, JP "Strength of Materials" Dover Publications, Inc, New York, 1949, p 85

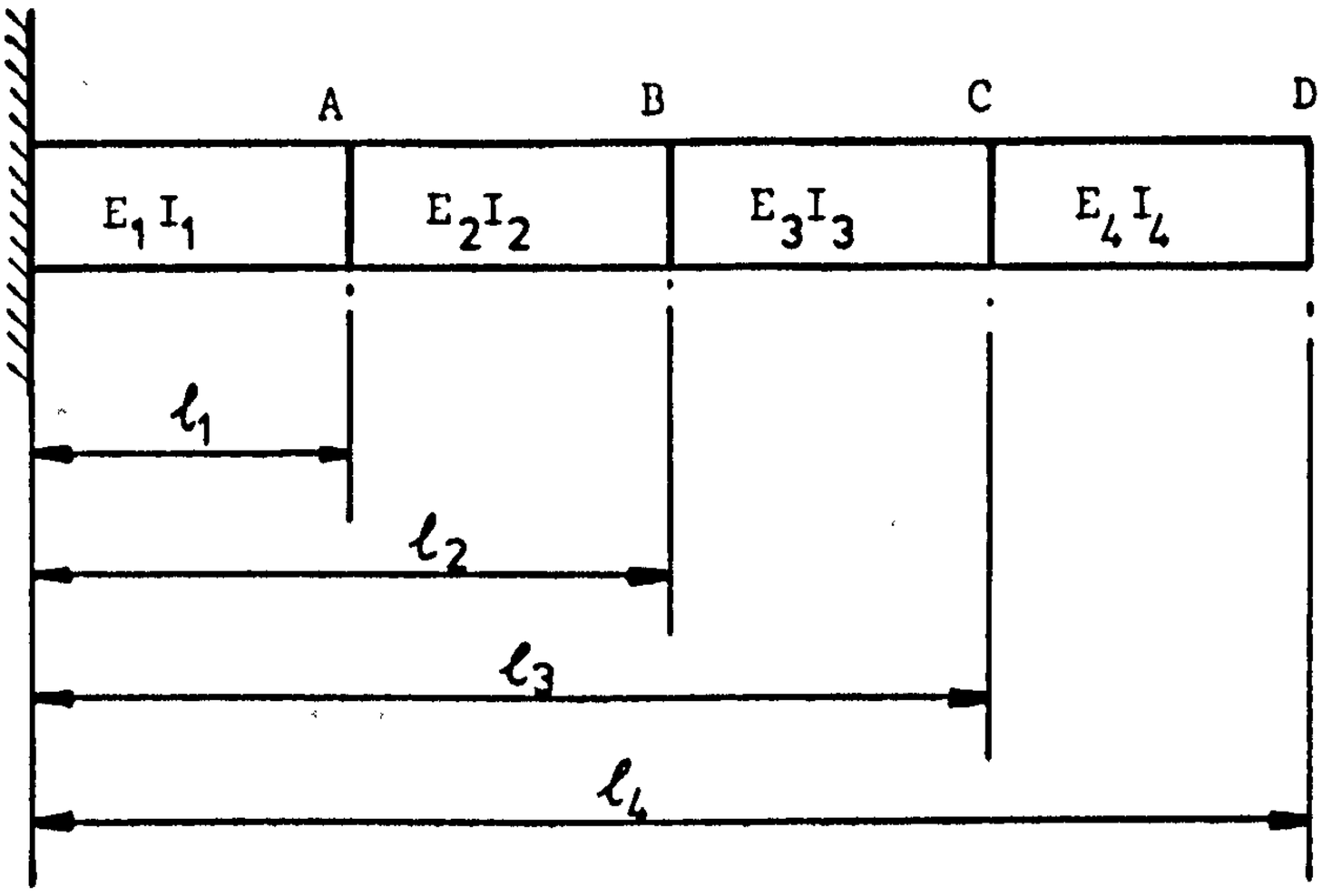

Fig A1 A cantilever with four sections of different flexural rigidities

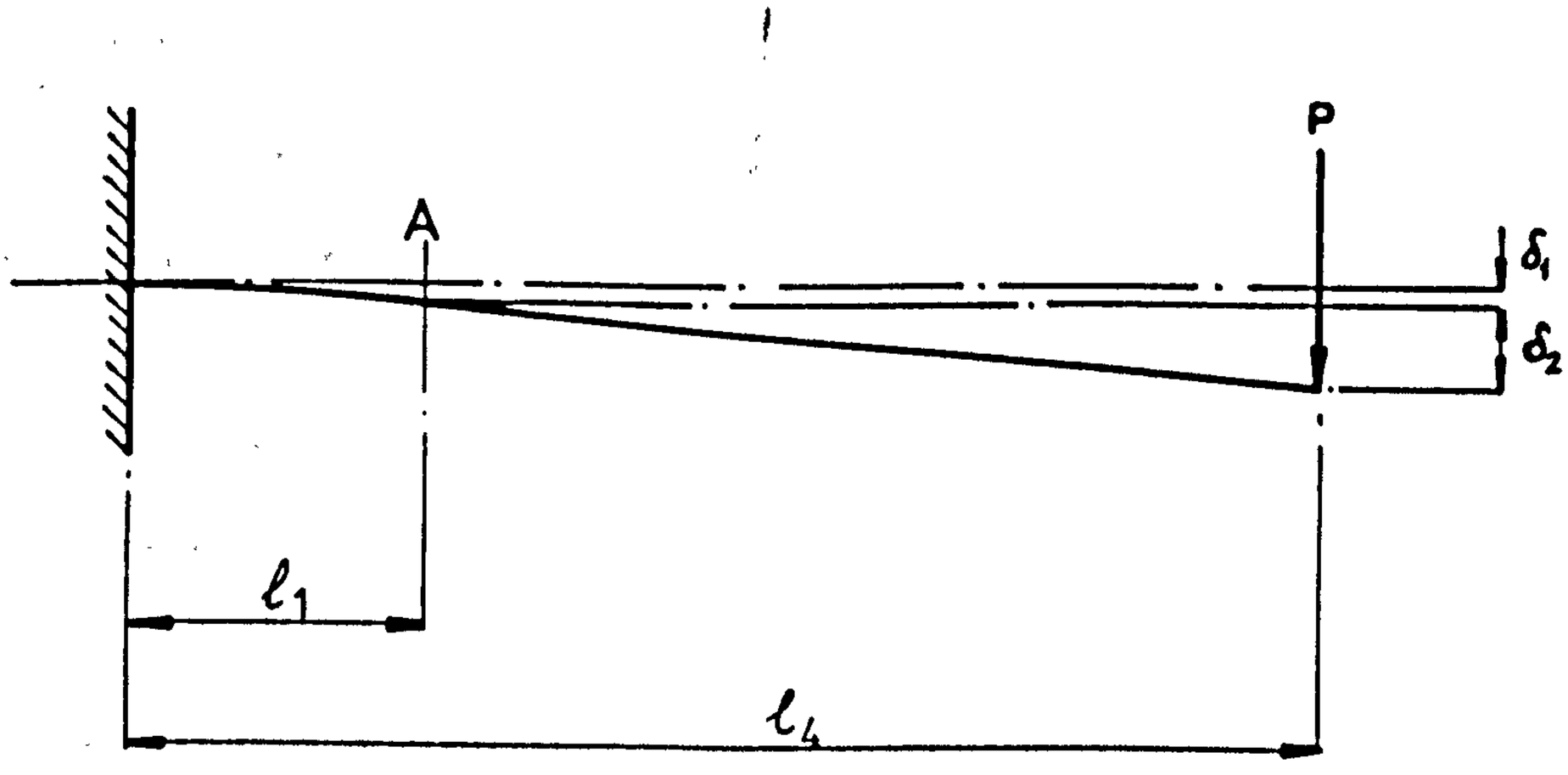

Fig A2 Deflection shape of cantilever under the end load P. Only the length from the fixed end to A bends, the rest of the beam is infinitely rigid.

APPENDIX B AMPLITUDE RATIO G AND KINETIC ENERGY T [1]

AMPLITUDE RATIO G

In boring bar practice the absorber slug is normally positioned within the bar some distance behind the toolpost as is depicted in Fig. B1. The slug m_s is at a distance ℓ_2 from the fixed end, and the equivalent mass of the boring bar at the free end without the slug is designated by m. It will be observed that the displacement of the bar at the central position of the slug m_s is x_1, as against x_o for m. It follows that the effectiveness of the slug is decreased when reckoned at the overhung end, because x_1 is less than x_o. Thus for the purpose of analysis

$$x_1 = Gx_o \qquad \text{(B1)}$$

where the value of G depends on the deflection shape of the boring bar.

KINETIC ENERGY

Fig. B2 shows the cross-section AA (in Fig. B1) through the bar at a point mid-way along the length of the slug. The slug is assumed to oscillate about an instantaneous centre. This is equivalent to the assumption that the slug rolls with such small oscillations that any possible vertical motions are ignored.

The total kinetic energy of the system is given by

$$T = T_B + T_{SL} + T_{SR} + T_f,$$

where T_B = K.E. of equivalent mass of bar,

T_{SL} = K.E. of slug, translational motion,

T_{SR} = K.E. of slug, angular motion,

and T_f = K.E. of damping fluid.

With reference to Fig. B2, the kinetic energies are respectively,

$$T_B = \frac{1}{2} m\dot{x}_o^2$$

$T_{SL} = \frac{1}{2} m_s \dot{x}_2^2$, where $\dot{x}_2$ is the instantaneous velocity of the slug,

$T_{SR} = \frac{1}{2} m_s \lambda^2 \dot{\alpha}^2$, where $\dot{\alpha}$ is the angular velocity of the slug, and λ is the radius of gyration about its instantaneous centre.

Assuming pure rolling without sliding and let R_2 be the radius of the slug,

$$R_2\dot{\alpha} = \dot{x}_1 - \dot{x}_2$$

from which

$$T_{SR} = \frac{1}{2} m_s \left(\frac{\lambda}{R_2}\right)^2 (\dot{x}_1 - \dot{x}_2)^2$$

and $T_f = \frac{1}{2} m_f \beta_c \ (\dot{x}_1 - \dot{x}_2)^2$

Thus, the total kinetic energy of the system is

$$T = \frac{1}{2} m\dot{x}_o^2 + \frac{1}{2} m_s \dot{x}_2^2 + \frac{1}{2} m_s \left(\frac{\lambda}{R_2}\right)^2 (\dot{x}_1 - \dot{x}_2)^2 + \frac{1}{2} m_f \beta_c (\dot{x}_1 - \dot{x}_2)^2$$

In terms of the two coordinates x_1 and x_2 and their time derivatives, the last equation becomes

$$T = \frac{1}{2} \frac{m}{G^2} \dot{x}_1^2 + \frac{1}{2} m_s \dot{x}_2^2 + \frac{1}{2} \left[m_s \left(\frac{\lambda}{R_2}\right)^2 + m_f \beta_c \right] (\dot{x}_1 - \dot{x}_2)^2 \qquad (B2)$$

Reference

1. Ng, K.W. and New, R.W. "Overhung Boring Bars - Part I, Dynamic Behaviour of New Designs of Damped Boring Bars under Forced Vibratory Conditions", Brunel University, Dept. of Production Technology, S.R.C. Research Report BB1, October, 1977.

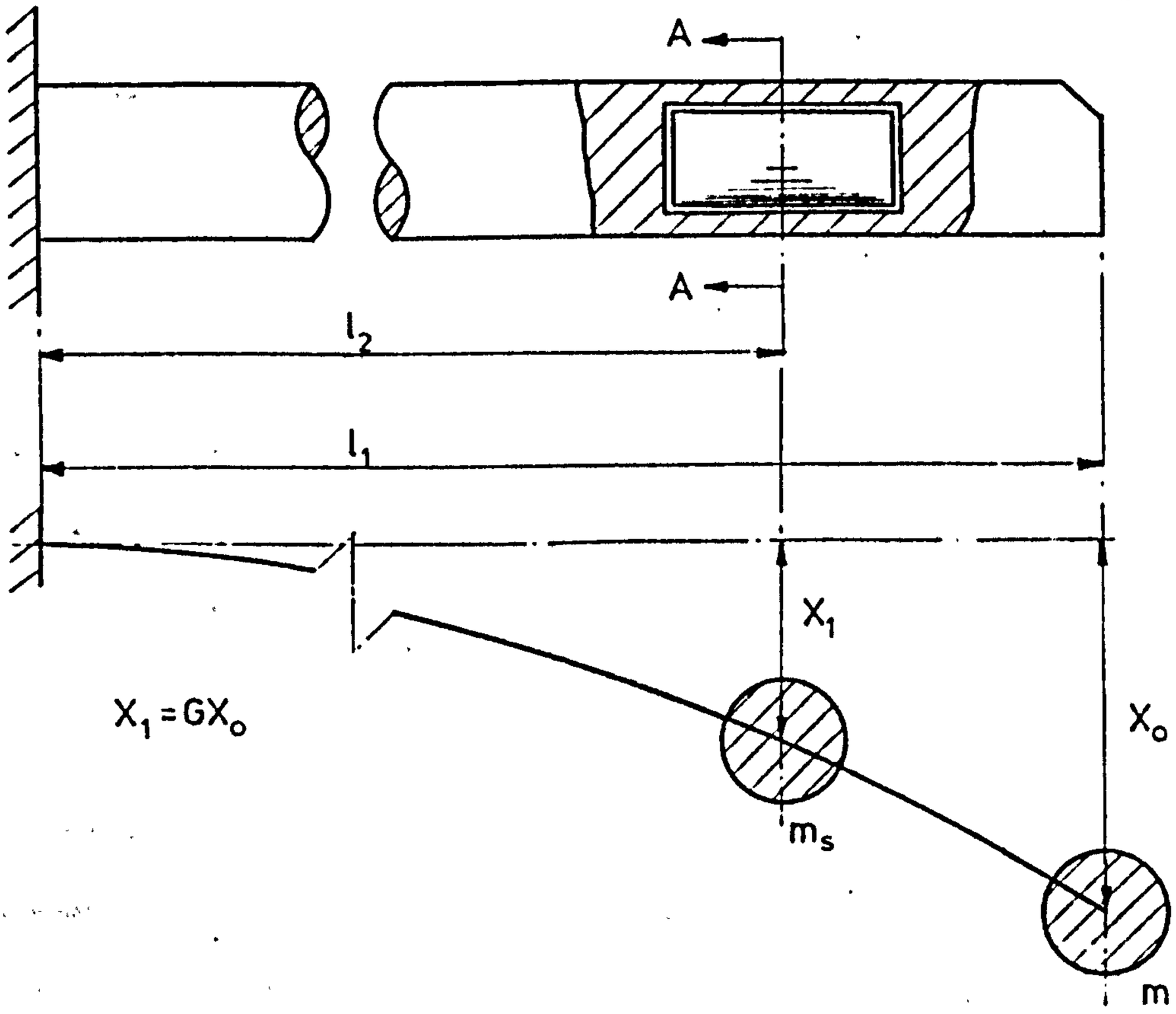

Fig B1 Position of slug absorber along bar (plan view)

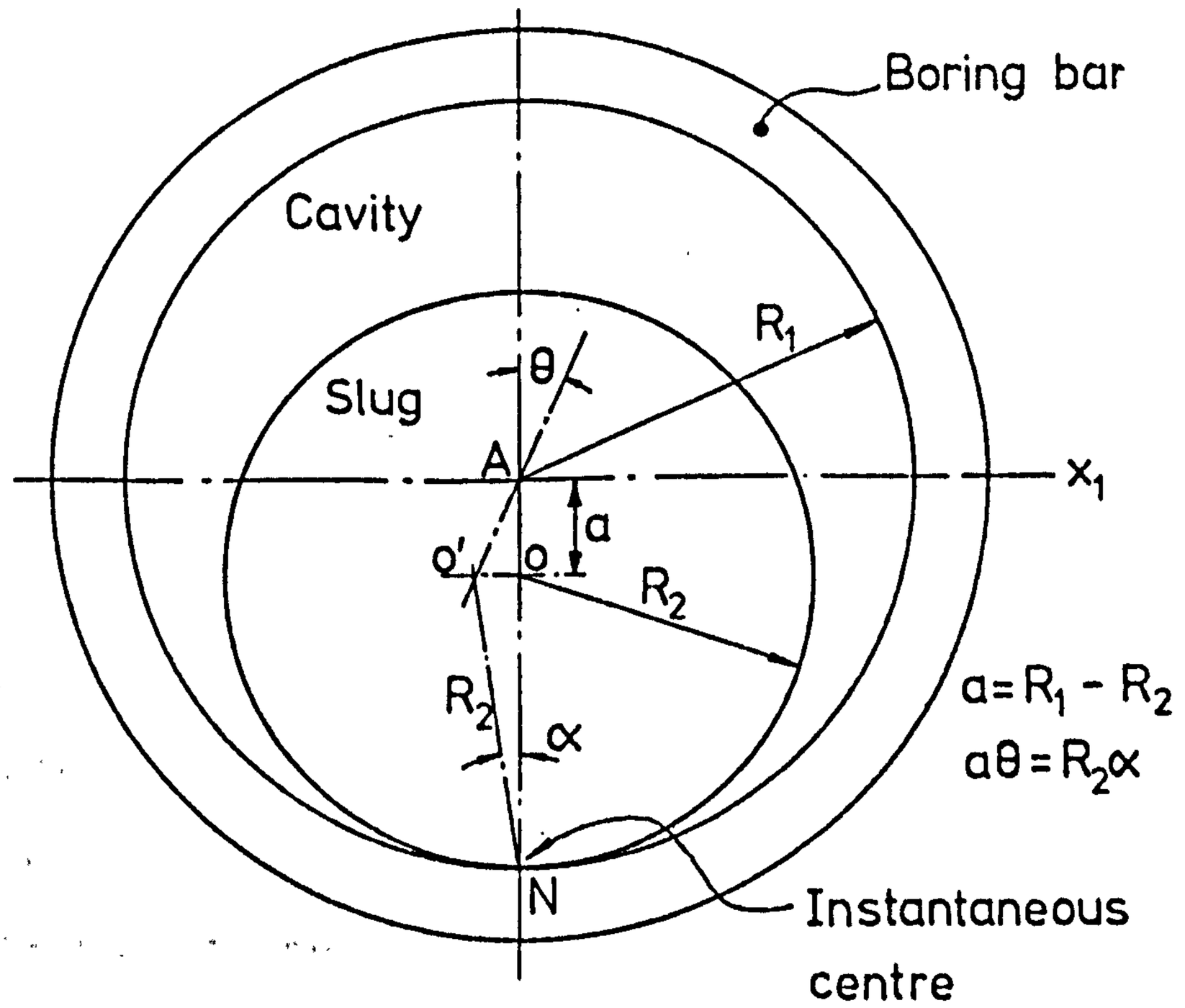

Fig B2 Absorber slug in bar (cross section on AA, Fig B1)

APPENDIX C OPTIMIZING BUNG LENGTH FOR MINIMUM AMPLITUDE AT RESONANCE

It was found in section 4.4 that the minimum amplitude response at resonance is

$$|X_o| = \frac{P_o}{K}\left[\frac{2(1+u)\ell}{u} - 1\right] \qquad (4.41)$$

We shall look at the physical significance of this equation. In the context of a slug-damped boring bar, the minimum amplitude response $|X_o|$ corresponds to when the bar is fitted with the optimum slug damper. Further reduction in $|X_o|$ can be achieved by a suitable choice of the stiffness K and the mass ratio μ. Of the different possible ways that enable K and μ to be changed, perhaps the most direct and effective way is to make use of the idea of a bung with a variable length as shown in Fig C1 so that the stiffness K and the mass ratio μ can be varied accordingly. Since high stiffness is always desirable, the use of materials with high tensile strength is suggested. Specifically, the bung in our design will be made of tungsten carbide. From a purely theoretical consideration and assuming that the bar deflects in the shape of a quarter cosine wave, the equivalent stiffness of the bar can be calculated from eqt(4.46), ie

$$K = \left(\frac{\pi}{2\ell_1}\right)^4 \sum_{i=1}^{n} E_i I_i \int \cos^2 \frac{\pi x}{2\ell_1}\, dx \qquad (4.46)$$

and the equivalent mass which is required in the evaluation of the mass ratio can be found from eqt(4.48), ie

$$m = \sum_{i=1}^{n} \bar{\rho}_i \int \left(1 - \cos \frac{\pi x}{2\ell_1}\right)^2 dx \qquad (4.48)$$

The optimization method essentially involves the successive computation of the equivalent stiffness K from eqt(4.46), the equivalent mass m from eqt(4.48) and the minimum amplitude at resonance $|X_o|$ from eqt(4.41) for the successive values that the bung length may be allowed to take. For obvious reasons, the optimum bung length corresponds to when $|X_o|$ becomes the minimum. The computation

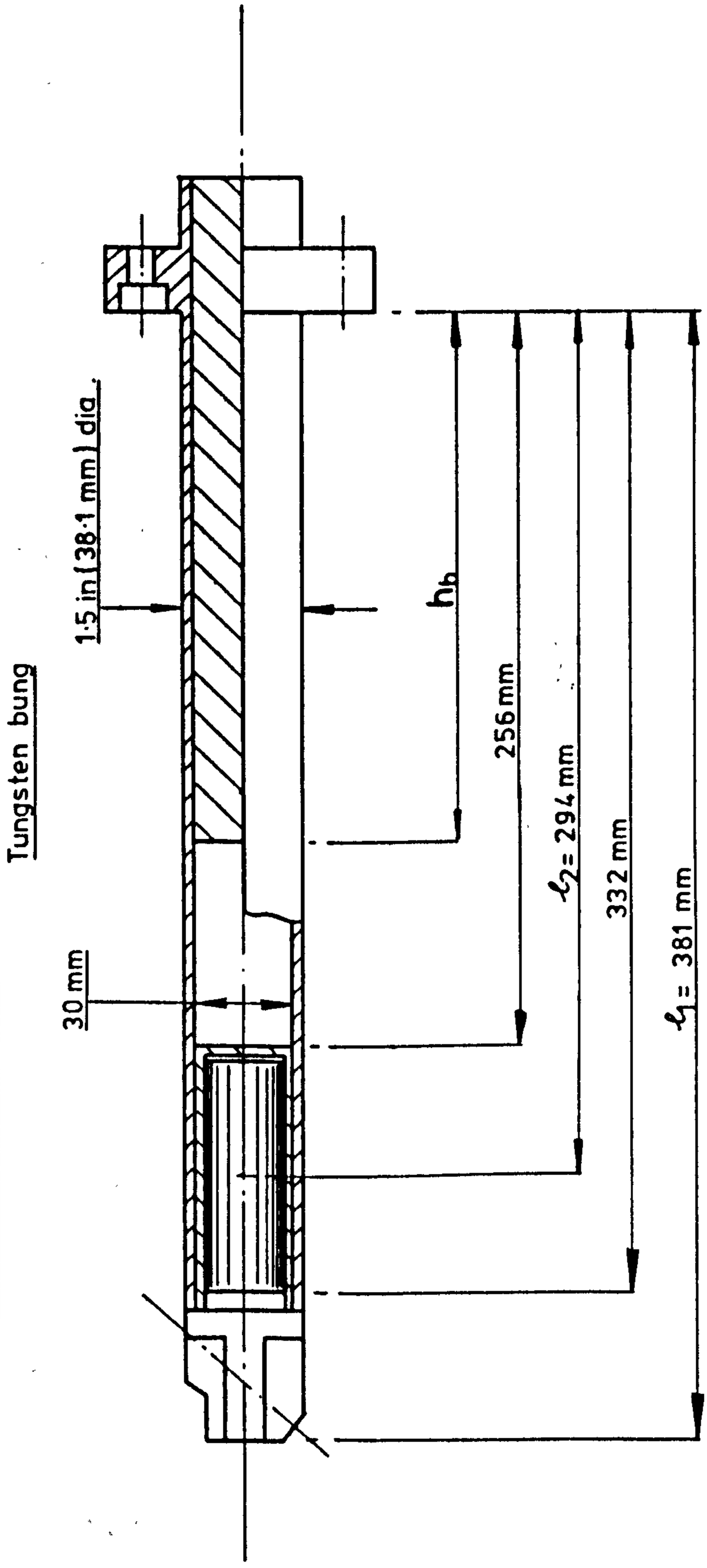

Fig C1 A single-slug-damped boring bar forced-fit with a tungsten bung of variable length h_b

involved in the design of the tungsten-bunged bar is presented in the rest of this Appendix. Initially we assign length dimensions arbitrarily to the bar as shown in Fig C1, whilst the bung length h_b is to be optimized and hence is allowed to vary.

(1) Amplitude ratio G

Assuming that the bar deflects in the shape of a quarter cosine wave, then the deflection at a point on the bar distant x from the root end is

$$y(x) = y_o \left(1 - \cos \frac{\pi x}{2\ell_1} \right) \qquad (4.45)$$

By the definition of G as in Appendix B, $G = \dfrac{y(\ell_2)}{y(\ell_1)}$

where, as is obvious from Fig C1, $\ell_1 = 0.381$ m and $\ell_2 = 0.294$ m.

Combining the last two equations gives $G = \dfrac{y_o \left(1 - \cos \frac{\pi \ell_2}{2\ell_1} \right)}{y_o \left(1 - \cos \frac{\pi \ell_1}{2\ell_1} \right)}$

$$\text{ie } G = 0.6490 \qquad (C1)$$

(2) Slug mass m_s

The slug has a nominal diameter of 0.0254 m and a length of 0.076 m. From materials handbook, its density is given as 16.8 Mg/m^3. The mass of the slug is, therefore,

$$m = \frac{\pi \times 0{\cdot}0254^2}{4} \times 0{\cdot}076 \times 16800 = 0{\cdot}6470 \text{ kg} \qquad (C2)$$

(3) Equivalent spring stiffness K

Being a free component in the cavity, the slug does not contribute towards the overall equivalent stiffness of the bar. On the basis of different

flexural rigidities, the bar may be considered to be composed of four sections which can be defined mathematically as (see Fig C1):

i) Section 1 $0<x<h_b$

ii) Section 2 $h_b<x<0.256$

iii) Section 3 $0.256<x<0.332$

iv) Section 4 $0.332<x<0.381$

where all length dimensions are understood to be in metres.

By eqt(4.46)and taking the end points of these intervals as the limits of integration,

$$K = \left(\frac{\pi}{2\ell_1}\right)^3 \left[E_1I_1\int_0^h \cos^2\frac{\pi x}{2\ell_1}\, d\left(\frac{\pi x}{2\ell_1}\right) + E_2I_2\int_{h_b}^{0.256} \cos^2\frac{\pi x}{2\ell_1}\, d\left(\frac{\pi x}{2\ell_1}\right) + E_3I_3\int_{0.256}^{0.332} \cos^2\frac{\pi x}{2\ell_1}\, d\left(\frac{\pi x}{2\ell_1}\right) + E_4I_4\int_{0.332}^{0.381} \cos^2\frac{\pi x}{2\ell_1}\, d\left(\frac{\pi x}{2\ell_1}\right)\right]$$

From the table of standard integrals, $\int \cos^2 u\, du = \frac{1}{2}u + \frac{1}{4}\sin 2u + C$.

and if we make the identification that $u=\frac{\pi x}{2\ell_1}$ and carry out the integration as indicated,

$$K = \left(\frac{\pi}{2\ell_1}\right)^3 \left\{(E_1I_1-E_2I_2)\left[\frac{1}{2}\left(\frac{\pi h_b}{2\ell_1}\right)+\frac{1}{4}\sin 2\left(\frac{\pi h_b}{2\ell_1}\right)\right]+(E_2I_2-E_3I_3)\cdot\left[\frac{1}{2}\left(\frac{0.256\,\pi}{2\ell_1}\right)+\frac{1}{4}\sin 2\left(\frac{0.256\pi}{2\ell_1}\right)\right]+(E_3I_3-E_4I_4)\left[\frac{1}{2}\left(\frac{0.332\pi}{2\ell_1}\right)+\frac{1}{4}\sin 2\left(\frac{0.332\pi}{2\ell_1}\right)\right]+E_4I_4\left[\frac{1}{2}\left(\frac{0.381\pi}{2\ell_1}\right)+\frac{1}{4}\sin 2\left(\frac{0.381\,\pi}{2\ell_1}\right)\right]\right\} \quad (C3)$$

The flexural rigidities E_1I_1 to E_4I_4 are taken to refer to the four sections or intervals. In the interval $0<x<h_b$.E_1I_1 is the sum of the flexural rigidities of the tubular steel shank and of the solid round tungsten bung. From the materials hnadbook, E's for steel and tungsten are respectively given as 200 and 534 GN/m^2.

From Fig C1 and by the definition of the second moment of area I, for the tubular shank,

$$I_s = \frac{\pi(0{\cdot}0381^4 - 0{\cdot}030^4)}{64} = 63{\cdot}67 \times 10^{-9}\,m^4$$

and for the tungsten bung,

$$I_t = \frac{\pi(0{\cdot}030^4)}{64} = 39{\cdot}76 \times 10^{-9}\,m^4$$

It follows that

$$E_1I_1 = (200\times10^9 \times 63{\cdot}67\times10^{-9} + 534\times10^9 \times 39{\cdot}76\times10^{-9}) = 33{\cdot}97\times10^3\ Nm^2$$

In the interval $h_b < x < 0.256$,

$$E_2I_2 = 200\times10^9 \times 63{\cdot}67\times10^{-9} = 12{\cdot}73\times10^3\ Nm^2$$

In the interval $0.256 < x < 0.332$,

$$E_3I_3 = 200\times10^9 \times \pi\,\frac{(0{\cdot}0381^4 - 0{\cdot}0254^4)}{64} = 16{\cdot}60\times10^3\ Nm^2$$

In the interval $0.332 < x < 0.381$,

$$E_4I_4 = 200\times10^9 \times \frac{\pi(0{\cdot}0381^4)}{64} = 20{\cdot}69\times10^3\ Nm^2$$

Substituting the numerical values thus calculated into eqt(C3)and noting that $\ell_1 = 0.381$, we obtain, after some simplifications,

$$K = 7{\cdot}1317\times10^5 + 3{\cdot}0683\times10^6 h_b + 3{\cdot}7212\times10^5 \sin\left(\frac{\pi h_b}{0{\cdot}381}\right) \qquad (C4)$$

In eqt(C4), K is now expressed as a function of a single independent variable, namely h_b. Five significant figures are retained at this stage of the calculation but at most three significant figures in the final results are reliable since some of the quantities, for example, E's for steel and tungsten are accurate to three significant figures only.

(4) Equivalent mass m

In the same manner as in the determining of equivalent stiffness, the bar is again divided into four sections or intervals. Use is then made of eqt(4.48)to find the equivalent mass. It can be shown that the integral

in eqt(4.48), ie

$$\int \left(1-\cos\frac{\pi x}{2\ell_1}\right)^2 dx = x + \frac{x}{2} + \frac{\ell_1}{2\pi}\sin\frac{\pi x}{2\ell_1} - \frac{4\ell_1}{\pi}\sin\frac{\pi x}{2\ell_1} + C$$

The densities of steel and tungsten carbide are respectively taken to be 7.83 Mg/m^3 and 14.4 Mg/m^3. The mass per unit length $\overline{\rho}_1$ in eqt(4.48) is not only a function of the density of material but also of the geometrical shapes within a given interval. Thus, in the interval $0 < x < h_b$,

$$\overline{\rho}_1 = 7{\cdot}83\times10^3 \times \frac{\pi(0{\cdot}0381^2-0{\cdot}030^2)}{4} + 14{\cdot}4\times10^3 \times \frac{\pi\times0{\cdot}030^2}{4} = 13{\cdot}571 \ \ kg/m$$

In the interval $h_b < x < 0.256$

$$\overline{\rho}_2 = 7{\cdot}83\times10^3 \times \frac{\pi(0{\cdot}0381^2-0{\cdot}030^2)}{4} = 3{\cdot}3922 \ \ kg/m$$

In the interval $0.256 < x < 0.332$, assuming that the bottom of the slug container has negligible mass,

$$\overline{\rho}_3 = 7{\cdot}83\times10^3 \times \frac{\pi(0{\cdot}0381^2-0{\cdot}0254^2)}{4} = 4{\cdot}9594 \ \ kg/m$$

In the interval $0.332 < x < 0.381$, assuming that the toolpost is of solid round shape,

$$\overline{\rho}_4 = 7{\cdot}83\times10^3 \times \frac{\pi(0{\cdot}0381^2)}{4} = 8{\cdot}9269 \ \ kg/m$$

By eqt(4.48), the equivalent mass is

$$m = 14{\cdot}066\int_0^{h_b}\left(1-\cos\frac{\pi x}{2\ell_1}\right)^2 dx + 3{\cdot}3922\int_{h_b}^{0{\cdot}256}\left(1-\cos\frac{\pi x}{2\ell_1}\right)^2 dx + 4{\cdot}9594\int_{0{\cdot}256}^{0{\cdot}332}\left(1-\cos\frac{\pi x}{2\ell_1}\right)^2 dx + 8{\cdot}9269\int_{0{\cdot}332}^{0{\cdot}381}\left(1-\cos\frac{\pi x}{2\ell_1}\right)^2 dx$$

which, when simplified with $\ell_1 = 0.381$, gives

$$m = 0{\cdot}56456 + 10{\cdot}179\left[\frac{3h_b}{2} + \frac{0{\cdot}381}{2\pi}\sin\frac{\pi h_b}{0381} - \frac{4\times0{\cdot}381}{\pi}\sin\frac{\pi h_b}{2\times0{\cdot}381}\right] \qquad (C5)$$

The equivalent mass is now expressed as a function of the single variable h.

If now we define the optimum compliance, as the name implies, as the

ratio $\frac{|X_o|}{P_o}$, then by eqt(4.41)

$$\frac{|X_o|}{P} = \frac{1}{K}\left[\frac{2(1+\mu)\ell}{\mu} - 1\right]$$

where K is calculated from eqt(C4); the mass ratio μ is calculated using eqts(C5), (C1) and (C2); and the mass correction factor ℓ is assumed to be unity. The bung length h_b is permitted to take on values in the interval $0 < h_b < 0.256$ as imposed by the design constraints.

Results of the calculation are depicted graphically in Fig C2 in which the variations of the optimum compliance $\frac{|X_o|}{P_o}$ in relation to the bung length is shown. The optimum bung length corresponds to the lowest dynamic compliance. But since the compliance varies very gradually in the region around the optimum, little error is incurred if the bung length is chosen to be 220 mm. Besides, this length will ensure a higher stiffness for the bar than is the case when the bung length is at the optimum. The corresponding equivalent mass and stiffness are calculated as 0.633 kg and 1.749 MN/m respectively. The mass ratio μ = 0.430. It must be noted that, at the design stage, the values for equivalent stiffness and mass thus calculated are based on a deflection shape of a quarter cosine wave. As experiments are performed and results obtained with the tungsten-bunged bar, it is observed that the assumed deflection shape is not accurate enough, and hence refinements are needed. In consequence, the values for stiffness and mass will be affected as described in section 7.6.5.

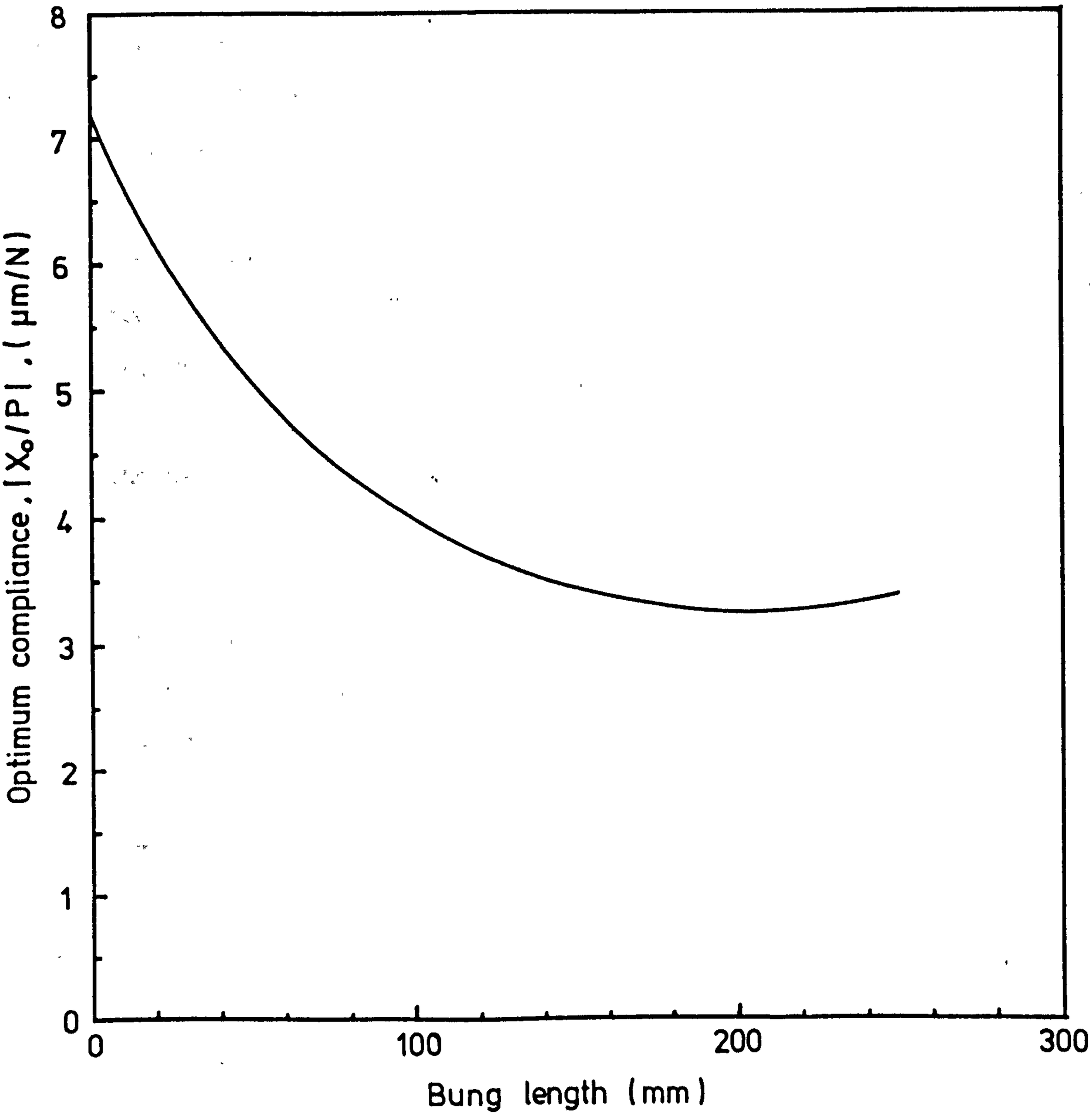

Fig C2 Relation between the optimum dynamic compliance and the bung length of a tungsten-bunged bar

APPENDIX D OPTIMIZING BUNG LENGTH FOR MAXIMUM STABILITY AGAINST CHATTER

It is to be noted that the following calculations are based on theories developed in Chapter 5 and on the schematic drawing of the tungsten-bunged bar shown in Fig C1. The cases of primary chatter and regenerative chatter will be considered separately as follows.

(1) Primary chatter

As shown in Appendix C, for the tungsten-bunged bar fitted with a slug damper, the amplitude ratio,

$$G = 0.6490 \qquad (C1)$$

and the mass of the slug

$$m_s = 0.6470 \text{ kg} \qquad (C2)$$

In addition, by assuming that the deflection shape of the bar be a quarter cosine wave, the equivalent stiffness K and the equivalent mass m of the bar taken at the free end have been shown to be

$$K = 7{\cdot}1317 \times 10^5 + 3{\cdot}0683 \times 10^6 h_b + 3{\cdot}7212 \times 10^5 \sin\left(\frac{\pi h_b}{0{\cdot}381}\right) \qquad (C4)$$

and

$$m = 0{\cdot}56456 + 10{\cdot}179\left[\frac{3h_b}{2} + \frac{0{\cdot}381}{2\pi}\sin\frac{\pi h_b}{0381} - \frac{4\times 0{\cdot}381}{\pi}\sin\frac{\pi h_b}{2\times 0{\cdot}381}\right] \qquad (C5)$$

In developing the primary chatter theory in Chapter 5, it was remarked that both the negative viscous damping coefficient f_1 and the radial force-depth of cut slope a provide a measure of the cutting condition the bar is to encounter. In particular, when the bar is optimally tuned, f_1 becomes f_{1o}, and for most practical purposes, at the stability borderline, a/K becomes insignificant. Hence, f_{1o} is given by eqt(5.22)which is repeated here.

$$f_{1o} \doteq \sqrt{Km(1+\mu)}\left[1 - \sqrt{\frac{\ell(1+\mu)-\mu}{(1+\mu)}}\right] \qquad (5.22)$$

where the mass ratio $\mu = \frac{G^2 m_s}{m}$; and the mass correction factor $\ell = 1$ assuming that the slug operates in the sliding or floating mode.

The optimization method involves the successive calculation of the equivalent stiffness K, the mass m, the mass ratio μ and the optimum negative viscous damping coefficient f_{1o} using the preceding equations for each bung length h_b assumed.

Results of the calculation are shown graphically in Fig D1 in which the optimum negative damping coefficient f_{1o} is plotted against the bung length h_b. The optimum bung length corresponds to the maximum value of f_{1o}. But since f_{1o} does not vary significantly with the bung length around its optimum, the bung length of 220 mm is chosen by virtue of higher stiffness.

(2) Regenerative chatter

Similar to the case of primary chatter, the optimization method makes use of the eqts(C4) and(C5) to find the equivalent stiffness and mass for each bung length assumed. To find the optimum negative bysteretic damping coefficient, use is made of eqt(5.45), ie

$$f_{2o} = \frac{K}{2} \frac{\mu}{\sqrt{[\ell(1+\mu)-\mu][\ell(1+\mu)]}} \qquad (5.45)$$

In particular, if, as before, the slug is assumed to slide or float during its operation, $\ell \doteq 1$ and the preceding equation is simplified to

$$f_{2o} \doteq \frac{K}{2} \frac{\mu}{\sqrt{1+\mu}} \qquad (C6)$$

Results of the calculation are depicted in Fig D2 in which f_{2o} is plotted against h_b. The optimum bung length corresponds to the maximum f_{2o}. But, for reasons as explained previously, the bung length is chosen to be 220 mm.

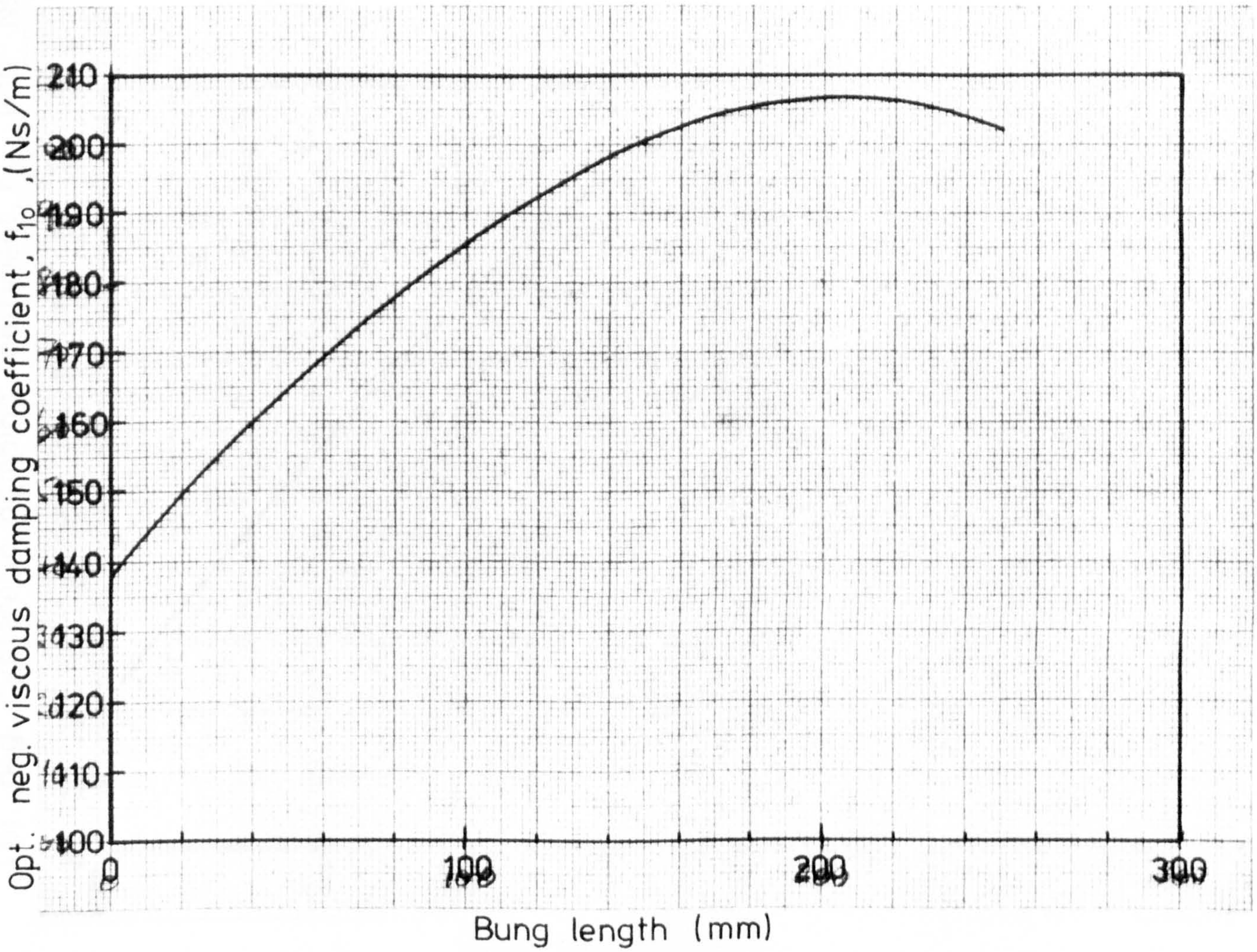

Fig D1 Relation between the optimum negative viscous damping coefficient and the bung length of a tungsten-bunged bar

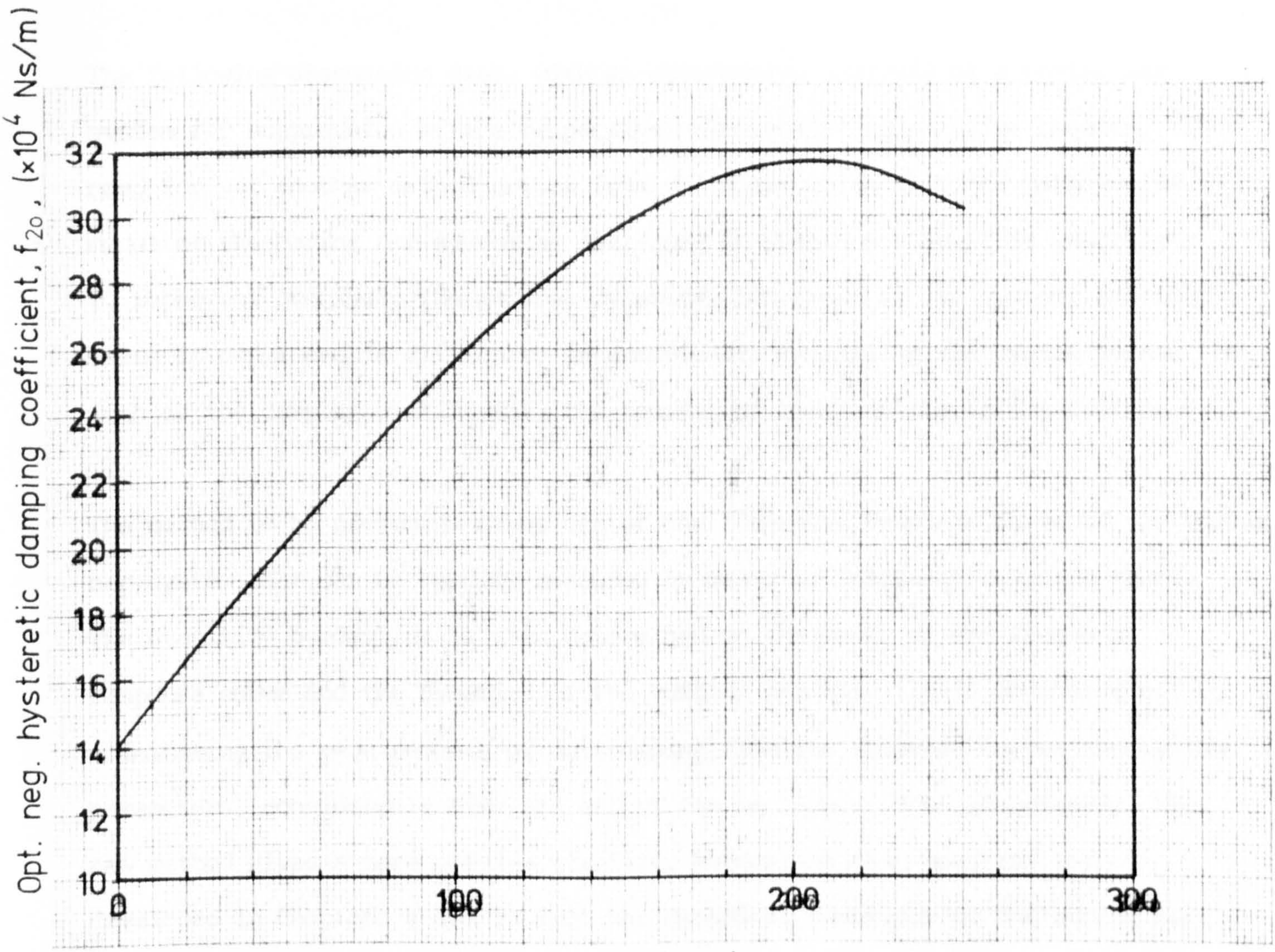

Fig D2 Relation between the optimum negative hysteretic damping coefficient and the bung length of a tungsten-bunged bar

APPENDIX E GRAPHICAL METHOD FOR STABILITY ANALYSIS OF BORING BAR

The following discussion deals with an alternative analysis of a boring bar system for suppression of the respective primary and regenerative chatter. The need for yet another method arises from the observation that the mathematical model of the boring bar system as developed in Chapters 4 and 5 is inadequate to represent precisely the general dynamical behaviour of the system; and that there is considerable difficulty in numerically evaluating the system parameters such as the damping coefficient, the equivalent mass and the spring stiffness.

The method to be presented makes use of the frequency response curve of the boring bar system that can be readily measured by means of frequency response tests. The stability borderline is then determined on the basis of the frequency response curve and the dynamics of the cutting process. It is obvious that, by eliminating the requirements of determining from the response curves the system parameters, considerable time and effort can be saved. More importantly, the new method gives a more precise stability borderline than does the method developed in Chapters 4 and 5 since the dynamical behaviour of the boring bar is characterised absolutely by the frequency response curve whereas in the previous method the mathematical model is inexact due to assumptions and simplifications made in its formulation.

(1) Suppression of primary chatter

The dynamical behaviour of the boring bar system is characterised by its frequency response curve which has a frequency transfer function $G_b(j\omega)$. It has been explained in section 5.2 that the source of primary chatter can be modelled by a hypothetical negative viscous damping force, and a spring force arising from the change of radial force with depth of cut.

In the form of a frequency transfer function, the cutting process dynamics is characterised by $G_c(j\omega) = a - jf_1\omega$ where a is the rate of change of radial force with respect to the depth of cut and $-f_1$ is the hypothetical negative viscous damping coefficient.

The process of cutting with the boring bar involves the interaction between the two frequency transfer functions, namely, $G_b(j\omega)$ and $G_c(j\omega)$. A block diagram representation is given in Fig E1 which is seen to incorporate a feedback loop. In this diagram the input signal is $R(j\omega)$ and is the desired change in the depth of cut, which is always zero for realistic constant-depth machining. The output signal $X(j\omega)$ is the actual change in depth of cut that is fed back in its entirety to the summation point from which the error signal $E(j\omega) = R(j\omega) - X(j\omega)$ is derived. Since $R(j\omega)$ is zero, it follows that $E(j\omega) = -X(j\omega)$. The dynamic force $F(j\omega)$ emerges from the cutting process and acts on the boring bar system.

From a control point of view, $G_c(j\omega)$ can be regarded as the gain of a proportional-plus-differential controller. Hence, the stability of the closed-loop system in Fig E1 depends on a combination of values that a and f_1 assume. It is to be noted that the physical interpretation of parameters a and f_1 is exactly identical to that described in section 5.2.2, according to which, it is correct to understand that in general as the depth of cut increases, f_1 increases whereas a decreases.

In subsequent discussions, the argument $j\omega$ in the signal functions and the transfer functions will be dropped for notational convenience. Thus for example, $G_c(j\omega)$ becomes G_c.

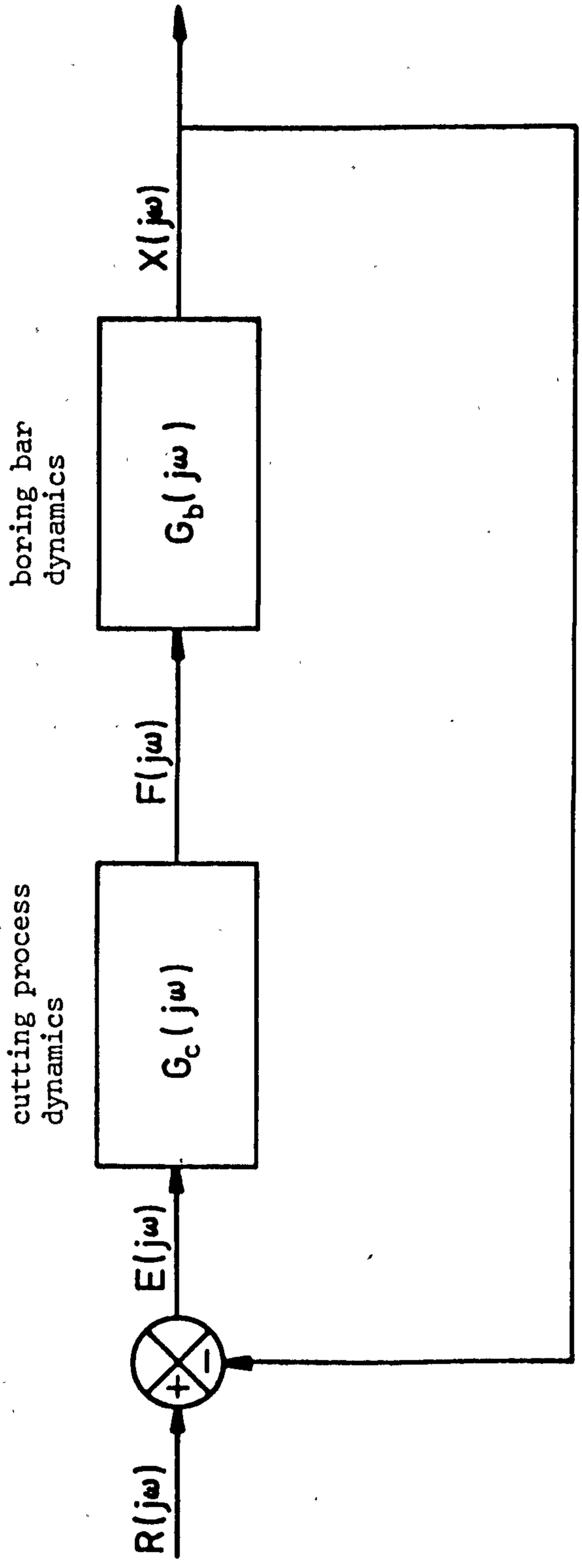

Fig 4.1 Block diagram representation of boring bar during machining

The stability analysis is carried out in a number of stages. First, we need to know the forward path frequency transfer function given by the product $G_c G_b$. It is noted that both G_c and G_b are complex variables. Thus, using the exponential form of representation,

$$G_c = r_c e^{j\varphi_c} \quad \text{and} \quad G_b = r_b e^{j\varphi_b}$$

where r_c and r_b are the gain magnitudes of the cutting process and the boring bar respectively. Both r and φ are a function of the angular frequency ω. Graphically, r is the gain amplitude response curve and φ is the phase shift curve. The product of

$$G_c \cdot G_b = r_c \cdot r_b \, e^{j(\varphi_c + \varphi_b)}$$

and it follows that the gain amplitude response curves of G_c and G_b will have to be multiplied whereas the corresponding phase shift curves are summed algebraically. The operation of multiplication is tedious and is, therefore, undesirable. To alleviate this difficulty, G_c and G_b are first converted to a decibel scale, ie dB using the conversion formula $20 \log_{10} r$. Then they are represented individually by a diagram which has a similar appearance to the ordinary frequency response curve except that the ordinate for gain is now expressed in dB. For this reason, we shall refer to this as the logarithmic frequency response curve. A typical plot in the frequency range of interest is shown in Fig E2. The virtue of logarithmic representation becomes immediately obvious when forming the product $G_c G_b$ in which the operation of multiplication $r_c \cdot r_b$ becomes one of addition, ie, $20 \log_{10} r + 20 \log_{10} r_b$. It is noted that the phase shifts for G_c and G_b are simply summed algebraically as before. The logarithmic plot of the product $G_c G_b$, based on results in Fig E2, is shown in Fig E3.

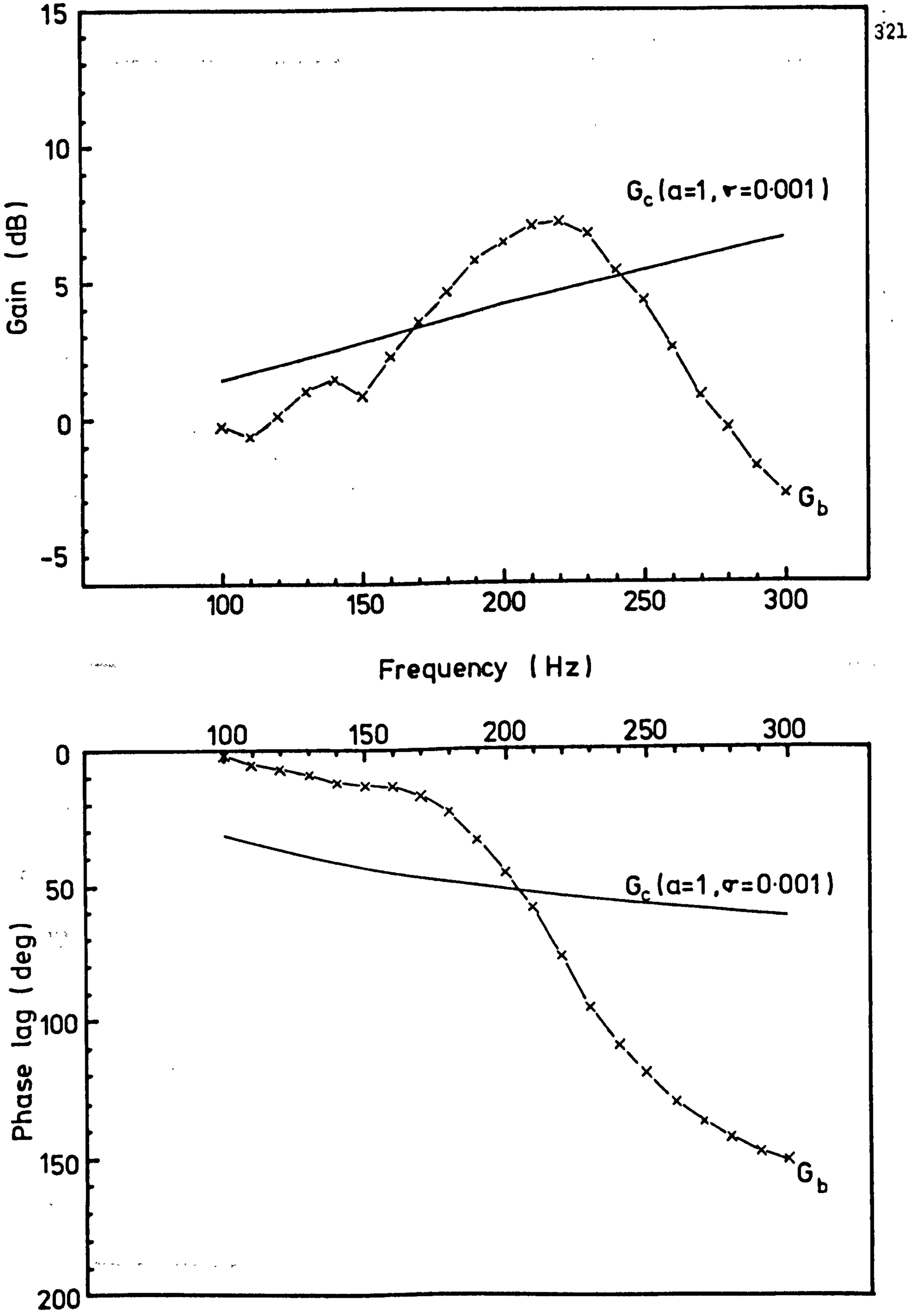

Fig E2 Logarithmic frequency response curves for G_c and G_b. σ = 0.001 and a = 1 in G_c; and G_b is the horizontal frequency response of optimally-tuned main-slug tungsten-bunged bar (Fig 7.21)

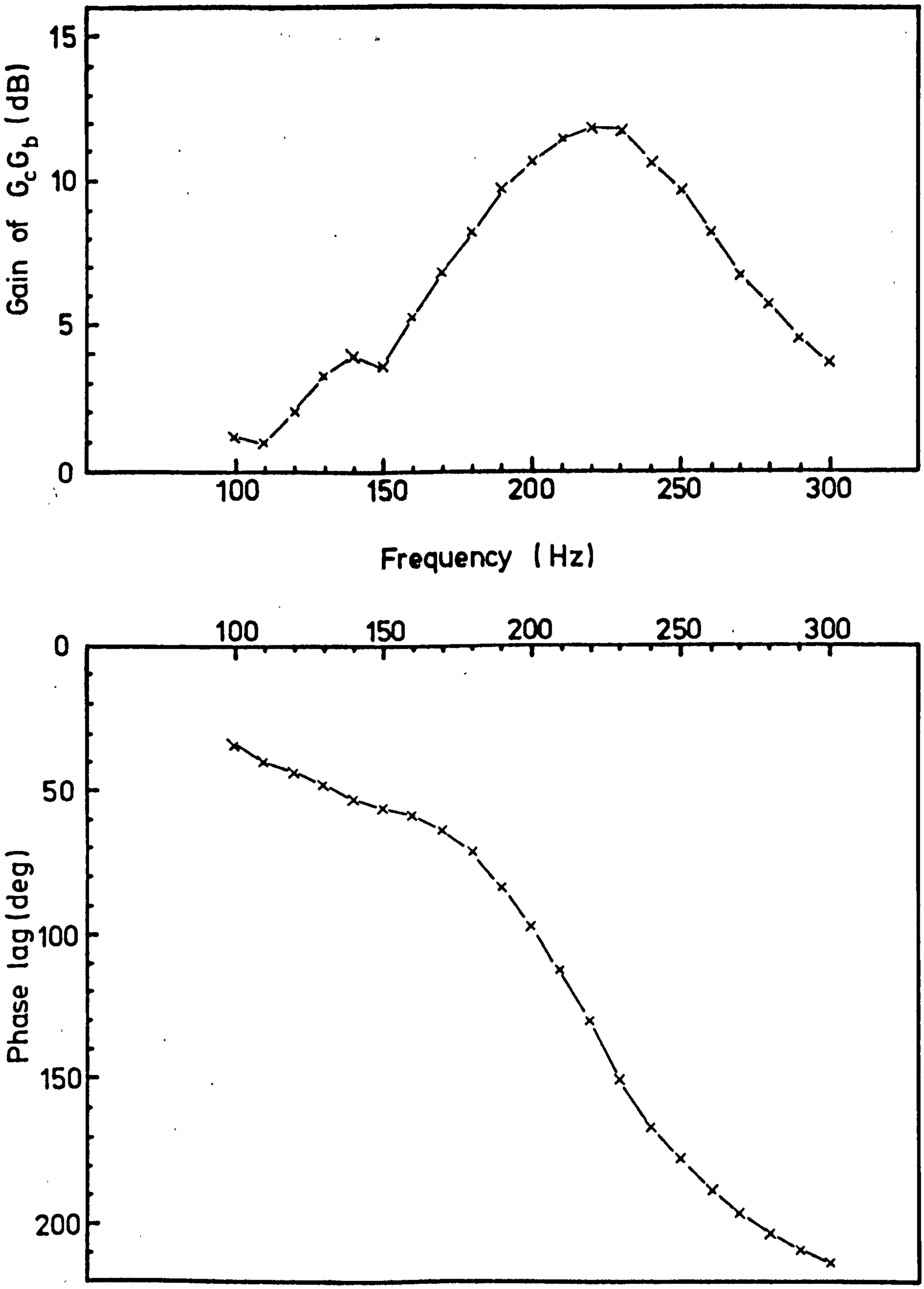

Fig E3 Logarithmic frequency response curves for $G_c G_b$, where $\sigma = 0.001$, $a = 1$; and G_b refers to the horizontal frequency response of optimally-tuned main-slug tungsten-bunged bar (Fig 7.21)

The second stage of the analysis deals with the transfer of results from the logarithmic plot to a Nichols chart which is a special form of graph for use in the analysis of stability behaviour of a closed-loop unity feedback linear system such as the one being studied. The chart is shown in Fig E4. To effect a transfer of result at a certain frequency, we note the gain and phase values at that frequency and locate a corresponding point in the Nichols chart using the gain and phase as its coordinates. We proceed in this fashion until every data point of interest is transferred.

In the final stage, we need to make use of the part of the linear control theory relevant to the utility of Nichols chart. According to the theory, a closed-loop system is stable when its forward path frequency response curve, ie G_cG_b passes to the left of the 0dB/-180^o point (see Fig E5) on the Nichols chart in the direction of increasing frequency ω . Hence, the closed-loop system as depicted in Fig E4 is unstable whereas that in Fig E5 is stable. The quality of stability, if stability exists, depends on the width of the phase and gain margins which are indicated in Fig E5. In most situations, a negative phase or gain margin has no practical significance because the closed-loop system is already unstable and, irrespective of the width of these negative margins, an unstable system serves no practical purpose. Nevertheless, in this discussion, we shall encounter and utilise the concept of negative gain margin as will be explained presently. In particular, the system is on the stability borderline when its forward path frequency response curve passes through the 0dB/-180^o point. Obviously, in this case both the gain and phase margins are zero.

So far, it has been assumed that G_c is known. However, unlike G_b which is

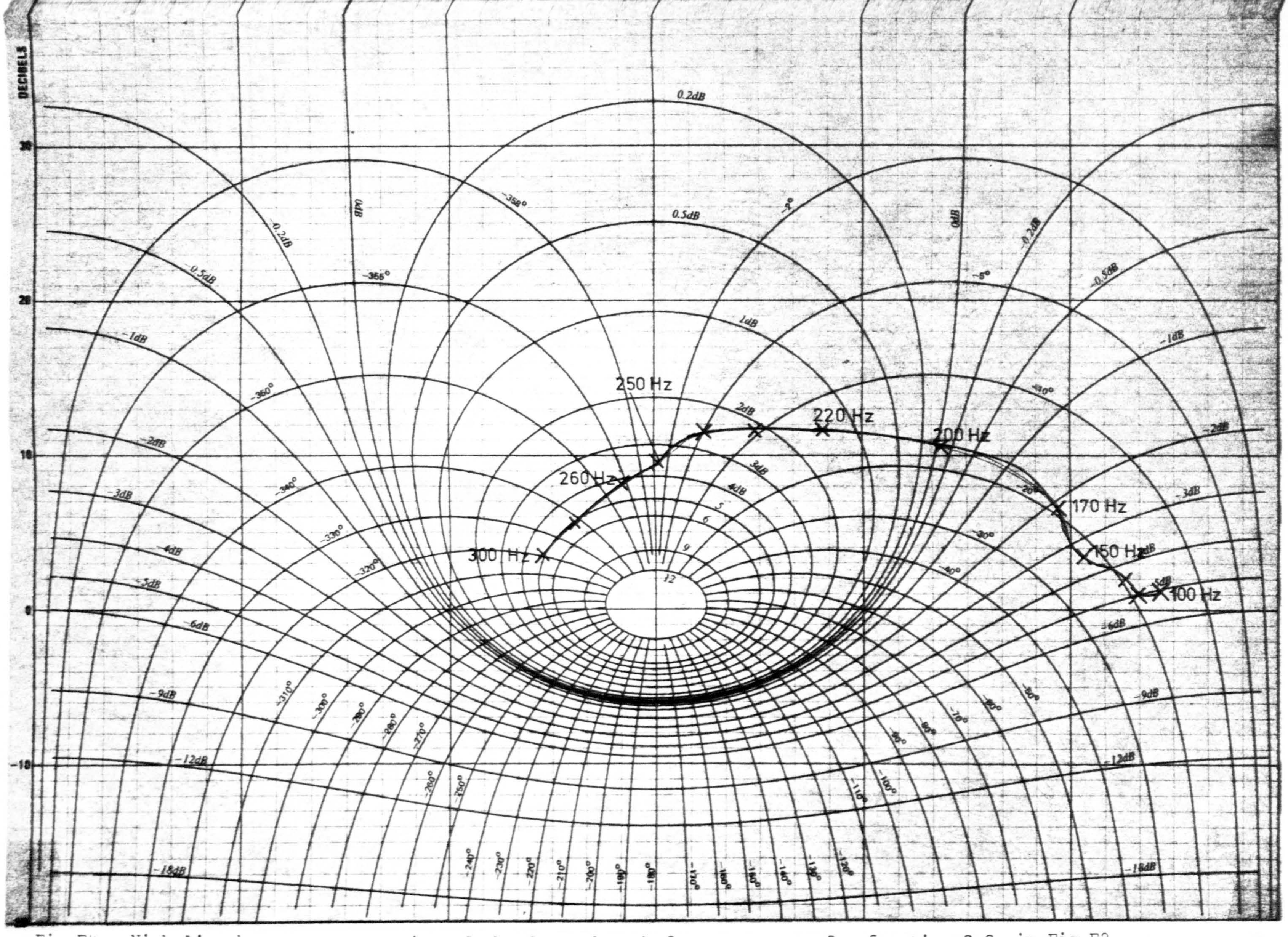

Fig E4 Nichol's chart representation of the forward path frequency transfer function $G_c G_b$ in Fig E3

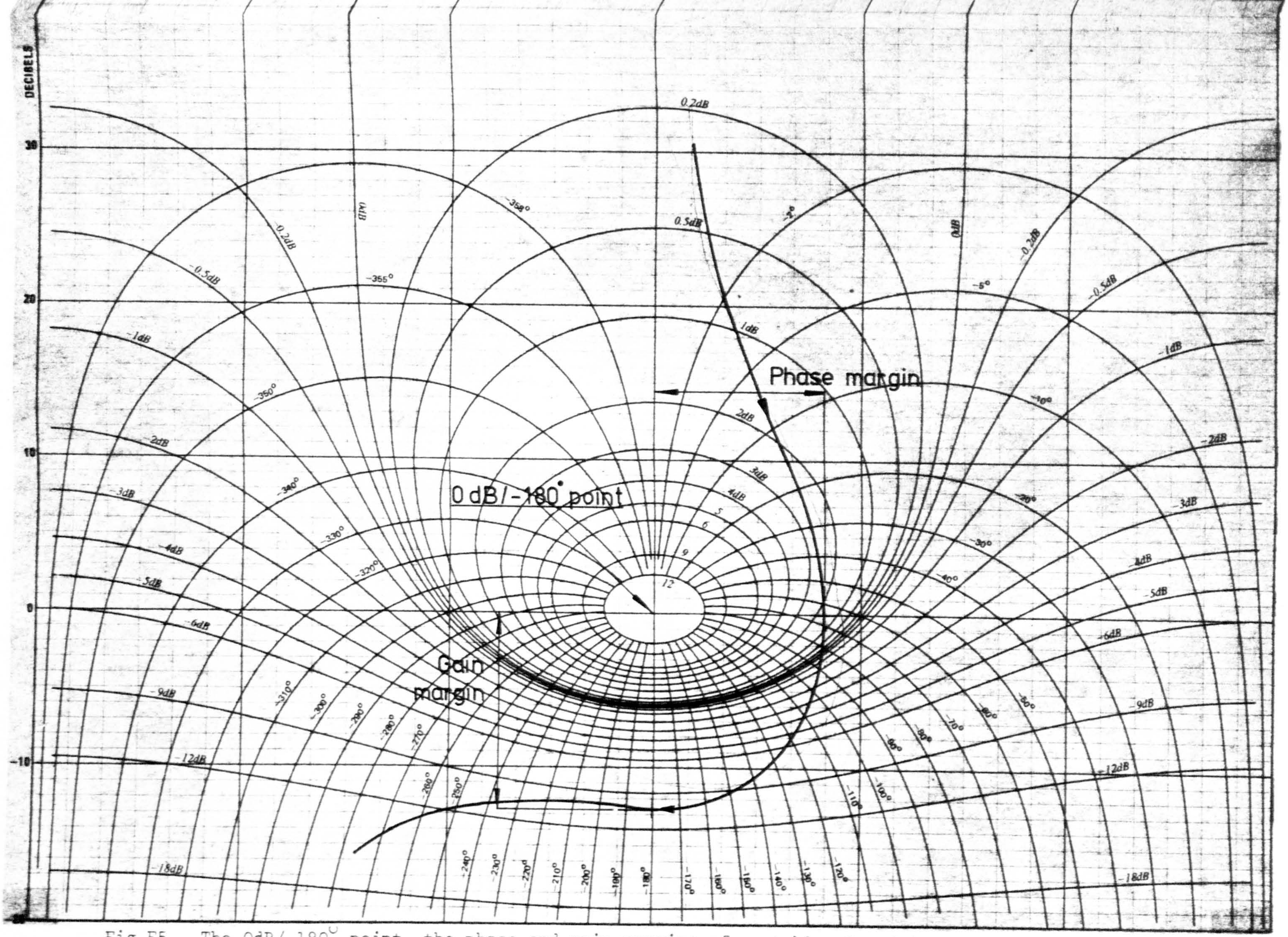

Fig E5 The 0dB/-180° point, the phase and gain margins of a stable closed-loop system

readily measurable from experiments, determining G_c for each and every cutting condition by way of experiments is a daunting task. In this analysis, G_c is modelled by the expression $G_c = a - j\omega f_1$, where f_1 and a are related to the cutting conditions as explained in section 5.2. This expression may be rewritten as $G_c = a\left[1 - j\frac{\omega f_1}{a}\right]$ so that $\frac{\omega f_1}{a}$ is taken as a single variable. The gain of G_c in decibels is

$$20 \log_{10}|G_c| = 20 \log_{10} a + 20 \log_{10}\sqrt{1 + (2\pi f \sigma)^2}$$

$$= 20 \log_{10} a + 10 \log_{10}[1 + 2\pi f \sigma)^2] \qquad \text{(E1)}$$

Where the ratio $\frac{f_1}{a}$ is replaced by σ and ω by $2\pi f$ with f as the frequency in Hz.

The first term on the right-side of the preceding equation is a constant when a is fixed. The second term is noted to be a function of frequency f when σ is fixed.

The phase shift φ_c of G_c is given by

$$\tan \varphi_c = -2\pi f \sigma \qquad \text{(E2)}$$

and since both f and σ are numerically positive, the phase shift φ_c will have to fall in the interval

$$0 \leqslant \varphi_c \leqslant -\frac{\pi}{2}$$

Graphically, once certain values are assigned to a and σ , a logarithmic frequency response diagram for the gain and phase can be drawn using the respective eqts (E1) and (E2). The diagrams of G_c and G_b can be added graphically and the result is then transferred onto a Nichols chart as described before. For convenience, in using eqt (E1) for drawing its logarithmic diagram, a is set to unity, and it follows that the first term

on the right-side of eqt (E1) becomes zero. To decide how far the closed-loop system is removed from the stability borderline, we note from the Nichols chart the gain margin designated by G_m which is negative if the system is unstable or positive if stable. Graphically, a change in the value of a from unity in eqt (E1) is equivalent to a vertical shift of the forward path frequency response curve without affecting its shape since σ is maintained constant. Specifically, an upward shift is equivalent to an increasing a from unity, and vice versa. At the stability borderline, the gain margin G_m is zero. Thus, the critical value of a for the system to border on stability is obtained from the following expression,

$$G_m = 20 \log_{10} a$$

from which

$$a = \text{Anti-}\log_{10} \frac{G_m}{20}$$

where the gain margin G_m may take on positive or negative values.

a) <u>A numerical example</u>

Fig E2 shows the logarithmic frequency response curves for G_c and G_b. G_b is the horizontal frequency response of the optimally-tuned main-slug tungsten-bunged bar as illustrated in Fig 7.21; but in the logarithmic representation as in Fig E2 the amplitude will have to be converted to decibels as shown in the following example.

Refer to Fig 7.21, at the frequency of 200 Hz, the response amplitude of the bar to an impressed force of 4.448 N is 9.3 μm. The logarithmic ratio of amplitude to force is 20 $\log_{10}$ (9.3/4.448) = 6.41 dB which is known as the gain. The corresponding phase shift, also from Fig 7.21 is 46°.

G_c is the frequency transfer function of the cutting process. Taking a = 1 N/um and σ = 0.001s, at the frequency f = 200 Hz, the gain of G_c, by eqt (E1), is

$$20 \log_{10} 1 + 10 \log_{10}\left[1 + (2\pi \times 200 \times 0{\cdot}001)^2\right] = 4{\cdot}11 \text{ dB}$$

Also, by eqt (E2), the corresponding phase shift is given by

$$-\varphi_c = \tan^{-1} 2\pi f\sigma = \tan^{-1}(2\pi \times 200 \times 0{\cdot}001) = 51{\cdot}5^\circ$$

Combining the gain and phase of both G_b and G_c in the manner described previously, we obtain the frequency response curves for G_cG_b as shown in Fig E3. Thus, at the frequency f = 200 Hz, the gain of G_cG_b = 4.11 + 6.41 = 10.52 dB, and the phase = $46^\circ + 51.5^\circ = 97.5^\circ$.

The Nichols chart representation of the forward path frequency transfer function G_cG_b is shown in Fig E4. The gain margin G_m is, by measurement, -9.6 dB. Since G_m is negative, the system is unstable for a = 1 N/um and σ = 0.001s. For the system to border on stability, the value of a, by eqt (E3), has to be a = anti-log (-9.6/20) = 0.3311 N/um. Since = f_1/a, it follows that $f_1 = \sigma a$ = 0.001 x 0.3311 = 331.1 x 10^{-6}N-s/um = 331.1 N-s/m.

The following table shows, for the optimally-tuned main-slug tungsten-bunged bar, the relations of σ, G_m, a and f_1.

σ,(s)	G_m,(dB)	a,(kN/m)	f_1,(N-s/m)
0.0005	2.72	731	366
0.001	9.6	331	331
0.005	23.89	63.9	319
0.01	30.00	31.6	316
0.05	43.96	6.34	317
0.1	49.98	3.17	317
0.5	63.97	0.63	317
1	69.97	0.32	317
2	76.01	0.16	317

Graphically, the variation of f_1 in relation to a is shown in Fig E6.

It is noted that as a decreases subsequent to an increasing depth of cut, the value of f_1 decreases at first but eventually settles down to a minimum constant value termed the asymptotic value which, in this case, is 317 N-s/m. Being a negative damping coefficient, the higher its value, the more stable the system becomes. It is convenient that we employ this minimum f_1 value as a measure of the degree of stability that a particular slug-damped bar can offer.

(2) Suppression of regenerative chatter

The approach is similar to that presented in section E1 for the case of primary chatter. The only difference is in the assumed mathematical form of G_c. For the case of regenerative chatter suppression, it has been shown in section 5.3 that the cutting process can be modelled by a negative hysteretic damping device with a coefficient $-f_2$ together with a spring element of stiffness a'. Thus, the frequency transfer function of the cutting process

$$G_c = a' - j f_2$$

or

$$G_c = a'(1 - j\sigma') = a'\sqrt{1+\sigma'^2}\, e^{j\varphi_c'}$$

where $\sigma' = \frac{f_2}{a'}$ and $\varphi_c' = -\tan^{-1}\sigma'$

It follows that the gain of G_c in dB $= 20 \log_{10} a' + 10 \log_{10}(1+\sigma'^2)$ ...(E4)

and the phase shift $\varphi_c' = -\tan^{-1}\sigma'$ ...(E5)

So, for the case of regenerative chatter, eqts (E4) and (E5) will replace eqt (E1) and (E2) respectively.

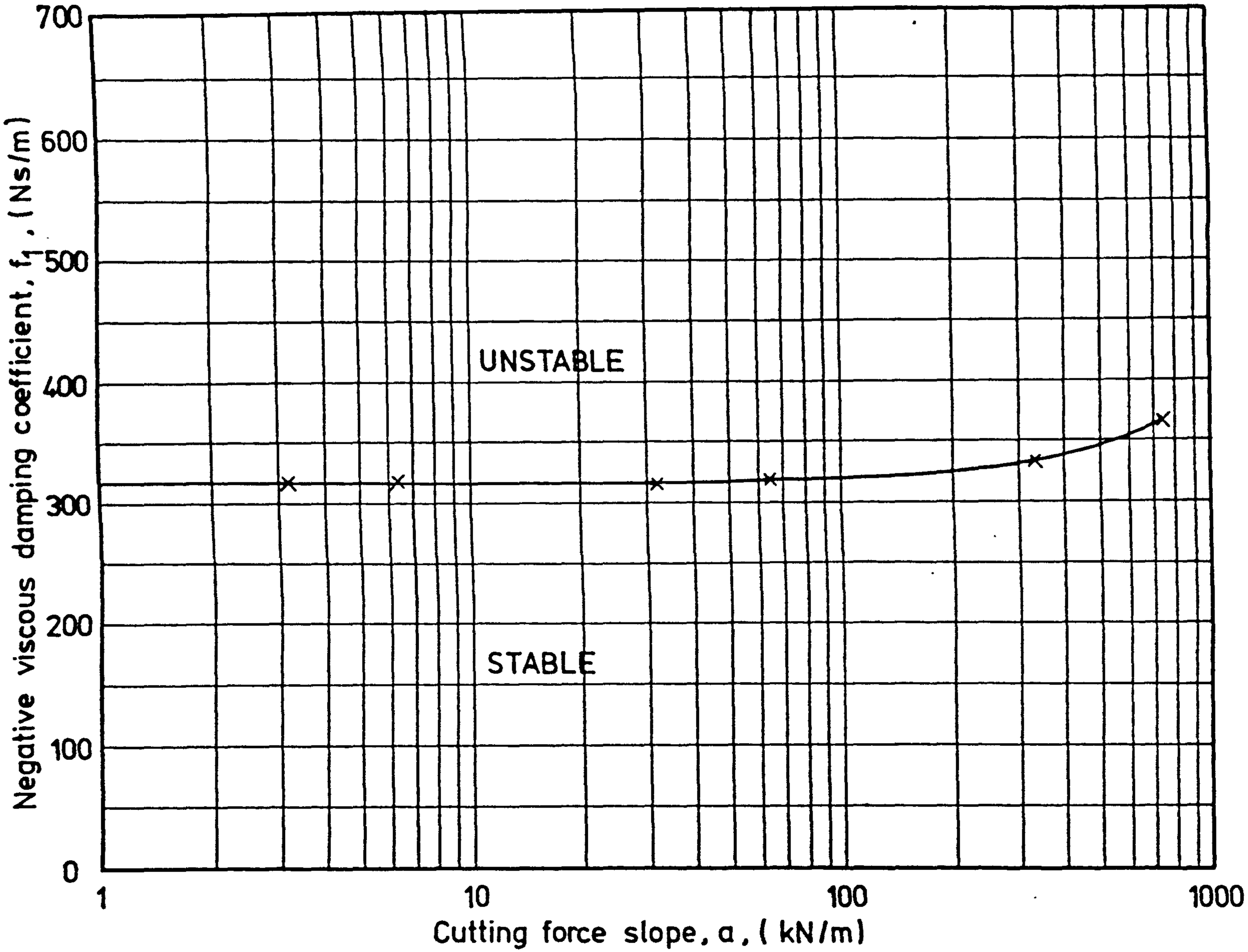

Fig E6 The stability borderline in the f_1-a plane for the optimally-tuned main-slug tungsten-bunged bar

Similar to the case of primary chatter, it is also observed that as τ' increases, leading to a decreasing a', the value of f_2 decreases at first but settles down to a minimum constant termed the asymptotic value. Fig E7 shows the manner f_2 decreases as a' decreases for the same bar employed in the previous example. Accordingly, this minimum f_2 value can be employed fruitfully as an indicator of the degree of stability that a particular bar can offer.

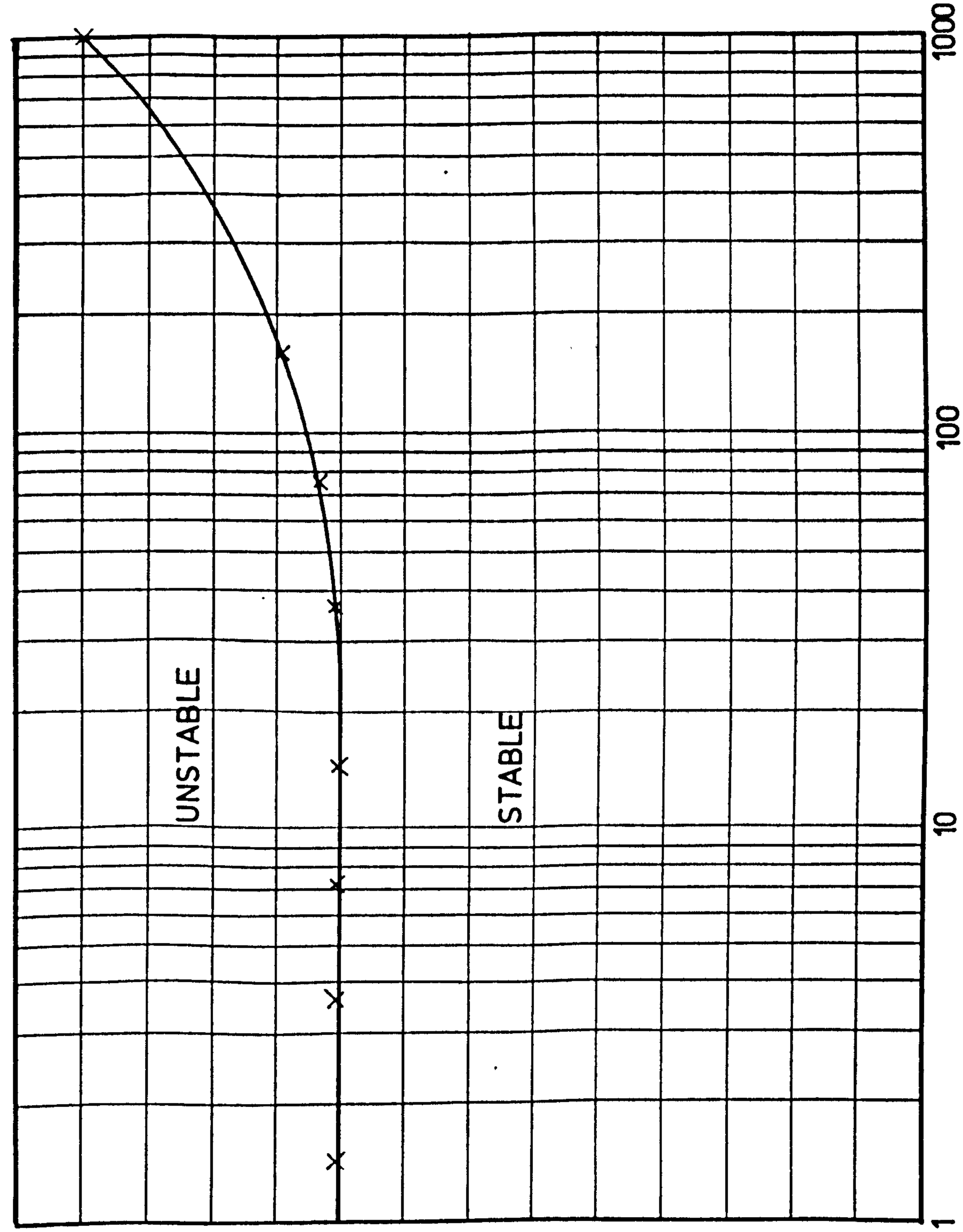

Fig E7 The stability borderline in the f_2-a' plane for the optimally-tuned tungsten-bunged bar